Heat and Mass Transfer from Jet Impingement Flow for Drying Machines

Wärme- und Stoffübertragung von Prallstrahl-Strömungen für Trockenmaschinen

Von der Fakultät für Maschinenbau

der Gottfried Wilhelm Leibniz Universität Hannover

zur Erlangung des akademischen Grades

Doktor-Ingenieur

Dr.-Ing.

genehmigte Dissertation

von

M.Sc. Ali Chitsazan

2022

1. Referentin: Prof. Prof. h.c. Dr.-Ing. Birgit Glasmacher

2. Korreferent: Prof. Dr.-Ing. Stephan Kabelac

3. Korreferent: Prof. Dr.-Ing. Georg Klepp

Tag der Promotion: 09.11.2020

Zusammenfassung

Titel: Wärme- und Stoffübertragung von Prallstrahl-Strömungen für Trockenmaschinen

Prallstrahlen werden wegen ihres guten Wärme- und Stoffübergangs häufig zum Trocknen von Materialien wie Papier und Textilien verwendet. Bei industriellen Trocknungsanlagen sind neben effizienten Transporteigenschaften die Kraft des Strahls auf dem zu trocknenden Material wichtig, insbesondere für empfindlichen Produkte (z.B. Papier, Textilien) oder empfindliche Oberflächen (z.B. Anstrich, Beschichtung). Dabei müssen zahlreiche Einflussfaktoren und Parameter für den einzelnen Strahl sowie bezüglich der Wechselwirkung zwischen den Strahlen berücksichtigt werden. Für eine Auslegung von Trocknungsanlagen mit komplexen Düsenströmungen fehlen oft die passenden Unterlagen sowie ein vertieftes Verständnis der Wechselwirkung aller Konstruktions- und Betriebsparameter. Diese werden jedoch benötigt, um industrielle Trocknungsanlagen zu optimieren, einerseits bezüglich der Kapitalkosten (Gerätegröße) andererseits bezüglich der Betriebskosten (Energieverbrauch).

Im Rahmen dieser Arbeit werden der Wärme- und der Stoffübergang sowie die Druckkraft für einzelne Runddüsen, Düsenreihen und Düsenfelder und einer bewegten Fläche untersucht. Dazu werden numerische Simulationen durchgeführt und der Einfluss folgender Parameter variiert: Austrittsgeschwindigkeit des Strahls, Düsendurchmesser, Abstand der Düse zur Oberfläche, Abstand der Düsen, Neigungswinkel des Prallstrahls, Krümmung der Oberfläche und Geschwindigkeit der Oberfläche. Anschließend wird auf Grundlage der maßgeblichen Einflussgrößen eine Optimierung des Düsenfeldes durchgeführt. Für die mittleren Nusselt-Zahlen- und Koeffizienten der Druckkraft werden Korrelationsgleichungen aus den Simulationsergebnissen abgeleitet.

Die vorliegende Arbeit zeigt, dass es möglich ist, die komplexen Strömungsphänomene, die bei industriellen Trocknungsprozessen auftreten, unter Verwendung von generischen Programmen zur Strömungssimulation (CFD) und Wirbelviskositätsmodellen zur Turbulenzmodellierung mit ausreichender Genauigkeit wiederzugeben. Auf diese Weise können komplexe und umfangreiche Berechnungen auf der Grundlage einer aufwändigeren Turbulenzmodellierung (z.B. Reynolds-Stress-Modell oder Large Eddy Simulation) ebenso vermieden werden wie die aufwändigen Messungen in Düsenfeldern mit bewegten Oberflächen. Unter Verwendung der aus den Berechnungen abgeleiteten Korrelationsgleichungen können die Abhängigkeiten der wichtigsten Einflussgrößen leicht bestimmt werden.

Die Analyse der berechneten Strömungsfelder zeigen unterschiedliche Strömungsbereiche aufgrund der unterschiedlichen Wechselwirkungen. Um diese Phänomene näher zu erforschenen sind weitere Untersuchungen möglich: Simulationen, die auch die Turbulenz weitgehend erfassen (z.B. Large Eddy Simulation, Direct Numerical Simulation) sowie Messungen der Prallstrahlströmung und des Wärme- bzw. Stoffübergangs.

Schlüsselwörter: Prallstrahlen, Wärmeübertragung, Druckkraft, Energieverbrauch, Oberflächenbewegung, Oberflächenkrümmung, Optimierung

Abstract

Title: Heat and Mass Transfer from Jet Impingement Flow for Drying Machines

Multiple impinging jets are widely used for their enhanced heat and mass transfer characteristics, especially for drying of material such as paper and textiles. Efficient transport characteristics between a drying medium and the material being dried as well as the jet impingement force acting on the force sensitive products (i.e. paper, fabrics) or force sensitive surfaces (i.e. painted, coated) are very critical in the industrial drying applications for the overall performance of the operation. Many variables and influencing factors and parameters need to be considered for the proper design of such multiple impinging jet systems. At present, a complete understanding of the effect of all the design and operating parameters is lacking. Designers should optimize the design parameters of industrial drying equipment to achieve the minimum capital costs (size of the apparatus) and running costs (energy consumption).

In the framework of this thesis, the heat and mass transfer rates and pressure force between the multiple impinging round jets and moving surface are investigated numerically. Numerical simulations have been conducted to characterize the impinging jet heat and mass transfer and pressure force on a moving surface with an array of impinging round jets varying the following parameters: jet Reynolds number, nozzle-to-surface distance, jet-to-jet spacing, jet exit angle, relative surface curvature and relative surface velocity. Then, the key controlling design variables such as the nozzle-to-surface distance and the jet-to-jet spacing both normalized by the jet exit diameter (i.e., H/d and S/d), the jet exit velocity, the surface velocity and the jet exit angle have been considered for a design optimization. Correlations describing the average Nusselt number and pressure force coefficient for single row jet configurations impinging on the flat and curved surfaces have been developed.

The present work illustrates that it is possible to address the effects of the complex flow phenomena as encountered in industrial drying process using generic CFD codes with good results. Thus complex and extensive computations based on elaborate and time consuming turbulence modelling (i.e. RSM or LES) may be avoided as well the expensive measurements of jet arrays impinging on moving surfaces. Using the correlation equations derived from the computations the dependencies for the main parameters over a wide range may be easily be determined. The analysis of the flow fields showed many different phenomena interacting, leading to different flow regimes. In order to assess these phenomena further investigations, preferably based on LES and DNS modelling and flow measurements are needed.

Preface

First and foremost, I would like to thank my supervisor Prof. Dr.-Ing. Birgit Glasmacher for the opportunity to complete this thesis during my time as an external doctoral student at the Institute for Multiphase Processes & Center for Biomedical Engineering at the Leibniz University Hannover. She supported my thesis by her guidance, expertise, and valuable advice.

I would like to express my special appreciation and gratitude to Prof. Dr.-Ing. Georg Klepp as co-supervisor for this thesis at the Institute for Energy Research, Ostwestfalen-Lippe University of Applied Sciences, Lemgo, for his continuous support, guidance, and patience that helped my thesis as well as given the privilege to work on several funded projects.

A special thanks goes to Mr. Dipl.-Ing. Walter Kamphausen at Ostwestfalen-Lippe University of Applied Sciences, Lemgo for the nice and friendly atmosphere. The financial support by Ostwestfalen-Lippe University of Applied Sciences, Lemgo for a part of this thesis is highly acknowledged. A special thanks to my neighbors in Lemgo for their invaluable support and friendship.

I would like to specifically thank my Parents for their love and constant support throughout the time of my education. They taught me patience and hope in life. Last, but not least, a special thanks goes to my siblings especially Roya Chitsazan, her husband Dr. Mahmoud Moazzami, and her children (Sina, Sara, and Sarina) who supported and assisted me in making important decisions before and during my thesis. There are no words that can express my appreciation for all the motivation.

Above all, thank you God for allowing me to come thus far.

Lemgo, August 2020

CONTENTS

List of Figures

List of Tables

List of Symbols

Latin notation

A_f: open area ratio, total jet area to heat transfer area

A: surface area

C_a: partial concentration of vapor in drying air

C_D: jet surface discharge coefficient

C_f: force coefficient

c_p: specific heat capacity

C_s: saturated vapor concentration

$\partial C / \partial n$: mass concentration gradient component normal to the wall

$ConViol_j$: amount by which the j-th constraint is violated

d: jet exit diameter

D: surface diameter or mass diffusion coefficient

F: force

G_c: channel cross-flow mass flux based on channel cross sectional area

G_j: individual jet mass flux based on jet hole area

$\overline{G}_j$: mean jet mass flux based on jet hole area for the array

h: heat transfer coefficient

H: nozzle-to-surface distance

h_m: surface mass transfer coefficient

$\dot{H}_j$: energy for heating the air jet

$\dot{H}_v$: enthalpy of evaporation of the water

Δh_v : evaporation enthalpy

i, j, k: tensor indices

k_c: fluid thermal conductivity

l: jet plate length

L: nozzle length

$LinWt_i$: linear weight for the i-th objective

Ma: Mach number

$\dot{m}$: mass flow rate through one jet orifice

$\dot{m}_v$: evaporation mass flux

N: number of cells

N_{con}: number of constraints

N_{obj}: number of objectives

$Norm_i$: normalization value for the i-th objective

$Norm_j$: normalization value for the j-th constraint

Nu: Nusselt number

Nu_{aveF}: averaged Nu determined from the correlation of Florschuetz et al. (1981)

Obj_i: response value for the i-th objective

p: apparent order of GCI method

P: pressure

P_a: partial pressure of the vapor in the ambient air

P_s: saturated vapor pressure

Pr: Prantel number

q: convective heat flux

q_Θ : sources or sinks for the scalar

Q: flow rate

$QuadWt_j$: quadratic weight for the j-th constraint

r: radial coordinate or refinement factor

R_1: Height of curved surface

R_2: Half of chord length

Re: Reynolds number

R_v: gas constant of the vapor

S: jet to jet distance

S_x: Streamwise jet-to-jet distances

S_y : spanwise jet-to-jet distances

S_{ij}: strain rate tensor

Sc: Schmidt number

Sh: Sherwood number

$Sign_i$: sign for the i-th objective

T: temperature

T_t: Reynolds stress tensor

$\partial T / \partial \vec{n}$: temperature gradient component normal to the wall

U_i: instantaneous components of the velocity vector in the direction X_i

u^*: friction velocity

V: jet exit velocity

W: jet surface width

X, Y, Z: coordinates

y^+: dimensionless wall distance

Greek notation

α: thermal diffusivity

ε: dissipation rate of turbulence kinetic energy *k*

ω: specific dissipation rate of turbulence kinetic energy

θ: jet exit angle with respect to the horizontal axes, degree

v: kinematic viscosity

v_t: turbulent viscosity

ρ: density of fluid

τ: shear stress

δij*:* Kronecker delta

Φ: general instantaneous variable

Φ′: general fluctuating quantity

$\overline{\Phi}$: general average quantity

Θ: general scalar variable

Γ_Θ: diffusivity of Θ

φ_k: solution on the *k*th grid

Subscripts

a: ambient

ave: average

aw: adiabatic wall

c: cross-flow

j: jet

max: maximum

min: minimum

opt: optimum

s: saturation

st: stagnation point

t: total

w: wall

Abbreviations

CFD: computational fluid dynamic

Cr: curvature ratio

DNS: direct numerical simulation

GCI: grid convergence index

LES: large eddy simulation

LRDM: low Re damping modification

RANS: Reynolds-average navier-stokes

RSM: Reynolds stress model

VR: velocity ratio; surface-to-jet velocity

SDEC: specific drying energy consumption

SST: shear stress transport

Chapter 1

1. Introduction

Multiple impinging jets are widely used for their enhanced heat and mass transfer characteristics, especially for drying of sheets such as paper and textiles. Efficient transport characteristics between a drying medium and the material being dried and also jet impingement force towards the force sensitive products (i.e. paper, fabrics) or force sensitive surfaces (i.e. painted, coated) are very critical in the industrial drying applications for the overall economics of the operation. Many variables and influences need to be considered for the proper design of such multiple impinging jet systems. Although a lot of studies on the impinging jet flow have been performed consistently up until recently, further studies are still required to understand the flow and heat transfer characteristics at challenging geometry and boundary conditions such as high Reynolds number, small jet-to-surface distance, small jet-to-jet spacing, surface motion and curvature more accurately, and to give a guideline for an optimum impinging jet design in industrial drying applications.

At present, a complete understanding of the effect of all the design and operating parameters is lacking. With the advent of high performance computing, the numerical simulation is gradually replacing the expensive and tedious laboratory and pilot-scale studies wherever possible. Many researchers simulated the turbulent impinging jets using different turbulence models. However, with the recent development of the numerous powerful computational fluid dynamics (CFD) programs, use of the commercial CFD programs has been proven to be a useful tool in numerically experimenting with multiple impinging jets as complex fluid flow problems.

Designers should optimize the design parameters of industrial drying equipment to achieve the minimum capital costs (size of the apparatus) and running costs (energy consumption).

This thesis is inspired by a project funded by the ZIM program. The project (an energy efficient dryer) aims at reducing the energy consumption of the dryer used for paper coating.

1.1 Research Objectives and Scope

Comprehensive numerical experiments on the heat and mass transfer from multiple impinging round jets will be conducted in this study. As the first case in this investigation, the single impinging jet is considered. The overall objective is a quantification of accuracy for the predicted results for single round jet and an understanding of the discrepancies that occur

between numerical simulation and experimental data. This is important for the correct interpretation of results obtained for the multiple impinging round jets.

The objectives of this work are to predict the heat and mass transfer rates and pressure force between multiple impinging round jets and moving surface using computational fluid dynamics (CFD). Numerical simulations have been conducted to characterize the impinging jet heat and mass transfer and pressure force on a moving surface with an array of angled impinging round jets varying the following parameters:

- Jet Reynolds number
- Nozzle-to-surface distance
- Jet-to-jet spacing
- Jet exit angle
- Relative surface curvature
- Relative surface velocity

Then, the key controlling design variables such as the nozzle-to-surface distance, the jet-to-jet spacing, the jet exit velocity, the surface velocity and the jet exit angle have been considered for the optimum design. These parameters affect the heat transfer rate, pressure force and drying energy consumption and therefore the optimization is required. Several correlations describing the average Nu number and the pressure force coefficient for single row jet configurations impinging on the flat and curved surfaces have been developed.

1.2 Outline of Chapters

In the beginning, the flow of impinging jets is briefly reviewed and the background of the methods used here are presented.

Next a literature review reveals the necessity of further investigations with regard to several parameters as used in industrial drying.

A numerical model is built and validated against a well-established reference test case of a single impinging circular jet.

The flow field for jet arrays with different geometric parameters and fixed as well as moving target surfaces are computed. The results are discussed and compared to data from the literature and correlation equations for the heat transfer and pressure force coefficient are derived.

Then the flow field for jet arrays for fixed and moving curved surfaces are computed and discussed and equations for heat transfer and pressure force are correlated.

Finally based on the computational model an optimization with regard to heat transfer rate, energy consumption and pressure force is undertaken.

Chapter 2

2. Literature Review

A review of the flow and heat transfer characteristics of multi-jet systems is presented. The main focus is on the factors that influence the heat and mass transfer rate as they occur in the drying of sheets. In the framework of this review, the flow and heat transfer characteristics of multiple impinging round jets are introduced and influencing factors on the rate of heat transfer and the pressure force are discussed. These include the effects of inlet condition, jet-to-jet spacing, jet-surface distance, number of jet rows, jet pattern, jet angle, surface curvature and surface motion. A review of all the correlations for predicting the Nusselt number is provided. In the review of numerical investigations, the suitability of turbulence models in predicting the local and averaged heat transfer coefficient is discussed.

2.1 Introduction

Impinging jets are widely used in a great variety of industrial applications ranging from cooling to heating and drying. Depending on the application, the relevant parameters of the impinging jets heat and mass transfer can vary. Therefore, much research on the flow patterns and the coupled heat and mass transfer of the impinging jet has been undertaken. Most analysis is for the single jet configuration due to the simplicity of the arrangement. With an increase in experimental and computational resources an ever increasing amount of research is being conducted for more complex arrangements.

Nevertheless, the wide variety of parameters (jet geometry, angel, velocity, interaction of different jets, moving surfaces) in use in the varying industrial applications have until now only been partially addressed in the research. So for many industrial applications the designer has to rely on heuristic approaches based on the overall performance of existing designs.

In order to assess the state of the art in jet impingement as used in the industrial drying of sheets (paper, textile, films), a literature review for jet impingement flow and heat and mass transfer will be conducted focusing on the parameters and their range as encountered in this application.

In convective drying of sheets, the drying good is dried by an array of hot air jets. Important factors are the mass transfer (evaporation of water) as well as the heat transfer (to transfer the required heat for the evaporation). For some sensitive goods, as well as for the force needed to hold the sheet, the force exhibited by the impinging jet has to be taken into account. If the drying process is continuous then the sheet is moving. In industrial applications,

a great variety of jet geometries is used. The drying is mostly at ambient pressure. The review focuses on the convective heat and mass transfer between the impinging jets and the drying material. The target for the designer is to minimize the energy required and/or the time needed for drying. In order to do this the influence of the physical phenomena caused by the complex flow patterns have to be taken into account.

Therefore, a review of the literature for impinging jets, with relevance to the drying of sheets, is now presented. The focus is on multiple impinging jets. When no such data is available, data for the single jet is presented. The influence of inlet conditions, jet spacing, jet patterns, jet angle, surface velocity, curvature and roughness are evaluated. Heat and mass transfer as well as the resulting forces are considered. The results from numerical as well as experimental investigations are taken into account.

A summary of several available review papers on the jet impingement flows are summarized in Table 2.1. Most of the review papers have been carried out on a single jet. The knowledge gathered from these papers cannot be directly applied to the real applications as the dynamics of the flow changes dramatically. The multiple jets are used in industrial applications and adjacent jet interactions occur in a multi-jet system that do not occur in the single jet case. A detailed review of work on an array of impinging jets can be found in Weigand et al. (2011). The review covers the effect of cross-flow, jet-to-jet interaction, and separation distance between a jet and target surface in a multiple impinging jet array.

Although a lot of studies on the impinging jet have been performed consistently until recently, further studies are still required to understand the flow and transport characteristics at challenging geometry and boundary conditions, such as a high Reynolds number, small jet- to-surface distance, small jet-to-jet spacing, surface motion and curvature more accurately, and to give guidelines for optimum impinging jet design in industrial cooling and drying applications.

In this paper, recent research trends on the heat and mass transfer in multiple impinging round jets are reviewed with an emphasis on the phenomena that are essential for the drying of sheets (i.e. textiles, paper). Effective parameters in the cooling and drying applications are reviewed with regard to the effects of inlet condition, jet-to-jet spacing, jet-surface distance, number of jet rows, jet pattern, jet angle, surface motion, surface curvature, surface roughness on the jet impingement heat transfer and force. A review of the correlations for predicting the heat-transfer (i.e. Nusselt number) is provided. With regard to the numerical methods, the various turbulence models are reviewed and compared. The review continues with a summary

of the main findings and future directions for accurate prediction of impinging flows as encountered in the drying of sheets.

Table 2.1 List of general reviews on jet impingement

Year	Authors	General Review on the Topic
1973	Livingood et al.	Impingement heat transfer from turbulent air jets to flat surfaces
1976	Becko	Impingement cooling
1977	Martin	Heat and mass transfer between impinging gas jets and solid surfaces
1981b	Hrycak	Heat transfer from impinging jets
1987	Downs et al.	Jet impingement heat transfer-a literature survey
1989	Polat et al.	Numerical flow and heat transfer under impinging jets
1992	Jambunathan	Heat transfer under single circular jet impingement
1993	Viskanta	Heat transfer under single and multiple isothermal turbulent air and flame jets impinging on surfaces
1995	Webb and Ma	Single phase liquid jet impingement heat transfer
1995	Mujumdar et al.	Impingement drying
2001	Han&Goldstein	Jet impingement heat transfer in gas turbine systems,
2005	Hong et al.	Review of studies on heat transfer in impinging jet
2006	Zuckerman&Lior	Jet impingement heat transfer: physics, correlations, and numerical modeling
2011	Weigand et al.	Multiple jet impingements-a review
2012	Dewan et al.	Recent trends in computation of turbulent jet impingement heat transfer
2013	Mahesh	The interaction of jets with cross-flow
2014	Carlomagno et al.	Thermo-fluid-dynamics of submerged jets impinging at short nozzle-to-surface distance
2015	Kaushik et al.	Review of computational fluid dynamics studies on jets
2015	Dayal&Paul	Heat transfer enhancement by using nanofluid jet impingement
2017	Agrawal	Flow visualization of air jet impingement on convex heated surface
2017	Shukla&Dewan	Flow and thermal characteristics of jet impingement: comprehensive review
2018	Nastase&Bode	Impinging jets – a short review on strategies for heat transfer enhancement

2.2 Effective Parameters

There is a large number of possible combinations for design parameters such as jet exit angle, moving surface, surface curvature, surface roughness, jet impinging force, jet velocity and temperature, cross-flow, jet-to-jet and nozzle to surface spacing and jet pattern. However, not all of these have been adequately investigated for design purposes in the literature. In this part, the effective parameters in industrial cooling and drying applications will be investigated. Table A.1 (refer to Appendix A) is a summary of experimental and numerical studies of effective parameters in impinging jet flow and heat/mass transfers over recent years. Table A.1 shows in four columns the information about the source, the research methods (experimental or numerical), validity range (when available) and research objectives. A survey of available correlations for predicting the local and averaged Nusselt number is provided as a reference for designers. Table B.1 (refer to Appendix B) summarizes the equation of correlations, the validity range (when available) and type of configurations. The influence of the different design parameters is reviewed and discussed:

2.2.1 Inlet Condition

2.2.1.1 Jet Velocity

Jet velocity primarily influences the Reynolds number. Goodro et al. (2007) and Park et al. (2007) emphasized the importance of addressing the effects of the Re and Mach number on the multiple jet impingement heat transfer separately, in particular for high jet velocities. Ito et al. (2007) observed that the Nu number for both flat and curved surfaces increased as the Re number increased. Based on the Table A.1, all researchers investigated the effect of the Reynolds number on multi-jet impingement heat transfer and all confirmed the observation of Ito et al. (2007).

2.2.1.2 Jet Temperature

Florschuetz et al. (1985) investigated the effects of cross-flow temperature relative to jet temperature. Heikkila and Milosavljevic (1998) observed that the drying air temperature can be elevated without risking paper quality. Heikkilä and Milosavljevic (2002) carried out a comprehensive study of the impingement heat transfer at high temperatures (100 – 700 C). Goodro et al. (2009) found that the heat transfer coefficient decreases as the target surface temperature to jet temperature increases due to the effects of temperature-dependent fluid properties. The effect of temperature ratio on cross-flow-to-jet mass velocity ratio and discharge coefficients is also examined. Martin (2012) implemented a high temperature study

of impinging jets on a concave surface. Nusselt number results show a strong dependence on the Reynolds number and the geometry, yet little or no dependence on the jet temperature.

2.2.1.3 Entrainment

In many applications, impinging jets are at a temperature other than that of the environment. When a temperature difference is present, the entrainment of surrounding fluid affects the performance of the jet [Viskanta (1993)]. Entrainment of surrounding flow into the jet may change the jet temperature as it approaches the target surface and influence the jet performance [Zuckerman&Lior (2006)]. The Nusselt number is independent of the temperature difference between the jet and the environment if it is defined with the temperature difference between the target surface and the adiabatic wall[1]. The entrainment was minimized by maintaining the jet temperature close to ambient temperature ($T_a - T_j = \pm 0.1C$) [Lee&Lee(1999)]. Huber (1994) used the jet exit temperature (approximately equal to the ambient air temperature) in the definition of the Nusselt number rather than the adiabatic wall temperature in order to minimize the entrainment effects. Garimella and Rice (1995) showed that the entrainment effect sucks the surrounding fluid into the jet flow and induces a recirculation flow. San et al. (2014) stated that the entrainment effect is higher for larger H/d value.

2.2.1.4 Turbulent Prandtl Number

Benhia et al. (1998) used several constant values for turbulent Pr (0.73, 0.85, and 0.92) to check the influence on the stagnation Nu and local Nusselt number along the target surface. Their results showed that there is not a strong influence of turbulent Pr on Nu. They also pointed out that Durbin (1993) obtained similar conclusions for the boundary layer flows. Coussirat et al. (2005) performed some tests to check the influence of turbulent Pr on the Nusselt number by varying the turbulent Pr between 0.7 and 1.2. No significant changes in the Nusselt number were observed. Subsequently, the turbulent Pr number equal to 0.85 was considered for all cases.

2.2.1.5 Turbulence Intensity

The jets themselves, and possible external disturbances, generate the turbulence and it varies significantly with the upstream conditions, the position within the jet, and the nozzle

---

[1] Viskanta (1993), Goldstein & Seol (1991), Fenot et al. (2008)

shape [Nastase&Bode(2018)]. Shi et al. (2002) stated the inlet turbulence intensity level did not affect the Nusselt number distribution significantly for the slot impinging jet. Meola (2009) stated that the turbulence level at the nozzle exit may significantly affect the heat transfer rate and it can be controlled by grid screens in the plenum upside the nozzle exit.

The active methods to enhance the heat transfer between an impinging jet and the target surface generally use acoustic or mechanical excitation to the exit plane of the flow. Passive methods are mainly based on the nozzle shape. Yeranee et al. (2017) found that one method for heat transfer enhancement on a target surface is to increase the turbulence intensity in the jet impinging flow. The mounting of an air-induced duct at the nozzle exit is a passive method for increasing the turbulence intensity due to the increase in the entrainment effect.

Thus it can be concluded from the literature that the inlet turbulent intensity seems to have no significant effect on heat transfer for slot jet impingement, but it may significantly affect heat transfer for round jet impingement.

2.2.1.6 Nozzle Shape

The shape of the jet nozzle plays a role in the development of an impinging jet. Discrepancies among different studies have been attributed to the slight differences in the shape of jet exit geometry such as orifice, contoured, and pipe nozzle [Ashforth-Frost& Jambunathan (1996)].

The area-averaged Nu value for the single round jet impingement from the pipe nozzle is two to three times higher than that of a contoured or orifice nozzle at the same Re number due to the higher initial turbulence in the fluid emerging from the pipe nozzle [Zuckerman&Lior(2006)]. The orifice nozzles have bored holes and the contoured nozzles have punched holes with a contoured shape. The orifice nozzle displays a vena contracta effect that is much less pronounced or even absent for the contoured nozzles. Thus, the orifice nozzle effectively has a higher initial core velocity resulting in higher impingement point heat transfer compared to the contoured nozzle at the same Re number [Geers et al. (2008)]. The orifice nozzle is easier to produce than pipes, as they only require the holes to be perforated [Specht (2014)]. Ansu et al. (2016) observed that a row of pipes has a higher average Nu number compared to a row of orifices due to the maximum centerline velocity and turbulence intensity level at the end of the potential core length.

It can be concluded from Table B.1 that only Goodro et al. (2009) presented a correlation between the Nusselt number and jet temperature and typical values for the exponent of Re have been reported to be in the range of 0.5–0.9. Figure 2.1 shows a comparison of selected

correlations over their range of validity for an arbitrary case of $A_f = 0.03$ and $H/d = 3$. In order to see the Reynolds number dependence of the data correlations more clearly, Nu/ $Re^{0.7}$ is plotted over the Reynolds number. As expected, $Nu_{ave}/Re^{0.7}$ is almost independent of the Reynolds number.

As can be seen in Table A.1, most works e.g. Gardon et al. (1962), Martin (1977), Huber et al. (1994), Garimella et al. (2001), Meola (2009) have been done experimentally at relatively low impingement temperatures and numerical work is very rare in this field.
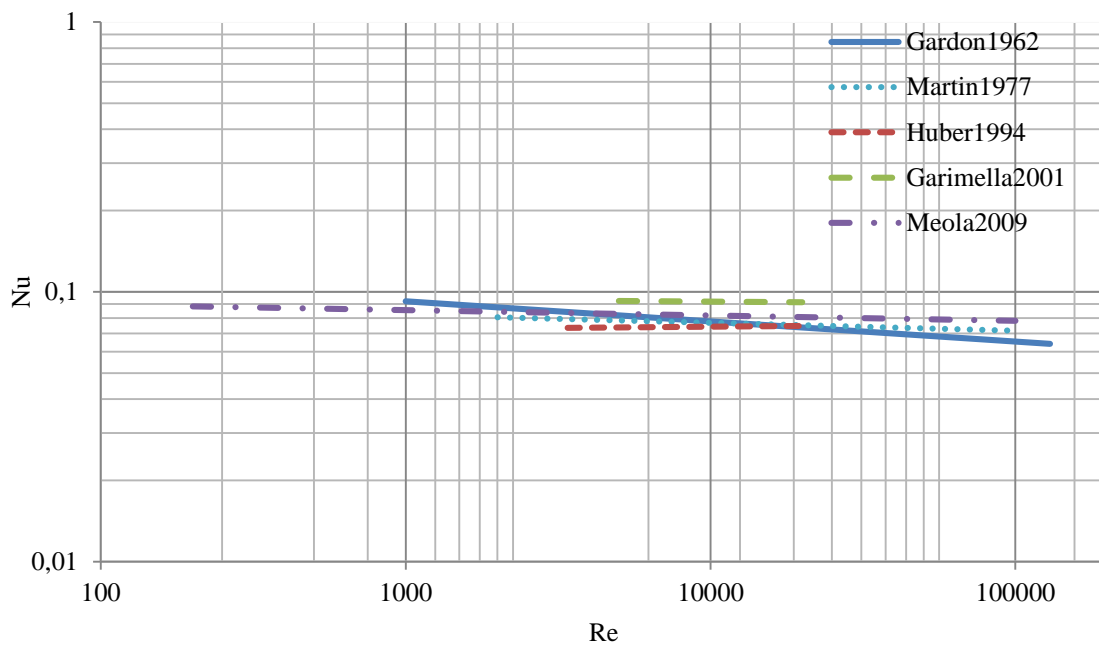
Fig. 2.1 Effect of the Reynolds number on the area-averaged Nusselt number at $H/d = 3$, $A_f = 0.03$, Pr=0.7

2.2.2 Jet-to-jet and Jet-Surface Spacing

An important difference in the heat transfer characteristics between single and multiple jets is the dependence on the separation distance between the jet nozzle and the target surface (H/d). Virtually all studies on multi-jet impingement heat transfer have included variations of H/d. However, with decreased jet-to-jet distances (S/d), or a small separation distance, the jet interaction increases significantly and the heat transfer rates can differ significantly from those of a single impinging jet [Weigand&Spring (2011)].

2.2.2.1 Jet-to-jet and Jet-Flat Surface Spacing

Hollworth et al. (1978) observed that the interference from neighboring jets affects the heat transfer coefficients only for a separation distance (H/d) of less than five. San et al. (2001) obtained an optimum S/d attributed to the jet-to-jet interaction before impingement and/or the

formation of a jet fountain between two adjacent jets. Hrycak (1981b) stated that the maximum heat transfer rate achieves at a small H/d values. Huber et al. (1994) found that the S/d affects the adjacent jet interference and the fraction of the target surface covered by the wall jet. The addition of spent air exits increased the heat transfer rate and affected the location of the optimum H/d. Significant enhancement in the uniformity and the heat transfer rate occurred at H/d = 0.25 and 1.0 compared to H/d = 6.0. Metzger (1987) found that large S/d and small H/d are favorable for uniform heat transfer distribution in a cross-flow configuration. Ekkad et al. (2002) found that increase in H/d reduces the cross-flow effect. Results also show that the increase in the S/d increases the lateral spreading. Katti et al. (2009) stated that the heat transfer rate deteriorates for lower S/d and higher H/d. Lee et al. (2014) found that the cross-flows are detrimental to the local heat transfer coefficient especially for small S/d. San et al. (2014) found that at small S/d and large H/d values (S/d = 2.0 and H/d≥2.0), the jet interference before impingement decreases the heat transfer and achieves a uniform heat transfer distribution. Yamane et al. (2012) observed that the position of the jet stagnation point does not shift at small H/d values and the fountain has little effect on the impinging jet. On the other hand, the fountain has more effect at small S/d. Taslim et al. (2012) observed a significant reduction in the discharge coefficients at small H/d and S/d.

Lee et al. (2013) described the local Nusselt numbers as having a strong dependence on small H/d values. Wae-Hayee et al. (2015) indicated that the Nu number peak increased by increasing the cross-flow velocity for short jet-to-surface distance. Goodro et al. (2008) observed that the Nusselt numbers have some dependence on the Mach number for the smaller S/d. These findings were in complete agreement with Goodro et al. (2010). Penumadu and Rao (2017) showed that the heat transfer in contrast to the pressure drop is extremely sensitive to minor changes in H/d but is insensitive to manufacturing tolerances in jet diameter. Yong et al. (2015) found that the strongest heat transfer is achieved for S/d= 3 under the same Reynolds number. With constant mass flux, a value of S/d = 5 is superior. For smaller S/d values, H/d = 2 gives better results. Xing et al. (2013) found that H/d=3, is best for different levels of cross-flow.

2.2.2.2 Jet-to-jet and Jet-Curved Surface Spacing

Ashok Kumar et al. (2009a and b) observed that the average heat transfer coefficient on the curved surface reduces as H/d increases beyond unity. This finding was in complete agreement with results for flat target surface. Patil and Vedula (2018) measured the effect of

nozzle length to diameter ratio (0.2-6) on the heat transfer rate from a row of round jets impinging on a curved surface for different H/d (0.67-8). Small nozzle length to diameter ratio at small H/d values has strong dependence on the stagnation zone Nusselt numbers, whereas the nozzle length to diameter ratio has negligible dependence on the heat transfer data at larger H/d values.

An overall functional relationship between the Nusselt number and nozzle-to-surface distance is complex, because the heat transfer does not exclusively depend on H/d, but also on flow conditions and other geometric parameters. Based on Table B.1, virtually all studies on multiple impinging jet heat transfer have included variations of H/d and S/d. The typical values for the exponent of H/d have been reported to be in the range of -0.1 to -0.3. Figure 4 shows the dependency of the area-averaged Nusselt number on the jet-to-surface spacing for in-line multiple jet configurations of different jet-to-surface spacings (Re=10,000, A_f =0.03, θ=90º). As expected from the literature, it can be observed that the area-averaged Nusselt number reduces as H/d increases.
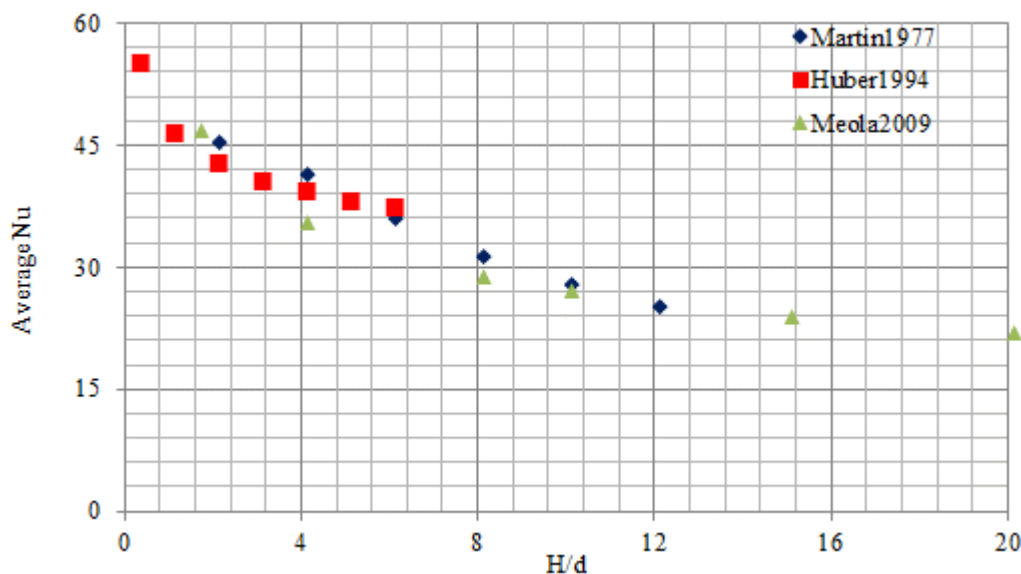
Fig. 2.2 Effect of jet to flat surface spacing on area-averaged Nusselt number for in-line arrays at Re= 10,000, A_f =0.03, θ=90º, Pr=0.7

Figure 2.3 shows the dependency of the area-averaged Nusselt number on the jet-to-jet spacing for in-line multiple jet configurations (Re=10,000; H/d=3; θ=90º). The jet-to-jet spacing affects the heat transfer rate by changing the adjacent jet interference and fraction of the target surface covered by the wall jet region. The typical values for the exponent of S/d have been reported to be in the range of -0.16 to -2 where the fraction of the target surface covered by the wall jet is concerned and 0.65 to 1.29 where the adjacent jet interference is concerned.
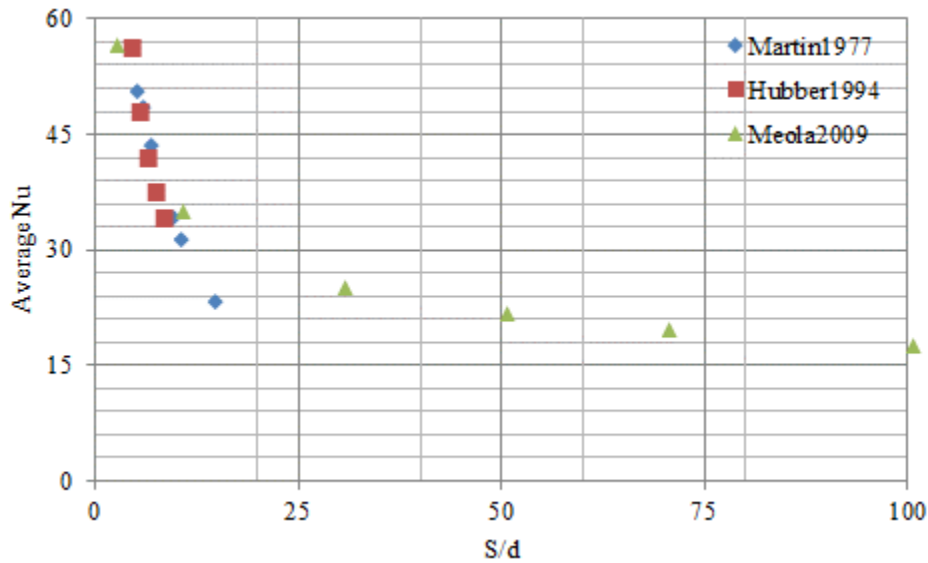
Fig. 2.3 Effect of jet-to-jet spacing on area-averaged Nusselt number for in-line arrays at Re= 10,000, H/d=3, θ=90°, Pr=0.7

Here smaller S/d values result in higher Nu values. This is to be expected because the jet array with small jet-to-jet spacing has the smallest surface area and thus a greater fraction of the target surface area is covered by the stagnation region with higher local Nu numbers than at larger jet-to-jet spacings where a larger fraction of the target surface is covered by the wall jet region, where the local Nu numbers are lower. Equivalently, the mass flow rate per unit surface area is higher for an array system with smaller S/d. This means that the surface area dried by one jet in an array having S/d = 4 is dried by two jets in an array with S/d = 2.

Two distinct regions can be observed in Figure 2.3: S/d>10 and S/d<10. The slope of the results at small jet-to-jet spacing (S/d<10) is much larger compared to the high jet-to-jet spacing (S/d>10). This means that the jet-to-jet distance has very little effect on the heat transfer at high values (S/d >10) as the interaction of the jets is less significant.

Most of the work shown in Table A.1 is concerned with the effect of jet-to-jet and jet-to-surface spacing at larger distances and has been studied experimentally.

2.2.3 Number of Jet Rows

When the spanwise spacing is large, the flow area available for spent air is large. Hence, the cross-flow is relatively weak and its effect on the Nusselt number is minor. Thus, the heat transfer has virtually no dependence on the number of rows in spanwise direction. For such arrays, the variation of the separation distance has a minor effect. For arrays of smaller spanwise distance, due to the associated more powerful cross-flow, the heat transfer rate is considerably more dependent on the number of spanwise rows, and heat transfer rates across

the span between the jets are lower. Consequently, a reduction of the spanwise distance caused by increasing the number of spanwise rows degrades the average heat transfer rates especially at large H/d.

Kumar and Prasad (2008) found that the multiple rows of round jets give the best performance compared to the single row of jets impinging on a concave surface. Li and Corder (2008) showed that the peak value of heat transfer from dual impinging jets (two jets close to each other) is slightly higher than a single jet. The dual impinging jets provide a higher average heat transfer around the stagnation region. Bu et al. (2015) observed two peaks in the local Nu number distribution in the chordwise direction for two row of jets due to the weak interference between adjacent jets and only one peak for three row of jets due to the strong interference between adjacent jets. Patil and Vedula (2015) found that the peak Nu values with single row and two rows of jet impinging on a concave surface are the same. The single row gives higher Nu values as compared to two rows with the same mass flow rate.

2.2.4 Effect of Jet Pattern

For regular configurations, the streamwise jet-to-jet spacing is equal to the spanwise jet-to-jet spacing ($S_x = S_y$), but for irregular configurations these distances are different ($S_x \neq S_{y)}$). One question arising in the design of multiple impingement systems applies to the selection of jet pattern for an optimum performance.

2.2.4.1 Jet Pattern on Flat Surface

Gromoll (1978) found that local heat transfer of a staggered array is enhanced compared to an in-line array. Metzger et al. (1979) pointed out that for the in-line pattern compared to the staggered pattern the local differences in the Nusselt number can be significant. For a configuration with one side outlet, differences between the jet patterns were largest towards the downstream end of the array where the cross-flow is very strong. Florschuetz et al. (1980, 81) showed that the differences due to the jet pattern can become significant for small S/d, large H/d, and increased cross-flow. For such configurations, in-line arrangement typically shows better heat transfer performance. Van Treuren et al. (1996) indicated that there is only minor difference in average heat transfer rates between in-line and staggered arrangement. Yan et al. (2003) found that the in-line jet array produces local and average heat transfer rates that are relatively higher than those of the staggered jet array. Geers et al. (2008) compared the heat transfer measurements from impinging jets in hexagonal and in-line arrangement. The experiments indicated that heat transfer is strongly influenced by jet interactions. They

constructed a new correlation for the averaged Nusselt number that takes the interactions into account. Yong et al. (2015) concluded that the heat transfer for the staggered pattern seems to be somewhat higher than that of the in-line array.

Zu et al. (2009) analysed the jet arrangement and angle. They found that the staggered arrangement gave a higher area-averaged Nusselt number in the region near the impinging jets, but lower values at greater distances (X/d>10) away from the jets. Especially for staggered jets, the Nusselt number in the near jet region increase slightly for an increased attack angle. Miao et al. (2009) investigated the heat transfer characteristics of round jet arrays for in-line and staggered arrangements and three different cross-flow directions, parallel, hybrid, and counter. In-line jets and hybrid cross-flow orientation have the highest average Nu numbers. Xing et al. (2010) concluded that if there is no dependence on jet-to-surface spacings or cross-flow, the in-line configuration outperforms the staggered pattern. Wae-Hayee et al. (2013) found that cross-flow has a stronger effect on the impinging jets in the staggered pattern than in the in-line pattern. The average Nusselt number of the in-line pattern is approximately 13-20% higher than that of the staggered pattern.

2.2.4.2 Jet Pattern on Curved Surface

Patil and Vedula (2015) found that the in-line and staggered patterns of multiple jets impinging on a concave surface result in the same average Nusselt number. Thus the influence of the surface curvature seems to be greater than the difference between in-line and staggered arrangement.

Based on Table B.1, references Florschuetz et al. (1981), Van Treuren et al. (1996), Geers et al. (2008), Miao et al. (2009) are available at present on the impact of flow pattern on the dimensional groups used in the correlations for average/local heat transfer coefficients. These correlations focus only on the separation distance $H/d \geq 1$. The typical values for the exponent of Re for both in-line and staggered patterns have been reported to be in the range of 0.5-0.9 (in-line pattern in the range of 0.5-0.85 and staggered pattern in the range of 0.7- 0.9). Figure 2.4 shows the dependency of the area-averaged Nusselt number on the jet pattern for different Reynolds numbers (H/d=1, S/d=6) by the different correlations. It can be observed that only minor differences in average heat transfer rates exist between the in-line and staggered pattern. There are no significant differences between the correlations of Florschuetz et al. (1981) and Van Treuren et al. (1996), which are valid for maximum cross-flow. The difference between these correlations with Miao et al. (2009) is significant, as the correlation of Miao et al. (2009) is valid for intermediate cross-flow.
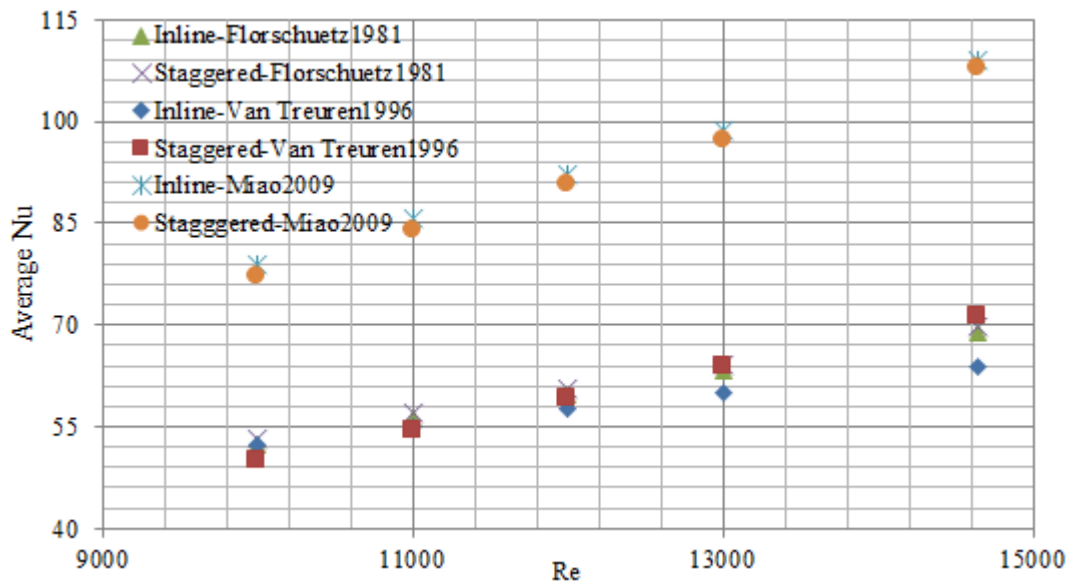
Fig. 2.4 Effect of jet pattern on area-averaged Nusselt number for H/d=1, S/d=6, Pr=0.7

It can be concluded from Table B.1 that the effect of jet patterns is only investigated on a fixed surface and almost all work has focused on a flat surface. The influence of nozzle arrangement on the jet impingement heat transfer is not significant compared to other influencing parameters. Moreover, it can also be concluded that cross-flow significantly affects the impinging jets heat transfer for the staggered and in-line arrangements on the flat surface.

2.2.5 Jet Angle

The jet impingement angle affects the heat transfer rate, as the angle distorts the heat transfer contours by generating the elliptical isoclines. Angled jets may be needed for the unique feature of the hardware design, reducing the penalties of jet interaction and the losses in the approaching or spent jet flow exit pathway [Zuckerman&Lior (2006)].

In the experimental investigations either the inclination of the surface varies or the angle of a jet impinging on a horizontal surface is changed.

2.2.5.1 Effect of Inclined Flat Surface

Hwang and Cheng (2001) tested three right triangular ducts of the same altitude and different apex angles of 30°, 45° and 60° respectively. Results show that at the same Reynolds number, Duct 60° has the highest averaged heat transfer rate due to the highest jet center velocity and the smallest jet angle. Hebert et al. (2005) compared the converging and diverging channels with parallel surface channels with different spacing to compare the effect of the streamwise pressure gradient. The parallel channels with even spacing throughout show similar trends where the converging channels match in dimension. Similarly, for the diverging

channels, this trend is clearly evident. Al-Mubarak et al. (2008) investigated the effect of orifice-jet surface configuration (centered, staggered and tangential) on the heat transfer behavior in a channel with inclined target surface. The centered holes have an 11% higher averaged Nusselt number as compared to the staggered configuration. The staggered configuration also has an 11% higher averaged Nusselt number as compared to the tangential configuration. Al-Hadhrami (2010) found that the inclined surface affects the local heat transfer coefficient. Al-Mubarak et al. (2013) studied the effect of the jet Re number and feed channel aspect ratios on the heat transfer rate of inclined target surface. They observed that the Nusselt number is high for higher aspect ratios.

2.2.5.2 Inclined Jets on Horizontal Flat Surface

Peper et al. (1995) observed that a pair of radial jets with a flow exit angle towards the surface of 10° has an 18% higher drying rate than that of a pair of in-line jets. Peper et al. (1997) found that the local and averaged Nusselt numbers of radial jets with flow exit angles of $+45° \leq \theta \leq +60°$ can be up to 60% and 50% higher than those of in-line jets at the same exit velocity and the volumetric flow rate. Ekkad et al. (2000) reported that the orthogonal jets have a higher Nusselt number at the stagnation point compared to the angled jets. However, the angled jets achieve more uniform heat transfer distributions than the orthogonal jets. El-Gabry et al. (2004) measured the local heat transfer distribution from an array of angled impinging jets on both smooth and roughened surfaces. Saeed (2008) revealed that the array with a $20°$ stagger provide better surface heat transfer than that of a $10°$ stagger. Zu et al. (2009) found that the area-averaged Nusselt number in the region near the impinging jets increases with the attack angle and the orthogonal jets gives the highest heat transfer rate.

2.2.5.3 Inclined Jets on Curved Surface

Heo et al. (2012) observed that the heat transfer coefficient increases with the pitch of orthogonal jet nozzles and the staggered inclination of jet nozzles enhances the heat transfer rate on a target curved surface. Jung et al. (2012) observed that the average Sh number of the angled jets was higher than that of the orthogonal jets due to the higher mass flow rate and mass interaction between the stagnation points of the angled jet. Imbriale et al. (2014) stated that 3D Nu maps showed the presence of streamwise vortices driven by the surface curvature, the jet angle and the jet pitch. Bu et al. (2015) found that decreasing the surface curvature and increasing the jet impingement angle can improve the Nu number at the stagnation point.

Bu et al. (2016) observed that the heat transfer rate at the stagnation point was enhanced by increasing the Re number and the jet impingement angle. Based on table B.1, only the reference of Bu et al. (2016) is available at present on the impact of jet impingement angle on the dimensional groups used for the correlation of the stagnation Nusselt number in terms of the jet Reynolds number (Re), relative nozzle-to-surface distance (H/d) and jet impingement angle (θ). Figure 2.5 shows that the stagnation Nusselt number is dependent on θ parameter and the exponent of θ has been reported to be equal to 0.847. Thus the target wall heat transfer increased with an increase in the jet impingement angle.
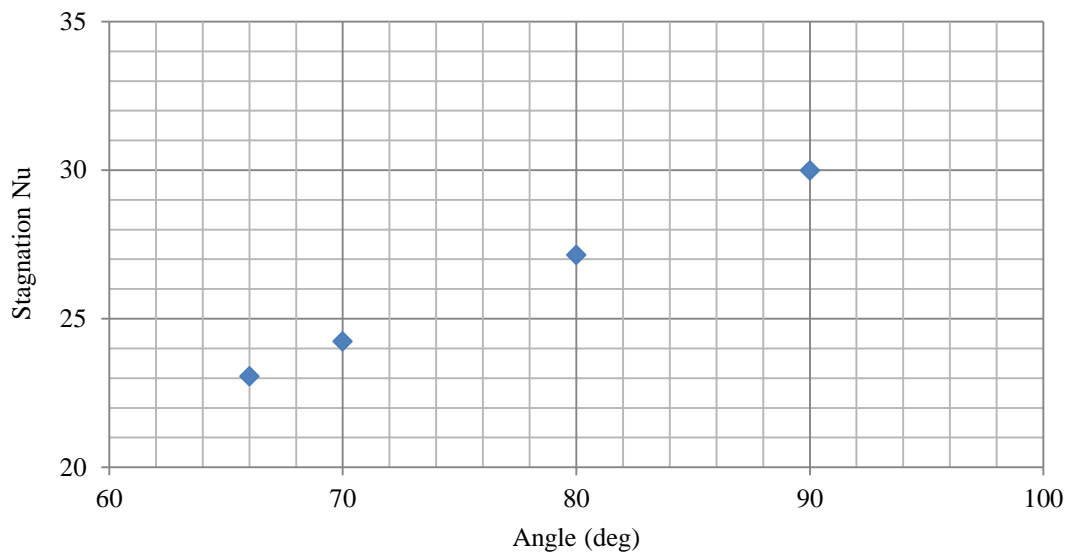
Fig. 2.5 Effect of the jet impingement angle on the stagnation Nu at Re=50,000, H/d=3

2.2.6 Surface Curvature

Flat surface results obtained with a single jet, can be applied to a row of jets impinging on a semi-cylindrical surface with certain modifications [Hrycak(1981a)]. For a curved surface, the optimum H/d is less than that of an equivalent flat surface [Metzger (1969)]. Fregeau et al. (2005) use the Dual-Kriging method to preserve the nonlinear nature of the Nusselt number distribution from a jet impinging on a curved surface. Furthermore, Fregeau et al. (2009) speculate that decreasing the jet-to-surface distance is probably more effective than increasing the jet Mach number or the jet numbers impinging on a concave surface. Ito et al. (2007) observed that the Nusselt number for both flat and curved surfaces increases as the Reynolds number increases.

Fenot et al. (2008) investigated the influence of a concave surface curvature by changing the jet tube diameter. They found that the surface curvature has two effects on the Nusselt number distributions: increasing the curvature causes a small growth of the Nusselt number in

the impingement region, but the curvature also leads to a confinement of the jet flow that decreases the Nusselt number. Li and Corder (2008) observed that the peak Nu number on the curved surface is lower than the flat surface. Rama Kumar et al. (2008) investigated the flow pattern and observed the presence of a pair of counter rotating vortices, fountain flow and entrainment on a concave surface. Ashok Kumar et al. (2009) studied the flow and heat transfer characteristic from the round jets impinging on a concave surface with and without effusion holes. They also. (2009) observed that the average heat transfer coefficient on the concave surface reduces as H/d increases. Harrington et al. (2017) showed that the very small relative curvature (d/D=0.016) did not cause any significant changes in the flow distribution and the heat transfer level compared to the flat target surface. Patil and Vedula (2018) investigated the arrangements with different nozzle length and curvatures. They observed that the longer nozzle lengths and smaller curvature ratios have better performance on the local heat transfer coefficient.

Based on Table B.1, references Chupp et al. (1969), Lovingood et al. (1973), Hrycak et al. (1981a), Fenot et al. (2008) and Patil &Vedula (2018) are available at present on the impact of surface curvature on the dimensional groups used in the correlations for the average/local heat transfer coefficients for a row of impinging jets. Although the validity range of these correlations is similar, the results for the average Nusselt number are of similar magnitude but seem differently affected by the curvature. Figure 2.6 shows the effect of non-dimensional target curvature d/D on the heat transfer due to a row of air jets impinging on a curved surface (Re=10,000, H/d=5, S/d=4). The relative curvature seems to have two opposite effects on the Nusselt number distributions. With an increase in the curvature, the heat transfer in the stagnation region increases but also the confinement of the flow leads to complex flow patterns that affect the heat transfer. The experimental set ups for the data for these correlations were different, leading to different areas used to average the Nusselt number and varying additional groups of dimensionsionless numbers in the correlations.

Here further investigations to describe the phenomena for jet arrays impinging on curved surfaces would be helpful.
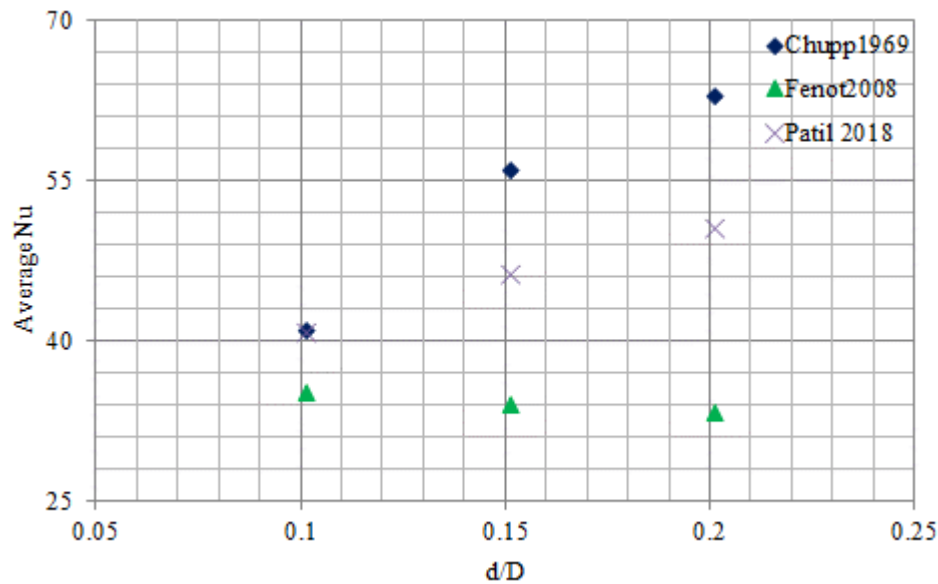
Fig. 2.6 Effect of the relative curvature for a row of air jets impinging on a concave surface at Re=10,000, H/d=5, S/d=4

2.2.7 Orthogonal Jets on Moving Flat Surface

Some industrial processes, such as paper dryer or rolling of sheet stock or external heat transfer to the rotating parts, require the target surface to move. Selection of an effective speed depends on several factors such as the jet spacing and a time constant associated with the heat and mass transfer rate to or from the target surface. For a small surface-to-jet velocity ratio up to 0.2, the surface motion has a negligible effect. For higher velocity ratios, the effect is like that of superposing a cross-flow [Zuckerman&Lior(2006)]. Journeaux et al. (1992) reported that the impingement heat transfer was not significantly affected by the velocity ratio up to 0.6, i.e. twice the maximum value for slot jets that was obtained by Polat et al. (1990, 91). Insensitivity to twice the motion in the case of round jets may be explained by the fact that, in this case, the spent flow has a higher degree of freedom to spread on the surface. Filipovic et al. (1994) developed a mathematical model to predict the thermal behavior of steel strips cooled by an array of circular jets. Chen et al. (1994) suggested that neglecting the surface motion effects can overestimate the heat transfer rate. Chattopadhyay et al. (2002) showed that, in the presence of a moving surface, the flow field is turbulent even at Re = 500. Chattopadhyay (2006) found that the surface velocity strongly affects the flow field over the target surface and reduces the heat transfer rate. Aldabbagh et al. (2009) observed that the surface velocity ratio has no effect on the oscillations of the Nusselt number at small nozzle-to-surface spacing. Badra et al. (2013) presented the CFD calculations of the transient heat transfer between a bank of round impinging jets and a moving surface and performed design optimization for the single and multiple impinging jet configurations. Kadiyala and Chattopadhyay (2017) investigated

numerically the heat transfer on hot moving surfaces due to an array of jets for laminar and turbulent flow regimes (Re < 5000).

Based on Table B.1, no explicit documentation on the impact of surface motion on the dimensional groups used in the correlations for average/local heat transfer coefficients is available at present. Due to the challenging experimental set up, the reported investigations in Table A.1 are numerical and there is not observed any investigation concerning the effect of inclined jets or surface curvature. The overall effect of the surface motion could be assessed by examining Table 2.2. Due to the absence of correlations and experimental data, the CFD results from the literature have been compared in Table 2.2. Increasing the surface velocity leads to a decrease in the average Nusselt number.

Table 2.2 Comparison of the effects of velocity ratio on total average Nusselt number from the literature (in-line arrays, H/d=2, S/d=10 and Re = 2,500)

Velocity ratio	Average Nu	
	Chattopadhyay (2006)	Kadiyala (2017)
0	13.15	12.9
1	10.38	9.6

2.2.8 Surface Roughness

In many industrial applications the impingement surface is not smooth. Trabold et al. (1987) indicated that roughness elements can be used to compensate the degradation of heat transfer on smooth target surfaces. El-Gabry et al. (2004) suggested for an optimization of the impingement target surface, the use of rough surfaces could enhance the heat transfer significantly and reduce the thermal non-uniformity at a negligible additional pressure drop. Xing et al. (2010) compared the jet impingement array on a flat and rib roughened surface. The rib roughened surface has higher heat transfer coefficients than the flat surface. Due to the great variety of roughness geometries, a quantification of the heat transfer enhancement with a general correlation is hardly realizable. For drying applications, the surface properties of the dried material is, in general, not a variable parameter.

2.2.9 Surface Thermal Condition

In order to achieve steady conditions for the experimental as well as the numerical investigations either a constant temperature or a constant heat flux is applied at the impingement surface. Chupp et al. (1969) found that varying the wall boundary condition from the isothermal to constant heat flux had no effect on the stagnation heat transfer and little effect

further away: up to 15% change in the Nusselt number. Baughn and Shimizu (1989) reported that once the heat flux is sufficiently small, the resulting variable heat flux has a minor effect on the Nu number and imposing a constant surface temperature is a good approximation.

2.2.10 Jet Impinging Force on the Flat Surface

Jet force on the surface is typical for impinging jets towards the surface and it is very important in drying applications for force sensitive products (i.e. paper, fabrics) or force sensitive surfaces (i.e. painted, coated). The nozzle exit velocity could be limited if the product is sensitive to deformation under the jet impinging force. Nevertheless, in the investigations reported this aspect is often omitted.

Kastner et al. (1988) calculated the jet impingement force through the integration of measured pressure distributions on flat surfaces due to an impinging jet. Peper et al. (1997) found that the total force exerted by radial jets on a plane surface is lower than that exerted by inline jets and total force exerted by radial jets decreases with decreasing the flow exit angle. Wang et al. (2015) found that the mean impact force coefficients from single circular jet impinging normally onto a flat surface are highly dependent on the distance, but relatively insensitive to the Reynolds number within the range examined.

No explicit documentation on the impact of pressure force on the dimensional groups used in the correlations is available at present, see Table B.1. Only few experimental studies exist for the impact of the pressure force of a single impinging jet on the fixed flat surface and no investigation for multiple jets either experimentally or numerically was found. Figures 2.7 shows the variation of the mean impact force coefficient C_f with the distance H/d at different Re from a single round jet impinging normally onto a flat surface. In the range from $4 < H/d < 10$, the pressure force decreases with increasing distance.

The data available in the literature are very scarce, so further experimental and numerical investigations are necessary to obtain useful correlations for design purposes.
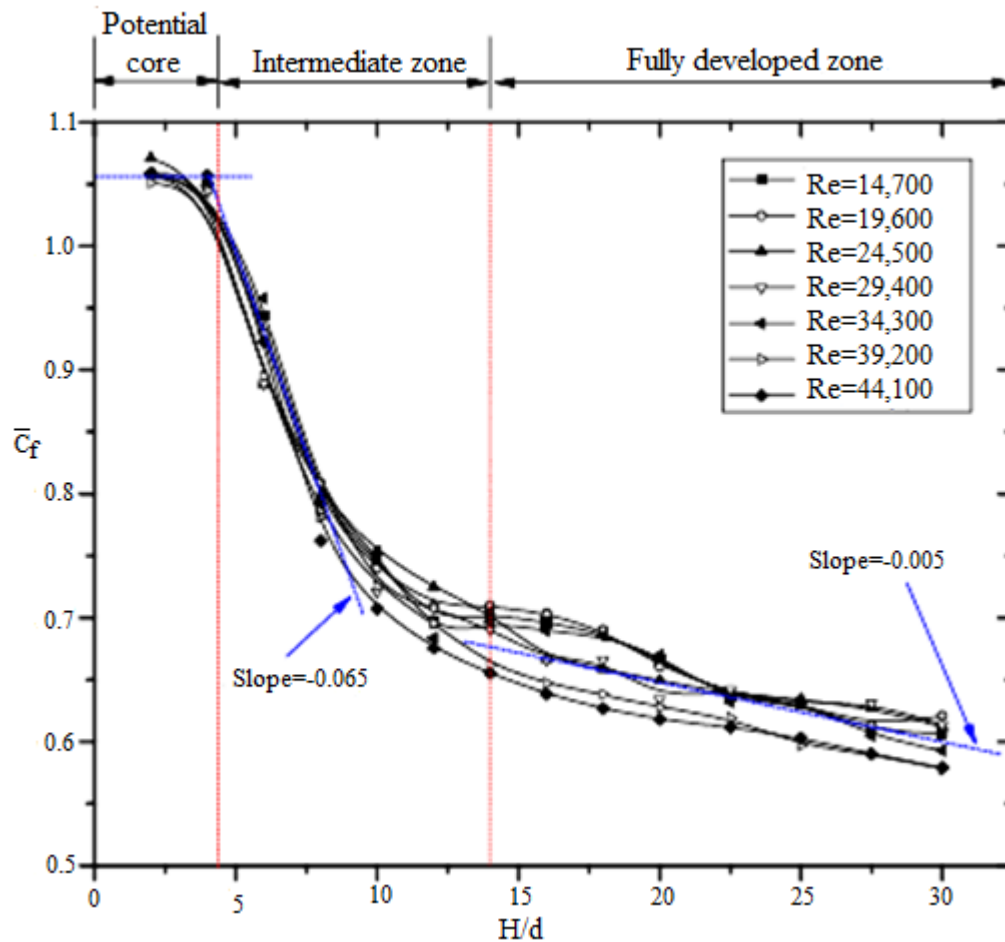
Fig. 2.7 Variation of the mean impact force coefficient with H/d at different Re [Wang et al. (2015)]

2.3 Optimum Design

The design parameters of industrial drying equipment should be optimized to achieve the minimum capital and running costs. Designs that require high jet velocity and temperature are not attractive due to the high energy costs [Etemoglu&Can(2013)]. In addition, excessively high temperature or strong temperature variations may damage the drying material. Maximizing the heat transfer does not necessarily lead to a minimum in capital costs (size of the apparatus) and running costs (energy consumption).

Huang (1963) indicates that the uniform distribution of the heat transfer coefficient can be achieved at an H/d ratio larger than 2. For economic power consumption, an open area factor of 0.0075 is recommended. Martin (1977) reported that with respect to the average Nusselt number for an array of round nozzles, the optimum value for the open area factor is 0.0152 and for the jet-to-surface distance it is 5.43, irrespective of any other geometric parameters. Similarly, Dyban et al. (1980) reported an optimum open area factor in the range of 0.007 to 0.018 with dependency on nozzle-to-surface distance with respect to the surface-average heat

transfer coefficient. Metzger et al. (1979) observed that for S/d of 1.67-6.67, the maximum average Nu number is for H/d of about one.

San et al. (2001) obtained an optimum value for S/d in the range of 6-12 for Re number=10,000 to 30,000 and H/d= 2 to 5 with respect to the relative maxima of the stagnation Nusselt number. Can et al. (2002) determined that the maximum average heat transfer coefficient for circular holes can be achieved at the optimum free area factor of about 0.03. Brevet et al. (2002) identified an optimum H/d=2-5 and optimum S/d=4-5 to achieve the maximum heat transfer rates on a flat surface.

Kamal et al. (2006) stated that the optimum case to satisfy the uniform pressure distributions beside largest drying rates along the drying plane is S/d = 3.5, H/d=6 and $\theta = 60°$. Heo et al. (2012) found that the optimum inclination angle and the pitch of staggered jet nozzles on a concave surface at Reynolds number of 23,000 is 59.09º and 8.074, respectively.

Xing et al. (2013) found that H/d=3 could provide higher heat transfer performance for a variety of cross-flow configurations. Etemoglu et al. (2013) showed that increasing the nozzle size and thus decreasing the relative distance and relative pitch results in a greater heat and mass transfer coefficient for single and multiple slot nozzles.

Specht (2014) found an optimum S/d=6 for single nozzle arrays and hole channels. For perforated surfaces the optimum maximum heat transfer is for S/d=4 and the minimum specific energy consumption is achieved with S/d=8-10.

Zhu et al. (2015) found a relationship between the injection height and nozzle spacing (H≈8S) for uniform heat transfer.

Bu et al. (2015) determined an optimal H/d=4.5 to achieve the best heat transfer performance for a single row of jet holes on a concave surface. Bu et al. (2016) determined an optimal H/d=4-5.75 corresponding to the maximum stagnation Nu number for three rows of jet holes on a concave surface.

Yang et al. (2017) indicated that optimum values of H/d = 10, S/d = 30, and $\theta = 15°$ enhance both the local and averaged Nu number of sonic impingement jets on the concave surface. Enlarging the jet diameters could not significantly improve the heat transfer performance.

A considerable amount of studies has been dedicated to determine the parameters for maximum heat transfer and minimum energy consumption in systems of multiple impinging jets focusing mainly on relative pitch S/d (or open area factor) and relative distance H/d. Generally, for maximum heat transfer the nozzle-to-surface distance should be decreased as

much as possible, the area factors reported are in the range of 0.007 − 0.05 (corresponding to pitch ratios S/d in the range of 4 − 7). The reported pitch ratios S/d for the minimum energy consumption are somewhat higher with 6–10. The results are strongly influenced by the nozzle shape, cross-flow, surface characteristics and jet angle. No reported optimum value of other key controlling design variables such as jet temperature, jet velocity, surface velocity and surface curvature was found in the literature.

2.4 Experimental Investigation

Impingement jet measurements involve the determination of the local distribution of the flow field characteristics as well as the surface heat or mass transfer coefficients. In an experiment a single jet or multiple jet arrays are constructed and positioned above a target surface. A pump or blower forces the fluid onto the target surface while the instrumentation collects the information in the fluid as well as on the target surface [Zuckerman &Lior (2006)].

2.5 Numerical Investigation

Numerical simulations are a complement to the experimental investigations. The numerical modelling of impinging jet flow and the coupled heat and mass transfer is connected to the particular challenges of appropriate turbulence modelling and near wall treatment. The impinging jet flow is characterised by low and high turbulence levels, anisotropy and shear layers, boundary layers and stagnation. These effects have to be properly represented by the chosen turbulence model. In order to correctly assess the heat and mass transfer in the near wall region a refined grid (y+<1) should be used at the wall.

However, the numerical simulation of multiple impinging jets for many industrial cooling and drying applications has the additional challenge of moving and curved surfaces in combination with the jet-to-jet and jet-to-cross-flow interference.

Many researchers have simulated the turbulent impinging jet using different turbulence models such as, Reynolds Averaged Navier-Stokes equation (RANS), Large Eddy Simulation (LES), Direct Numerical Simulation (DNS) and hybrid models. However, these studies show significant deviations among themselves and also from the relevant experiments. For numerical predictions of multi-jet impingement heat transfer, a quantification of the numerical accuracy is equally significant. Table A.1 is a summary of turbulence models used by researchers on the impinging jet flow over recent years.

2.5.1 Reynolds-averaged Navier–Stokes Equations

Impingement problems are difficult to simulate numerically using conventional Reynolds Averaged Navier-Stokes (RANS) models. It is worth noting that typical RANS models contain a number of calibrated constants, and these have been adjusted with respect to specific types of shear flows. Thus, there are differences in the results for different models but also for different implementations of one model. In addition, isotropic eddy viscosity models fail in predicting the correct heat transfer values and trends in the impingement problems where the flow is highly anisotropic [Hossain et al. (2016)]. Especially here, with different flow regimes, the use of hybrid models as a combination of efficient 2-equation models is advisable. The successful SST k-ω model as a combination of the k-ε and the k-ω model for the near wall region is an obvious choice.

Chattopadhyay et al. (2006) studied the heat transfer from impinging round jet banks over a moving surface by using a k-ε model. However, Badra et al. (2013) and Kadiyala & Chattopadhyay (2017) used SST k-ω model to evaluate the heat transfer from the round jet array impinging on the moving surface. Due to the absence of experimental data, results were validated for the array of round nozzles impinging on the stationary surface. However, Badra et al. (2013) reported that the second peak in the Nusselt number at low jet-to-surface distances was well predicted by the SST k-ω model and many researchers[2] confirmed that the SST k–ω turbulence models succeeded with reasonable accuracy in reproducing the experimental data. They predict the complex interaction of the wall jets and the flow structure associated to the impinging jets on a flat target surface. Moreover, Yang et al. (2017) reported that only the SST k-ω model predicts the secondary peaks of the local Nusselt number from jets impinging on a concave surface successfully and many researchers[3] observed that the SST k-ω model is the best suitable model for predicting the jet impingement phenomenon on the curved surface.

In the literature, many informative studies are reported using the k-ε model to predict the heat and mass transfer of impinging round jets with only limited success (with 0 to nearly 60% error)[4]. Examination of RANS numerical modeling techniques showed that the various implementations of different turbulence models (algebraic stress model to Reynolds stress model), models even with high-resolution grids, give large errors compared to the experimental

---

[2] Zu et al. (2009), Rao et al. (2009), Xing et al. (2010), Chougule (2011), Prasad (2012), Zhu et al. (2015), Wae-Hayee et al. (2015), Kadiyala&Chattopadhyay (2017)

[3] Rama Kumar&Prasad (2008), Ashok Kumar&Prasad (2009a), Heo et al. (2012), Yang et al. (2017)

[4] El-Gabry et al. (2005), Chattopadhyay (2006), Zu et al. (2009), Chougule et al. (2011), Badra et al. (2013)

data. The SST k-ω model (hybrid 2 equation model) and the more expensive V2F model (4 equation model) can predict the jet impingement heat transfer with a reasonable solution speed and accuracy and are recommended as the best turbulence models [Zuckerman&Lior(2006)].

2.5.2 LES and DNS

Large eddy simulation (LES) tracks the behavior of the large eddies due to the generally more energetic of large scale motions compared to the small scale ones. Direct numerical simulation (DNS) is the most natural and straightforward approach in that these simulations directly compute the mean flow and all turbulent velocity fluctuations without the time averaging done in the RANS approach. For high Reynolds numbers and arrays of jets, these approaches are computationally very expensive.

Taslim et al. (2012) concluded that the realizable k–ε model produced the closest heat transfer results to the experimental data compared to LES and other RANS turbulence models such as k-ω, V2F and k–ε model for multiple round jets impinging normal to a target surface at the separation distance less than one. Yu et al. (2013) also compared five different turbulence models (RNG k–ε, realizable k–ε, the V2F, the SST k-ω, and LES models). The V2F and SST turbulence models can, surprisingly, produce better predictions of fluid properties in the impinging jet flows compared to other models. Zu et al. (2009) compared the relative performance of seven versions of turbulence models, including standard k-ε, renormalization group k-ε, realizable k-ε, standard k-ω, SST k-ω, RSM and LES model, for the prediction of jet impingement flow and heat transfer. They found that the LES model can give better predictions of fluid flow and heat transfer. Hossain et al. (2016) carried out LES and three other RANS turbulence models (SST k-ω, RSM and V2F) to find out the best numerical model for the jet impingement heat transfer problem. Despite the high computational cost to perform LES, it shows very promising capability in the prediction of the flow field, when compared to the RANS models. Flow features, like the jet-to-jet interaction, stagnation flows, upwash fountain flows, and recirculation between adjacent jets due to the collision of wall jets, were captured accurately by LES. Penumadu and Rao (2017) investigated the flow and heat transfer characteristics of the multiple impinging round jet at low Re number with RANS, URANS and LES approach. The LES results provided a deeper insight into the flow physics of impinging jet array.

Turbulent flows are highly anisotropic in nature but RANS models assume the flow is isotropic and use only one length scale to solve the Navier-Stokes equation. Using a one length scale in a problem like the jet impingement flow poses a tremendous burden for the RANS

models. RSM overcomes this problem by solving transport equations for each individual Reynolds stress component but this model yields a poor prediction of the Nusselt number as the model fails to model the pressure-strain term near the stagnation region. The LES technique resolves the large scale eddies and models the smaller scale eddies which are universal in nature [Hossain et al. (2016)]. SST k-ω and LES model can give better predictions of heat transfer and flow phenomena, while the simulations using standard, RNG and realizable k-ε models, standard k-ω, and RSM, all give large errors compared to the experimental results[5].The actual computational cost will, of course, vary with turbulence model complexity and computing power system. In comparison, the LES model has computation times at least two orders of magnitude higher than the SST and V2F models. Thus the SST k-ω model is recommended as the best compromise between the computational cost and accuracy[6].

In order to reduce the high computational cost of LES, a RANS-LES coupled approach may be used. With hybrid RANS-LES models, part of the turbulence is modeled (i.e. the near wall region) and part of the turbulence is resolved (i.e. the outer flow region). Hybrid RANS-LES model can predict the intensity and location of peak in the local Nusselt number distribution with reasonable accuracy [Taghinia (2014)].

2.6 Summary and Conclusion

A review of heat transfer characteristics due to the multiple impinging jets as encountered in industrial drying and cooling applications has been presented. In order to do this the relevant experimental and numerical studies on the subject including the latest results from the literature were summarized. In the review, the flow and heat transfer characteristics of multi-jet impingement systems were described and the dimensional groups influencing the flow and heat transfer pattern were listed. The different investigations studied for this work were reviewed with regard to the effects of surface curvature, jet exit angle, moving surface, jet velocity and temperature, entrainment, jet-to-jet and jet-surface spacing, jet pattern, number of jet rows and pressure force. In the review of numerical studies, the focus of interest was set on the suitability of present CFD tools in predicting the local multi-jet heat transfer rates.

Most experimental as well as numerical works include an investigation on the effect of the Reynolds number. All correlations include the Reynolds number and typical values for the

---

[5] Zu et al. (2009), Hossain et al. (2016), Penumadu&Rao (2017)

[6] Zu et al. (2009), Yu et al. (2013), Hossain et al. (2016), Penumadu&Rao (2017)

exponent have been reported to be in the range of 0.5–0.9. The heat and mass transfer on both flat and curved surfaces increases as the Reynolds number increases.

Turbulence intensity and surface roughness can enhance the jet impingement heat transfer significantly. The entrainment of surrounding flow into the jet can deteriorate the jet performance especially at large jet-to-surface distance. The turbulent Prandtl number has no strong influence on the heat and mass transfer.

All correlations on the multi-jet impingement heat transfer include a dependence on the jet-to-jet and jet-to-surface spacing. On the other hand, most experimental investigations focus on large distances. For small jet-to-surface distances, a second peak in the radial distribution of the heat transfer can be detected. Different physical explanations for the occurrence of this peak are proposed, but there has been no consensus yet. The case of very small jet-to-place distances (H/d < 1) has generally not been considered.

For many parameters of importance in industrial drying applications, the data available in the literature are scarce: Few, and mainly experimental, studies exist for heat transfer distribution on the stationary surfaces under an angled impinging jet array.

The effect of the jet pattern is investigated experimentally and numerically for fixed surfaces with a focus on flat surfaces. On the other hand, few correlations are available at present on the impact of flow pattern on the dimensional groups for average/local heat transfer coefficients.

Few numerical studies exist for heat transfer distribution on the moving flat surfaces under an array of orthogonal impinging jets and experimental work is very rare in this field. There is no information on the effect of inclined jets on the moving surfaces, either flat or curved. In addition, no explicit documentation on the impact of surface motion on the dimensional groups used in the correlations for average/local heat transfer coefficients is available at present.

Heat transfer distribution from the orthogonal jets impinging on some fixed curved surfaces has been investigated experimentally and numerically, but no investigations concerning the effect of moving surfaces have been observed.

A few experimental studies exist for the impact of the pressure force from single radial and in-line jets, but only for a flat surface. Thus the data available on the pressure force under multiple round jets for an adequate design and optimization of impinging jet applications is lacking.

A considerable amount of studies has been dedicated to the optimization of heat transfer in systems of multiple impinging jets with varying jet angle, jet-to-surface and jet-to-jet distance. Optimizations with regard to other key controlling design variables such as the jet velocity, the jet temperature, surface velocity and surface curvature are scarce.

It was observed that only some of the wide variety of RANS turbulence models predict the impinging flows accurately. The SST k-ω model is suitable for the numerical prediction of jet impingement flow for different geometrical and physical parameters. The numerical results are in reasonable agreement with experimental data at a reasonable computational cost.

LES are capable of predicting the flow field and heat transfer data with good accuracy but are computationally more expensive. That is why most of the investigations focus on LES of single jets. As far as the author knows, DNS work on multiple jet impingement has been very rare until now. In the future, these methods will help to investigate the physics involved in the complex flow patterns of multiple jet impingement. However, today these methods are computationally very expensive for the analysis of industrial relevant flows with multiple jets at high Reynolds numbers and moving surfaces.

Although there is a large amount of experimental and numerical data for the jet impingement heat transfer, there is still a lack of knowledge with regard to the jet impingent heat and mass transfer for the drying of sheets. The influence of main parameters (Reynolds number, jet-to-surface distance, jet-to-jet distance) is described by general correlations, and the influence of other parameters (curvature, jet angle) was investigated for some configurations. Nevertheless, for very small jet-to-surface distance, complex multiple jet patterns or moving surface, the data available are very scarce. This situation is even worse with regard to the forces exerted by the jets on the surface. Here further experimental and numerical investigations are highly desirable.

Chapter 3

3. Fundamentals and Methods

3.1 Impinging Jet Drying

Impinging jets provide the best configuration for convective heat and mass transfer to or from a target surface. Impinging jets are used extensively in paper, textile, coatings, photographic film, veneer industries and so on. In some products, such as textiles, double-sided coated papers and pulp sheets, the target surface may be supported by jets impinging on both sides of the surface for the contactless drying [Mujumdar (2004)].

Array of jets rather than a single jet is used in most industrial applications to optimize the heat or mass transfer rates. Nozzles may be either round or slot-shaped with in-line or staggered arrangements. Figure 3.1 illustrates the basic principle of the drying process using an array of nozzles. Ambient air at temperature T_a is heated in a heat exchanger or combustion chamber to temperature T_o, requiring the energy $\dot{H}_0$. The heated air is blown through the nozzles to dry the product. These conditions result in a product at temperature T_s. The evaporating mass flow has the enthalpy $\dot{H}_V$ [Specht (2014)].
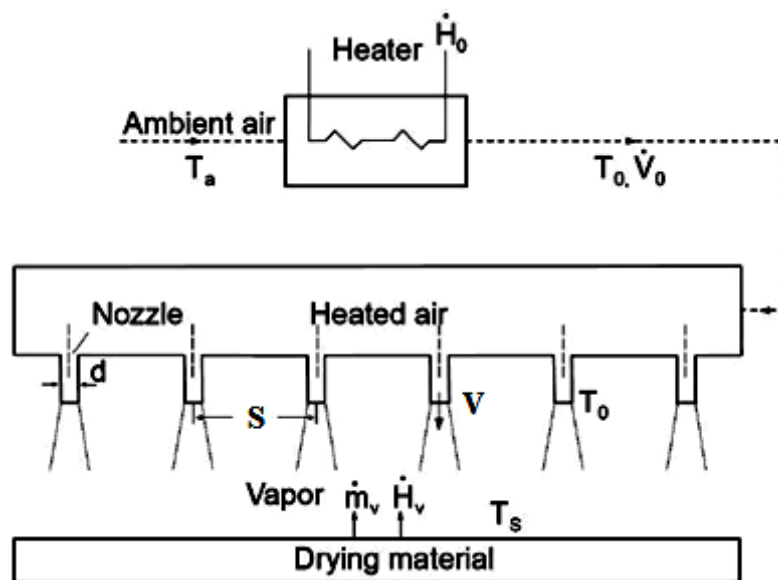
Fig. 3.1 Drying using a nozzle array [Specht (2014)]

3.2 Industrial Dryer Specifications

In industrial drying applications, a thin sheet of material with a temperature in the range of 20-100ºC is drawn through the dryer. The application of alternating jets from above and below lead to the development of a sinusoidal waveform. Typical values for paper drying

would be periods of 200-800 mm and an amplitude of up to 40mm. The paper sheet velocity lies in the range of 0.2-2 m/s. In order to increase the production, higher speeds up to 10m/s are desirable. The jets with an exit velocity between 10-50 m/s emerge from orifices (diameter d) in a confining surface parallel to the material surface. The round jets are arranged in rows or arrays with diameters of 5-20mm. The jet-to-jet spacing (S) in both directions of space may be between 2d-12d and the distance between the target surface and the jets (H) between 1d-20d. The fluid is mostly hot air at ambient pressures.

3.3 Flow Characteristics

Within impinging jets, different distinct flow patterns occur: free jets with a shear layer, stagnation zones with strong pressure gradients and boundary layer zones. Depending on the geometry there are recirculation zones, interaction between jets, entrainment and cross-flow. Due to their relevance for technical applications, only turbulent jets are considered. There are regions with high and low turbulence and the turbulence is highly anisotropic. As most industrial drying applications are at low Mach-numbers the influence of compressibility is neglected.

3.3.1 Single Jet

Three distinct flow regions can be identified in the flow structures of a single impinging jet: the free jet region, the stagnation flow region, and the wall jet region (Fig. 3.2). In the free jet region, which is the region that is largely unaffected by the presence of the target surface, a potential core exists, within which the velocity is still equal to the jet exit velocity and it is typically visible up to a distance of 6–7 jet diameters from the nozzle. A shear layer exists between the potential core and the ambient fluid and the shear layer entrains the ambient fluid and causes the jet to spread radially. As the jet approaches the target surface, the axial velocity component is decreased and transformed into an accelerated horizontal velocity component. The stagnation region extends to a radial location defined by the spread of the jet and includes the stagnation point where the mean velocity is zero. Within this region, the free jet region is deflected into the wall jet region. Finally, the wall jet region extends beyond the radial limits of the stagnation region. The wall parallel velocity component in the wall jet region is first accelerated linearly from zero to a maximum value at a distance of about one jet diameter from the stagnation region. The wall parallel velocity component is again decelerated in the fully developed wall jet region and it will generally be accompanied by transition from the laminar

to the turbulent flow as the stabilizing effect of acceleration to keep the flow laminar is lost [Weigand&Spring (2011)].
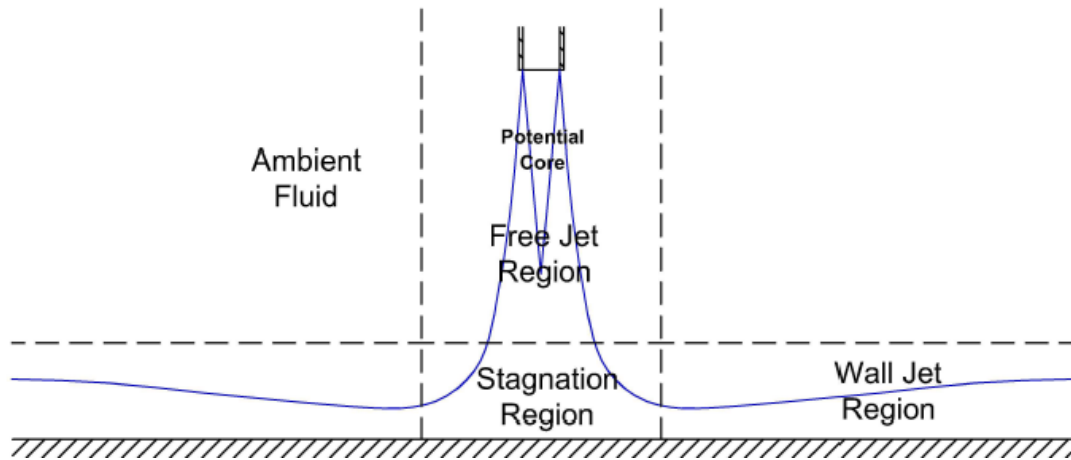
Fig. 3.2 Impinging jet regions [Weigand&Spring (2011)]

3.3.2 Multiple Jets

The flow characteristics from multiple impinging jets have similar regions to the flow field from a single impinging jet. However, there are two types of interaction that do not occur in a single impinging jet (Fig.3.3). The first is the possible jet interaction before impingement onto the target surface. This type of interaction occurs for arrays with very low jet-to-jet spacings and large nozzle-to-target surface distances. The second is the interaction due to the collision of wall jets from the adjacent jets and it results in an upward flow from the wall, called a fountain. The presence of the fountain can cause recirculating flow zones and vortices. This type of interaction predominantly occurs for arrays with small S/d, small H/d and large jet velocities [Weigand&Spring (2011)].
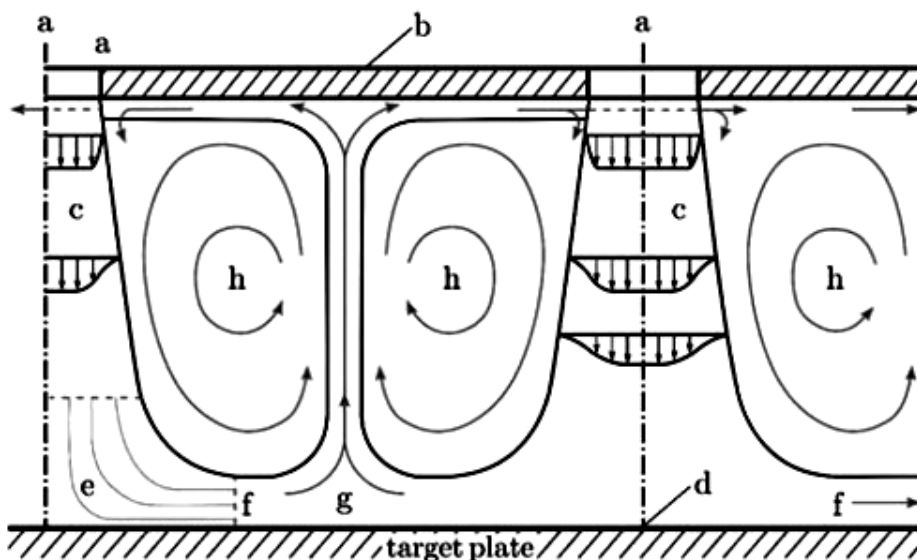
Fig. 3.3 Flow pattern within multiple impinging jets: a – orifice, b – target surface, c – free jet, d – stagnation point, e – stagnation region, f – decelerated flow, g – recirculating flow, h – vortices [Glaser (1962)]

The above effects can be accentuated further by an additional interaction with the cross-flow formed by the spent air of the jets. The cross-flow strength is based on the design of spent flow. There are basically three possible designs with regard to the spent flow of the air, addressed as minimum, intermediate, and maximum cross-flow (Fig. 3.4) [Weigand&Spring (2011)].
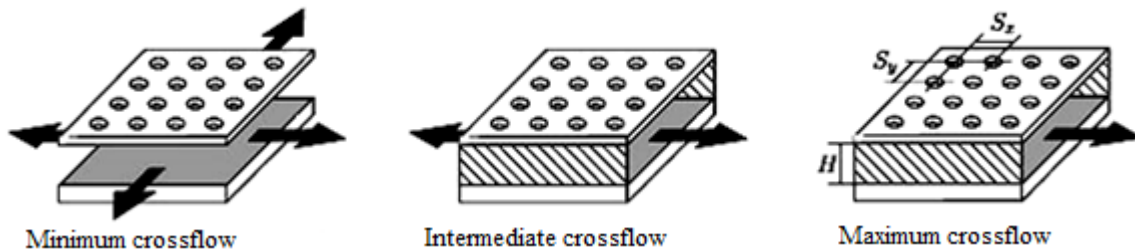
Fig. 3.4 Definition of cross-flow schemes in multi-jet systems [Goldstein&Seol (1991)]

3.4 Heat and Mass Transfer Characteristics

Heat transfer between an impinging jet and a target surface is affected by many different factors, such as jet exit velocity, velocity profile, turbulence level, entrainment conditions, nozzle geometry, separation distance between a jet and target surface, the thermal wall boundary conditions, surface motion and surface curvature. Due to this manifold dependence, the variation of local heat transfer coefficients is very complex.

For a single impinging jet, the point of maximum heat transfer is typically the stagnation point (except for very low separation distances), from which the heat transfer rates decrease monotonously in the radial direction. Heat transfer coefficients at the stagnation point increase with the jet Reynolds number. For low separation distances or high jet Reynolds numbers, the secondary peak can appear in the local heat transfer distribution. Great scientific interest has been shown in the origins of the secondary peak. It has been speculated that secondary peaks are related to the transition from a laminar to a turbulent flow. The heat transfer rates due to the arrays of impinging jets give qualitatively similar results for a single impinging jet when the jets are widely spaced and, as a consequence of this, no significant jet interaction is present. However, low jet-to-jet spacing or small jet-to-surface distance increases the jet interaction and the heat transfer rate changes significantly compared to the single jet. The changes in the heat transfer rate are due to the two types of jet interaction described above [Weigand&Spring (2011)].

The mass transfer processes are similar to heat and momentum transport phenomena. The fluid dynamic processes that cause the heat transfer across a temperature difference also result in a mass transfer across a concentration difference. For example, in evaporative drying, the

vapor concentration is highest at the surface and lowest in the drying air. Due to this concentration difference, the vapor is transferred across the boundary layer to the drying air. During the drying process, the heat is transferred toward the surface while the vapor is also simultaneously transferred. The heat supplied serves for evaporation and, if necessary, raising the system temperature [Etemoglu&Can(2013)]. Thus for drying applications there is a similarity in the temperature distribution and the water content distribution in the air.

3.5 Definition of Characteristic Numbers and Dimensional Groups

The complex physical phenomena of heat and mass and momentum transfer are best described based on similarity theory. For impinging jets this leads to a set of familiar dimensionless numbers and characteristic ratios.

Laminar and turbulent jets are distinguished by the jet Reynolds number, defined using mean jet velocity issued from the orifice inlet (V_j), the kinematic viscosity of the jet (ν), μ is the dynamic viscosity of the jet, $\dot{m}$ is the mass flow rate through one jet orifice, and the characteristic length that is the nozzle exit diameter (d). The jet inlets were modeled as the circular plane in contrast to a real geometry where the actual diameter is smaller than the orifice diameter and the flow might be subjected to local acceleration (vena contracta phenomenon). However, the measurements of local discharge coefficients in the impinging jet arrays show that the discharge coefficients are independent of the jet Reynolds number [Florschuetz&Su (1987), Robertson (2005)].

$$Re = \frac{V_j d}{\nu} = \frac{4\dot{m}}{\pi d \mu} \tag{3.1}$$

The nondimensional Nusselt number is defined by the following expression:

$$Nu = \frac{hd}{k} \tag{3.2}$$

The local heat transfer coefficient (h) is defined as

$$h = \frac{q}{T_w - T_j} = \frac{-k \partial T / \partial \vec{n}}{T_w - T_j} \tag{3.3}$$

Where q is the convective heat flux, $\partial T / \partial \vec{n}$ gives the temperature gradient component normal to the wall, T_w is the local wall temperature, and T_j is the jet temperature, d is the jet exit diameter, and k is the thermal conductivity of the air at jet exit temperature. For computation of the Nu number, the jet and target surface temperatures are preset and the heat

flux on the target surface is provided by the numerical solution. The Nusselt number is then obtained from the above equation.

The nondimensional Sherwood number is defined as the rate of mass transfer in a similar fashion to the heat transfer:

$$Sh = \frac{h_m d}{D} \tag{3.4}$$

$$h_m = \frac{\dot{m}_v}{C_s - C_a} = \frac{D\partial C / \partial n}{C_s - C_a} \tag{3.5}$$

Where h_m is the surface mass transfer coefficient, m/s; $\dot{m}_v$ is the mass flux, kg/m^{2}s; $\partial C / \partial n$ gives the mass concentration gradient component normal to the wall; C_s is the saturated vapor concentration, kg/m^3; C_a is the partial concentration of vapor in the drying air, kg/m^3; and D is the mass diffusion coefficient, m^2/s.

The Prandtl number (Pr) is defined as the ratio of kinematic viscosity (ν) to thermal diffusivity (α) and the Schmidt number (Sc) is defined as the ratio of kinematic viscosity (ν) to the mass diffusion coefficient (D):

$$Pr = \frac{\nu}{\alpha} = \frac{c_p \mu}{k} \tag{3.6}$$

$$Sc = \frac{\nu}{D} \tag{3.7}$$

Additional quantities (such as the surface temperature and velocity) have to be scaled accordingly by the temperature and the velocity used for the Reynolds and Nusselt number:

V_w/V_j: wall to jet velocity ratio;

T_w/T_j: ratios of target surface temperature to jet temperature

In addition, the distances characterizing the geometric configuration are scaled by the orifice diameter.

r/d: nondimensional radial position from the center of the jet;

H/d: ratio of nozzle height to nozzle diameter;

S/d: ratio of jet center-to-center spacing (pitch) to nozzle diameter;

d/D: ratio of jet diameter to the impingement surface diameter;

Additional geometric parameters are

θ: jet inclined angle with respect to the horizontal axes, degree;

A_f: open area ratio, total jet area to heat transfer area, e.g. for an in-line array, relates to the pitch-to-diameter ratio in both coordinate directions (X,Y)

$$A_f = \frac{d^2\pi/4}{S_x S_y} = \frac{\pi}{4(S_x/d)(S_y/d)} = \frac{\pi}{4}(\frac{d}{S_x})(\frac{d}{S_y})$$

(3.8)

The definition of these functions is not without drawbacks. The diameter used is the geometric diameter of the orifice. Differences in contraction, velocity distribution or turbulence are neglected. The temperature and fluid properties used are also at the jet inlet. For most drying applications the velocities are well below the speed of sound and thus the effect of compressibility (Mach number) is not taken into account. The incompressible air as working fluid with constant fluid properties at $T_j = 298.15$ K, Pr=0.71, and an atmospheric pressure of 101325 Pa entered the domain. For all configurations, the pattern was regular i.e. the streamwise and spanwise jet-to-jet distance was equal.

A major objective of the research on the multi-jet impingement systems is to find a reasonable empirical correlation for both average and local Nusselt numbers in the following general form:

$$Nu = f(Pr, Re, Ma, r/d, H/d, S/d, A_f, d/D, V_w/v_j, T_w/T_j, \theta)$$

(3.9)

For the sake of simplicity these numbers are often arranged in the form of potential functions, although sometimes more complex functions might be more fitting. A famous correlation for prediction of the jet impingement heat transfer is a correlation produced by Martin (1977) as follow:

$$Nu_{ave} = Re^{0.67} Pr^{0.42} \left[1 + (\frac{H}{d}\frac{\sqrt{A_f}}{0.6})^6 \right]^{-0.05} \times \sqrt{A_f} \frac{1 - 2.2\sqrt{A_f}}{1 + 0.2(H/d - 6)\sqrt{A_f}}$$

(3.10)

Martin's correlation was obtained by modifying the equation for a single round nozzle, and thus it is valid for arrays with good outlet flow conditions where the outlet planes are placed at a sufficiently large distance from the impingement region. Generally, the turbulence is not considered in the correlation because this is not a design parameter and it makes no sense to include it in an engineering correlation [Martin (1977)].

3.5.1 Heat and Mass Transfer Analogy

The mass transfer processes are similar to the heat and momentum transport phenomena in that, if a complex case cannot be solved by analysis of the mass transfer problem only, a mathematical model used for the heat or momentum transfer can be transferred to solve the

mass transfer problem by using the analogy between them. The mean heat and mass transfer coefficients for both single and arrays of nozzles (both round and slot) could be correlated by the following equation [Martin (1977)]:

$$\frac{\overline{Sh}}{Sc^{0.42}} = \frac{\overline{Nu}}{Pr^{0.42}}$$

(3.11)

3.5.2 Specific Drying Energy Consumption

The specific drying energy consumption is defined as the ratio of energy for heating the air jet $\dot{H}_j$ to the enthalpy of evaporation of the water $\dot{H}_v$:

$$\frac{\dot{H}_j}{\dot{H}_v} = \frac{\pi d^2 \rho c_p V}{4S^2} \left(\frac{1}{h} + \frac{T_s - T_a}{\dot{m}_v \Delta h_v} \right)$$

(3.12)

In the above equation, T_a is the ambient temperature, c_p is the average specific heat capacity between the temperatures of the jet and the environment, ρ is the jet density, V is the discharge velocity from the nozzles with a diameter of d, T_s is saturation temperature, S nozzle pitch, $\dot{m}_v$ is the evaporating mass flux, Δh_v the evaporation enthalpy and h the heat transfer coefficient. The air jet temperature is calculated based on the condition that the transferred heat has to cover the evaporation enthalpy and the enthalpy to heat the dry material flow from the ambient temperature (T_a) to the saturation temperature (T_s). The evaporating mass flux is obtained from the mass transfer relationship [Specht (2014)]:

$$\dot{m}_v = h_m \frac{P}{R_v T_s} \ln \frac{P - P_a}{P - P_s}$$

(3.13)

Here, the gas constant of the vapor is represented by R_v, the surface mass transfer coefficient by h_m, the total pressure by P, the partial pressure of the vapor in the ambient air by P_a, and the saturated vapor pressure by P_s. The saturation pressure is approximated from the equilibrium relationship with the reference condition P_0, T_0, for example, $P_0 = 1$ bar, $T_0 = 373$ K [Specht (2014)]:

$$P_s = P_0 \exp\left[-\frac{\Delta h_v}{R_v} \left(\frac{1}{T_s} - \frac{1}{T_0} \right)\right]$$

(3.14)

3.5.3 Pressure Force Coefficient

Pressure force on the surface is the force that the fluid exerts in the direction of normal to the surface. Pressure force on the impingement surface (F) is presented in dimensionless form by a force coefficient C_f. The force coefficient of a surface is defined as follows [STAR-CCM$^+$ User guide]:

$$C_f = \frac{F}{0.5\rho V^2 (\pi d^2 / 4)}$$

(3.15)

Where F is the pressure force on the surface, ρ is the density of fluid, d is the diameter of the nozzle and V is the jet exit velocity. The pressure force on surface is computed as:

$$F = P_{max} A$$

(3.16)

Where P_{max} is the maximum pressure and A is the target surface area.

3.6 Mathematical and Numerical Background

The present section intends to provide a compact overview on the method of Computational Fluid Dynamics (CFD) and optimization, which is used for obtaining the mathematical and numerical results presented in this work. In the present investigation, the CFD model is set up and run with the commercial code STAR-CCM+ 13.02.2013 by CD-Adapco following the general procedures described in the product user guide for the heat transfer simulation.

3.6.1 Governing Equations

The fundamental laws that govern the mechanics of fluids are the conservation of mass, momentum, and energy. In the following, the conservation laws are expressed for an incompressible fluid with the constant fluid properties in steady state form.

The mass conservation equation or continuity equation expresses the balance of mass through a control volume:

$$\frac{\partial U_i}{\partial X_i} = 0$$

(3.17)

Where U_i is the instantaneous components of the velocity vector in the direction X_i, and X_i represents the coordinates.

The momentum conservation equations and also known as the Navier-Stokes equations are defined as

$$U_j \frac{\partial U_i}{\partial X_j} = \frac{\partial}{\partial X_j} \left(\nu \frac{\partial U_i}{\partial X_j} \right) - \frac{1}{\rho} \frac{\partial P}{\partial X_i}$$ (3.18)

Where ν is the kinematic viscosity of the fluid, ρ is the density, P represents the instantaneous pressure.

The energy conservation can be written as:

$$U_j \frac{\partial \Theta}{\partial X_j} = \frac{\partial}{\partial X_j} \left(\Gamma_\Theta \frac{\partial \Theta}{\partial X_j} \right) + q_\Theta$$ (3.19)

Where Θ is the general scalar variable (e.g. temperature), Γ_Θ is the diffusivity of Θ (thermal diffusivity for energy conservation), and q_Θ represents the sources or sinks for the scalar [STAR-CCM+ User guide].

3.6.2 Reynolds-Averaged Navier-Stokes (RANS) Turbulence Models

For turbulent flows the length scale and time scales are so small that a computation of the instantaneous flow is very demanding and for many engineering applications still not realizable. Thus some form of averaging or filtering of the Navier-Stokes equation and appropriate modelling of the turbulent effects have to be considered.

The Reynolds-Averaged Navier Stokes equations are solved for the transport of mean flow quantities with an appropriate RANS turbulence models to describe the influence of the turbulent quantities to provide the closure relations. Each solution variable in the instantaneous Navier-Stokes equations Φ should be decomposed into an averaged value $\overline{\Phi}$ and a fluctuating component Φ' in order to obtain the Reynolds-Averaged Navier-Stokes equations:

$$\Phi = \overline{\Phi} + \Phi'$$ (3.20)

Where Φ represents the velocity components, pressure, energy, or species concentration.

The resulting equations for the mean quantities are essentially identical to the original equations, except that an additional term now appears in the momentum transport equation. This additional term, known as the Reynolds stress tensor, has the following definition [STAR-CCM+ User guide]:

$$T_t = -\overline{U_i' U_j'} \qquad (3.21)$$

The challenge is thus to model the Reynolds stress tensor to close the time-averaged equations. Two basic approaches are used in STAR-CCM$^+$ [STAR-CCM$^+$ User guide]:

- Eddy viscosity models
- Reynolds stress transport models

3.6.2.1 Eddy Viscosity Models

Eddy viscosity models employ the concept of a turbulent viscosity ν_t for modeling of Reynolds stress tensor. The most common model is known as the Boussinesq approximation:

$$T_t = 2\nu_t S_{ij} - \frac{2}{3}\delta_{ij}k$$

(3.22)

Where ν_t is the turbulent viscosity, k is the turbulence kinetic energy, δ_{ij} is the Kronecker delta (=1 if i=j, otherwise =0) and S_{ij} is mean strain rate tensor and given by [STAR-CCM$^+$ User guide]:

$$S_{ij} = \frac{1}{2}\left(\frac{\partial \overline{U}_i}{\partial X_j} + \frac{\partial \overline{U}_j}{\partial X_i} \right) \qquad (3.23)$$

Since the assumption that the Reynolds stress tensor is linearly proportional to the mean strain rate and does not consider the anisotropy of turbulence, some two-equation models extend the linear approximation to include the non-linear constitutive relations. The use of hybrid models as a combination of efficient two-equation models is advisable. The Shear Stress Transport (SST) k-ω model as a combination of the k-ε model in the freestream and the standard k-ω model in the inner parts of the boundary layer are an obvious choice [STAR-CCM$^+$ User guide].

3.6.2.2 Reynolds Stress Transport Models

A Reynolds stress transport (RST) model, also known as second-moment closure model, calculates all individual components of the Reynolds stress tensor directly by solving their governing transport equations. This type of model is potentially able to predict the complex flows more accurately than the eddy viscosity models, because the transport equations for the Reynolds stresses naturally account for the effects of streamline curvature, swirl rotation,

turbulence anisotropy and high rate of strain, but are often unstable when used in the complex flows [STAR-CCM$^+$ User guide].

3.6.3 Scale-Resolving Simulations

In contrast to the RANS models, the scale-resolving simulations resolve the large scales of turbulence and model the small scale motions. Two approaches are available in STAR-CCM+:

- Large Eddy Simulation (LES)
- Detached Eddy Simulation (DES)

A Large Eddy Simulation resolves the turbulent structures everywhere in the flow domain. To resolve the crucial turbulent structures near the target wall, this approach requires an excessively high grid resolution in the wall boundary layer: not only in the direction normal to the wall but also in flow direction. As a result of the high computational costs that go with the high cell count, the LES is used mainly for academic applications or for flows with the low Reynolds numbers [STAR-CCM$^+$ User guide].

A Detached Eddy Simulation (DES) is a hybrid LES-RANS approach that resolves the turbulent structures only away from the walls and covers the wall boundary layers by a RANS model. Thereby, the DES avoids the expensive grid requirements of LES [STAR-CCM$^+$ User guide].

3.6.4 Near-Wall Treatment

Walls are a source of vorticity in most flow problems of practical importance. Hence, an accurate prediction of flow and turbulence parameters across the wall boundary layer is required. The inner region of the boundary layer can be split up into three sublayers. In each of them the flow has different characteristics and can be modeled using different empirical approaches [STAR-CCM$^+$ User guide]:

- Viscous sublayer: the fluid layer in contact with the wall is dominated by the viscous effects and is almost the laminar. The mean flow velocity only depends on the fluid density, viscosity, distance from the wall, and the wall shear stress.
- Log-law layer: the turbulent log-law layer is dominated equally by the viscous and turbulent effects.
- Buffer layer: the buffer layer is a transitional layer between the viscous sublayer and the log-law layer.

The non-dimensional wall distance y^+ can be used to define the extents of the sublayers. Figure 3.5 shows the velocity distribution of a viscous fluid across the three sublayers. The velocity is given in its non-dimensional form u^+ as a function of y^+ which is defined as:

$$y^+ = \frac{yu^*}{\nu} \tag{3.24}$$

$$u^* = \sqrt{\tau_W / \rho} \tag{3.25}$$

$$u^+ = \frac{u}{u^*} \tag{3.26}$$

Where u is the component of wall-cell velocity parallel to the wall, y is the normal distance from the wall to the wall-cell centroid, τ_w is the wall shear stress, ν is the kinematic viscosity, ρ is the density and u^* is the friction velocity [STAR-CCM$^+$ User guide].
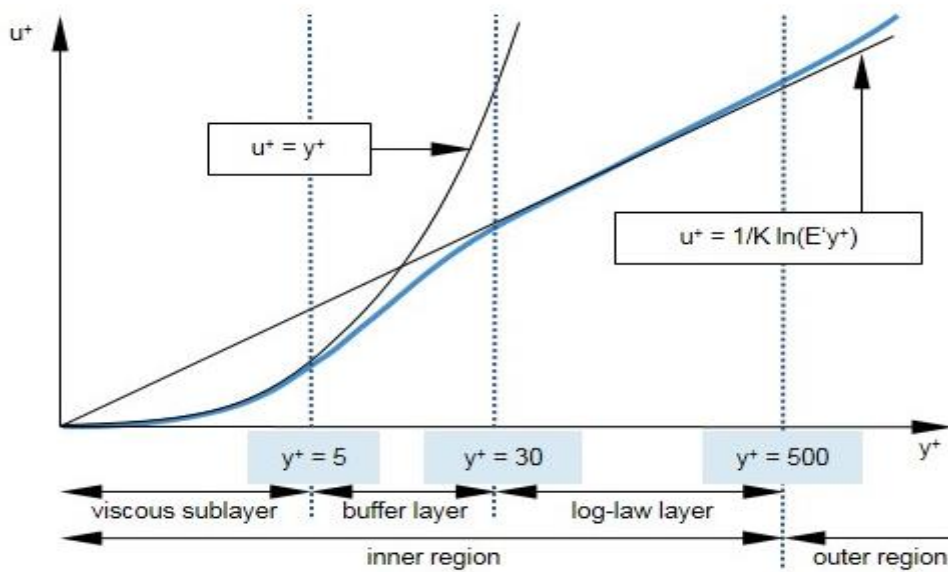
Fig. 3.5 Velocity profile of a viscous fluid in the near-wall region [STAR-CCM$^+$ User guide]

Numerical models of turbulence near the wall commonly feature a method, i.e. the low-Reynolds-number method, to account for the effects in the boundary layer, whereas the naming refers to the turbulent Reynolds number, which is low near the wall. In this method, the viscous sub-layer is fully resolved by using very small grid sizes in the direction normal to the wall. To resolve the viscous sublayer, these models require a sufficiently fine grid with near-wall cells located at y^+ around unity. The computational expense that is associated with this approach can be significant, particularly for large Reynolds number flows where the viscous sublayer can be

very thin. Therefore, this wall treatment is suitable only for low-Reynolds number flows [STAR-CCM$^+$ User guide].

3.6.5 Solution Procedure

The governing equations are discretized using finite volume discretization. In the finite volume method, the solution domain is subdivided into a finite number of small control volumes, corresponding to the cells of a computational grid. The velocities and pressures were predicted using the semi-implicit pressure linked equations (SIMPLE) algorithm. Spatial discretization was based on the second order upwind scheme. The discretized equations are then linearized and solved iteratively [STAR-CCM$^+$ User guide]. All governing equations are solved under steady-state conditions. The SST k-ω turbulence model in combination with a low Re damping modification is selected for all computations as a compromise between accuracy and the computational cost shown by researchers in the literature (see Chapter 2). The flow in the near‑wall regime was simulated using a low-Reynolds number method.

The convergence criteria for the continuity, momentum, and energy equations is 10^{-4}. Convergence is also monitored by plotting the average Nu number on the target surface until the variation of the average Nu number levels off with iteration. The local discretization error distribution is calculated by applying the Grid Convergence Index (GCI) method [Roache 1994 and 2003]. It can be regarded as a uniform method to describe the numerical discretization errors through gradual grid refinement in order to evaluate the grid independence of the solution (see appendix C).

3.6.6 Type of Optimization Study

Optimization techniques are coupled with STAR-CCM$^+$ to enable full optimization. In an optimization study, one or more objectives are defined which must be met by the analysis as closely as possible. Along with the objectives, the input parameters are defined. During the analysis, a search algorithm chooses the parameter values for the designs so as to best meet the analysis objectives. There are two types of optimization study.

3.6.6.1 Weighted Sum of All Objectives

This type of optimization study allows an optimization based on a single objective or based on multiple objectives. For the multiple objectives, a linear weighting is used that combines all objectives into a single performance function. Running a weighted sum of all

objectives analysis with multiple objectives returns a single best design [STAR-CCM+ User guide]:
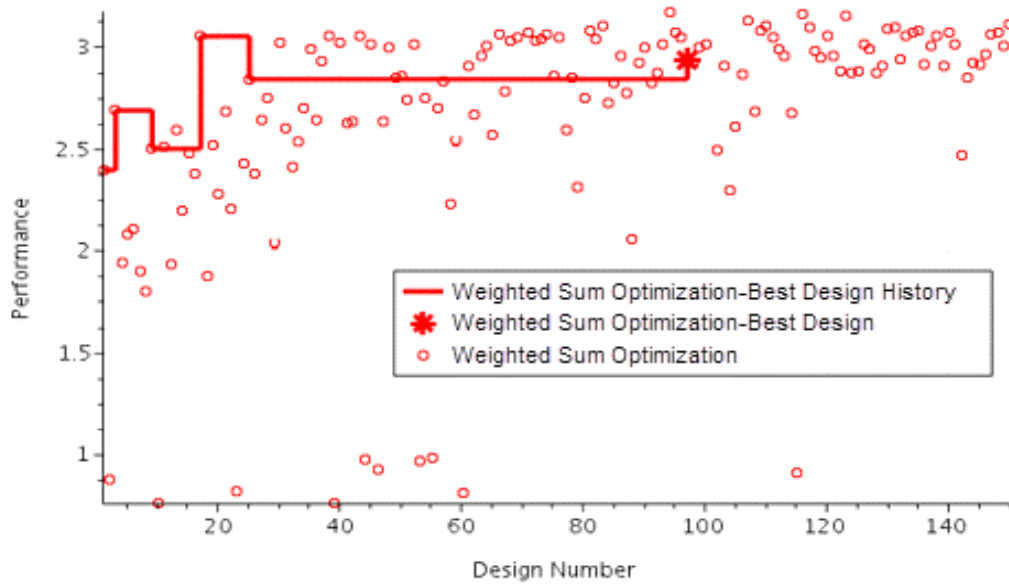
Fig. 3.6 Weighted sum of all objectives [STAR-CCM+ User guide]

A design performance is based on the value returned for the objectives together with the degree to which a design satisfies its constraints. Once the constraints are satisfied, only the objectives contribute to the evaluation of performance using the following equation [STAR-CCM+ User guide]:

$$\sum_{i=1}^{N_{obj}} \frac{LinWt_i.Sign_i.Obj_i}{Norm_i} - \sum_{j=1}^{N_{con}} \frac{QuadWt_j.ConViol_j^2}{Norm_j^2} \tag{3.27}$$

Where:

- N_{obj} is the number of objectives in the design study.
- $LinWt_i$ is the linear weight for the i-th objective.
- $Sign_i$ is the sign for the i-th objective. The value is -1 for objectives being minimized and +1 for objectives being maximized.
- Obj_i is the response value for the i-th objective for that design.
- $Norm_i$ is the normalization value for the i-th objective.
- N_{con} is the number of constraints in the design study.
- $QuadWt_j$ is the quadratic weight for the j-th constraint. This value is 10,000.
- $ConViol_j$ is the amount by which the j-th constraint is violated. $ConViol_j$ is 0.0 if the constraint is met.

- Norm$_j$ is the normalization value for the j-th constraint, which is the value of the constraint itself. If the constraint value is 0, then the normalization value is 1.

Weighted sum of all objectives optimization uses the SHERPA search algorithm [STAR-CCM$^+$ User guide].

3.6.6.2 Multiple Objective Tradeoff Study (Pareto Front)

This type of optimization study is based on the competing objectives. Pareto optimization is suited to cases where there are two objectives which are competitive in nature. In such cases, there is no single optimum design. Instead, the optimization returns a curve along which all designs are optimum in one objective for a given value in the other objectives, known as the non-dominated design condition. This curve, known as Pareto front, expresses the optimum trade-off relationship between two competing objectives. Finding the Pareto front for cases where there are more than two competing objectives requires a large number of design evaluations. A multiple objective tradeoff study (Pareto front) uses the Multi Objective SHERPA search algorithm [STAR-CCM$^+$ User guide].
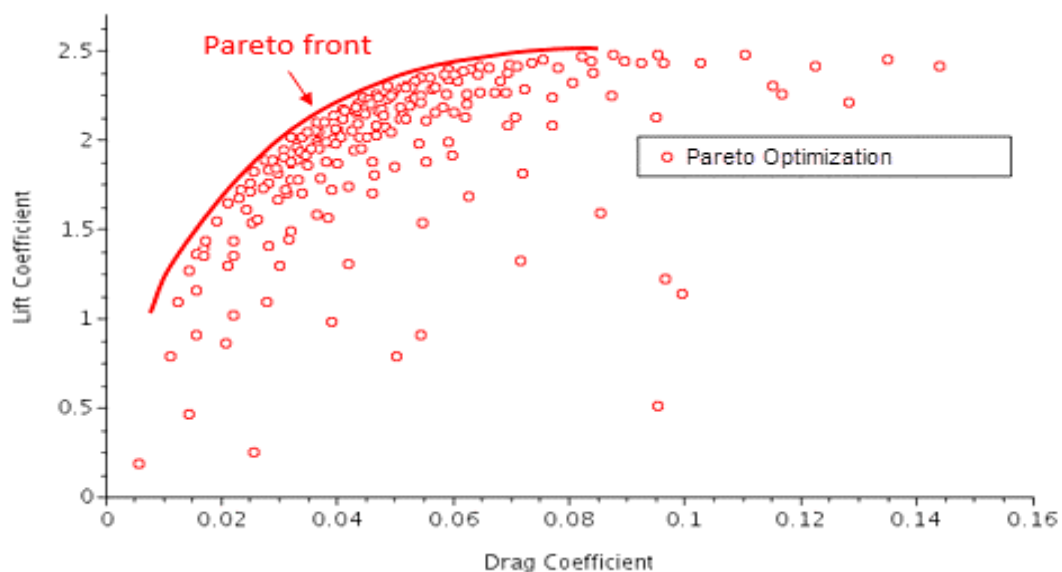
Fig. 3.7 Multiple objective tradeoff study (pareto front) [STAR-CCM$^+$ User guide]

3.6.6.3 SHERPA Algorithm

SHERPA Algorithm employs the multiple search methods simultaneously rather than sequentially. This approach uses the best attributes of each search method. If a particular search method is deemed to be ineffective, this algorithm reduces its participation. While running this algorithm, a combination of different search methods is used. At any given time, the number of different methods that are used can range between two and ten. Unlike traditional

optimization algorithms that require you to tune parameters manually, the tuning parameters in each method that SHERPA uses are modified automatically during the search. As it learns more about the design space, it determines when and to what extent to use each search method. Therefore, the SHERPA algorithm (Simultaneous Hybrid Exploration that is Robust, Progressive and Adaptive); a combination of different search methods is used in order to optimize the efficiency. A comparison between a traditional optimization approach and this approach is displayed below [STAR-CCM$^+$ User guide].
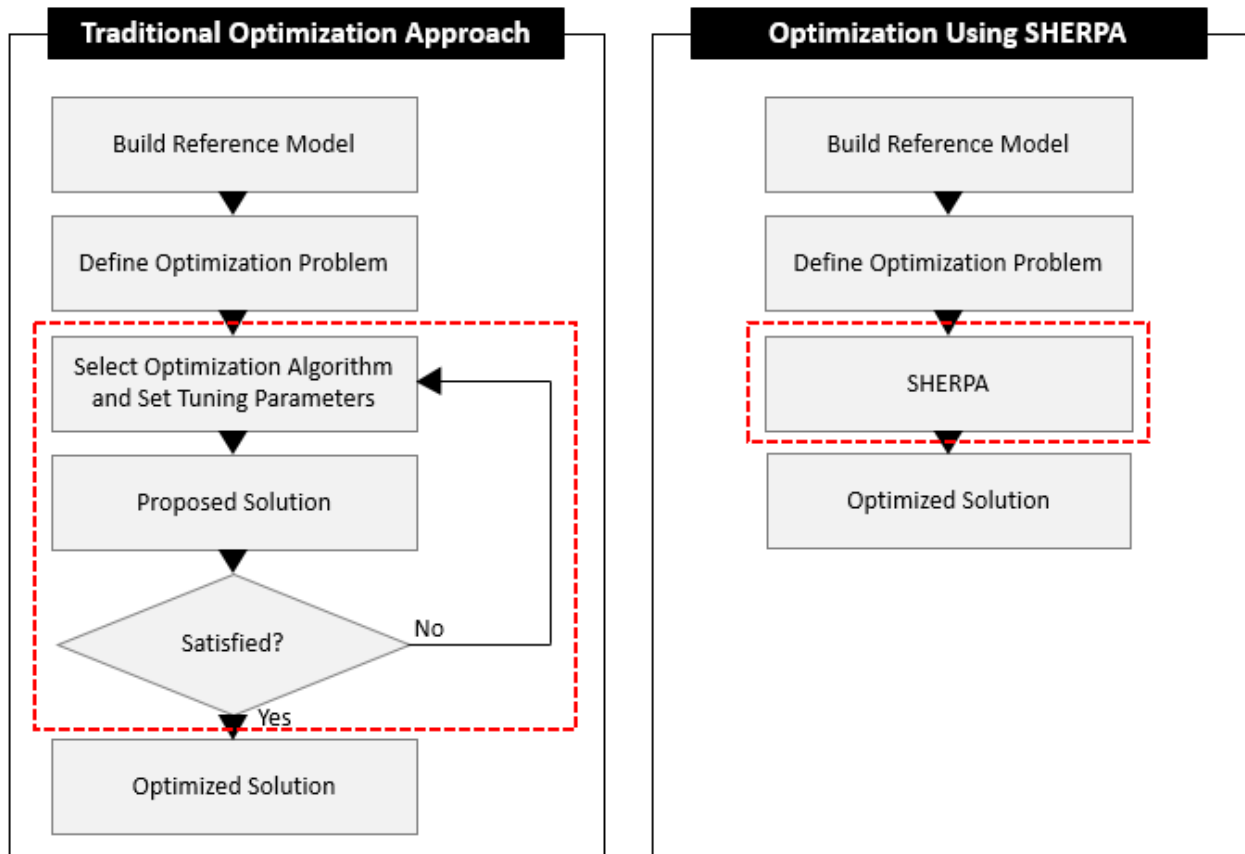
Fig. 3.8 A comparison of a traditional optimization approach and of the SHERPA approach [STAR-CCM+ User guide]

Chapter 4
4. Single Jet Impinging on Flat Surface

The single impinging jet as a simple geometry has been widely studied and therefore forms a good platform for the validation of numerical models. As the first case in this investigation, the single impinging round jet for symmetric configuration (2D) is considered. The CFD simulations of the local heat transfer coefficient are compared to the experimental data from the literature to understand the discrepancies between CFD and experimental results. This is important for the correct interpretation of results obtained in the next chapters for the multiple impinging jets as a more complex configuration.

The chapter starts with a brief description of the selected test case specifications. Next, the information on the computational details such as domain, the boundary conditions, and the grid is provided. In the results section, the discretization errors are quantified by means of a grid sensitivity analysis. The possible factors in the prediction of local heat transfer distribution are investigated in detail, such as effect of different turbulence models, transition model, grid size and grid shape. The chapter continues with a summary of the main findings.

4.1 Benchmark Case

Although the impinging jet problem appears simple, it is in fact a challenging phenomenon especially at low nozzle-to-surface distance and high jet Reynolds number to predict accurately. The present investigation focus on the conditions that seem representative for drying applications, i.e. high jet Reynolds number and low nozzle-to-surface distance. A considerable amount of experimental investigations on the flow and heat transfer characteristics of single and multiple impinging jets exist in literature and tabulated in Table A.1. In the present investigation, an ERCOFTAC[7] test case (Re = 23,000, H/d =2) [Manceau (2004)] is used as a benchmark for the evaluation of different turbulence models.

4.2 Computational Details
4.2.1 Domain and Boundary Conditions

Figure 4.1 shows a schematic of the axi-symmetry computational domain for the single impinging round jet. The domain size was 10d and H+2d (d=26.5mm) in radial and axial direction respectively to ensure that the outlet planes are placed at a sufficiently large distance

---

[7] European research community on flow, turbulence and combustion

from the impingement region. The validity of the present approach is confirmed by Spring (2010).
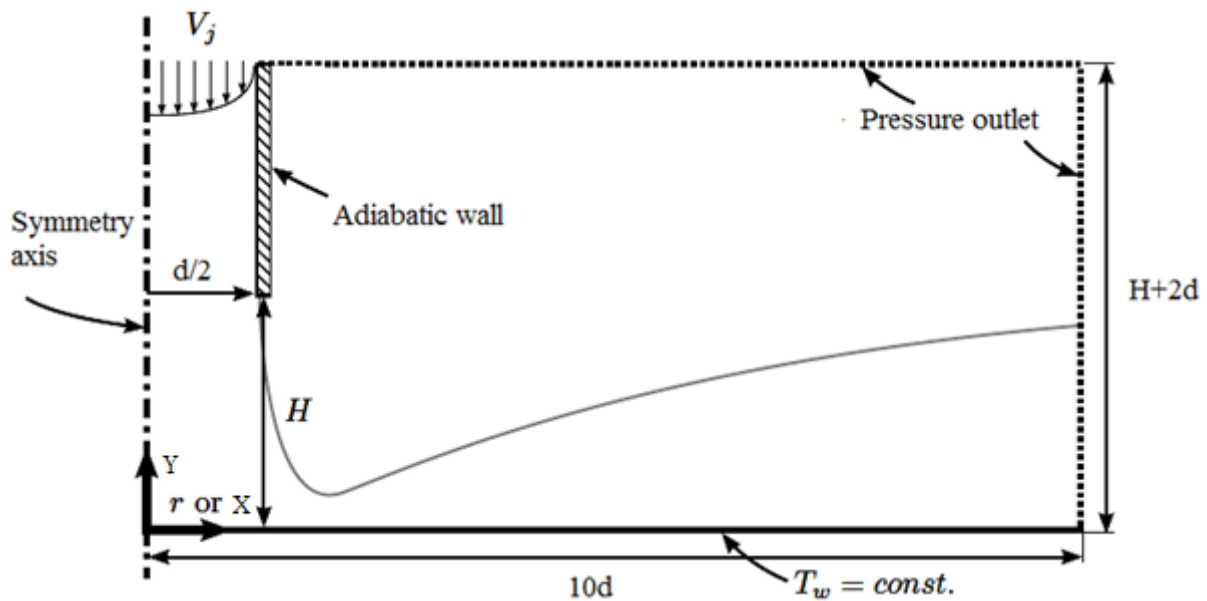
Fig. 4.1 Computational domain for the single impinging jet [Baughn et al. (1991)]

The incompressible air as working fluid with constant fluid properties at T_j = 298.15 K, Pr=0.71 and the turbulence intensity equal to 0.045 entered the domain with a fully developed turbulent velocity profile. The top and lateral sides of the domain are set to a pressure outlet boundary condition and kept constant at an atmospheric pressure of 101325 Pa. The target surface is modeled as a no-slip wall with a constant temperature (T_w = 330 K) [Baughn et al. (1991)].

4.2.2 Grid Generation

Discretization of the computational domain was realized by an unstructured polyhedral grid using STAR-CCM+. Thirty prism layers are used near the wall (i.e., target surface) and pipe wall to capture the near wall boundary layer viscous effects. The requirements of the low-Reynolds formulations of the turbulence models regarding the near-wall resolution ($y_1^+ \leq 1$) were fulfilled for the target surface. The resulting grid is shown in Fig. 4.2.
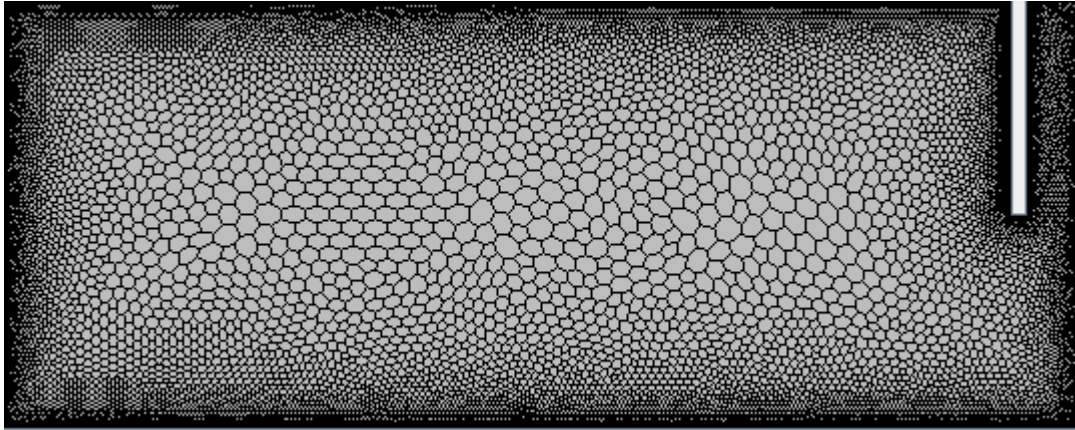
Fig. 4.2 two-dimensional view on an unstructured polyhedral grid

4.3 Results and Discussion

4.3.1 Grid Sensitivity Study

The benchmark case (H/d = 2, Re= 23,000) was taken for a quantification of the discretization error. Three simulations with the same geometry but different grid sizes were carried out to check the grid independence of the simulation. The grid sizes are summarized in Table 4.1 indicating that the y^+ requirement $(y^+_{1,max} \leq 1)$ was fulfilled for all investigated grids. The value of $y^+_{1,max}$ refers to the maximum dimensionless wall distance on the target surface. Base size specifies the reference length value for all relative size control.

Table 4.1 Grid parameters used for the grid sensitivity analysis

Grid	Base size(mm)	Cell number	$y^+_{1,max}$	Average GCI %
Coarse	2.0	8,862	0.22	---
Intermediate	1.0	19,143	0.11	0.63
Fine	0.5	40,579	0.087	0.26

The local Nusselt number distributions obtained by the three different grid sizes used in the grid sensitivity study for the single impinging jet are shown in Figure 4.3.
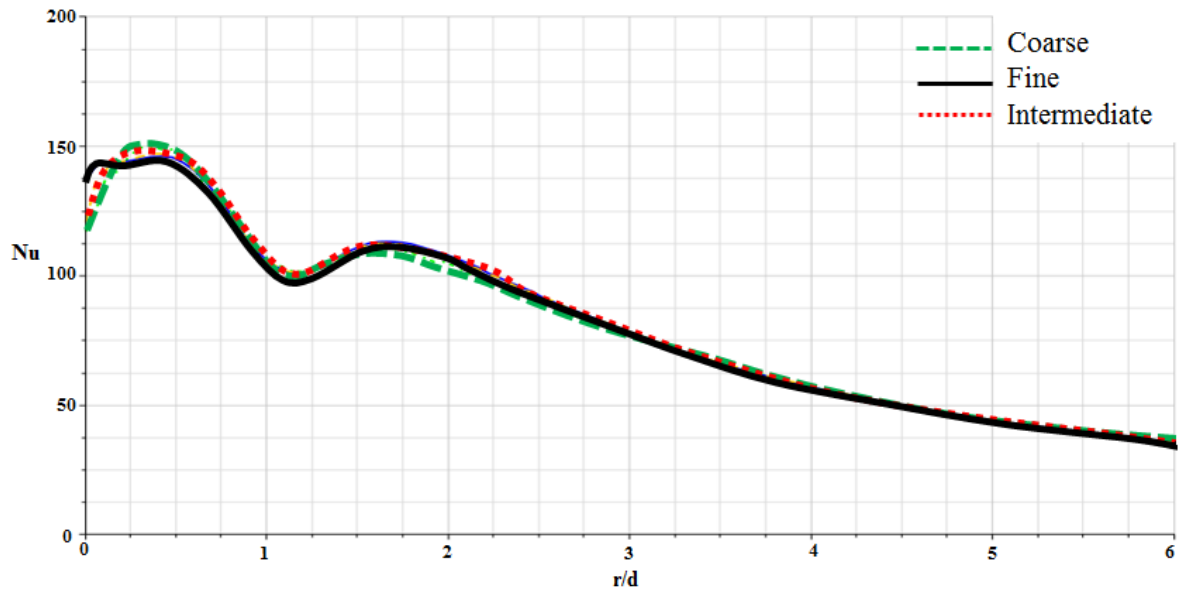
Fig. 4.3 Nusselt number distributions obtained by the grids used in the grid sensitivity study

The local discretization error distribution is calculated by applying the Grid Convergence Index (GCI) method to the local Nu distribution in order to evaluate the grid independence of the solution. The GCI is based on the Richradson-extrapolation of the values computed on a coarser and on a finer grid and the small values of GCI indicate that the solution is within the asymptotic range. The overall discretization error for the fine grid was very small (average 0.26%) and the largest values of the error (around 5.15) were found at the stagnation point (r/d=0) due to the large gradients in this region. Also, the overall discretization error for the intermediate grid was very small (average 0.63%). Therefore, the small values of GCI indicate that the solution is in fact grid-independent. In order to reduce the computational cost, the intermediate grid is selected as the final grid for the following analysis.

4.3.2 Evaluation of Turbulence Model

Figure 4.4 shows a typical distribution of the local Nu number for a single impinging jet along the target surface (Re =23,000, H/d = 2). As shown in this figure, the local Nusselt numbers increase from the stagnation point toward the primary peak at 0.5 nozzle diameter (r/d ~ 0.5) and then decrease rapidly to reach the local minima and again increase along the wall, giving the second peak in the transition region at approximately r/d= 2. Moving outward from the secondary peak, the heat transfer rates decrease monotonically into the wall jet region. Great scientific interest has been shown in the origins of the secondary peak, and it has been speculated that the formation of the secondary maxima is related to the increased momentum transport due to the transition from a laminar to a turbulent boundary layer. Baughn (1991)

gave similar results, but did not show the first peak. This may be attributed to the lower spatial resolution in the stagnation region compared with the present study. The primary peak might be attributed to the accelerated radial flow at the edge location of the nozzle and to the local thinning of the boundary layer [Gardon &Akfirat (1965)]. The CFD results show that the main characteristics of the heat transfer pattern, i.e. stagnation point, primary peaks and secondary peaks, are adequately reproduced. The heat transfer level agrees very well for the stagnation point, primary and secondary peaks. The SST turbulence model is able to predict the strong shape of primary and secondary peaks of the Nu number. Although the SST turbulence model from this work predicted the strong shape of the secondary peak, it was mismatched in position. However, the secondary peak was not represented correctly by other implementation of SST model as shown in the literature (see Fig. 4.4).
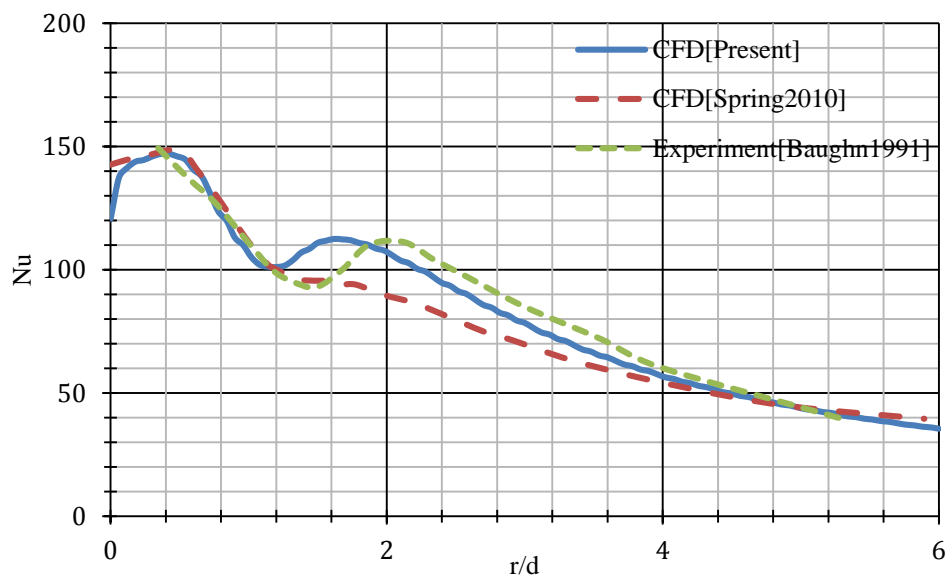
Fig. 4.4 Local Nu number distributions predicted by STAR-CCM⁺ in comparison to the experimental and numerical results from literature

Figure 4.5 shows the Nusselt number and turbulent kinetic energy distributions of jet impingement flow near the wall region. It can be observed that the location of the primary and secondary peak of turbulent kinetic energy is coincident on the location of the primary and secondary peak of the Nu number. This predicted effect has correlation well with the findings of Den Ouden and Hoogendoorn (1974). Therefore, the accuracy of the Nusselt number computation correlates with the quality of the turbulence model used.
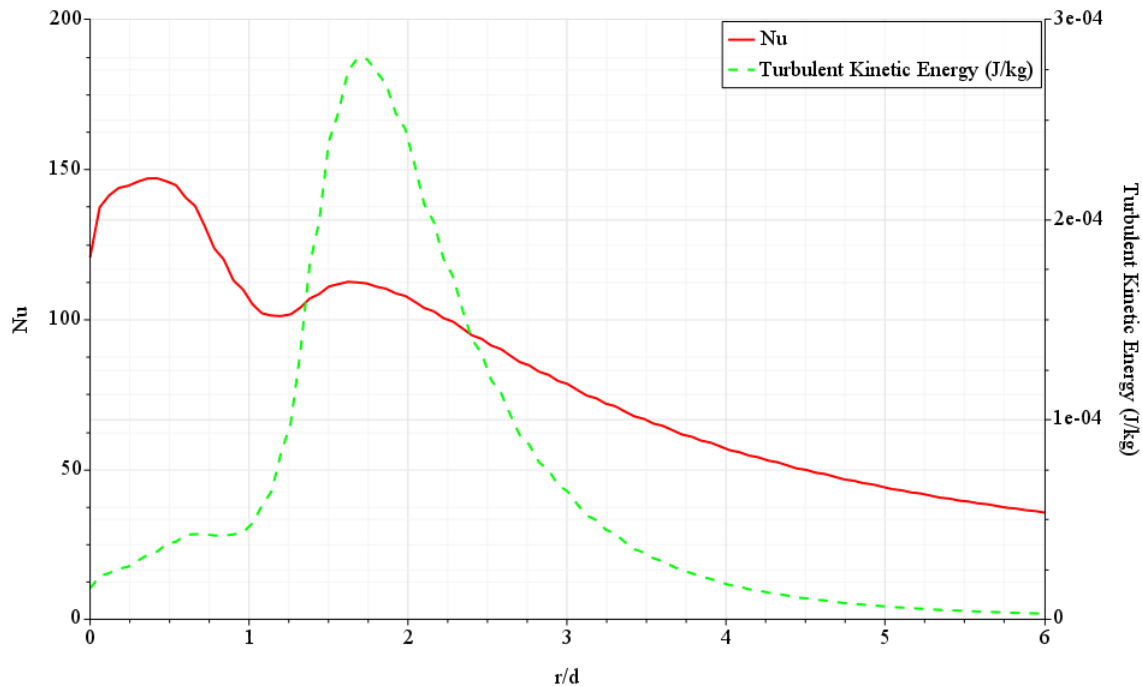
Fig. 4.5 Nu number and turbulent kinetic energy distributions of jet impingement flow near the wall region

4.3.3 Distribution of Nusselt number

The Nusselt number distribution, especially the secondary peak, is strongly influenced by the turbulence model used. The possible factors of the origin of this behavior, such as the effect of different turbulence models, transition model, grid shape and grid size are investigated in more detail.

4.3.3.1 Turbulence Models

The choice of turbulence model is of fundamental importance for an accurate numerical simulation of jet impingement heat transfer, as the resulting heat transfer rates are directly dependent on the predicted flow and turbulence characteristics. As representatives for various types of RANS models, V2F, SST and Reynolds stress models were included, due to the recommendations of researchers in the literature. This selection represents the most commonly used groups of turbulence models for engineering applications in turbomachinery. The performance of the other turbulence models as implemented in STAR-CCM+ is not further investigated. For the analysis of the flow structures, a LES or DNS is preferable, as these kinds of simulations are possible with the increasing computational power available, as well as the advance in the use of efficient and higher order numerical schemes. The result of LES was extracted from Uddin et al. (2013) and the experimental result was extracted from Baughn(1991) for comparison with the numerical simulations (Figure 4.6).
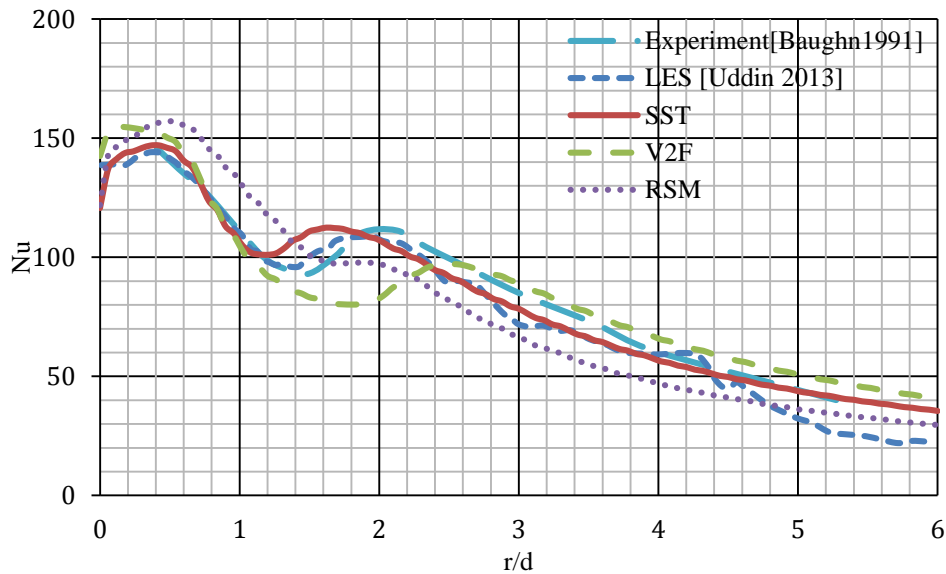
Fig. 4.6 Local Nusselt number distributions predicted by different turbulence models in comparison to experimental data

Figure 4.6 shows that the V2F and RSM models give large errors compared to the experimental results. The computational times will vary with model complexity and computing power. In comparison, the RSM and V2F could need more computational times (around 53% and 40% respectively) and memory requirement (around 10% and 4% respectively) than SST (see Table 4.2). Giovannini and Kim (2006) stated that a LES model could take a day to provide a solution. On the other hand, the SST turbulence model predicted the strong shape of the primary and secondary peak of the local Nusselt number distributions better than other models, and it is the best compromise between solution speed and accuracy. Thus the SST model performs surprisingly well, especially compared to the more elaborate and physical accurate V2F and RSM turbulence models.

Table 4.2 Total solver CPU time and memory requirement for different turbulence models

Turbulence model	Total solver CPU time (s)	Memory requirement (KB)
RSM	168	6.112
V2F	154	5.691
SST	110	5.484

4.3.3.2 Transition Model

Since the secondary peak is related to the transition of the flow from laminar to turbulent, the prediction of the secondary peak might be enhanced by using a transition model in combination with a turbulence model. The low-Reynolds number damping modification (LRDM) can be used to account for low-Reynolds number and transitional effects.
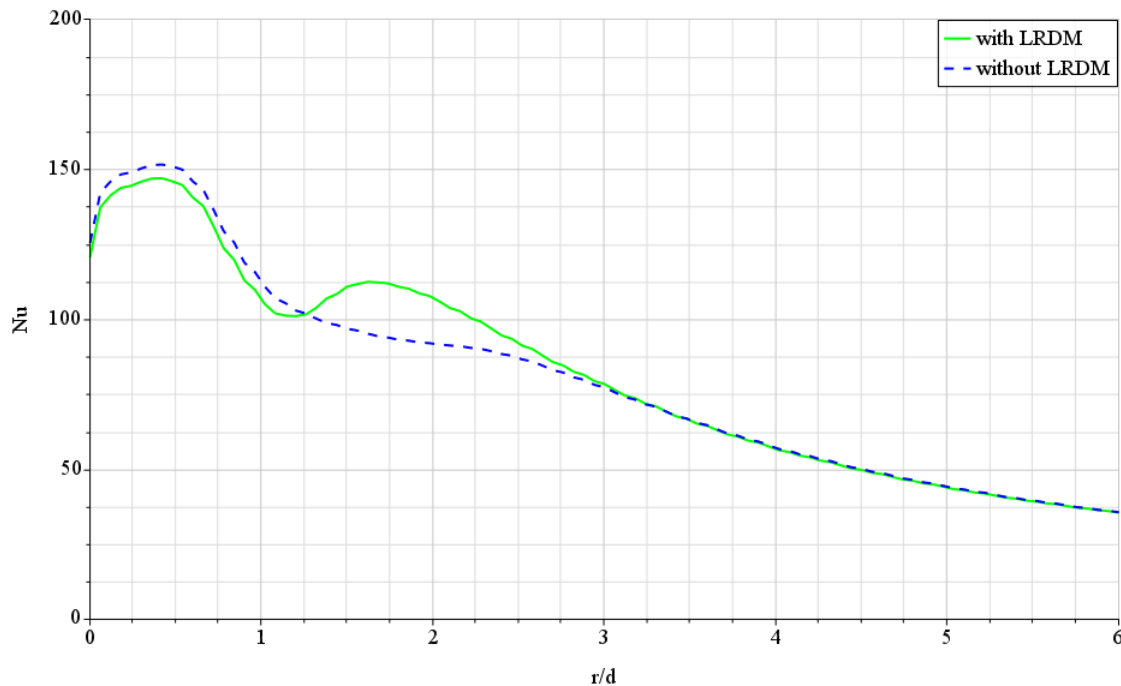
Fig. 4.7 Effect of low-Reynolds number damping modification (LRDM) in the prediction of local Nu number

Figure 4.7 indicates the effect of the low-Reynolds number damping modification (LRDM) in combination with SST k–ω model in the prediction of local Nu number distribution. This modification has an important role in the prediction of location and intensity of the secondary peak and, therefore, this is the most important reason for the better prediction of the present research in comparison with other CFD simulations, such as Spring (2010) who did not use a transition model in combination with a turbulence model (see Fig. 4.4).

4.3.3.3 Grid Shape

Researchers have usually used the hexahedral gird and no investigation with regard to the effect of other grid shapes in the prediction of the secondary peak was observed. In order to investigate this matter, three different unstructured grid shapes (tetrahedral, hexahedral and polyhedral) is considered. A two-dimensional view of these grids is shown in Fig. 4.8.
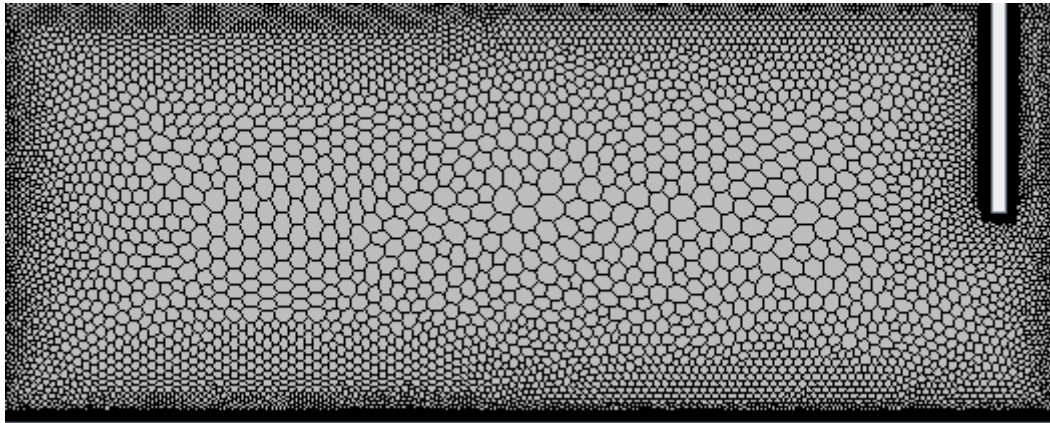
(a) Polyhedral grid
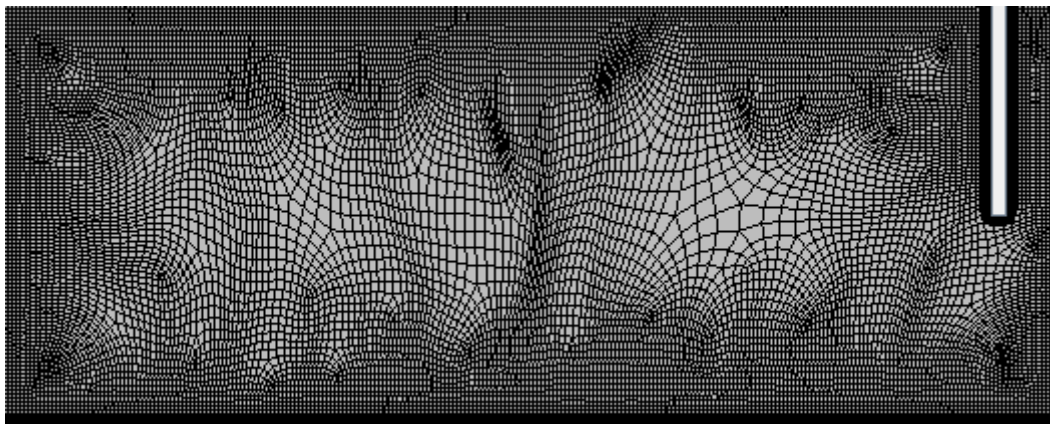
(b) Hexahedral grid
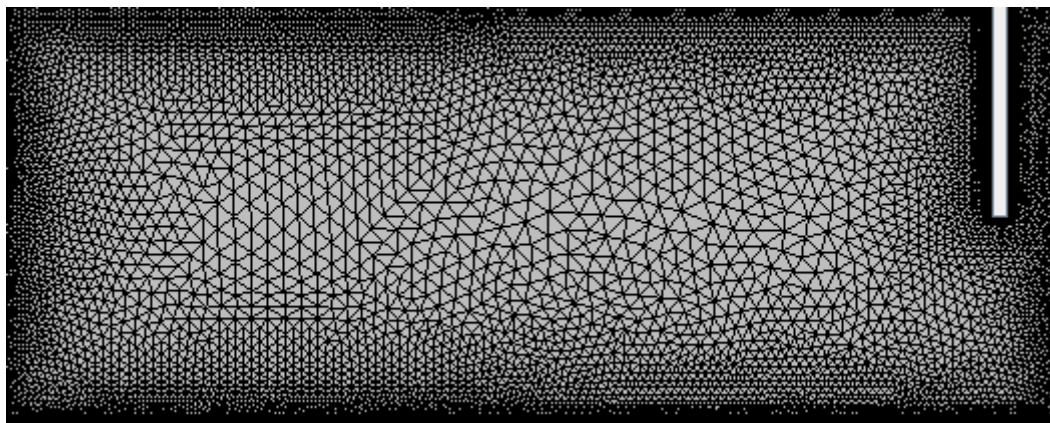
(c) Tetrahedral grid

Fig. 4.8 Two-dimensional view of these grid shapes

Figure 4.9 indicates the effect of grid shape on the local Nusselt number distribution. No significant change was observed in the prediction of position and intensity of the Nu number at the primary and secondary peak for different grid shapes, in contrast, the Nu number at the stagnation point was very sensitive to the grid shape.
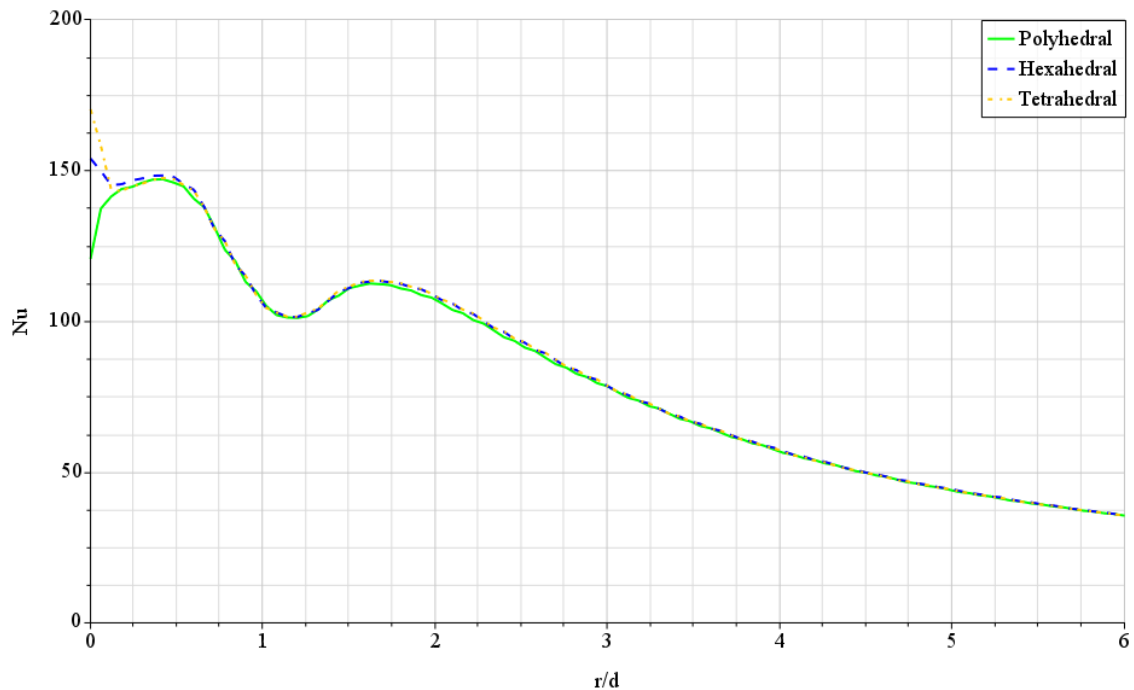
Fig. 4.9 Effect of grid shape in prediction of the Nu number distribution for intermediate grid

It is very important to investigate the effect of the grid shape for the coarse grid, which is equal to approximately 8000 cells. Figure 4.10 indicates the result of this investigation. There is not observed any difference in the different grid shapes in the prediction of the secondary peak. However, the hexahedral and tetrahedral grids cannot predict the strong shape of the primary peak as accurately as the polyhedral grid. Moreover, the stagnation point still has sensitivity to the grid shape similar to the intermediate grid (see Fig. 4.9).
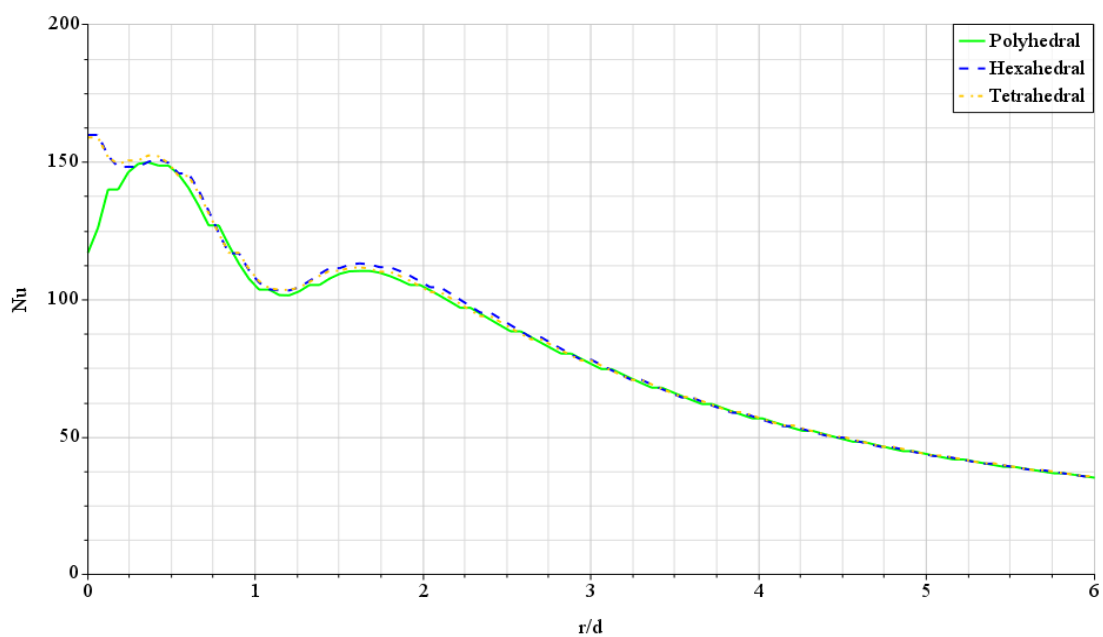
Fig. 4.10 Effect of grid shape in prediction of the Nu number distribution for coarse grid

On the other hand, Table 4.3 shows the total solver CPU time and memory requirement for different grid shapes. The polyhedral grid requires less computational memory and cell numbers and provides faster processing time compared to the two other grid shapes. The results therefore demonstrate the ability of polyhedral grids to produce good quality results with lower memory requirement and shorter run times than other grid types and there is only a minor difference in the quality of the results from the three grids at the primary and secondary peaks, although there is a significant difference between the three grids at the stagnation point.

Table 4.3 Total solver CPU time and memory requirement for different grid shapes

Grid shape	Cell number	Total solver CPU time (s)	Memory requirement (MB)
Polyhedral	19143	111	175.33
Tetrahedral	25380	224	172.72
Hexahedral	25429	318	190.05

4.3.3.4 Grid Size

First of all, it is very important to investigate the grid size and amount of deviation in the prediction of the secondary peak related to a very fine grid as the exact solution. Table 4.4 shows the grid size in conjunction with position and intensity of the Nu number at the stagnation point, primary peak and secondary peak. Base size=0.1mm is considered as a very fine grid and a reference for deviation of other coarser grids with base size up to 3mm. The $y_{1,max}^{+} \leq 1$ requirement was fulfilled for all investigated grids.

Table 4.4 Grid parameters used for the deviation analysis

Base size (mm)	Cell number	Stagnation point r/d	Nu	Primary peak r/d	Nu	Secondary peak r/d	Nu	Total solver CPU time(s)
3.0	5695	0.0	180.125	--	--	1.62	103.203	25
2.5	6932	0.0	165.5	0.42	149.032	1.62	108.6	32
2.0	8862	0.0	116.955	0.36	149.83	1.62	110.33	41
1.0	19143	0.0	120.7	0.42	147.0	1.62	112.5	111
0.5	40579	0.0	137.231	0.42	146.02	1.68	113.07	326
0.25	84770	0.0	144.018	0.48	145.30	1.68	112.9	954
0.1	220713	0.0	142.4	0.48	145.34	1.68	111.5	3927

Figure 4.11 shows the effect of grid size in the prediction of local Nu number distribution. The relative deviation of Nu number value for coarse grids up to base size=2mm, related to the reference grid at the primary peak, secondary peak and stagnation point, is approximately

1.18%, 1.15% and 11.12% on average. The relative deviation of Nu number location for coarse grids up to base size=2mm, related to the reference grid at the primary peak, secondary peak and stagnation point, is approximately 12.5%, 0.0% and 0.0% on average. It can be concluded from Table 4.4 and Fig. 4.11 that the coarse grids up to base size=2mm can successfully predict the location and intensity of the Nu number at the stagnation point, primary and secondary peaks with a reasonable level and lower computation time compared to the very fine grid.
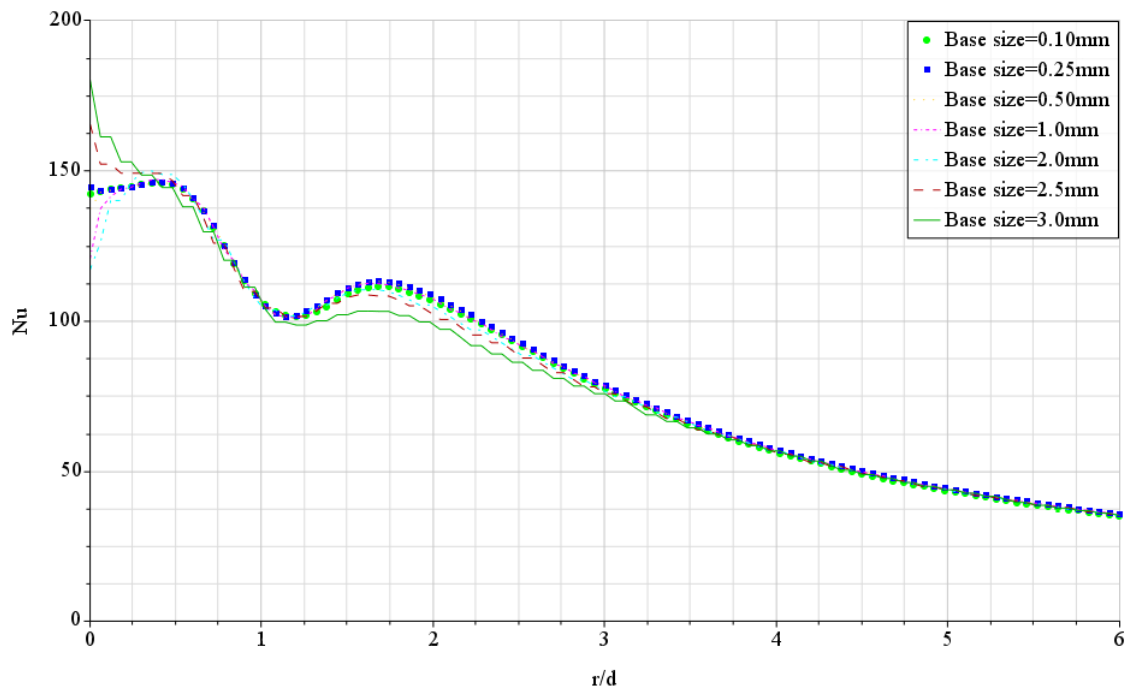
Fig. 4.11 Effect of grid size in the prediction of local Nu number distribution

4.4 Summary

In this chapter, the single impinging jet for symmetric configuration (2D) is considered. For the problem, a computational model was generated to represent the experimental investigations used as reference. Aspects on domain size, boundary conditions, and grid sensitivity by applying the GCI method were discussed. By means of a particular configuration (Re=2.3×10^4, H/d=2), for which several independent sources of experimental data exist, the predictions from SST turbulence models were analyzed. The findings of this investigation follow below.

It can be concluded from the evaluation of the SST turbulence model with regard to predictions of heat transfer, that the SST turbulence model represents a good compromise between the accuracy of its results and the computational effort. Although the SST turbulence model from the literature did not represent the secondary peak correctly, the SST turbulence model from this work predicted the strong shape of the secondary peak. The secondary peak in

the literature was mismatched in its position. The low Re damping modification in the implementation of SST K-ω plays an important role in the prediction of location and intensity of the secondary peak. The coarse grids which fulfill the requirement of $y^+_{1,max} \leq 1$ can successfully predict the position and intensity of the Nu number at the stagnation point, and primary and secondary peaks with a reasonable level and much lower computation time compared to the very find grids. The results demonstrate the ability of polyhedral grids to produce good quality results with lower memory requirement and cell number as well as shorter run times than other grid types. There is little difference in the quality of the results from the three grids, although the result from the polyhedral grid is slightly better than the other two at the stagnation point.

Chapter 5

5. Multiple Jets Impinging on Flat Surface

In this chapter, the multiple round jets impinging on the flat surface are investigated. The flow and heat transfer characteristic of multiple jet configuration is a combination of the single impinging jets and the cross-flow effects. However, these configurations are much more complicated than the single jet geometry due to the jet interactions, and it is a challenging subject as the jet interactions are very complex. As most numerical investigations have considered the configurations with relatively few numbers of impinging jets and rows (see Chapter 2), the objective of the present work was the prediction and assessment of achievable accuracy of configurations with large-scale impingement arrays in terms of local and average heat transfer coefficient.

The chapter starts with a summary of the investigated parameters. Next, the details of the computations are provided. In the results section, the discretization errors are quantified by means of grid sensitivity analysis. The analysis includes the effect of temperature difference between jet and target surface, jet Reynolds numbers, nozzle shapes, number of jet rows, separation distance i.e. nozzle-to-surface distances (H/d), nozzle-to-nozzle distances (S/d), jet angle (θ) and relative velocity ratio (VR) on the heat transfer and pressure force from multiple jets impinging on flat surfaces that are characteristic for drying machines. The accuracy of the CFD results from the present investigation is evaluated by a comparison with the experimental data. Two correlations are developed and validated for the average Nusselt number and the force coefficient as a function of the Re number, H/d, S/d, θ and VR. The chapter concludes with a summary of the main findings.

5.1 Investigated Parameters

For multiple jet impingements, a significant amount of experimental investigations exists. The investigated range of design parameters is correspondingly wide. A tabulated summary is given in appendix A. The parameters investigated in the present study for comparison with the experimental or numerical results from the literature include the temperature difference between the jet and target surface (T_w-T_j), the nozzle shape, number of jet rows, jet Reynolds number (Re), nozzle-to-surface distance (H/d), nozzle-to-nozzle spacing (S/d), jet angle (θ) and velocity ratio (VR) i.e. ratio of surface velocity to jet velocity. The parameters which are maintained constant are jet nozzle diameter (d=3.68mm) and jet

temperature (T_j = 298.15 K). The value of inlet velocity is so selected that it matches with the corresponding Reynolds number. The variation of velocity ratio is brought about by varying the surface velocity and maintaining the inlet velocity. For all configurations, the pattern was regular i.e. the streamwise and spanwise jet-to-jet distance was equal. Details of the parameters investigated are presented in Table 5.1.

Table 5.1 Parameters investigated for multi-jet configurations

Parameters	Values
Temperature difference (T_w-T_j)	30, 50, 75, 100, 125, 150, 175, 200 K
Number of jet rows	1, 2, 4, 8, infinity
Reynolds number (Re)	2,500, 3,400, 10,000, 20,000, 23,000
Relative nozzle-to-surface distances (H/d)	0.5, 1, 2, 4, 5.4, 6
Relative nozzle-to-nozzle distances (S/d)	4, 5, 6, 7.2, 8, 10
Jet angle (θ)	45, 60 , 90°
Relative velocity ratio (VR)	0, 0.1, 0.5, 1.0

The grid sensitivity analysis for both flat and curved surfaces was conducted for a high Reynolds number value (Re = 23,000) in order to estimate the maximum error.

5.2 Computational Details

5.2.1 Domain and Boundary Conditions

As first case for investigation, the multiple jets with one row in the in-line arrangement are considered and the number of jets is assumed to be infinity according to the schematic shown in Fig. 5.1. The jet-to-jet spacing in both directions of space was 7.2d and the distance between the target surface and the jets (H) was 5.4d. These geometrical parameters are reported by Martin (1977) for an optimum design. All jet inlets were modeled as circular planes in the top wall. The incompressible air as working fluid with constant fluid properties at T_j=298.15 K and Pr=0.71 entered the domain with a uniform velocity profile. The value of inlet velocity is so selected that it matches with the corresponding Re number. The target surface was modelled as a no-slip wall held at a constant temperature T_w = 311.15 K. All remaining walls were modeled as the adiabatic no-slip walls. A constant pressure boundary condition was used at the outlet. The two sides confining the domain in the Y-Z plane were modelled as the

symmetry planes. For numerical treatment, due to the symmetric geometry, the problem was simplified according to the schematic shown in Fig. 5.2.
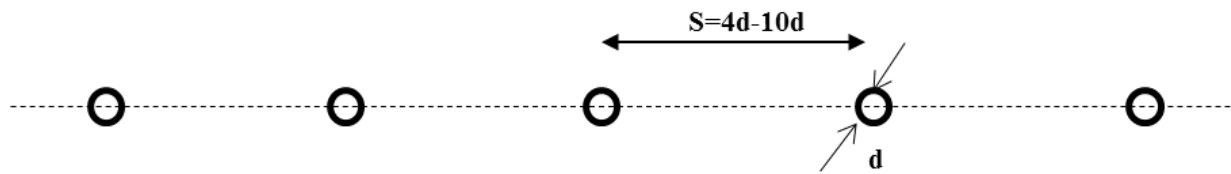
Fig. 5.1 Details of holes arrangement; Single row of jets
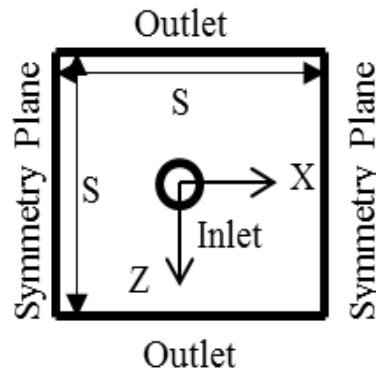
Fig. 5.2 Schematic of the computational domain; Top view of confinement plate

5.2.2 Grid Generation

Similar to the single round jets, the grids for the multiple jets configuration were constructed analogously using the same parameters and therefore only differed in overall base size. A polyhedral grid type was generated using STAR-CCM$^+$. Boundary layers with a proper y_1^+ value, i.e. less than one, were built on the target surface of the model in order to enable a better resolution of the flow in this part. The final numerical model accounted for about 2,328,819 grid cells. In Figure 5.3, a 3D view of the grid is provided.
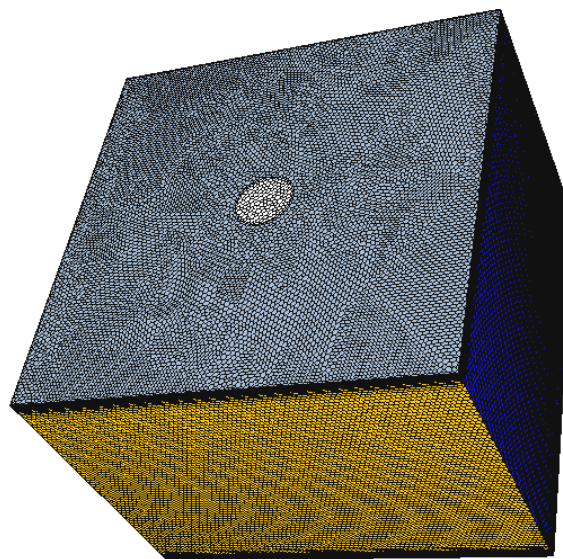
Fig. 5.3 Three-dimensional view of the grid of an in-line impingement array for one row

5.3 Results and Discussion

5.3.1 Grid Sensitivity Study

A grid sensitivity analysis was performed at Re =23,000 in order to estimate the numerical accuracy of the CFD results. The grid sizes are summarized in Table 5.2 indicating that the y_1^+ requirement was generally fulfilled for all investigated grids. The value of $y_{1,max}^+$ refers to the maximum dimensionless wall distance on the target surface.

Table 5.2 Grid parameters of the refinement study

Grid	Base Size (mm)	Cell Number	Max y_1^+	Average GCI %
Course	0.395	476,561	0.493	---
Intermediate	0.285	1,049,923	0.507	2.3
Fine	0.205	2,328,819	0.510	1.65

Figure 5.4 shows the Nusselt number distributions obtained by the three different grids used in the grid sensitivity study for the multiple impinging jets.
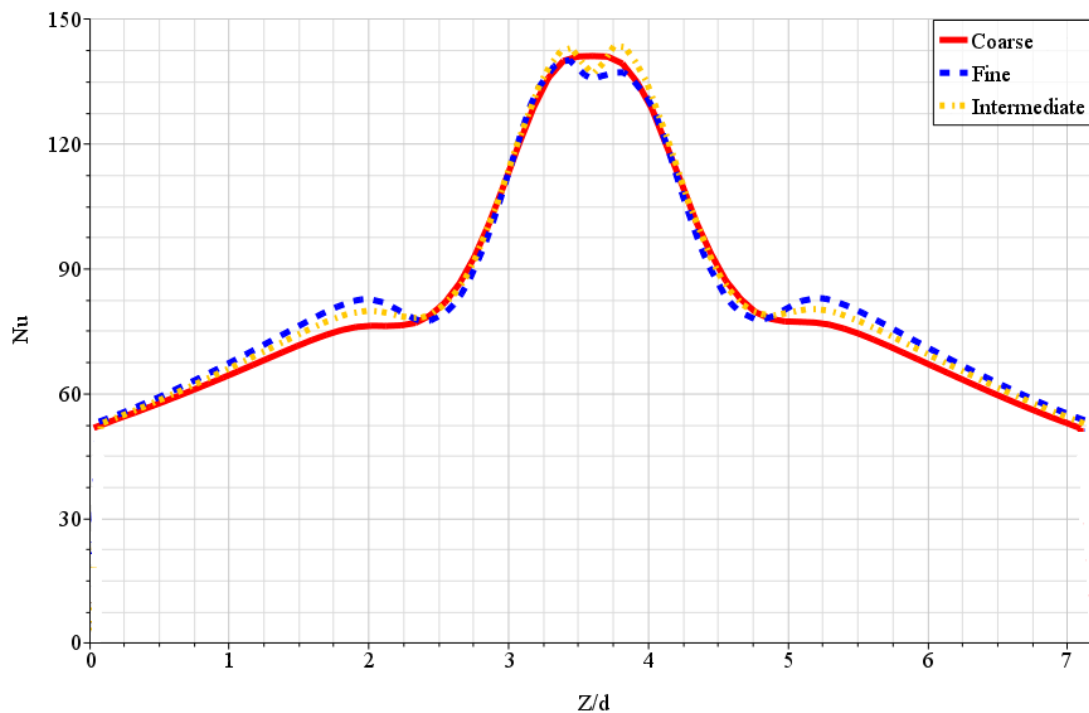
Fig. 5.4 Nusselt number distributions obtained by the grids used in the grid sensitivity study

The local discretization error distribution is calculated by applying the GCI method to the Z-centerline Nu distribution. The overall discretization error for the fine grid was very small (average 1.65%) and the largest values of the error (around 5.0%) were found unreasonable around Z/d≈3.0. Also, the overall discretization error for the intermediate grid was very small

(average 2.3%) and the largest values of the error (around 8.3%) were found unreasonable around $Z/d \approx 3.0$. Therefore, the small values of GCI indicate that the solution is within the asymptotic range and grid-independent. In order to reduce the computational cost, the intermediate grid is selected as the final grid.

5.3.2 Temperature Difference

It is very important that the Nu number be independent of thermal boundary condition. In order to verify this matter, the variation of temperature difference between surface and exit jet is investigated. The typical range of temperature variation is $10K < T_w - T_j < 200K$ with T_j = 298.15 K at ambient temperature and Re=23,000. The following figure shows the results of this investigation.
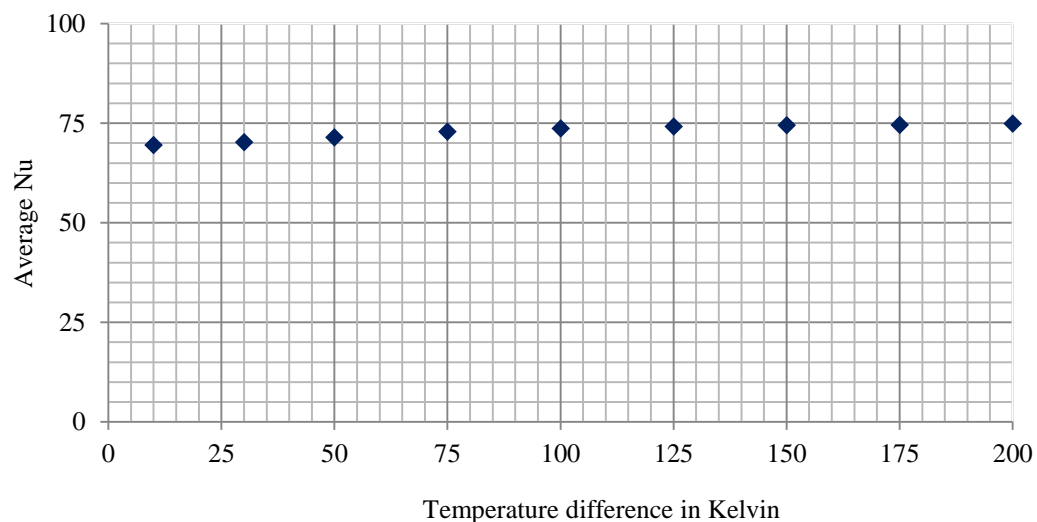
Fig. 5.5 Effect of the temperature difference on the average Nu number at Re=23,000

It can be concluded from Figure 5.5 that the average Nu number remains with only a small variation, and maximum variation is around 7%, which occurred between the temperature difference 10 K and 200 K. Thus, the thermal boundary condition has a minor effect on the accuracy of the numerical simulation. However, in order to increase the numerical accuracy, the thermal boundary condition which was reported in the literature is imposed (if it was available). Note that for all investigations, a constant temperature for the target surface (311.15 K) is imposed.

5.3.3 Geometry Variation

The effect of geometry variation i.e. the nozzle shapes and the number of jet rows is addressed next. The jet nozzle shape has a role in the development of an impinging jet and also

the number of jet rows has an important role in the magnitude of the cross-flow. The degree to which these geometry variations differ is strongly influenced by the jet-to-jet spacing, the separation distance, and the magnitude of cross-flow. Due to these complicated relations, the numerical consideration of geometry variation is equally important for the suitability of CFD for the impingement heat transfer in the turbomachinery applications, in which different geometry variation is also commonly found.

In the present study, the two commonly used nozzle types, i.e. pipe and orifice, are selected. The multiple jets with a different number of jet rows in the in-line arrangement are considered and the number of jets is assumed infinity according to the schematic shown in Fig. 5.6 (left sides). For numerical treatment, due to the symmetric geometry, the problem was simplified according to the schematic shown in Fig. 5.6 (right sides). In all cases, the pattern was regular with $S_x = S_z = 7.2d$ and data were taken for Re = 10,000, H/d = 5.4. All jet inlets of orifice nozzle were modeled as circular planes and the length of pipe to diameter ratio (L/d) was 10, which is a sufficient length to obtain a fully developed exit jet flow.
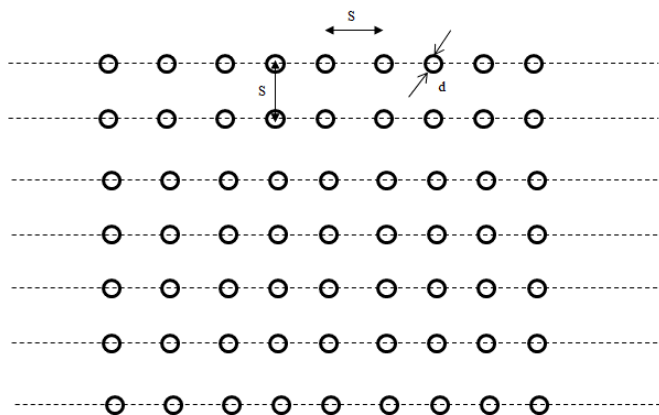
Case 1 (a) Infinity rows of jets, Nozzle: pipe
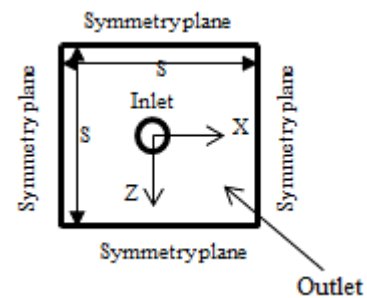
Case 1 (b) Schematic of the computational domain for case 1
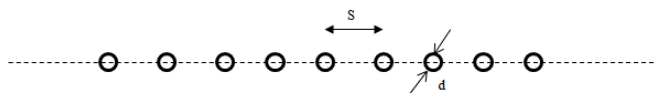
Case 2 (a) Single row of jets; Nozzle: orifice or pipe
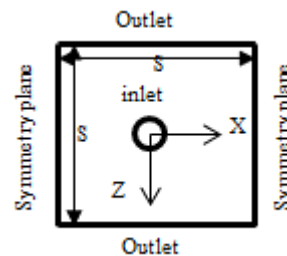
Case 2 (b) Schematic of the computational domain for case 2
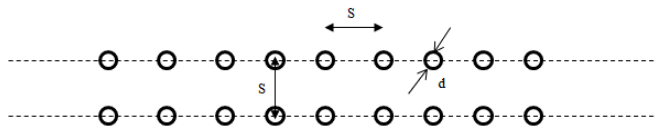
Case 3 (a) Two rows of jet; Nozzle: orifice or pipe
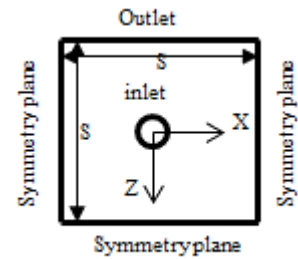
Case 3 (b) Schematic of the computational domain for case 3
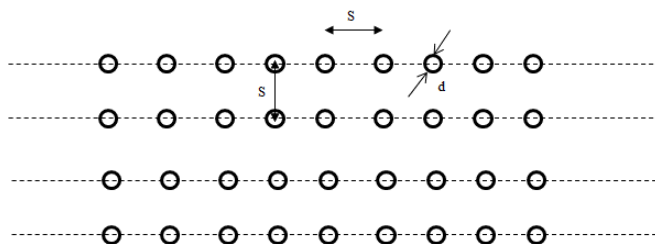
Case 4 (a) Four rows of jet; Nozzle: orifice or pipe
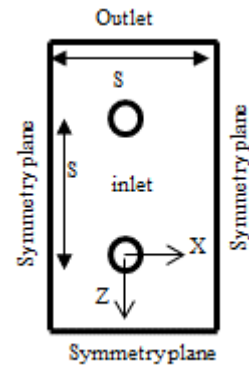
Case 4 (b) Schematic of the computational domain for case
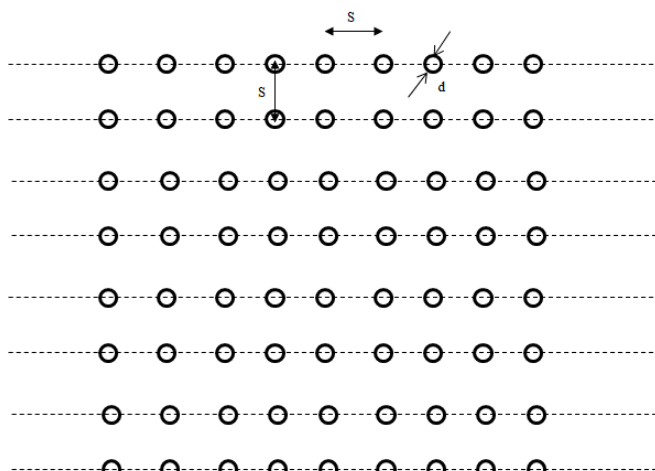
Case 5 (a) Eight rows of jet; Nozzle: orifice or pipe
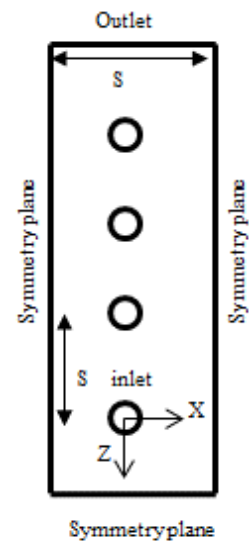
Case 5 (b) Schematic of the computational domain for case 5a

Fig. 5.6 Details of nozzle arrangement and schematic of the computational domain (top view of confinement plate)

5.3.3.1 Effect on Heat Transfer

Figure 5.7 compares the centerline Nusselt number distributions from CFD for different numbers of jet rows and nozzle shapes.
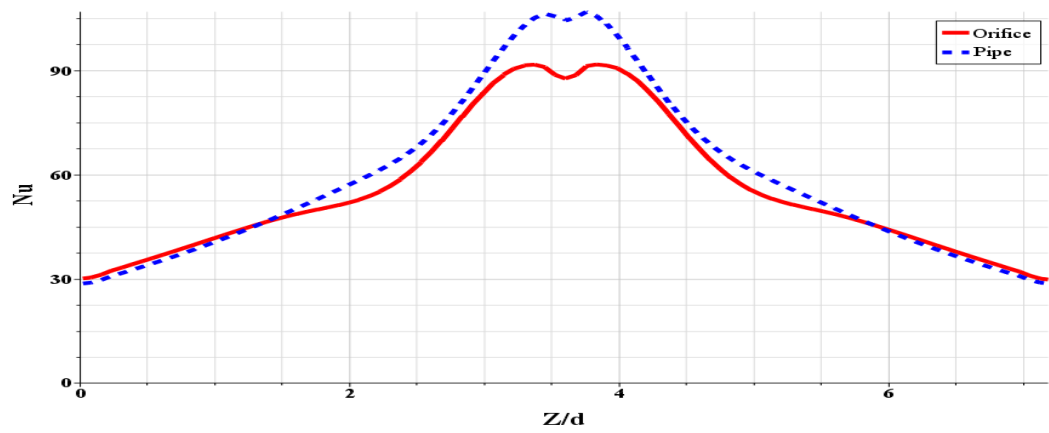
(a) Number of rows: One
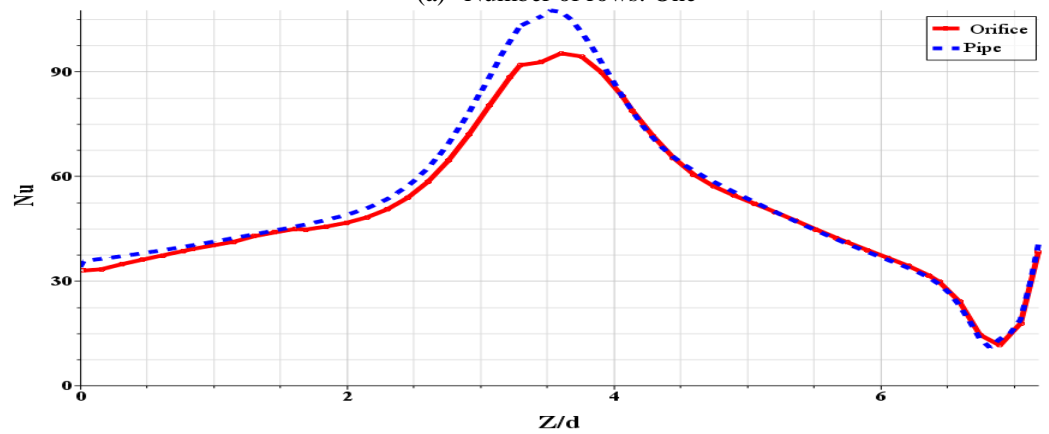
(b) Number of rows: Two
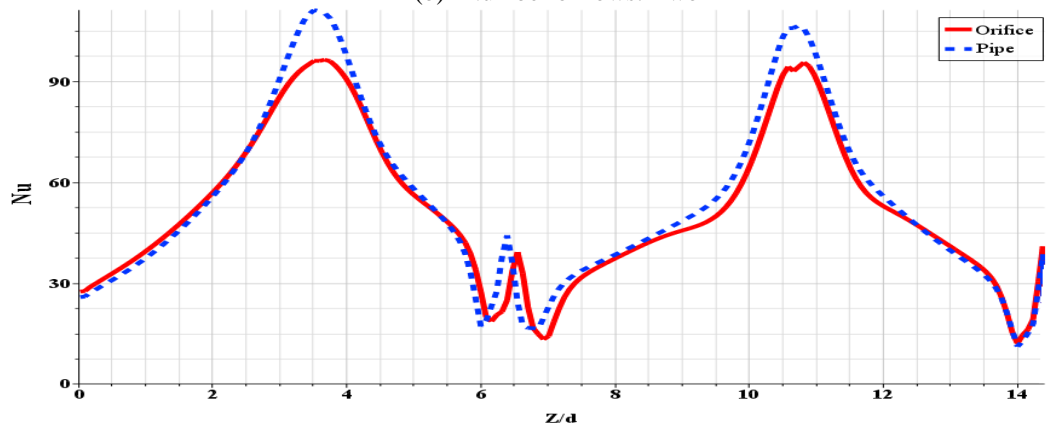
(c) Number of rows: Four
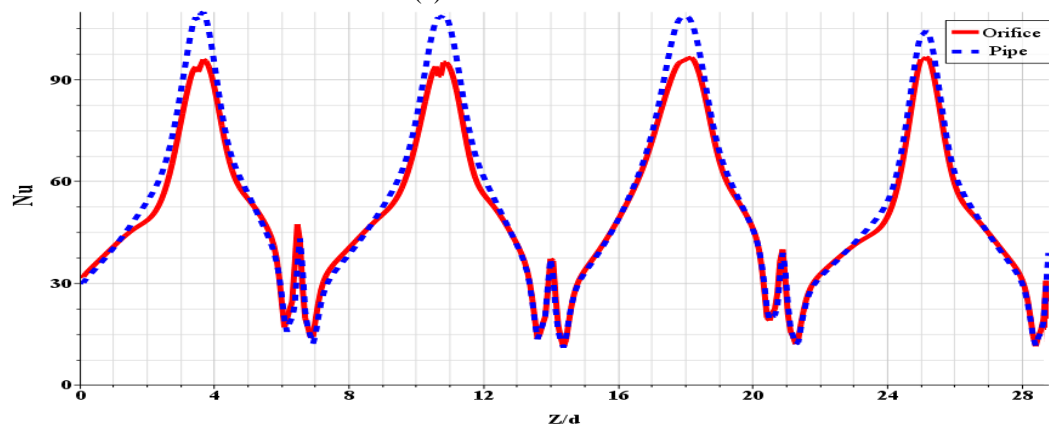
(d) Number of rows: Eight

Fig. 5.7 Local Nusselt number for different nozzle shapes and jet rows at H/d = 5.4, S/d=7.2, Re=10,000

Based on comparisons with the Nusselt functions for the pipe nozzle array, it is evident from Figure 5.7 that the peak of the local Nusselt number at the stagnation region of pipe nozzles and also the average value of Nu number on the target surface are the higher than that of the orifice nozzle (see Figure 5.9), because for the same Reynolds number, pipe nozzles effectively have a higher initial core velocity resulting in higher impingement point heat transfer (see figure 5.8). For the cases 4 and 5, the flow within such a large array is quite complex due to the cross-flow effects and a significant difference in the total average Nu number on the target surface was not observed between these two cases. However, the heat transfer from the orifice nozzles is somewhat less but their manufacture is easiest and consequently are commonly used. This observation has a correlation with the findings of Ansu et al. (2016).

Figure 5.8 shows the velocity contours along the symmetry plane for different nozzle shapes and number of jet rows. As each fluid jet ejects from the pipe with the parabolic velocity profile and from the orifice with a fairly flat velocity profile, a continuous reduction in the velocity takes place from the jet exit nozzle to the outer boundary. As the jet approaches the target surface, the axial velocity component is decreased and jet strongly affected by the target surface which creates a stagnation zone. Then, the axial velocity component is transformed into an accelerated horizontal component, similar for all cases. The wall-jet region is characterized by flow directed radially outwards.

Figure 5.9 compares the total average Nusselt numbers from CFD for different nozzle shapes and number of jet rows. It was found that in case 1 (infinity rows), where the air jets exit through the top side, impingement provides the highest values of the total average Nusselt numbers on the entire target surface compared to the other cases, because in case 1 the exit opening area is the least for this configuration and the momentum exchange between the fluid jet and ambient is minimum. Case 2 (single row, either pipe or orifice) provides the highest Nusselt numbers after case 1. This is due to the symmetrical distribution of velocity around the jet axis, since there is no cross-flow and the jet hits the target surface without any distortion (See Fig. 5.8 a,b,c).

(a) Infinity rows, pipe

(b) One row, orifice

(c) One row, pipe

(d) two rows, orifice

(e) two rows, pipe

(f) Four rows, orifice

(g) Four rows, pipe

(h) Eight rows, orifice

(i) Eight rows, pipe
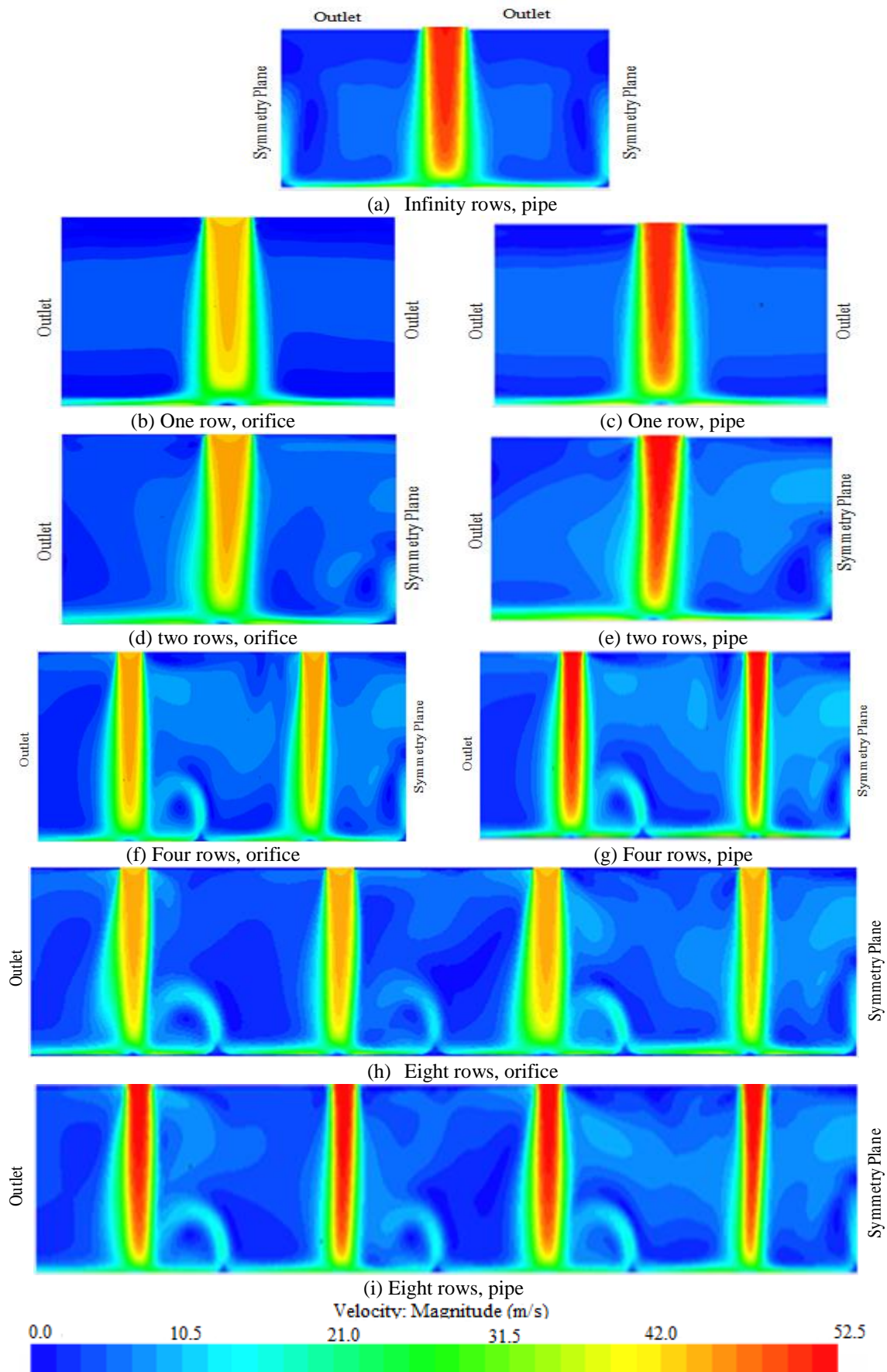
Fig. 5.8 Velocity magnitude contours along symmetry plane for different nozzle shapes and number of jet rows at H/d = 5.4, S/d=7.2, Re=10,000
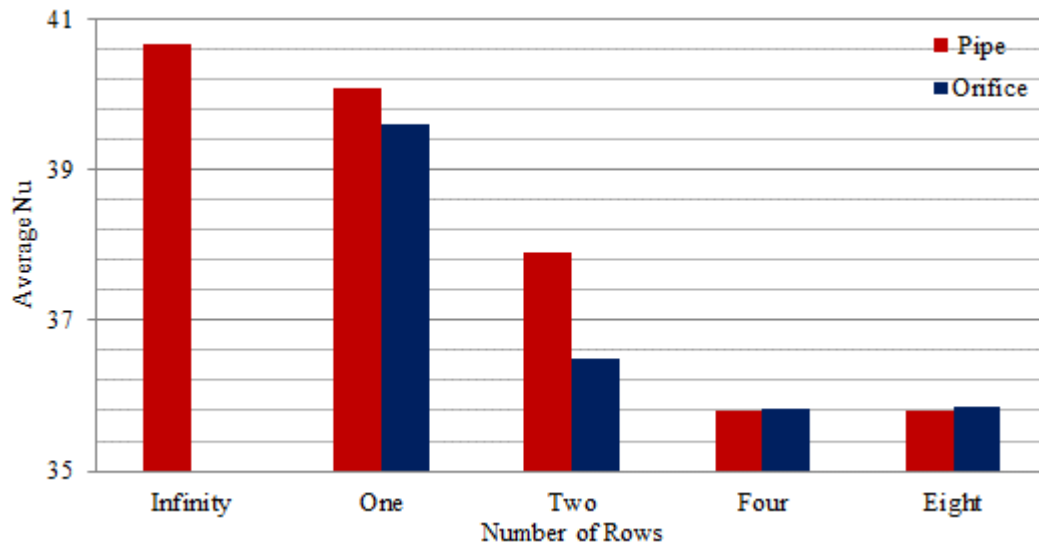
Fig. 5.9 Comparison of total average Nusselt numbers from CFD for different nozzle shapes and number of jet rows at H/d = 5.4, S/d=7.2, Re=10,000

It was found that, for multiple rows cases (rows 2, 4 and 8), the wall jet interference and cross-flow effects cause significant degradation of the average Nu number when compared to the single row. The cross-flow is defined as the spent air from the upstream jets which flows parallel to the target surface and thus interferes with the impinging orthogonal jets on the surface. The strength of cross-flow increases along the channel and therefore the last jet in the channel experiences the maximum cross-flow. The presence of the cross-flow will disturb the impinging jet flow pattern, thicken the wall boundary layers and degrade the heat transfer rates. On the other hand, the wall jets from the adjacent jets, when interacting with each other, result in an upward flow from the wall, called an upward fountain, as shown in Figure 5.8 (d)-(i). The presence of the fountain can cause recirculating flow zones, which then re-enter the neighboring jet cores and affect the impinging jet behavior, weaken the kinetic momentum and distort the impinging jet. The thermal exchange occurring between the recirculating flow and the impingement surface has a negative impact on the target surface heat transfer. However, where these wall jets of adjacent nozzles impinge upon each other, further peaks may occur in the lateral variation of the heat transfer rate due to the secondary stagnation zones (see Figure 5.7 b, c and d).

The two rows case (either pipe or orifice) provides higher Nusselt numbers compared to cases 4 and 5 due to the weaker wall jet interference and cross-flow effects (see Fig. 5.8 (d)-(i)).

For eight rows (either pipe or orifice) the magnitude of the total average Nusselt number on the target surface remains the same compared to the four rows due to the same flow pattern and mass flow rate per unit surface area.

A difference in average Nu number between pipe and orifice is only for a small number of rows. As the number of rows increases, the effect of cross-flow and entrainment get predominant (see Fig. 5.9).

5.3.3.2 Effect on Pressure Force

Figures 5.10 show the distributions of pressure for different nozzle shapes and number of jet rows on the target surface. Figure 5.11 shows the comparison of the pressure force coefficient from CFD for different nozzle shapes and number of jet rows. The pressure has the maximum value at the first stagnation point. It reduces as the flow accelerates in the wall jet region, for all the cases.

Based on comparisons with the pressure for the pipe nozzle array, it is evident from Figure 5.10 that the peak of pressure at the stagnation region of pipe nozzles is higher than that of orifice nozzles. This is because for the same Reynolds number, the pipe nozzles effectively have a higher exit velocity resulting in higher pressure at the stagnation point. Therefore, in the case of orifice nozzles, the pressure force is somewhat less but they have a high potential in drying applications for force sensitive products when high drying rates and/or small pressure forces are of interest and also they are the easiest to manufacture and consequently are commonly used.

Infinity rows, where the air jets exit through the top side after impingement, and also the single row (either pipe or orifice), where the flow exits in both directions after impingement, provide the highest values of pressure at the stagnation point and subsequently of the pressure force coefficient on the entire target surface compared to the other cases. This is due to the symmetrical distribution of pressure around the stagnation point (see Figure 5.10 a, b, c). On the other hand, there is no significant difference in the pressure force coefficient between the single row (pipe) and the infinity rows (see Fig. 5.11).

It was found that, for multiple row cases (2, 4 and 8 rows), the wall jet interference and cross-flow effects cause a significant effect on the pressure force coefficient when compared to the single row. The strength of cross-flow increases along the channel and therefore the last jet in the channel experiences the maximum cross-flow. The presence of the cross-flow will disturb the impinging jet flow pattern and degrade the pressure at the stagnation point. On the other hand, in the upwash fountain zone, where the wall jets from the adjacent jets interact with each other, further peaks in the lateral variation of pressure may occur due to the secondary stagnation zones, as shown in Figure 5.10 (g).

(a) Infinity Rows

(b) One Row, Orifice

(c) One Row, Pipe

(d) Two Rows, Orifice

(e) Two Rows, Pipe

(f) Four Rows, Orifice

(g) Eight Rows, Pipe

(h) Eight Rows, Orifice

(i) Four Rows, Pipe
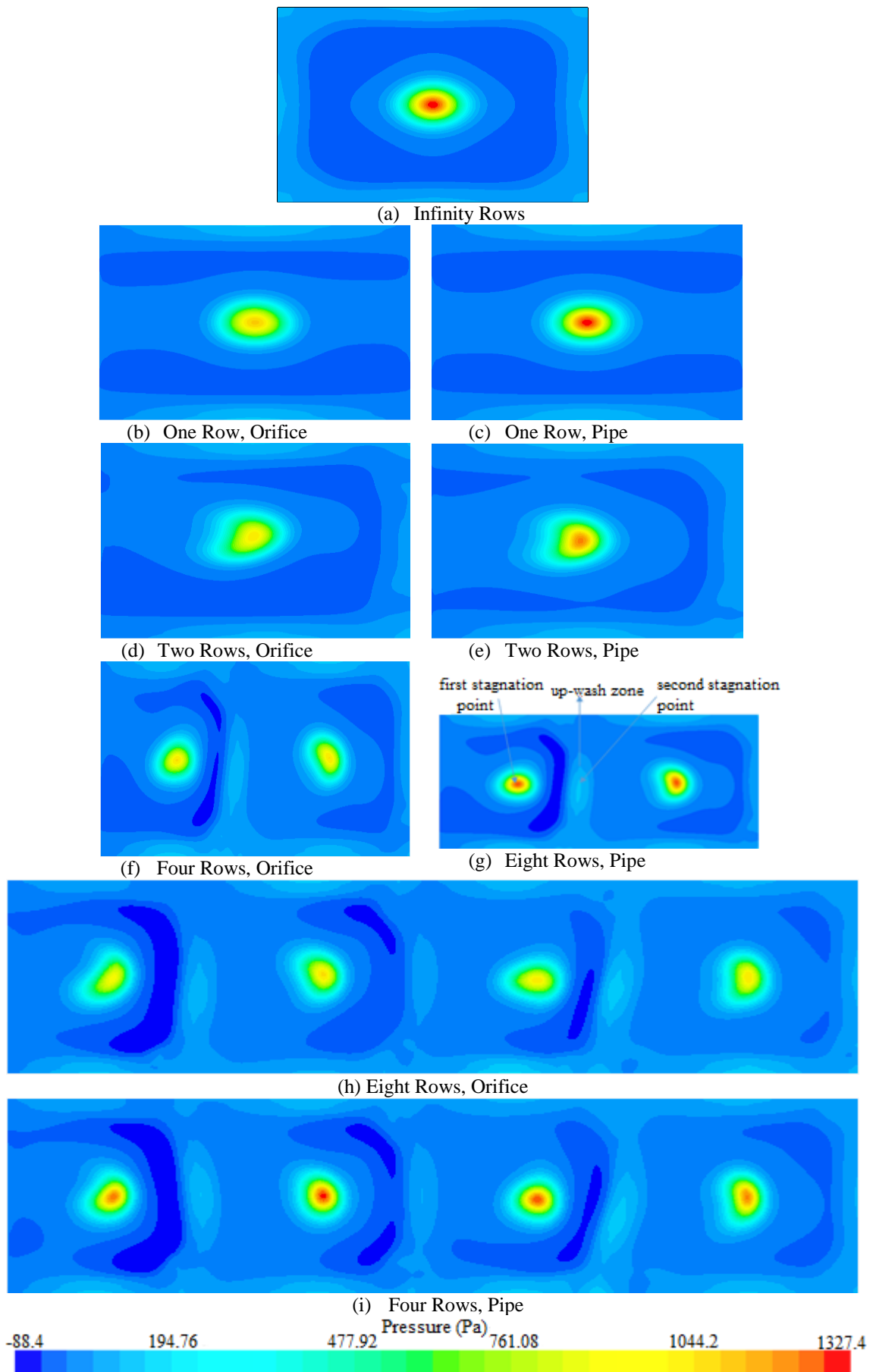
Fig. 5.10 pressure distribution on target surface

The presence of the fountain can cause the recirculating flow zones, which then re-enter the neighboring jet cores and affect the impinging jet behavior, weaken the kinetic momentum and distort the impinging jet. Therefore, the pressure force coefficient from multiple row cases (2, 4 and 8 rows) is lower than the single row. This could be attributed to the strong wall jet interference and cross-flow effect for multiple rows compared to the single row.

The stagnation region has the strongest pressure for both single and multiple row cases. However, it is observed that the peak Nu values for multiple row cases (2, 4 and 8 rows) increases as the number of jet rows increases from 2 to 8. This slight difference is due to the much larger interaction of the multiple row cases before impingement increases the turbulence in the flow and thus increases the pressure and consequently the pressure force at the stagnation region. Therefore, the pressure force coefficient increases as the number of jet rows increases from 2 to 8 and this is even more obvious for the pipe nozzles.
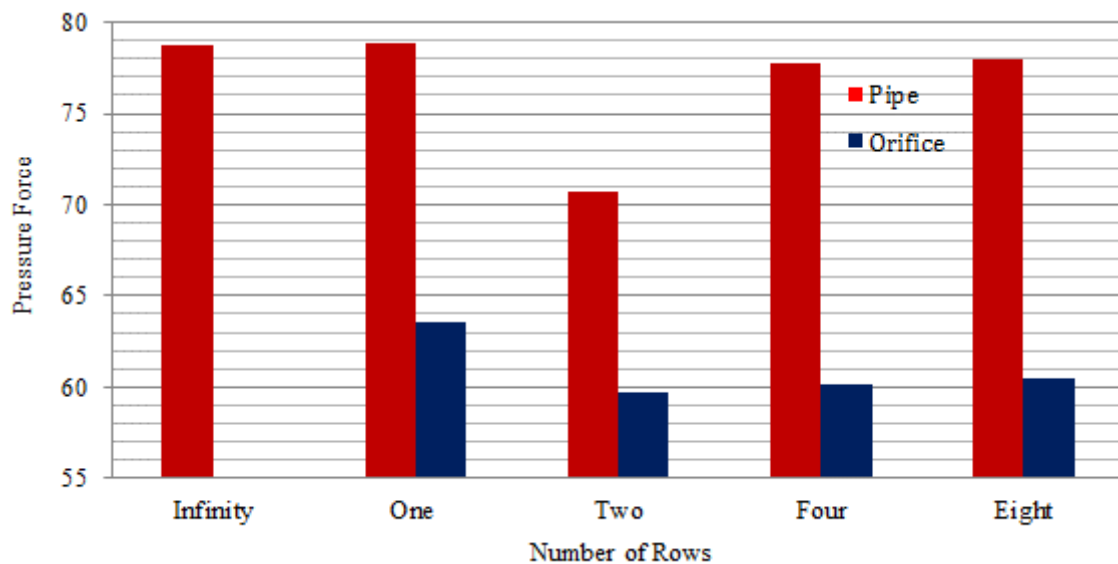
Fig. 5.11 Comparison of pressure force coefficient from CFD for different nozzle shapes and number of jet rows at H/d = 5.4, S/d=7.2, Re=10,000

The pipe nozzle always has a higher average Nu and pressure force coefficient compared to the orifice nozzle and the maximum difference is around 12% and 24% respectively. The orifice nozzle seems to have a high potential in drying applications for force sensitive products and when high drying rates and/or small pressure forces are of interest. The effect of multiple rows with regards to the impact on the heat transfer and pressure force is negligible compared to the single row within the range examined and the maximum difference is around 10% and 8% respectively. In the following, the effect of Re number, relative nozzle-to-surface distance, relative nozzle-to-nozzle spacing, jet angle and surface motion on the heat transfer and pressure force from the single row and multiple rows are compared.

5.3.4 Jet Reynolds Number (Re)

5.3.4.1 Effect on Heat Transfer from Single Row

It is important to investigate the effect of jet Reynolds number for the multiple impinging jets due to the very complex flow interactions occurring in multi-jet systems. The objective is therefore to assess whether the numerical simulations are able to predict such complicated flow conditions at different Reynolds numbers. Fig. 5.12 shows the comparison of total average heat transfer coefficients for in-line arrays at H/d = 5.4 and S/d=7.2. The average Nusselt numbers for different Reynolds numbers are also compared to the correlation presented by Martin (1977) and Huber et al. (1994).
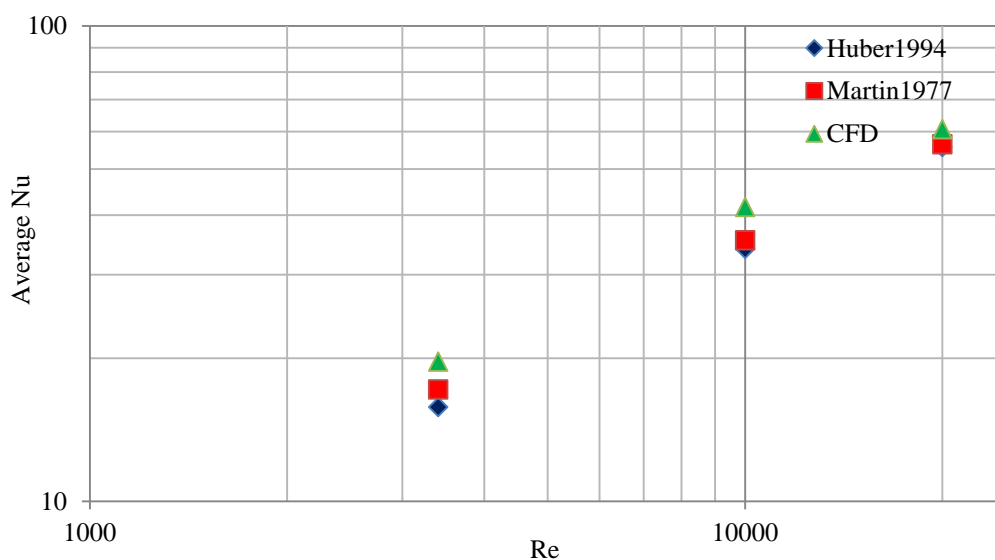
Fig. 5.12 Comparison of total average Nusselt numbers from experiments and CFD for in-line arrays at H/d = 5.4, S/d=7.2 for different Reynolds numbers in the logarithmic scale

Numerically predicted results are shown together with the correlations provided by other investigators, to which the CFD predictions compare very well. The trends and the slope of the CFD predictions are in agreement with the experiments; however, the level of heat transfer is overestimated. The CFD data has more agreement with Martin's correlation (average error is around 13%) in contrast with Huber's correlation (average error is around 18%). Because Huber's correlation was obtained with spent air exits and no cross-flow, while Martin's correlation was shown to have good agreement with arrays which experienced minimal cross-flow [Ichimiya&Okuyama(1991)]. Differences in nozzle arrangement and upstream flow conditions also influence the comparison. The average Nusselt number varies quite strongly with the Reynolds number. This dependence is generally approximated by power law dependence: Nu_{ave}–Re^n, with n depending on several factors and especially jet-to-jet spacing and distance from impinging point. By means of least square analysis, a value of 0.6408 fits

the data ($Nu_{ave}=0.1093(Re)^{0.6408}$). Martin (1977) and Huber et al. (1994) proposed the Reynolds number exponent n=0.67 and 0.71 for multi-jet systems respectively.
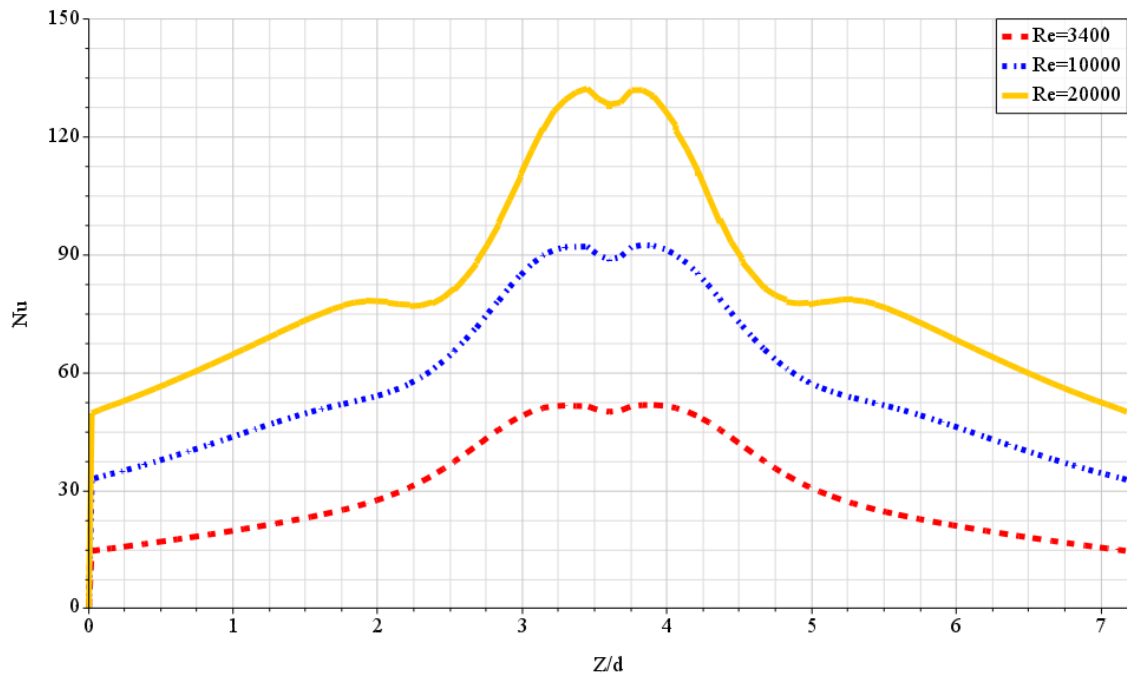
Fig. 5.13 Comparison of centerline Nusselt number distributions from single row at H/d = 5.4, S/d=7.2 for different Re numbers

Fig. 5.13 shows the comparison of centerline Nusselt number distributions for different Re numbers. Increasing the Reynolds number increases the peak Nusselt number for all Reynolds numbers. Generally, as the Reynolds number increases, the peaks and troughs in the Nusselt number line plots become more defined. At the low Re of 3400, the secondary peaks are virtually nonexistent. As the Re increases, the secondary peaks appear and become more pronounced due to the increase in the turbulent kinetic energy. Thus, the average Nusselt number increases significantly. This means that at low Reynolds numbers, the Nusselt number distribution is more uniform.

5.3.4.2 Effect on Heat Transfer from Multiple Rows

Fig. 5.14 shows the comparison of total average heat transfer coefficients between single and multiple rows for in-line arrays at H/d = 5.4 and S/d=7.2. The trends and the slope of the CFD predictions are the same for both single and multiple rows (Fig. 5.6, case 5) and the level of heat transfer for multiple rows is lower than that of the single row by approximately 15% on average. As already discussed, the stronger wall jet interference and cross-flow effects from the multiple rows cause a significant degradation of the convection coefficient when compared to the single row (see Figure 5.8 (b and h)).
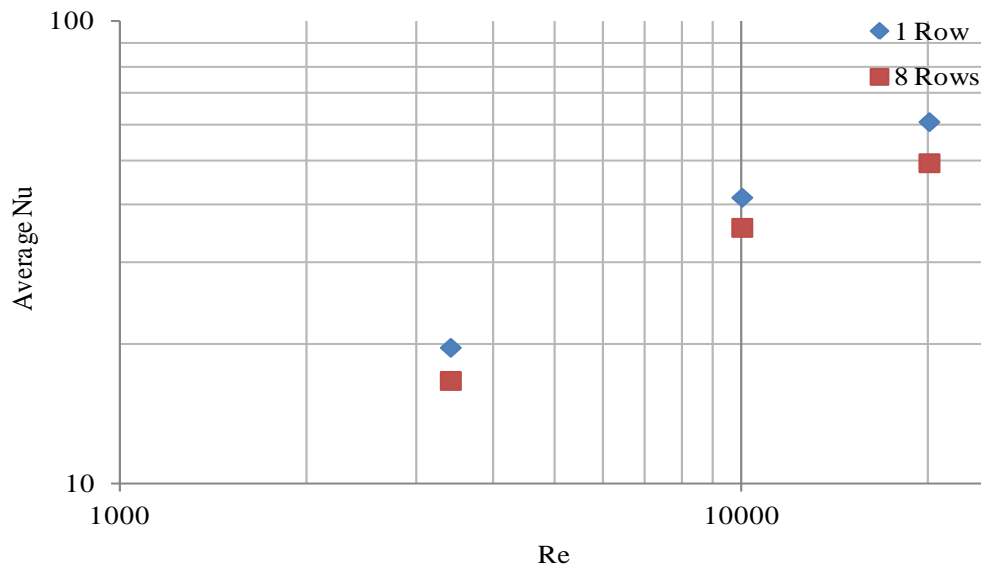
Fig. 5.14 Comparison of total average Nusselt numbers between single and multiple rows for in-line arrays at H/d = 5.4, S/d=7.2 for different Reynolds numbers in the logarithmic scale

The dependence on the Re is also strengthened because of the relationship between the secondary peaks and the Reynolds number, and increasing the Reynolds number increases the peak Nusselt number for all Reynolds numbers (see Figure 5.13), but for multiple rows, the wall jet interference and cross-flow effects dampen out the secondary peaks and create a more uniform Nusselt number distribution (see Figure 5.13 and 15). Therefore, the maximum difference between the single and multiple rows (around 20%) occurred on the total average Nu number at the high Reynolds number (Re=20,000).
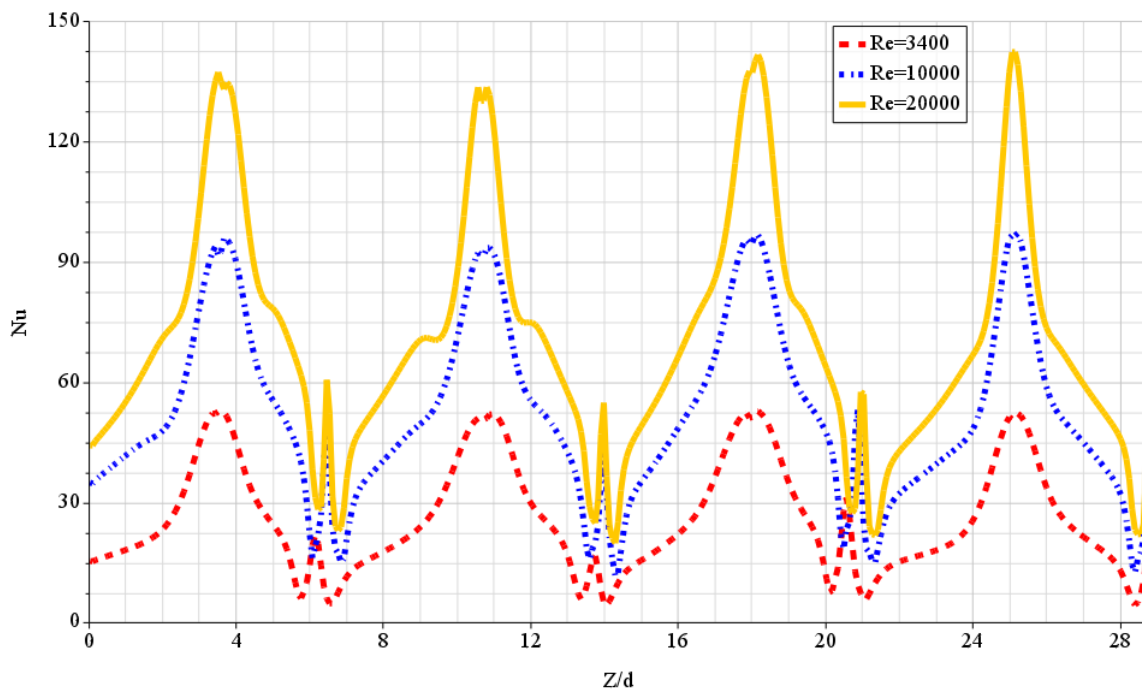
Fig. 5.15 Comparison of centerline Nusselt number distributions from CFD for multiple rows at H/d = 5.4, S/d=7.2 for different Reynolds numbers

5.3.4.3 Effect on Pressure Force

Fig. 5.16 shows the comparison of pressure force coefficients from single and multiple rows for in-line arrays at H/d = 5.4 and S/d=7.2 for different Reynolds numbers.

Fig. 5.16 Comparison of pressure force coefficient from CFD for single and multiple rows at H/d = 5.4, S/d=7.2 for different Reynolds numbers

Due to the definition of the force coefficient, the force coefficients on the target surface are relatively insensitive to the Re number for single row and multiple rows within the range examined. This result has a correlation with the findings of Wang et al. (2015) for single impinging jet. The trends and the slope of the CFD predictions are almost the same for both single and multiple rows. As expected, the level of pressure force for the multiple rows is lower than the single row by approximately 5% on average. Therefore, there is a negligible difference in the force coefficient between single row and multiple rows.

5.3.5 Separation Distance (H/d)

5.3.5.1 Effect on Heat Transfer from Single Rows

The separation distance is of specific importance for multiple impinging jets arrays as it determines the degree of flow interaction. The objective is therefore to assess whether the numerical simulations are able to predict such complicated flow interaction at different separation distance. Figure 5.17 compares the effect of separation distance on the total average Nusselt number from experiments and CFD.
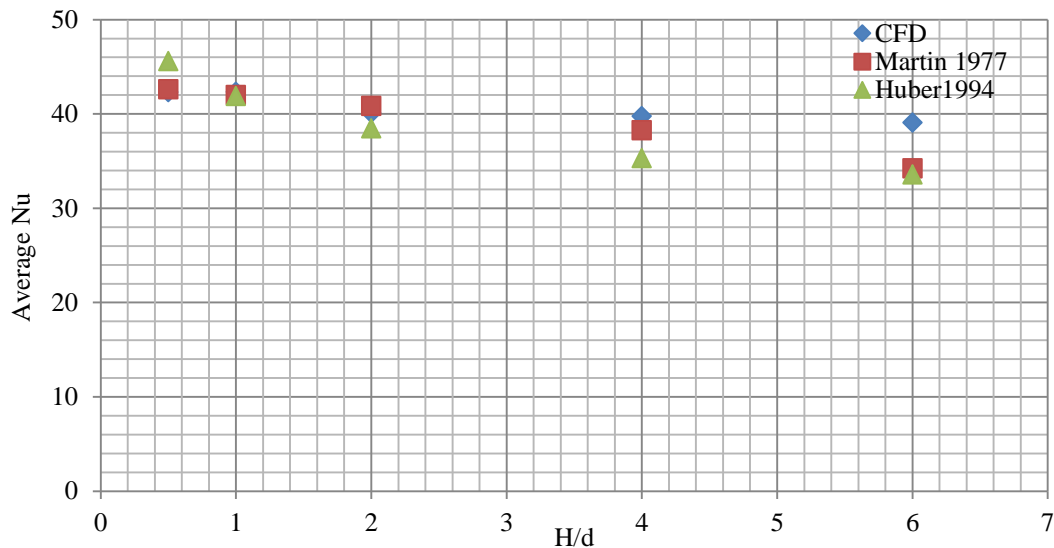
Fig. 5.17 Comparison of the effects of separation distance on total average Nusselt number from experiments and CFD (in-line arrays, S/d=7.2 and Re = 10,000)

Figure 5.17 reveals that the CFD results are in agreement with the experiments in terms of trends, slope and heat transfer level. The CFD data are more in agreement with Martin's correlation (average error is around 4%) than with Huber's correlation (average error is around 8%). Differences in nozzle arrangement and upstream flow conditions also influence the comparison.

The average Nu number varies with H/d. This dependence is generally approximated by power law dependence: $Nu_{ave}–(H/d)^n$, with n depending on several factors such as jet-to-jet distance and Re number. By means of least square analysis, a value of -0.035 fits the data ($Nu_{ave}=41.621(H/d)^{-0.035}$). Huber et al. (1994) proposed n= -0.123 for multi-jet systems.

Figure 5.18 shows the effect of separation distance on the centerline Nusselt number distributions. Increasing the separation distance decreases both peak and average Nusselt numbers for the array of jets. However, when the separation distance is decreased, there is a considerable enhancement of the average heat transfer coefficients. This is due to the secondary maximum peaks in the local Nusselt number which appears as a ring and significantly increase the surface area where the local Nu numbers are high. There is also a tendency of the intensity of the secondary peak being decreased at higher values of H/d, as shown in Figure 5.18. That's why, with H/d = 0.5, the secondary peaks are more pronounced than at other H/ds and H/d=6 has a more uniform Nusselt number distribution.
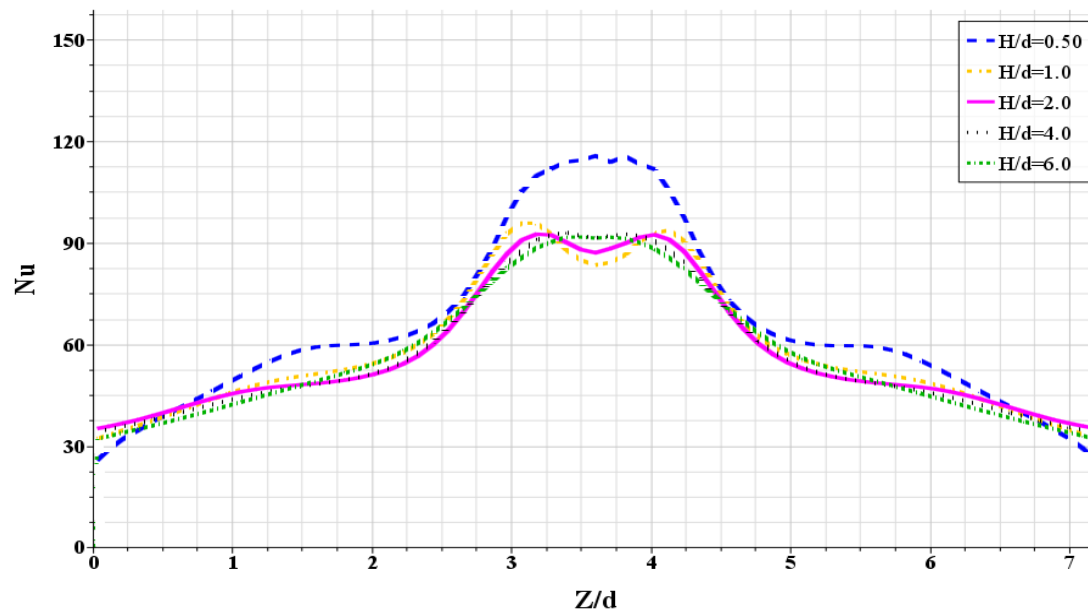
Fig. 5.18 Comparison of streamwise Nusselt number distributions from CFD for in-line arrays at S/d= 7.2 and Re=10,000

Figure 5.19 depicts the velocity contours for the five separation distances namely H/d = 0.5, 1, 2, 4 and 6 for Reynolds number 10,000. It can be clearly seen that in the case of H/d =0.5, 1, 2 the potential core is extended up to the target surface shown in Fig. 5.19 (a, b, c). In the case of H/d= 4 and 6, the potential core region has vanished by the time the flow reaches the target surface, shown in Fig. 5.19 (d and e). These differences in the velocity pattern are due to the variation in the momentum exchange between the jet flow and ambient fluid. Increasing the separation distance, the momentum exchange between the jet flow and the ambience increases. Hence, the flow in the case of low H/d (0.5, 1, and 2) has more momentum compared to the higher H/d (4 and 6).

5.3.5.2 Effect on Heat Transfer from Multiple Rows

Fig. 5.20 shows the comparison of total average heat transfer coefficients between single and multiple rows for different separation distance at S/d = 7.2 and Re=10,000. The trends and the slope of the CFD predictions are the same for both single and multiple rows (Fig. 5.6, case 5) except for $H/d < 2$. This is because for multiple rows with small separation distance the jet interaction increases significantly and the resulting heat transfer rates can differ substantially from those of single row. As expected, the level of heat transfer from multiple rows is lower than the single row by approximately 18% on average and the maximum difference between the single and multiple rows is around 25% for $H/d < 2$ due to the stronger wall jet interference and cross-flow effects from the multiple rows compared to the single row and also low H/d values intensify this matter (see Fig.5.8 b and h).

(a) H=0.5d

(b) H=1d

(c) H=2d

(d) H=4d

(e) H=6d
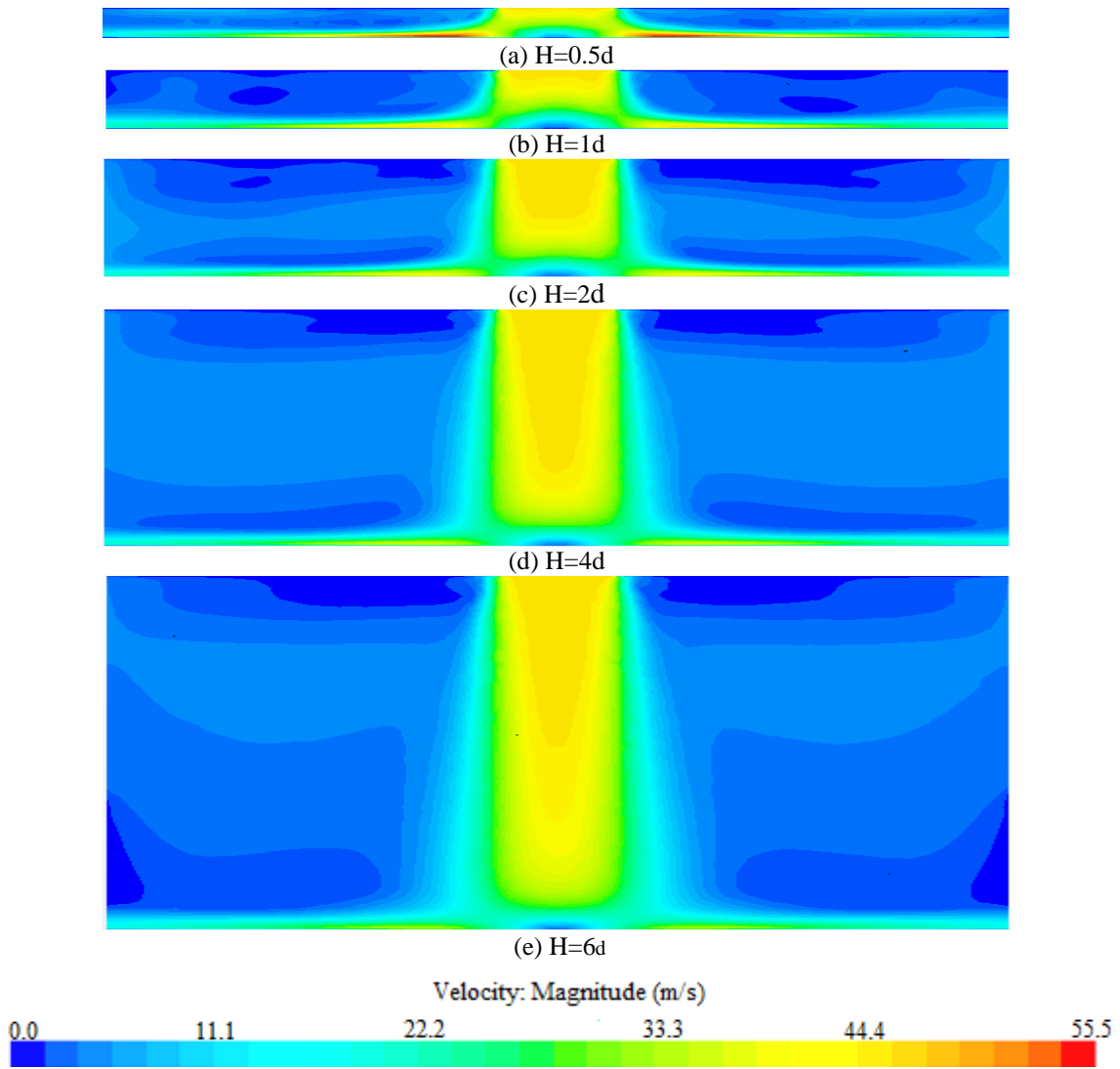
Fig. 5.19 Velocity magnitude contours along symmetry plane for Re = 10,000, S/d= 7.2 and different separation distances
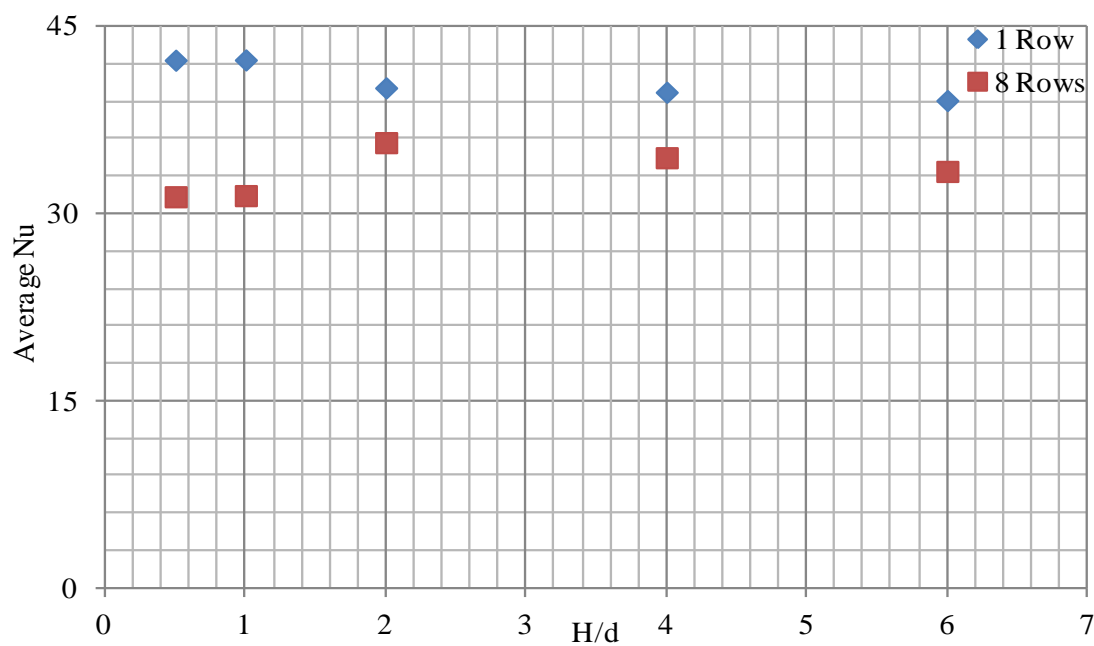
Fig. 5.20 Comparison of average Nu between single and multiple rows at S/d=7.2, Re=10,000 for different H/d

5.3.5.3 Effect on Pressure Force

Figure 5.21 depicts the comparison of pressure force coefficients for in-line arrays at S/d=7.2, Re=10,000 for different separation distance (H/d). The pressure force coefficients is highly dependent on H/d and it always increase with decreasing the H/d values, because when H/d decreases, the pressure on the impingement surface increases. Therefore, low H/d values lead to both high heat transfer and surface force. This result has a correlation with the findings of Wang et al. (2015) for single impinging jet. Therefore, the identification of optimum H/d is very important for a product sensitive to the pressure force such as paper. Also, the trends and the slope of the CFD predictions are the same for both single and multiple rows. Difference between the pressure force coefficient from single row and multiple rows is around 12% in average. As expected, the level of pressure force for multiple rows at high H/d values (H/d=4 and 6) is lower than the single row approximately 4% and 3%, respectively. The level of the pressure force coefficient for multiple rows at low H/d values $(H/d \leq 2)$ is higher than the single row. Where impingement jet fluid distributions are confined by smaller jet to target surface distance, the cumulative accumulations of cross-flows from sequential rows of jets can also result in the local augmentation of pressure force in the vicinity of the stagnation point.
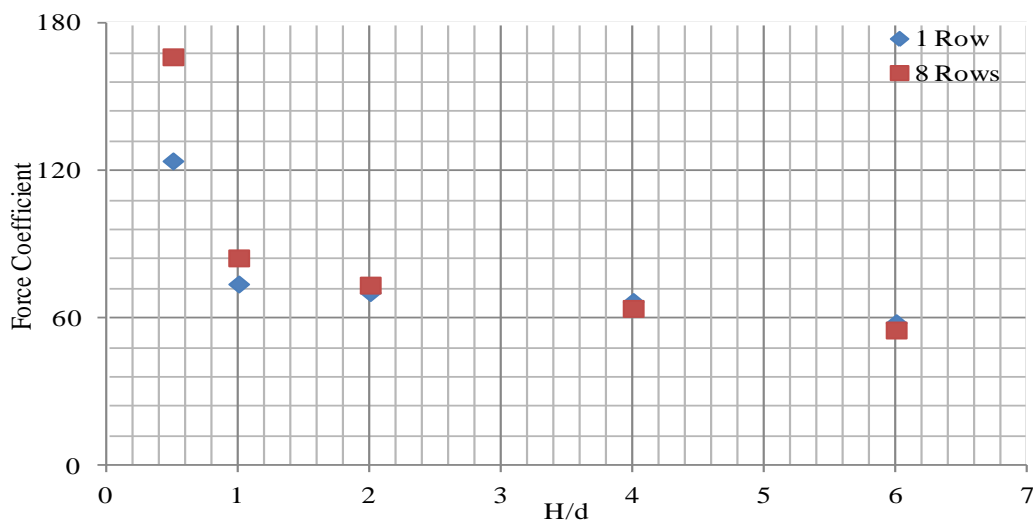
Fig. 5.21 Comparison of pressure force coefficient from single and multiple rows at S/d = 7.2 and Re=10,000 for different separation distance

5.3.6 Jet-to-Jet Spacing (S/d)

5.3.6.1 Effect on Heat Transfer from Single Row

A comparison of average Nu values for the three jet-to-jet spacings is given in Fig. 5.22. The averaging is done over the total target surface area. Thus with increased spacing the values of the corresponding surface area increases resulting in decreasing averaged dimensionless numbers. The results reveal a good agreement between the correlations and CFD data. The

CFD predicted the average heat transfer rates by approximately 15% on average. Differences in nozzle geometry, upstream and outlet flow conditions influence the comparison. The average Nu number varies quite strongly with S/d. This dependence is generally approximated by power law dependence: $Nu_{ave}–(S/d)^n$, with n depending on several factors such as nozzle-to-surface distance and Re number. By means of least square analysis, a value of -0.604 fits the data ($Nu_{ave}=129.07(S/d)^{-0.604}$), while Huber et al. (1994) proposed n= -0.725 for multi-jet systems.
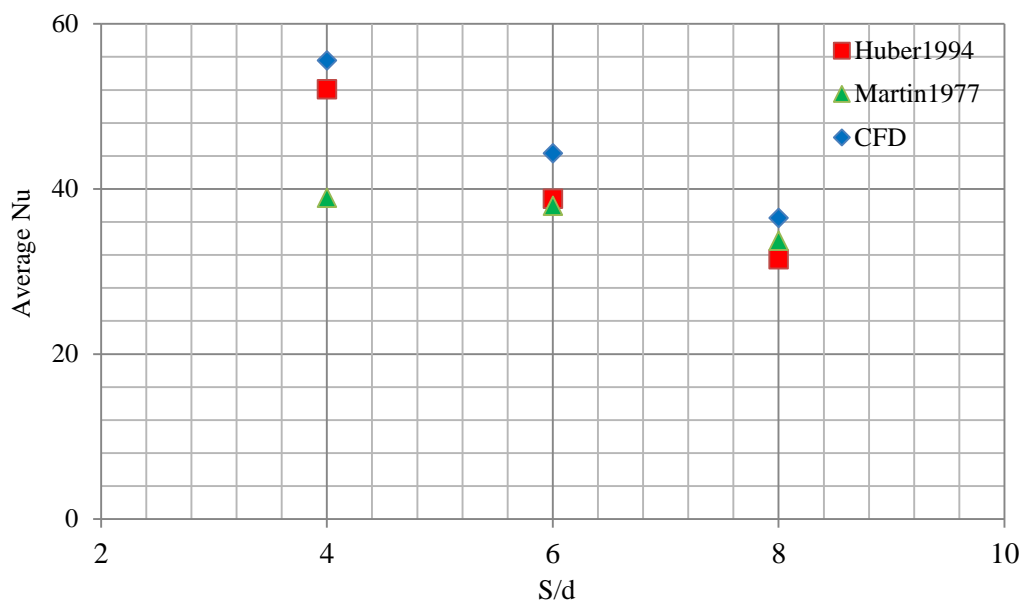
Fig. 5.22 Effects of jet-to-jet spacing on average Nu from experiments and CFD (H/d=5.4 and Re= 10,000)

Figure 5.23 shows the effect of jet-to-jet spacing on the spanwise Nusselt number distributions. The jet-to-jet spacing affects the heat transfer coefficient by varying the influence of the adjacent jet interference and fraction of the target surface covered by the wall jet. It is clear that Nu values for a given Re and H/d are largest for S/d =4. The average Nusselt numbers for S/d = 6 are then next highest, with those for S/d = 8 being the lowest. Thus, for the parameters used in this study, smaller S/d values result in higher Nu values. This is to be expected, because the jet array with a small S/d value has the smallest surface area and thus a greater fraction of the target surface area is covered by the stagnation region with high local Nu numbers than at the larger S/d where a larger fraction of the target surface is covered by the wall jet region, where the local Nu numbers are low (see Fig.5.23). Equivalently, the mass flow rate per unit surface area is highest for a configuration with smaller S/d. This means that the surface area dried by one jet in an array having S/d = 4 is dried by two jets in an array with S/d = 2.

With decreased jet-to-jet distances, the wall flows of the two jets are impinging upon each other and hence form a new stagnation region with higher Nusselt numbers. This interaction is more obvious in the case of S/d =4 and it is very weak in the case of S/d =8. Thus S/d=4 has the highest possible average heat transfer coefficents and least uniform heat transfer distribution across the impingement surface.
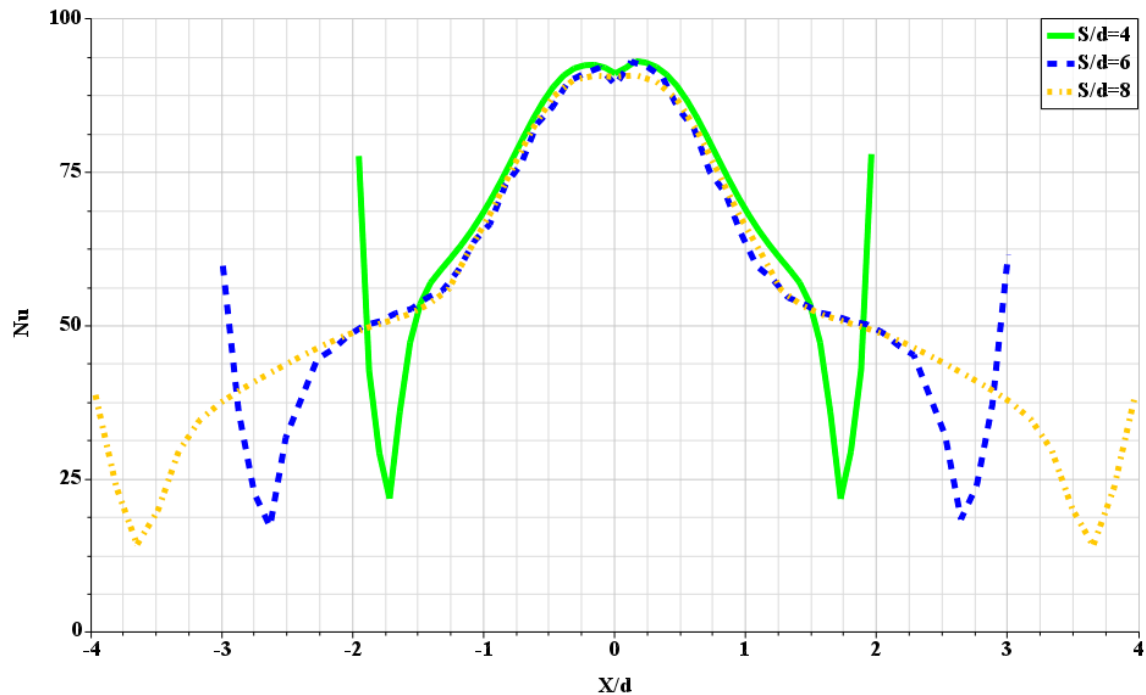
Fig. 5.23 Comparison of spanwise Nusselt number distributions from CFD for in-line arrays at H/d= 5.4 and Re=10,000

5.3.6.2 Effect on Heat Transfer from Multiple Rows

Fig. 5.24 shows the comparison of total average heat transfer coefficients between single and multiple rows for in-line arrays at H/d = 5.4 and Re=10,000. The trends and the slope of the CFD predictions are the same for both single and multiple rows (Fig. 5.6, case 5). As expected, the level of heat transfer for multiple rows is lower than the single row by approximately 10% in average and the maximum difference between the single and multiple rows is around 15% at S/d=4. This could be attributed to the stronger wall jet interference and cross-flow effects from the multiple rows compared to the single row and, also, low S/d values intensify this matter (see Figure 5.8 (b and h)).
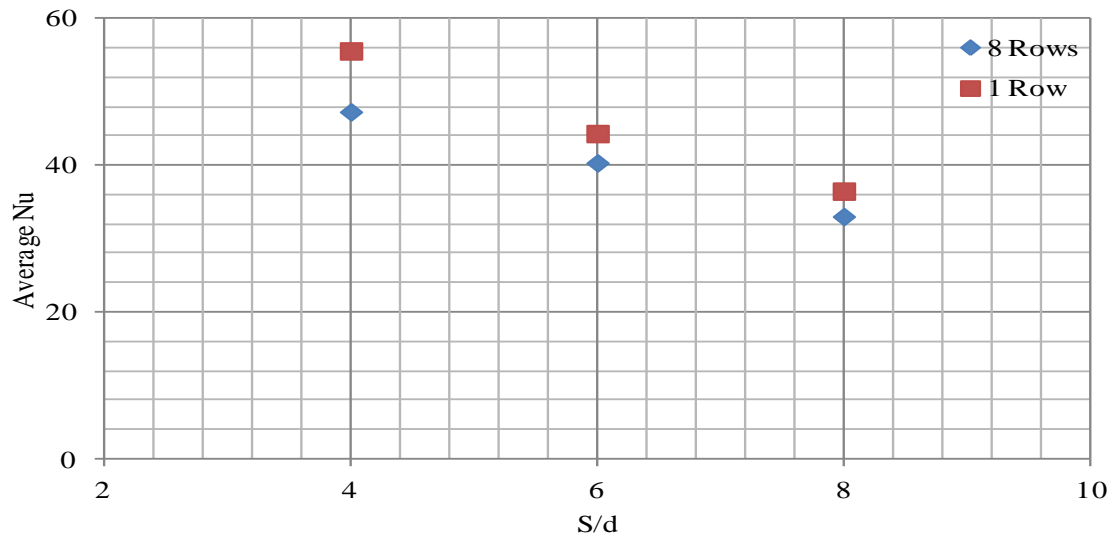
Fig. 5.24 Comparison of total average Nusselt numbers between single and multiple rows for in-line arrays at H/d = 5.4, Re=10,000 for different jet-to-jet spacing

5.3.6.3 Effect on Pressure Force

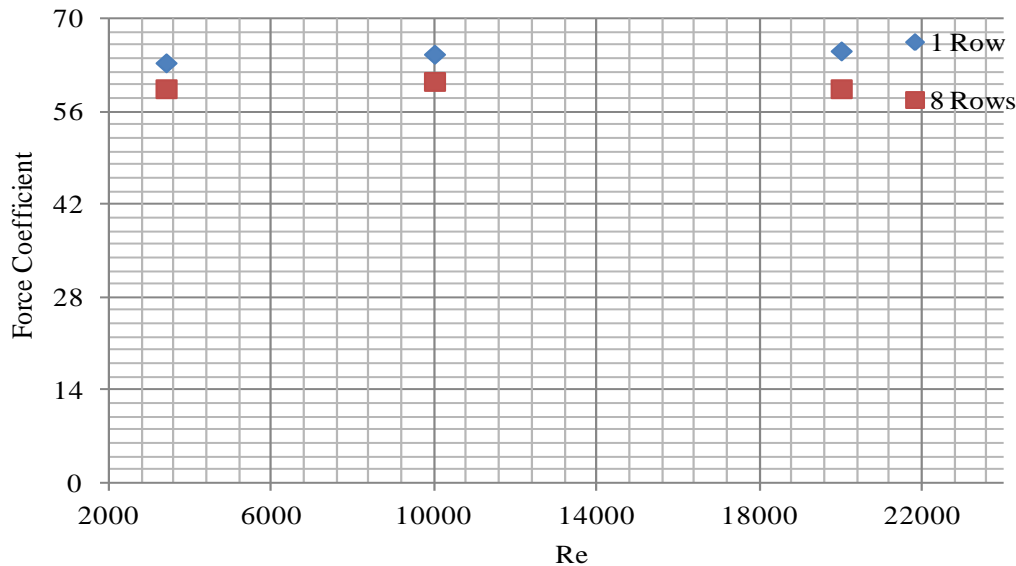Fig. 5.25 shows the comparison of pressure force coefficients from single and multiple rows for in-line arrays at H/d = 5.4 and Re=10,000 for different jet-to-jet spacing (S/d). The pressure force coefficient is calculated based on the total area and is thus by definition also dependent on the spacing. The pressure force coefficient increases with increased jet-to-jet spacing, because the closer jet-to-jet spacing has a smaller impingement surface area. Moreover, the trends and the slope of the CFD predictions are the same for both single and multiple rows. As expected, the level of pressure force for multiple rows is lower than the single row by approximately 10% on average. This could be attributed to the stronger wall jet interference and cross-flow effects from the multiple rows compared to the single row (see Fig. 5.10 (b and h)).
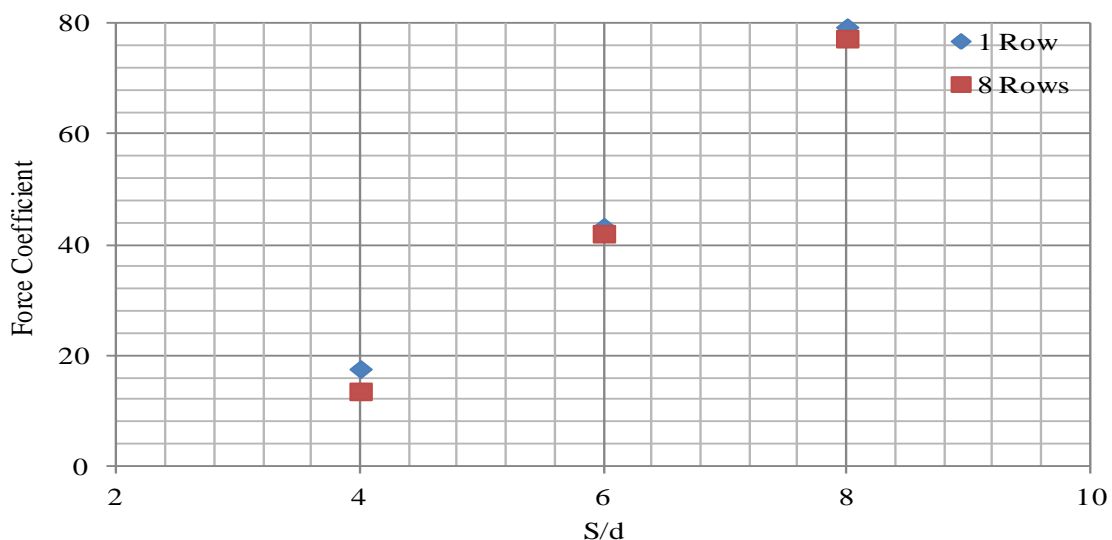
Fig. 5.25 Comparison of pressure force coefficient from CFD for single and multiple rows at H/d = 5.4, Re=10,000 for different jet-to-jet spacing

5.3.7 Jet Angle

5.3.7.1 Effect on Heat Transfer from Single Row

Attention is now turned to the effect of the jet exit angle. Figure 5.26 compares the effect of the jet angle on the total average Nusselt number from experiments and CFD (in-line arrangement, Re = 23,000, H/d=1 and S/d=5). The jet angle varies between 60, 45 and 90 degree as measured from the target surface and exits in one direction (45 degree isn't available in the literature for comparison). The average Nusselt numbers for different angles are also compared to the measurements presented by El-Gabry et al. (2004). These measurements were presented under a square array (8×8) of angled impinging jets. It can be seen from Figure 5.26 that the trends and the slope of the CFD predictions are in agreement with the experiments; however, the level of heat transfer is underestimated. The present work predicted the average heat transfer rates by approximately 5% on average.

With decreasing jet angle, the distance covered from jet exit to the surface increases and the orthogonal component of the jet flow decreases but on the other hand one flow component parallel to the wall increases and leads to increases the cross-flow effect and adjacent jets interference. It is clear that the surface average Nusselt number increases with increasing the jet angle, i.e. with decreasing inclination. This is to be expected because when the jet impinging orthogonal on the surface (90°), it can pick up the most heat upon striking the surface. Therefore, the inclined jets (60°) produce around 9% (11 for experimental results) lower overall-averaged Nusselt numbers for jet distances about 15% longer than for the orthogonal jets.
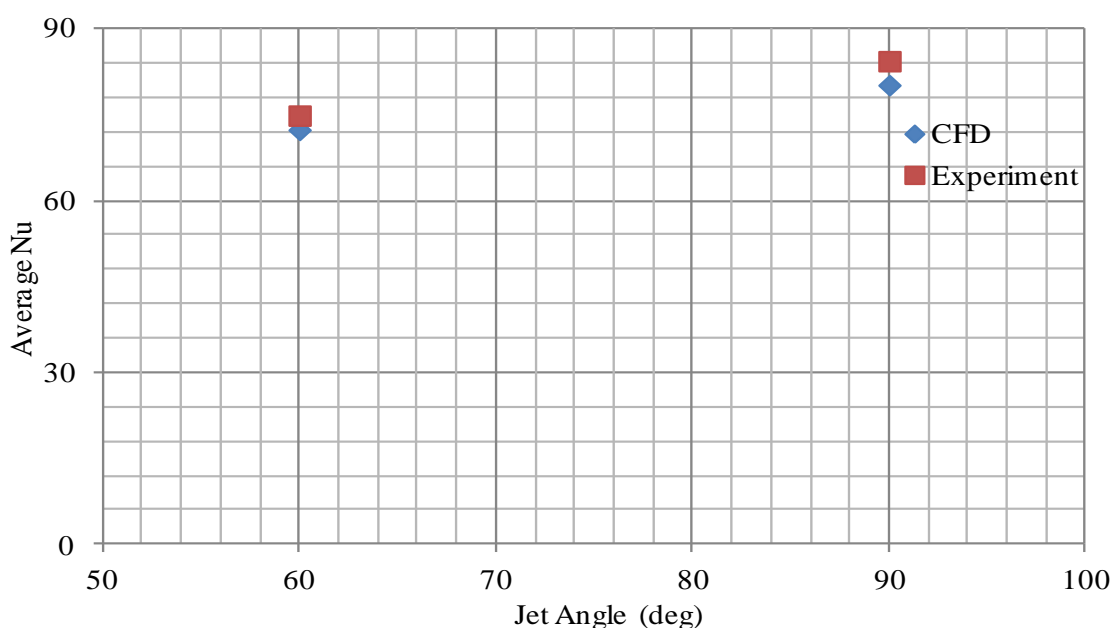
Fig. 5.26 Comparison of the effects of jet angle on total average Nusselt number from experiments and CFD (in-line arrays, H/d=1, S/d=5 and Re = 23,000)

The average Nu number varies quite strongly with the jet angle (θ). This dependence is generally approximated by power law dependence: Nu_{ave}–$(\theta)^n$, with n depending on several factors such as the nozzle-to-surface distance, jet-to-jet spacing and Re number. By means of least square analysis, a value of 0.2527 fits the data ($Nu_{ave} = 25.733 (\theta)^{0.2527}$). No correlation between Nu_{ave} number and jet angle related to present work was found in the literature for comparison.

Figure 5.27 shows the effect of the jet angle on the centerline Nusselt number distributions. The primary and the secondary peaks are observed in the Nu distribution of orthogonal impinging jets. The primary peak is not observed for the angled jets but the secondary peak is observed with very weak intensity compared to the orthogonal jets. The value of the Nusselt number at the stagnation point and secondary peaks shows significant change for angled jets compared to the orthogonal jet with shifted locations of the peak values. For angled jets, the Nusselt number on the right side is much larger than that on the left side. This is because the angled jet leads to a main flow toward the right side of the impinging surface, so the flow toward the left side will be confined. Thus the Nu curves for angled jets exhibit an asymmetrical trend and produce more uniform heat transfer distributions than the orthogonal jets. The jet exit angle ($\theta = 60°$) is here the optimum case which satisfies the largest heat transfer rate beside the uniform heat transfer along the target surface (see Fig. 5.26 and 27). Hence, the jet angle is yet another parameter that can be varied in a design to reduce the thermal gradients, especially when maximizing the overall heat transfer coefficients is not the only important objective.
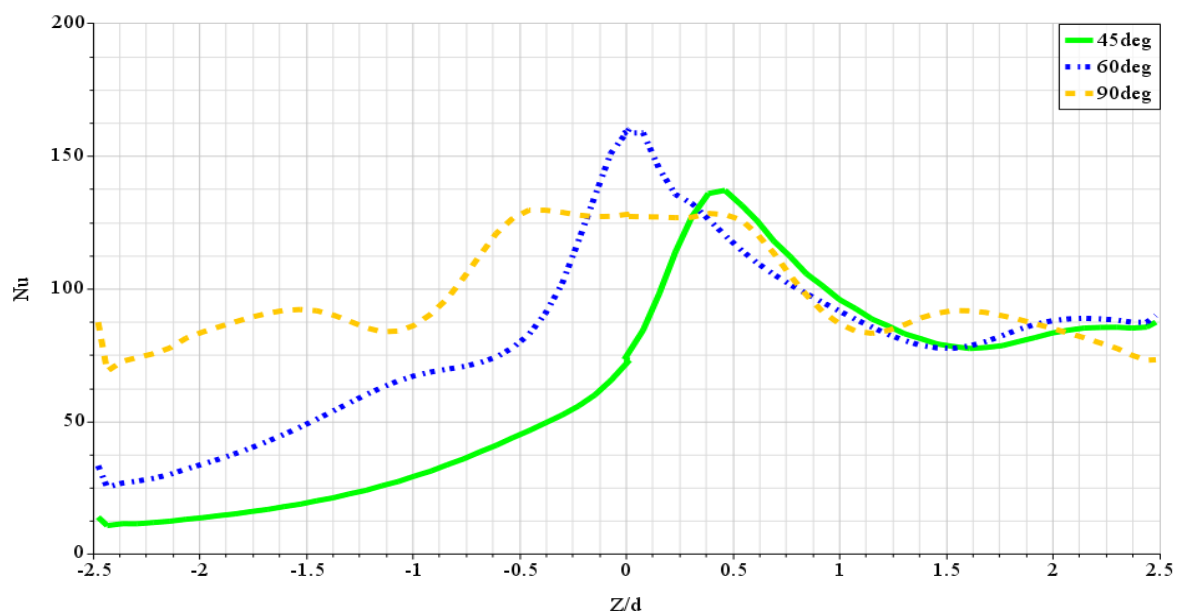
Fig. 5.27 Comparison of Nusselt number distributions in the exit flow direction from CFD for in-line arrays at H/d=1, S/d=5 and Re= 23,000 for different jet angles

5.3.7.2 Effect on Heat Transfer from Multiple Rows

Fig. 5.28 shows the comparison of total average heat transfer coefficients between single and multiple rows for in-line arrays at H/d = 1, S/d=5 and Re=23,000 for different jet angles. The trends and the slope of the CFD predictions are the same for both single and multiple rows (four rows). As expected, the level of heat transfer for multiple rows is lower than the single row by approximately 15% on average and the maximum difference between single and multiple rows is around 15% for orthogonal jet. This could be attributed to the stronger wall jet interference and cross-flow effects from the multiple rows compared to single row and also the orthogonal jets intensify this matter (see Figure 5.8 (b and h)).
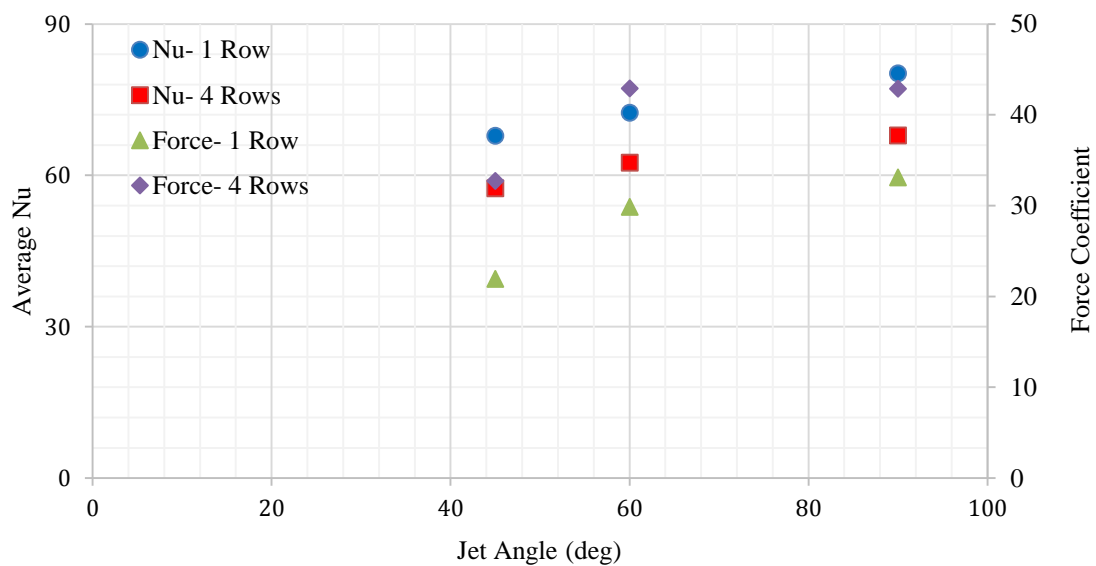
Fig. 5.28 Comparison of average Nusselt numbers and force coefficients from single and multiple rows for different jet angles at H/d = 1, S/d=5 and Re=23,000

5.3.7.3 Effect on Pressure Force

Fig. 5.28 shows the comparison of pressure force coefficients from single and multiple rows for in-line arrays at H/d = 1, S/d=5 and Re=23,000 for different jet angles. The pressure force coefficient correlates strongly with the orthogonal component of the jet, i.e. the sine of the jet angle and the pressure force coefficient increases if the jet angle is increased, because increasing the jet angle increases the pressure on the impingement surface. Therefore, the force on the impingement surface can be controlled by altering the flow exit angle. The trends and the slope of the CFD predictions are the same for both single and multiple rows. The level of pressure force for multiple rows has a significant difference and is higher than the single row by approximately 50 % on average. This could be attributed to the very complex flow which has occurred at the small jet-to-target surface distance; H/d=1 (See Fig. 5.21).

5.3.8 Surface Motion

5.3.8.1 Effect on Heat transfer from Single Row

The flow field with a circular confined jet impinging on a moving surface is essentially three-dimensional. The movement of the surface is considered in the Z-direction. Thus, a symmetry could be considered in the Y-Z plane. Pressure outlet boundary conditions are adopted on left and right sides of computational domain while front and back sides are symmetric planes for assuming an array of round jets as shown in Fig. 5.29.
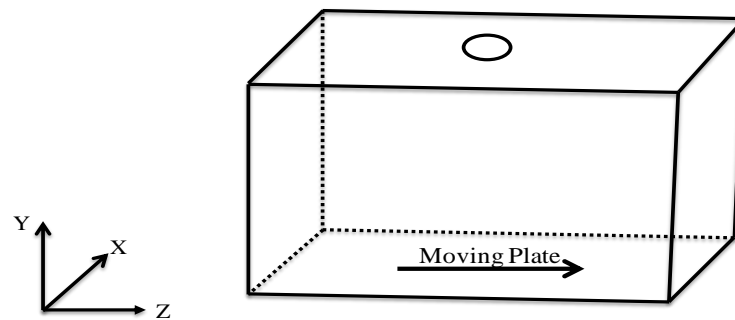
Fig. 5.29 Schematic of the computational domain

It can be mentioned here that RANS computations were performed for Re = 2,500. At the jet inlet, a uniform velocity profile has been imposed. The inlet turbulence intensity was kept at 5%. The target surface was modelled as no-slip wall held at a constant temperature (T_w = 311.15 K) and the inlet temperature was assumed at the ambient level (i.e., T_{in} =298.15 K). The velocity ratio defined as the ratio of surface velocity to jet velocity is varied up to 1.0.
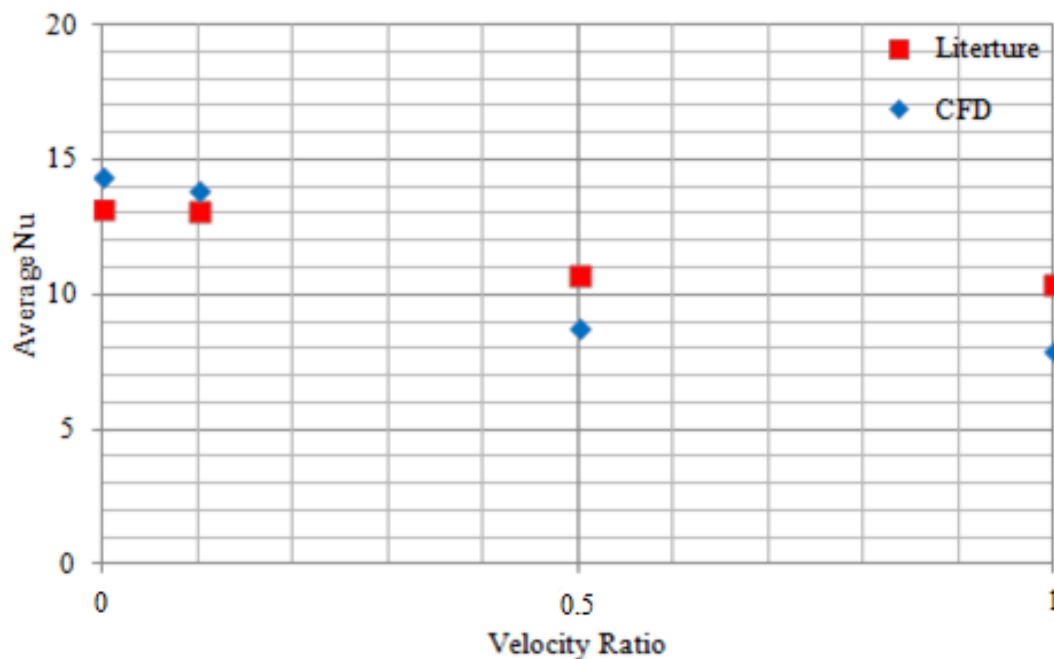
Fig. 5.30 Comparison of the effects of velocity ratio on total average Nusselt number from literature and CFD (in-line arrays, H/d=2, S/d=10 and Re = 2,500)

The overall effect of the surface motion could be obtained by examining Figure 5.30. Due to the absence of experimental data, the CFD results from this work have been compared with a numerical investigation conducted by Chattopadhyay et al. (2006). They chose the realizable k-ε model to simulate the circular jet bank impinging on a moving surface. Here the values of area averaged Nu are presented at different velocity ratios and varied up to 1.0. This reveals the good agreement between the literature and CFD data from this work. The trends and the slope of the CFD predictions are in agreement with the literature. The average Nu nnumber is predicted by approximately 14% on average. Differences in the turbulence model (realizable k-ε and SST K-ω), thermal boundary condition at target surface (due to the unknown boundary condition in the literature) and software (FLUENT and STAR-CCM$^+$) influence the comparison. It can be seen that the average Nu reduces with an increase of the velocity ratio. The total reduction is around 25% on average as compared to the case of a stationary surface.

The average Nu number varies quite strongly with the velocity ratio (VR). This dependence is generally approximated by power law dependence: Nu_{ave}–$(VR)^n$, with n depending on several factors such as-nozzle-to surface distance, jet-to-jet spacing and Re number. By means of least square analysis, a value of n=-0.25 fits the data (Nu_{ave}=7.707$(VR)^{-0.25}$). No correlation between the average Nu number and velocity ratio for multiple impinging round jets was found in the literature for comparison.
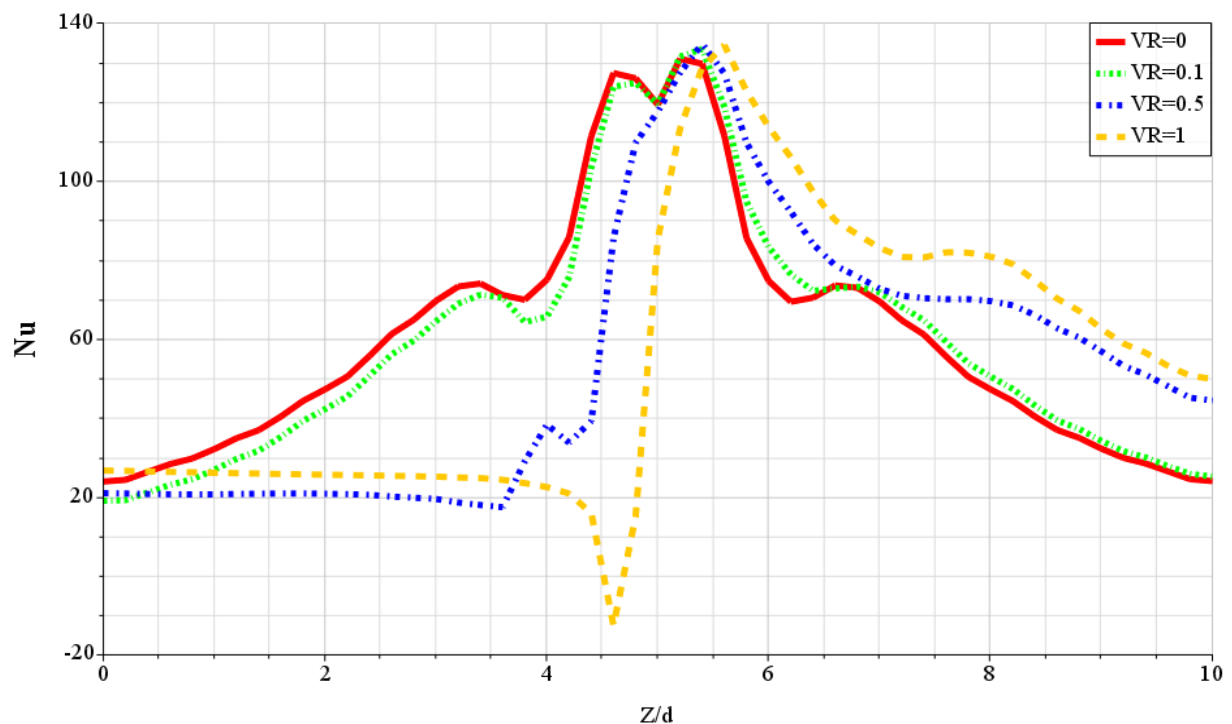
Fig. 5.31 Comparison of Nusselt number distributions in the direction of motion from CFD for in-line arrays, H/d=2, S/d=10 and Re = 23,000

Figure 5.32 shows the distribution of Nu at the target surface at varying surface velocity for Re=23,000. Distributions are shown for the Z-direction, i.e. the direction of surface motion. Due to the surface velocity, the impinging jet is entrained in the direction of the moving surface and the wall flow in the opposite direction is considerably hampered. For the case of the stationary surface, the heat transfer peaks are seen slightly away from the stagnation point, as reported earlier in our previous results. It can be seen here that along the direction of surface motion, the heat transfer peak shifts with an increase in the velocity ratio (VR). At higher values of velocity ratio, the heat transfer at the one ends, i.e. nears the one of the outlet locations, increases though the average heat transfer diminishes. In the cross-plane, the heat transfer reduces at all locations with increased velocity ratio. It can be observed that, by increasing the surface velocity, the high heat transfer zone, which originally occurs at the impinging zone, shifts the downstream and the shape of the zone is also distorted in the downstream direction. In a jet impingement array, this decreases the overall heat transfer rate, because, for an array of nozzles, the surface motion increases the interaction between neighboring jet flows and leads to significant reductions in the local Nu number. Therefore, the effect of surface motion is like that of superposing a cross-flow. However, the higher velocity ratio helps to achieve more uniform heat transfer distribution, which may be desirable for certain products.

At high velocity ratio (VR=1.0), a negative Nu number can be detected around the impingement region (see Fig. 5.32) due to the flow separation from the target surface that results in overall loss of the flow kinetic energy and a rapid decrease in the heat transfer rates, as shown in Figure 5.33. Therefore, much effort and research must go into the design of turbomachinery systems, which include the heat transfer on the moving surfaces at a high velocity ratio which keep the local flow attached and delay the flow separation from the target surface and for as long as possible.
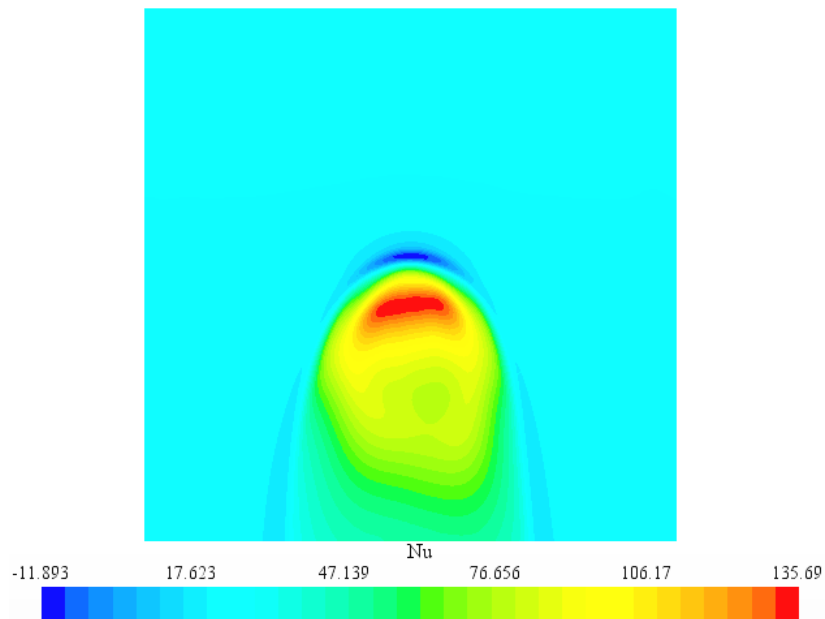
Fig. 5.32 Nusselt number contour for the target surface, Re=23,000

Zoomed view of the flow separation region (local flow reversal)
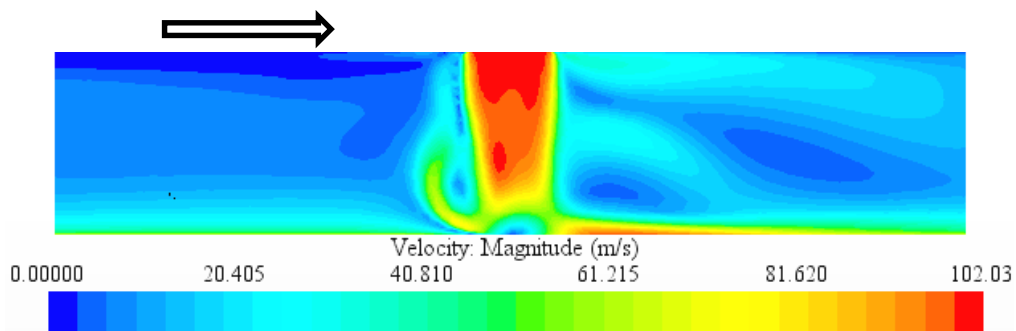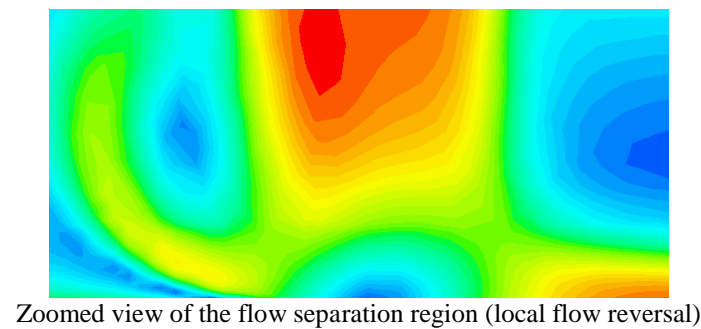
Fig. 5.33 Velocity magnitude contours in the symmetry plane, Re=23,000

5.3.8.2 Effect on Heat transfer from Multiple Rows

Fig. 5.34 shows the comparison of total average heat transfer coefficients between single and multiple rows for in-line arrays at H/d = 2, S/d=10 and Re=23,000 for different velocity ratio. The trends and the slope of the CFD predictions are the same for both single and multiple rows (four rows). The level of heat transfer for multiple rows is lower than the single row by approximately 5% in average and the maximum difference between the single and multiple rows is around 15% for VR=1 due to the higher wall jet interference and cross-flow effects

from multiple rows compared to the single row and, also, the high relative surface velocity intensifies this matter (see Figure 5.8 (b and h)).
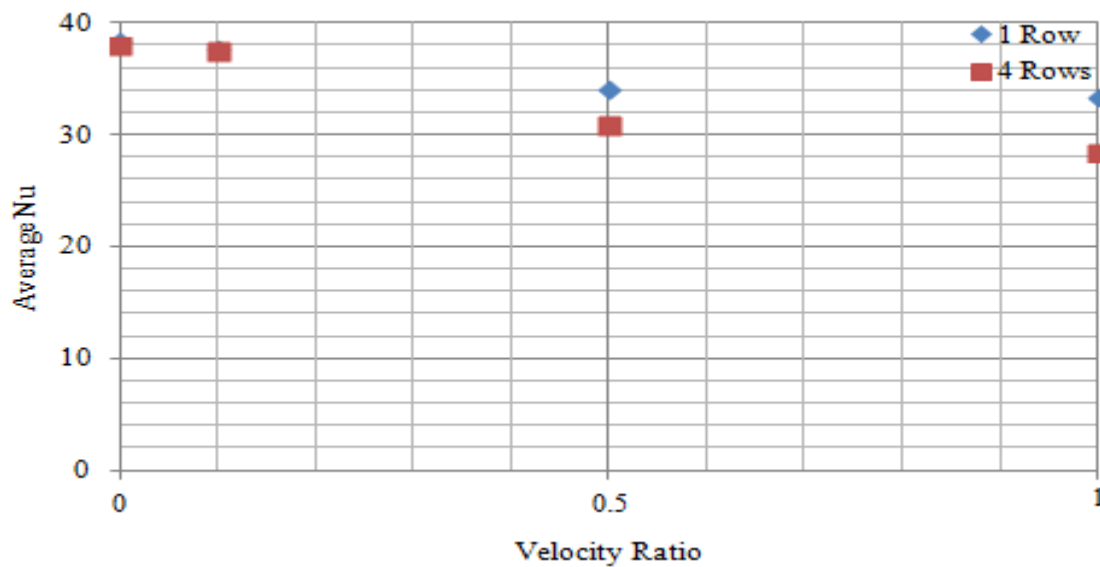
Fig. 5.34 Comparison of total average Nusselt numbers between single and multiple rows for in-line arrays at H/d = 2, S/d=10 and Re=23,000 for different velocity ratio

5.3.8.3 Effect on Pressure Force

Fig. 5.35 shows the comparison of pressure force coefficients from single and multiple rows for in-line arrays at H/d = 2, S/d=10 and Re=23,000 for different velocity ratio (VR). The pressure force coefficient decreases as the velocity ratio increases due to the entrainment of the impinging jet by the moving surface. The trends and the slope of the CFD predictions are the same for both single and multiple rows. The level of pressure force coefficient from the multiple rows has no significant changes compared to the single row.
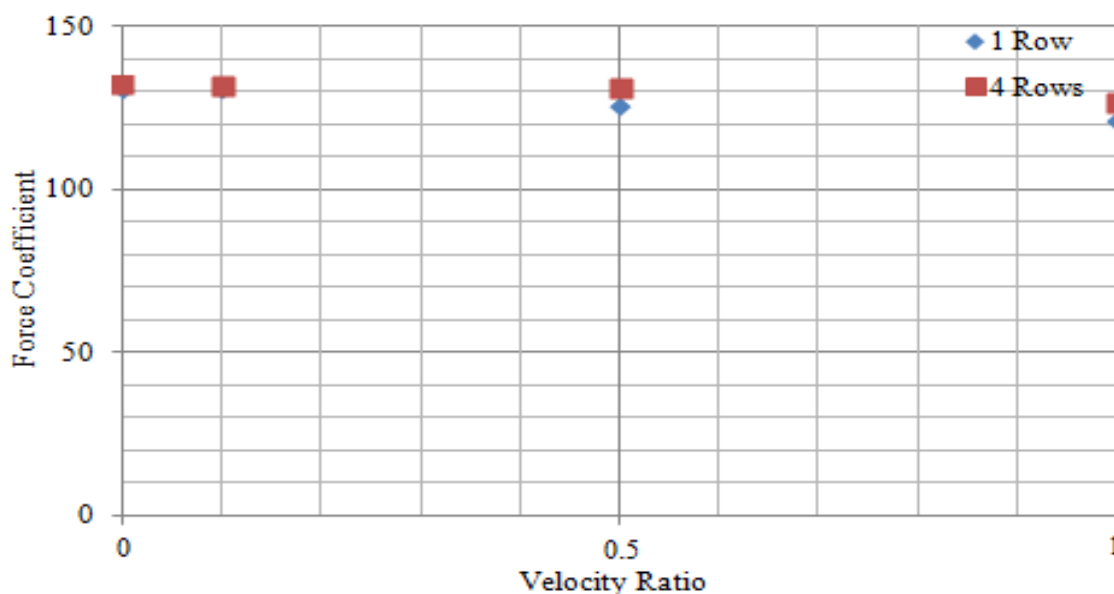
Fig. 5.35 Comparison of pressure force coefficient from CFD for single and multiple rows at H/d = 2, S/d=10 and Re=23,000 for different velocity ratio

5.3.9 Correlation Equations

Two correlations for the average Nusselt number and pressure force coefficient from the numerical simulations are developed by a multiple regression fit for the single row of orifices impinging on a flat surface:

$$\text{Nu}_{\text{ave}} = 1.12\,\text{Re}^{0.54}\,(H/d)^{-0.016}\,(S/d)^{-0.77}\,\theta_{\text{rad}}^{0.3}\,(1+VR)^{-0.9} \tag{5-1}$$

$$C_f = 0.8\,\text{Re}^{-0.002}\,(H/d)^{-0.09}\,(S/d)^{2.2}\,\theta_{\text{rad}}^{0.6}\,(1+VR)^{-0.24} \tag{5-2}$$

The above correlations are proposed in terms of Re, H/d, S/d, θ, and VR as the independent variables for Re number in the range of 2500 to 23000, H/d from 0.5 to 6, S/d from 4 to 10, θ from 45 to 90° and VR from 0 to 1. Prandtl number is set to Pr=0.71. The observed trends in the CFD simulations are shown by the exponents of the independent parameters in the correlations.

Figures 5.36 and 5.37 show the parity plot for comparison of the CFD simulation and predicted results by correlations. The agreement is found to be reasonable and all the data points deviate from the correlation by less than 7% and 3% for the average Nu number and force coefficient respectively.
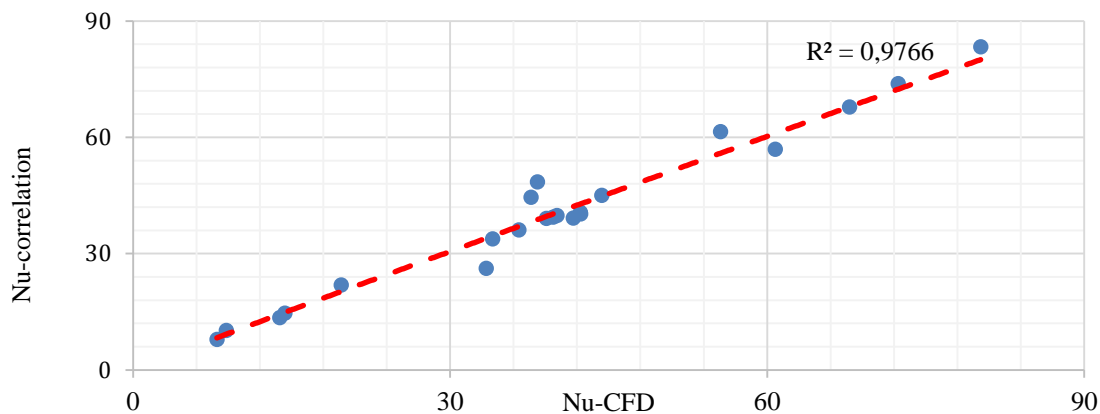
Fig. 5.36 Parity plot showing a comparison between the average Nu predicted by the CFD and correlation
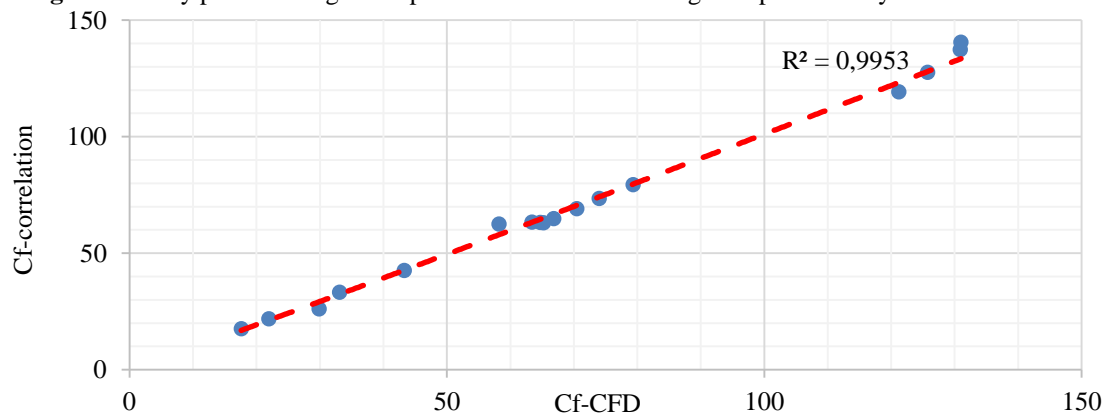
Fig. 5.37 Parity plot showing a comparison between the force coefficient predicted by the CFD and correlation

5.4 Summary

The consideration of large arrays with an infinite number of impinging jets and rows is of particular interest as most studies in the present literature have considered array configurations with relatively few numbers of impinging jets and rows. In the computations, the numerical simplification allowed a substantial reduction of the problem size. Numerical accuracy was shown to be reasonably high to allow for a discussion of the main flow and heat transfer characteristics.

In the course of this chapter, the effects of impinging jet and row number, nozzle shapes (orifice and pipe), Reynolds number, separation distance, jet-to-jet spacing, jet angle and surface motion were discussed to gain understanding of the physical mechanisms which affect the uniformity of the local heat transfer coefficient, the average heat transfer coefficient and pressure force coefficient from single row and multiple rows. For this, the local and averaged Nusselt number was compared with experimental data. The overall agreement found was good which showed that CFD is generally suited for the prediction of complex impingement configurations by using reasonably simplified problems. The functional relations between the heat transfer and the geometric influencing parameters were all reproduced correctly.

As the jet-to-surface distance is decreased to one jet diameter $(H/d \leq 1)$, the adjacent jet interference before impingement is minimized and the secondary maxima occur in the local convective coefficient for a jet in an array. These secondary maxima enhance the average convective coefficients.

The small jet-to-jet spacing resulted in the highest average Nusselt number for a given separation distance. This is because a large fraction of the target surface is covered by the stagnation region and the influence of the low heat transfer coefficients associated with the wall jet region is minimized.

Non-orthogonal jets reduce the heat transfer but tend to generate more uniform heat transfer distributions. Hence, the jet angle is yet another parameter that can be varied in a design to reduce the thermal gradients especially when maximizing the average heat transfer coefficients is not only an important objective.

Numerical solutions were carried out for the circular jet impingement on the moving surface. Surface motion reduces the heat transfer but tend to generate more uniform heat transfer distributions. The flow separation from the target surface has occurred at high velocity ratio (VR=1.0, Re=23,000) and much effort and research is needed to delay the flow separation for as long as possible.

Pressure force coefficient on the impingement surface is highly dependent on H/d, S/d and jet angle but relatively insensitive to the Re number and surface motion within the range examined. Pipe always has a higher averaged Nu and pressure force coefficient compared to the orifice nozzle. For multiple rows of aligned air jets, the Nu number curves exhibited very different shapes due to the different intensity of interference between adjacent jets. The effect of multiple rows with regard to the impact on heat transfer and pressure force is negligible compared to the single row by approximately 12 and 16% on average.

Two correlations describing the average Nu number and the pressure force coefficient for single row jet configurations have been developed as a function of Re, H/d, S/d, θ and VR. The agreement in prediction of the average Nu number and pressure force coefficient between the CFD and correlation is found to be reasonable.

Chapter 6

6. Multiple Jets Impinging on Curved Surface

Multiple impinging jets are much more complicated than the single jet due to the jet interaction. As all numerical studies have considered array configurations with impinging jets on the fixed curved surface or moving flat surface at relatively low Re number (see Chapter 2), the objective of the present work is the prediction of impinging jets on the moving curved surface at high Re number by means of a computational model in terms of the local and average heat transfer and also the pressure force coefficient for the drying applications. The heat transfer between multiple jets and a moving curved surface is more difficult to study due to the changing boundaries and the effect of surface curvature but is also very relevant in engineering applications such as drying process.

The chapter starts with a brief description of industrial dryer specifications and a summary of the investigated parameters. Next, details on the computations are provided. In the results section, the CFD simulations are compared to the experimental data from the literature to quantify the degree of accuracy in prediction of the local heat transfer coefficient from multiple jets impinging on a fixed curved surface. First, the analysis includes the effect of surface curvature on the heat transfer and pressure force from the multiple jets impinging on the fixed curved surface. Next, the effect of jet numbers, number of jet rows, cross-flow, jet arrangement (in-line and staggered), surface motion, jet Reynolds numbers (Re), separation distance i.e. relative nozzle-to-surface distances (H/d), relative nozzle-to-nozzle spacings (S/d) and the jet angle (θ) on the heat transfer and pressure force from multiple jets impinging on a moving curved surface is investigated. Two correlations are developed for the average Nusselt number and the force coefficient as a function of Re number, H/d, S/d, θ, VR and Cr. The chapter concludes with a summary of the main findings.

6.1 Investigated Parameters

A numerical study has been performed to determine the flow and heat transfer characteristics of multiple impinging round jets on a moving curved surface. The parameters investigated in the present study include the effect of relative surface curvature i.e. the ratio of height to the half of chord length of the curved surface, number of jets, number of jet rows, nozzle arrangement (in-line and staggered), cross-flow, jet Reynolds number (Re), relative nozzle-to-surface distances (H/d), relative nozzle-to-nozzle spacing (S/d), jet angle (θ) and relative surface velocity (VR) i.e. ratio of surface velocity to the jet velocity on the moving

curved surface. The parameters which are maintained constant are: jet nozzle diameter (d=10mm), inlet jet temperature (25 C), ambient temperature (25 C) and surface temperature (60 C). The value of inlet velocity is so selected that it matches with the corresponding Reynolds number. For all configurations, the pattern was regular i.e. the streamwise and spanwise jet-to-jet distance was equal. Details of the parameters investigated are presented in Table 6.1.

Table 6.1 Parameters investigated for a real industrial dryer

Parameters	Values
Number of jet rows	1, 3
Jet numbers	3, 5, 7, 13, 25, 49
Jet Reynolds number (Re)	1,980, 10,000, 23,000, 40,000, 66,200
Relative nozzle to surface distances (H/d)	1, 2, 5, 10, 15, 20
Relative nozzle to nozzle spacing (S/d)	2, 4, 6, 10
Jet angle (θ)	45, 60 , 90 (°)
Relative surface curvature (Cr)	0, 0.1, 0.2, 0.4, 0.6, 0.8, 1.0
Relative surface velocity (VR)	0, 0.0047, 0.047, 0.28

6.2 Fixed Curved Surface

In this study, the local Nusselt number distributions and averaged Nu of multiple jets on a fixed curved surface are investigated. Therefore, corresponding numerical simulation is conducted to investigate its applicability and complex flow structures induced by the multiple jets. Numerical simulations using STAR-CCM+ were also conducted to compare the predicted results with measured data obtained by Fenot et al. (2008).

6.2.1 Domain and Boundary Conditions

For industrial dryers; the variation of relative curvature (Cr) is brought about by varying the height of the impingement surface (R_1) between 0-40 mm and the half of chord length of the impingement surface (R_2) between 50-200 mm. The relative surface curvature (Cr) is defined as the ratio of height (R_1) to the half of chord length (R_2) of the curved surface. The physical model for present numerical investigation is chosen in line with the experimental set-

up used by Fenot 2008. As seen in Fig. 6.1, the jets are formed from tubes. The diameter of injection tubes (d) is 10mm and the tubes' length to diameter ratio is 10, which is a sufficient length to obtain a fully developed exit jet flow. The target surface is a semi-cylinder of 100mm of inner diameter ($R_1=R_2=50$mm). Distance between injection tubes (S) is four times jet diameter and length of confinement plate is 30mm.
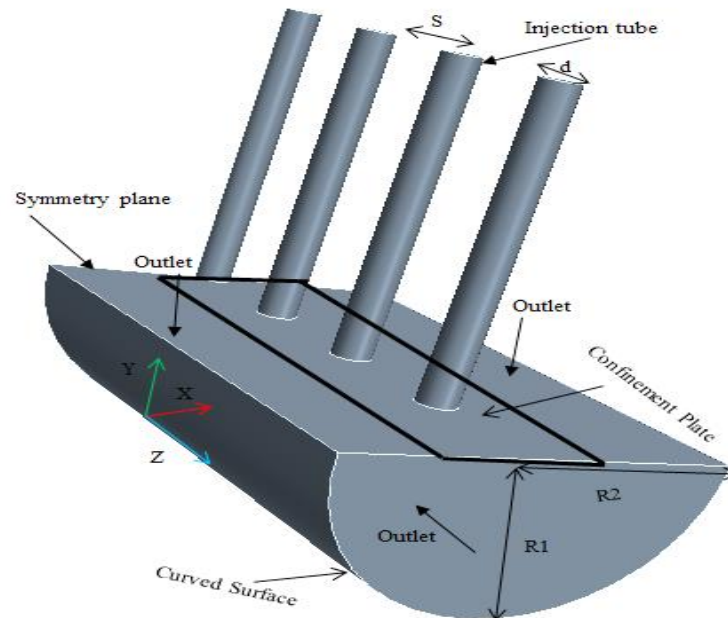
Fig. 6.1 Schematic of the computational domain for fixed curved surface

Mass flow condition is imposed at the inlet. The value of inlet velocity is so selected that it matches with the corresponding Re number. A turbulence intensity of 5% is chosen at the inlet fluid. Ambient air of constant temperature at 298.15$^°$ K is specified as the inlet fluid. Uniform heat flux of 4000 W/m^2 was applied to the target surfaces to simulate the condition of the target wall in the experiment. On all other solid surfaces, no-slip with adiabatic wall boundary condition is imposed. Constant pressure outlet boundary condition is applied to all open boundaries. Atmospheric pressure is applied at these outlets. Symmetric boundary condition was also applied in X-Y plane for the central jet to reduce the computational cost.

6.2.2 Grid Generation

Similar to the multiple impinging jets on a flat surface, the grids for on curved surface were constructed analogously using the same parameters and therefore only differed in overall base size. An unstructured polyhedral grid was generated using STAR-CCM$^+$. Boundary layers with a proper y_1^+ value, i.e. less than one, were built on the concave surface of the model in order to enable better resolution of the flow in this part. The final numerical model accounted for about 2,157,431 grid cells. In Figure 6.2, a 3D view of the grid is provided.
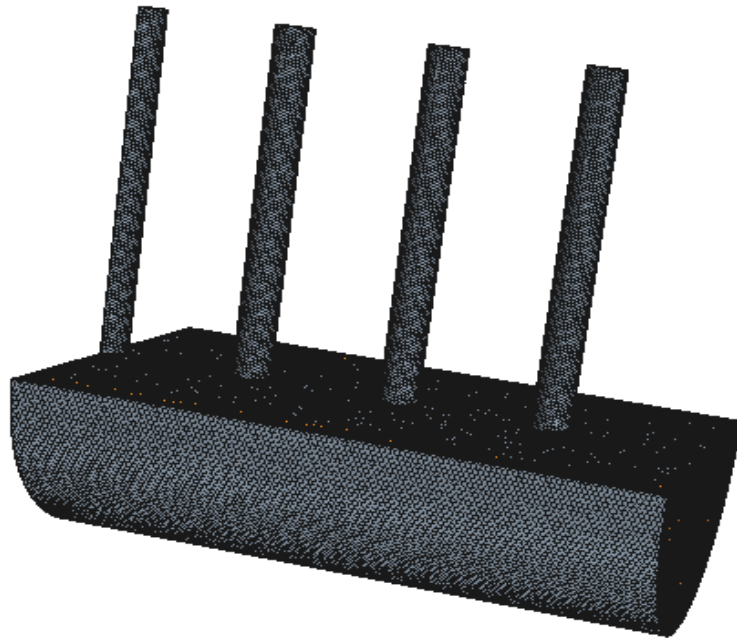
Fig. 6.2 Grid used for H/d = 5, S/d = 4, Cr=1

6.3 Results and Discussion

6.3.1 Grid Sensitivity Study

The grid sensitivity study is performed by analyzing the variation of local Nu number distribution on the target surface along Z direction, shown in Fig. 6.3. Two lines seem particularly interesting: the Z-centerline (the line passes the stagnation points) along which the interactions between the jets should be the strongest and the curvilinear axis along which the curvilinear effect should be dominant.
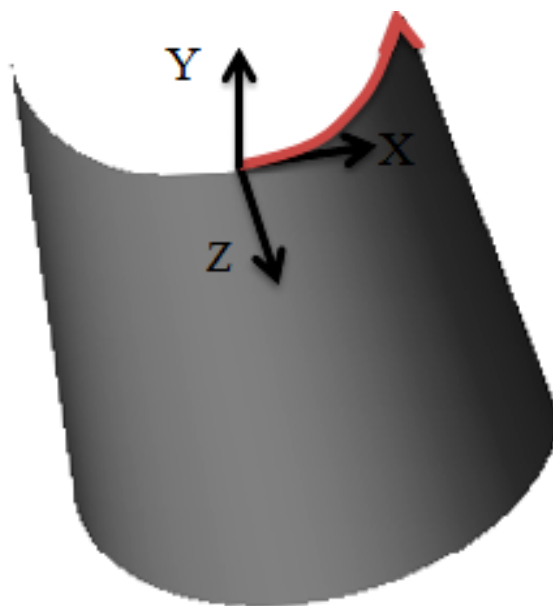
F**ig. 6.3** Axes selected for plotting the results

The grid sensitivity analysis was performed at Re =23,000 and the grid sizes are summarized in Table 6.2 indicating that the y_1^+ requirement was generally fulfilled for all investigated grids. The value of $y_{1,max}^+$ refers to the maximum dimensionless wall distance on the target surface and was obtained.

Table 6.2 Grid parameters of the refinement study

Grid	Base Size(m)	Cell Number	Max y_1^+	Average GCI %
Course	0.00192	447431	0.44	---
Intermediate	0.00127	970045	0.31	4.12
Fine	0.00088	2157431	0.23	2.6

Figure 6.4 shows the Nusselt number distribution along the Z-centerline with different grid sizes. The local discretization error distribution is calculated by the GCI method. The overall discretization error for fine grid was very small (average 2.6%) and the largest values of the error (around 17.4%) were found unreasonable around Z/d≈3.65, close to the stagnation point. Also, the overall discretization error for intermediate grid was very small (average 4.12%) and the largest values of the error (around 16.4%) were found around Z/d ≈ 5.33, i.e. the location of secondary stagnation zone. Therefore, the small values of GCI indicate that the solution is within the asymptotic range and grid-independent. But the results of the different grids were not as good as identical, especially in the direct vicinity of the stagnation point due to the large gradients that occur in this region. In order to reduce the computational cost, the intermediate grid is selected as final grid.
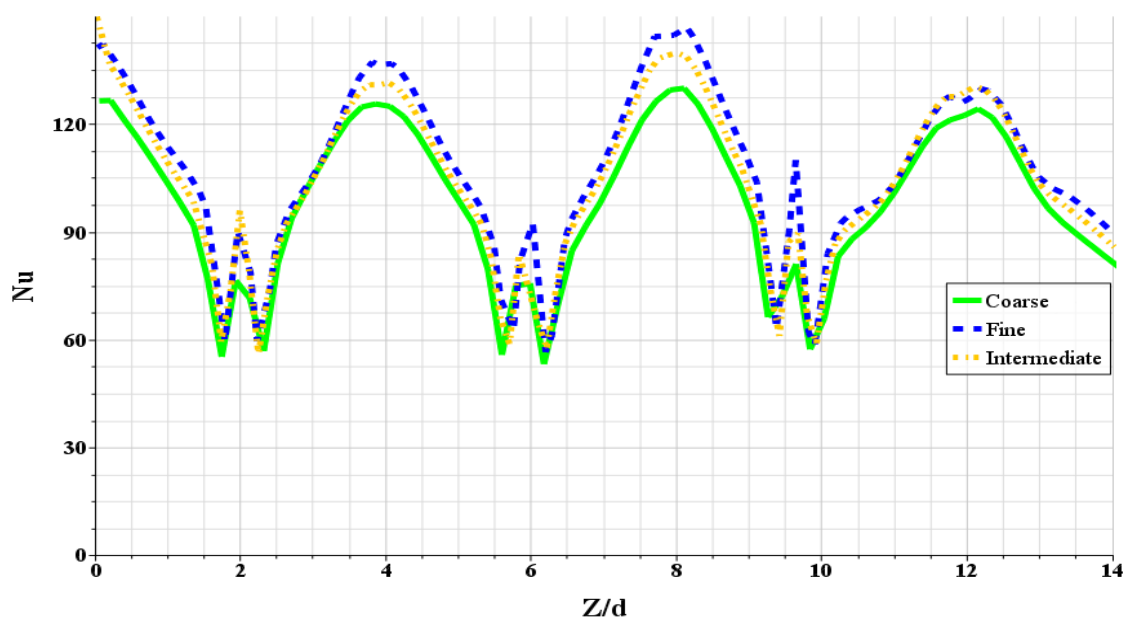
Fig. 6.4 Nu number distributions obtained by the grids used in the grid sensitivity study (H/d=5, S/d=4, Re = 23,000, Cr=1.0 and VR=0)

6.3.2 Evaluation of Computational Model

Figure 6.5 indicates the local Nu distributions along the curvilinear axis on the target surface. The CFD results of this work have been compared with the available data of Fenot et al. (2008). The difference between the experiment and corresponding values of CFD data is approximately 15% on average. The agreement between the two is very good and closely followed the same trend as the experimental data. It can be concluded from the evaluation of the turbulence model with regard to the predictions of heat transfer that the computational model (discretization, numerical scheme, turbulence model) represents a good compromise between the accuracy of its results and the computational effort.
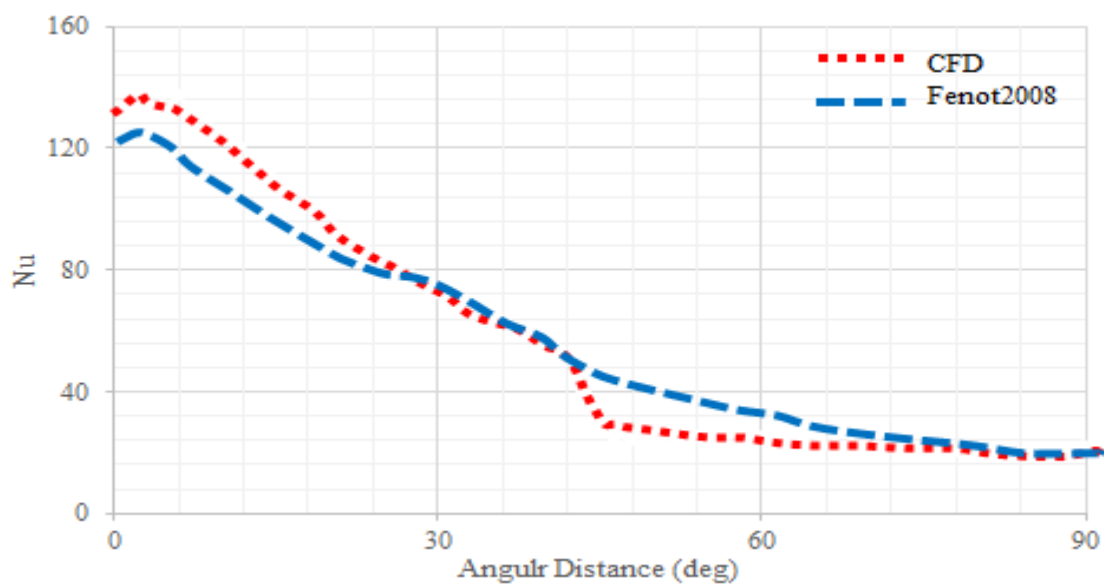
Fig. 6.5 Comparison of the local Nu distributions along curvilinear axis on target surface from experiments and CFD (H/d=5, S/d=4, Re = 23,000, Cr=1.0 and VR=0)

6.3.3 Effect of Chord Length
6.3.3.1 Effect on Heat transfer from Single Row

The variation of relative curvature of 0.1, 0.2, 0.4 is brought about by varying the chord length of impingement surface ($2 \times R_2$) and maintaining the height of the impingement surface (R_1=20mm). Figure 6.6 compares the effect of relative curvature on the total average Nusselt number on the target surface from CFD. It can be concluded from Fig. 6.6 that the average heat transfer increases with the increase of the relative curvature (Cr), because the higher relative curvature, which has lower chord length, leads to the lower surface area.
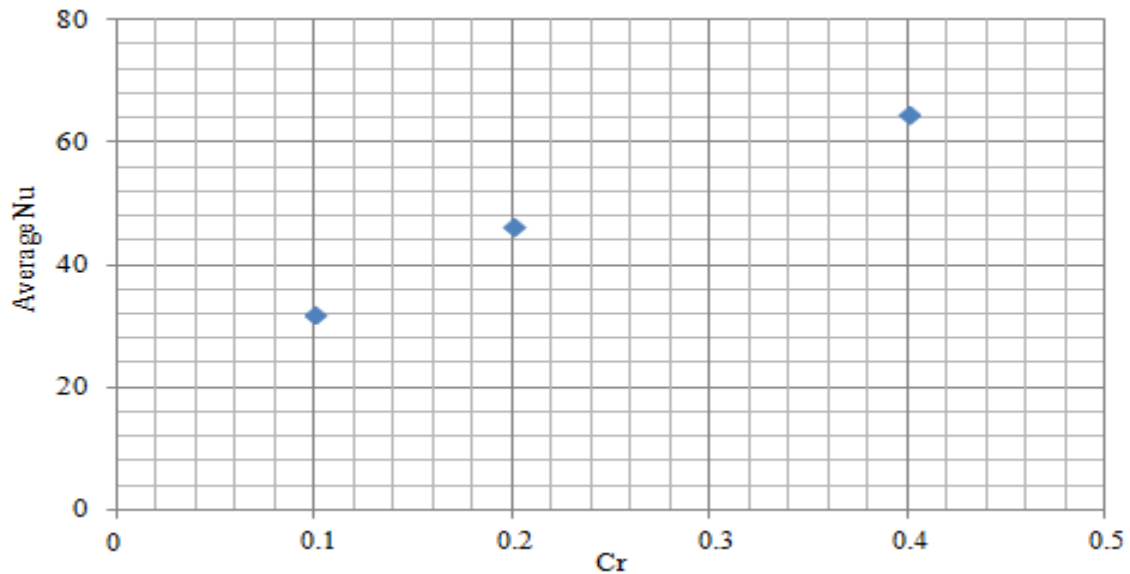
Fig. 6.6 Comparison of the effect of relative curvature on the total average Nusselt number on the target surface (H/d=5, S/d=2, Re = 23,000, R_1=20mm and VR=0)

The average Nu number varies quite strongly with relative curvature (Cr). For a curved surface, this dependence is generally approximated by power law dependence: Nu_{ave}–$(Cr)^n$, with n depending on several factors such as the nozzle-to-surface distance, jet-to-jet spacing and Re number. By means of least square analysis, a value of n=0.5034 fits the data (Nu_{ave}= $103(Cr)^{0.5034}$). There is not observed any correlation between the average Nu number and relative curvature for comparison as a ratio of height by half of chord length for multiple impinging round jets in the literature. Researchers have usually considered the target surface as a semi cylinder (R_1=R_2) and defined the relative curvature as ratio of jet diameter to surface diameter and based on this definition Chupp et al. (1969), Hrycak et al. (1981a) and Fenot et al. (2008) proposed n= 0.6, 0.402 and -0.085 respectively for a row of round impinging jets on the curved surface.

6.3.3.2 Effect on Pressure Force from Single Row

Fig. 6.7 shows the comparison of pressure force coefficients from a single row for in-line arrays at H/d = 5, S/d=2, Re=23,000 for different relative curvature (Cr). The pressure force coefficient decreases with the increase of the relative curvature, because the higher relative curvature which has a lower chord length leads to the lower surface area. It can be concluded from Figure 6.6 and 6.7 that the chord length of 100 mm has the most heat transfer beside the lowest pressure force coefficient and it is considered for the further investigation.
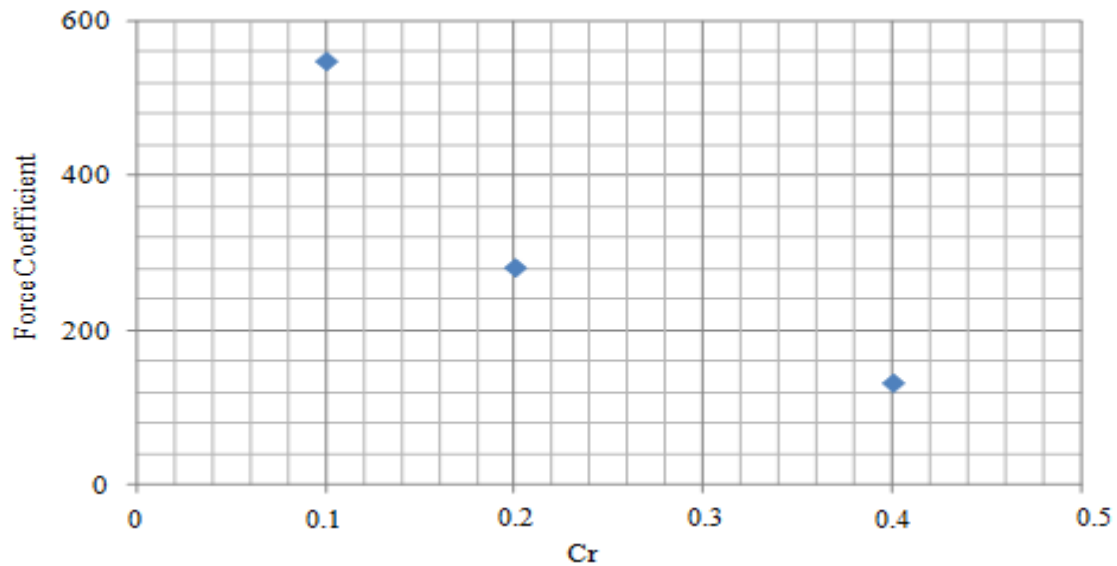
Fig. 6.7 Comparison of pressure force coefficient from CFD for in-line arrays at H/d=5, S/d=2, Re=23,000, R_1=20mm and VR=0 for different relative curvature

6.3.4 Effect of Height of Curved Surface

6.3.4.1 Effect on Heat transfer from Single Row

The variation of relative curvature of 0.0 (flat surface), 0.2, 0.4, 0.6 and 0.8 is brought about by varying the height of impingement surface (R1) and maintaining the chord length of the impingement surface (R_2=50mm). Figure 6.8 compares the effect of relative curvature on the velocity distribution along the curvilinear axis on the target surface from CFD. It can be concluded that the outflow of spent fluid is impeded by the concave curvature and adversely affects the heat transfer. Therefore, the concavity of the target surface produces a sort of confinement (see Figure 6.9).

Figure 6.10 shows the effect of relative curvature on the total average Nusselt number on the target surface from CFD. It can be concluded from Figure 6.10 that for higher relative curvature (Cr), which has a higher height (R_1), the confinement effect reduces the average heat transfer on the target curved surface. There is a small difference between the flat surface (Cr=0) and other relative curvatures (approximately 7.2 % in average). By means of least square analysis, a value of n=-0.081 fits the data (Nu_{ave}= 58.64(Cr)$^{-0.081}$). These results have a correlation with the findings of Fenot et al. (2008), who stated that the relative curvature involves the overall reduction of the Nu number and this effect is probably of the confinement variety. Cr=0.2, i.e. the relative curvature with the lowest height, is the optimum case which satisfies the largest heat transfer rate besides the uniform heat transfer along the target surface (see Figure 6.9 and 6.10).

(a) Cr=0.0

(b) Cr=0.2

(c) Cr=0.4

(d) Cr=0.6

(e) Cr=0.8
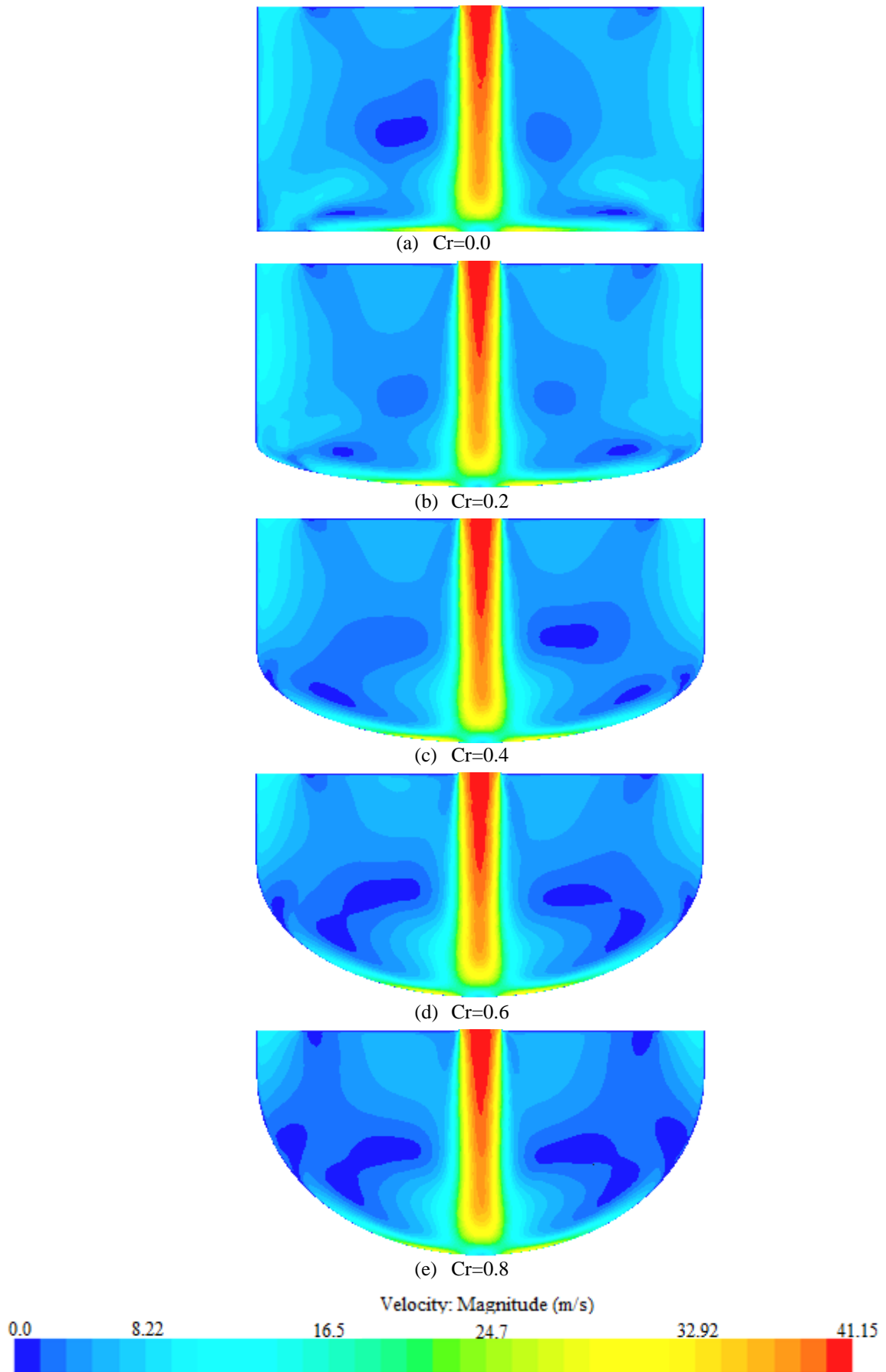
Fig. 6.8 Velocity distribution near the wall jet region for different relative curvature (H/d=5, S/d=2, Re = 23,000, R2=50mm and VR=0)
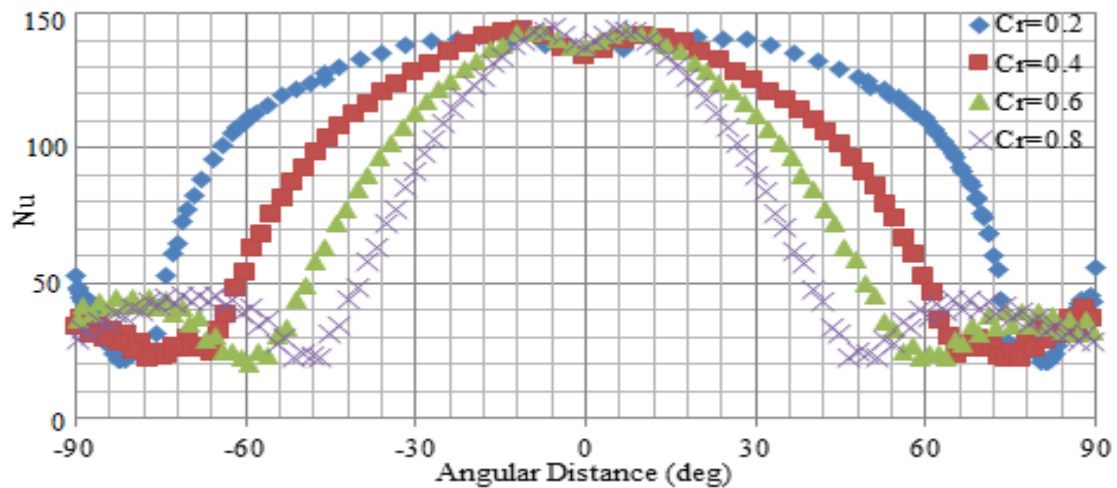
Fig. 6.9 Comparison of the effect of relative curvature on the local Nu distributions along curvilinear axis on target surface from CFD (H/d=5, S/d=2, Re = 23,000, R_2=50mm and VR=0)
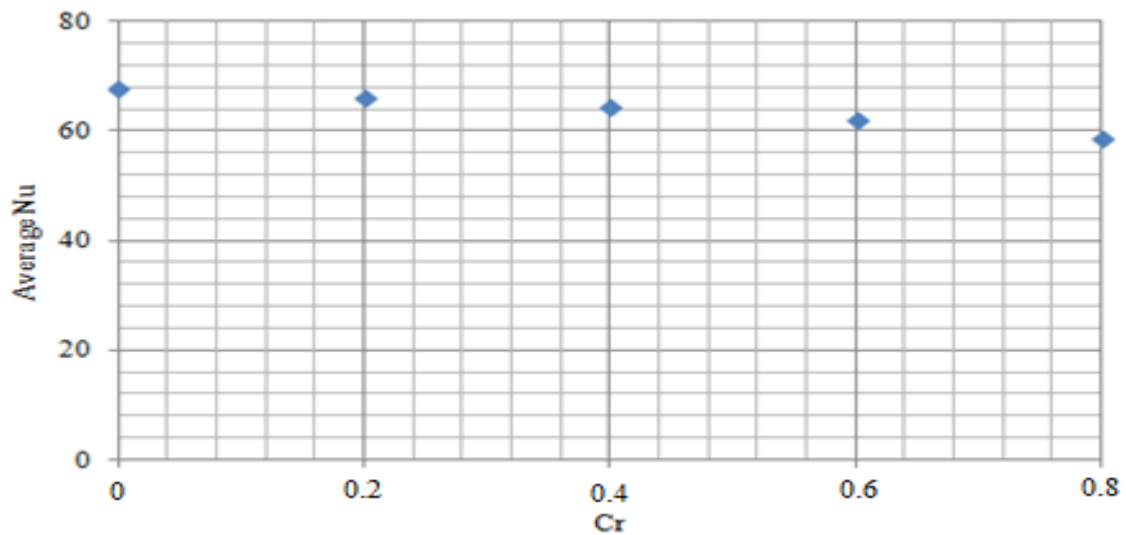
Fig. 6.10 Effect of relative curvature on the total average Nusselt number on the target surface (H/d=5, S/d=2, Re = 23,000, R_2=50mm and VR=0)

6.3.4.2 Effect on Heat Transfer from Multiple Rows

Figure 6.11 shows the contour plot for local Nu distribution for single row in-line and three row in-line configurations for different relative curvature. For the single row case the contours are seen to be stretching more in the outward chordwise direction due to the jet-to-jet interaction in between two neighboring jets. However, for the three row case the stretching is uniform in both chordwise and spanwise direction. As found in many other studies, the stagnation region has the strongest heat transfer for both single and three row cases. However, it was observed that the peak Nu values for three row cases is higher than the single row cases. This slight difference is due to the much larger interaction of the three row cases, which increases the turbulence in the flow and thus improves the heat transfer at the stagnation region

and consequently the averaged Nu number along the Z-centerline (see Fig. 6.12). These results have correlation with the findings of Patil and Vedula (2015).

Cr=0

Cr=0.8
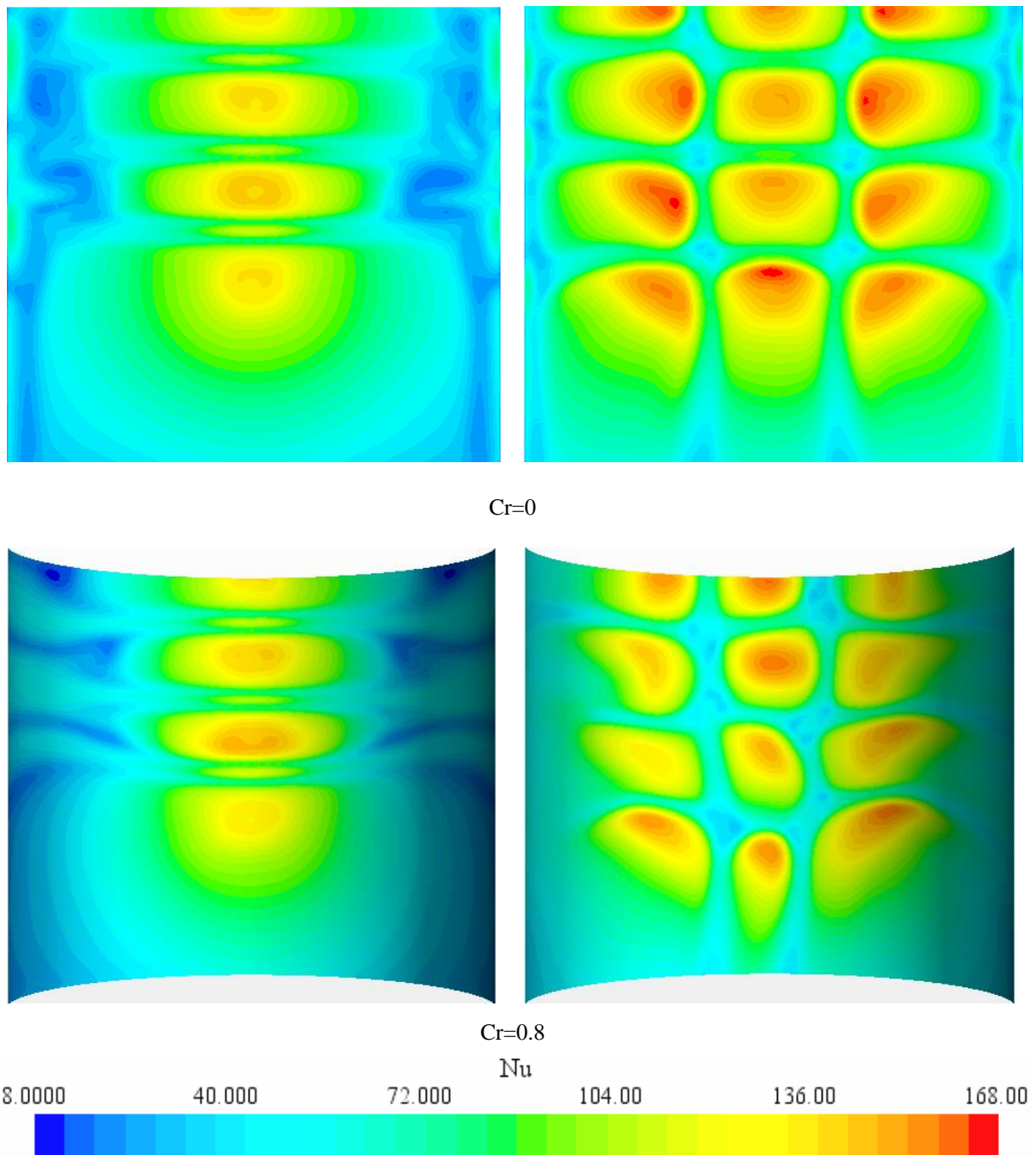
Fig. 6.11 Contour plots for single and multiple rows configuration at H/d = 5, S/d=2, Re=23,000, R2=50mm and VR=0 for different relative curvatures

The averaged Nu number along the Z-centerline (spanwise direction, the line passes the stagnation points) from single and multiple rows (3 rows) is compared for in-line arrays at H/d = 5, S/d=2, Re=23,000 for different relative curvatures (Cr=0 and Cr=0.8). The slope and trends of the CFD predictions are the same for both single and multiple rows. The level of heat transfer

from multiple rows on both flat and curved surface (~116.9) is higher than the single row (~106.5) by approximately 9% on average.

6.3.4.3 Effect on Pressure Force

Fig. 6.12 shows the comparison of pressure force coefficients from the single and multiple rows for in-line arrays at H/d = 5, S/d=2, Re=23,000 for different relative curvature (Cr). The pressure force coefficient from both single and multiple rows decreases with increasing relative curvature, because the higher relative curvature, which has a higher height, leads to lower pressure on the curved surface. The slope and trends of the CFD predictions are the same for both single and multiple rows. The level of pressure force coefficient for multiple rows is lower than the single row by approximately 20% on average due to the stronger wall jet interference and cross-flow effect from multiple rows compared to the single row (see Fig. 6.11).
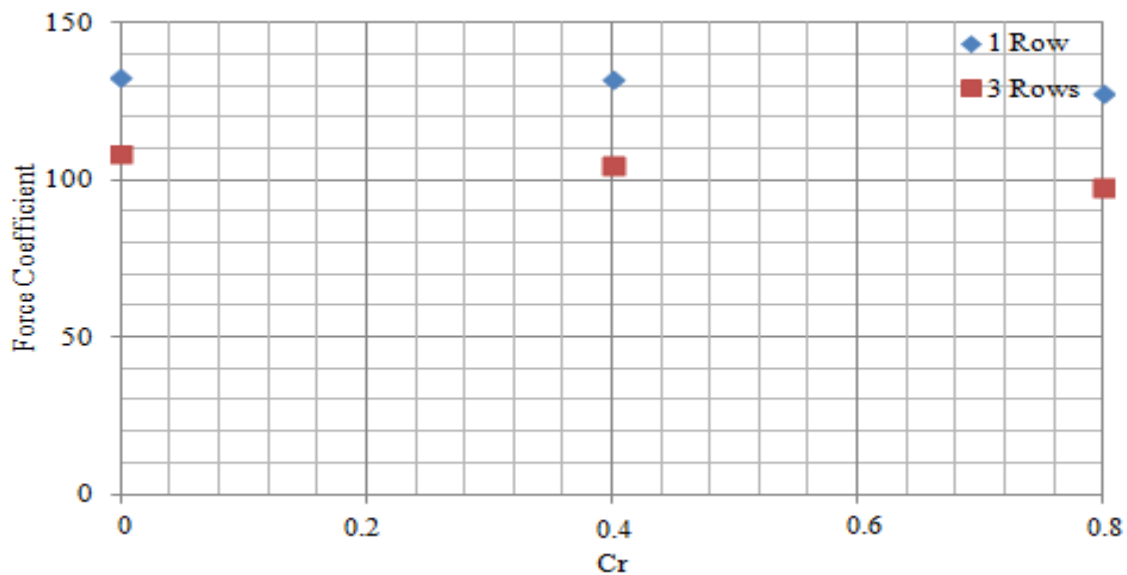
Fig. 6.12 Comparison of pressure force coefficient from CFD for in-line arrays at H/d=5, S/d=2, Re=23,000, R_2=50mm and VR=0 for different relative curvature

6.3.5 Moving Curved Surface

Figure 6.13 shows the geometry of the impinging jet and boundary condition used in the present work for multiple round jets impinging on a moving curved surface. Since there was a negligible difference between different relative curvatures on the pressure force and heat transfer coefficient from both single and multiple rows impinging on a fixed curved surface, the discussion of results could be reduced to only one relative surface curvature (Cr=0.8) in the further investigation. All jet inlets were modeled as circular planes in the top wall. The incoming flow was assumed to have constant fluid properties at T = 298.15K, and entered with

a uniform velocity profile. The value of inlet velocity is so selected that it matches with the Re number over the range of 1980-66200. The target surface, i.e. a moving curved surface, was modeled as a no-slip wall held at a constant temperature $T_w = 60^{\circ}$C. On all other solid surfaces, no-slip with adiabatic wall boundary condition is imposed and on all open boundaries, the constant pressure outlet boundary condition is applied. The movement of the curved surface is considered along curvilinear axe. Symmetric boundary condition was also applied in X-Y plane for the central jet to reduce the computational cost.
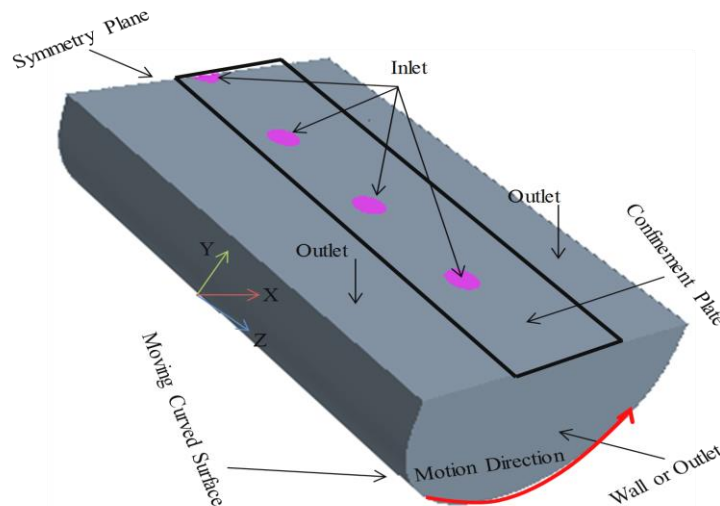
Fig. 6.13 Schematic of the computational domain for moving curved surface

6.3.5.1 Number of Jets

A sketch of the different configurations with in-line arrangement and variation of jet numbers is shown in Figure 6.14. The diameter of each round orifice (d) through a confinement plate with the length over the range of 120mm (3jets), 200mm (5jets), 280 mm (7jets), 520mm (13jets), 1000 mm (25 jets) and 1960mm (49 jets) is 10 mm. All configurations have the same array of 1 row with constant jet-to-jet distance S=4d and jet-to-surface distance H=5d.

(a) 7Jets   (b) 5 Jets   (c) 3Jets
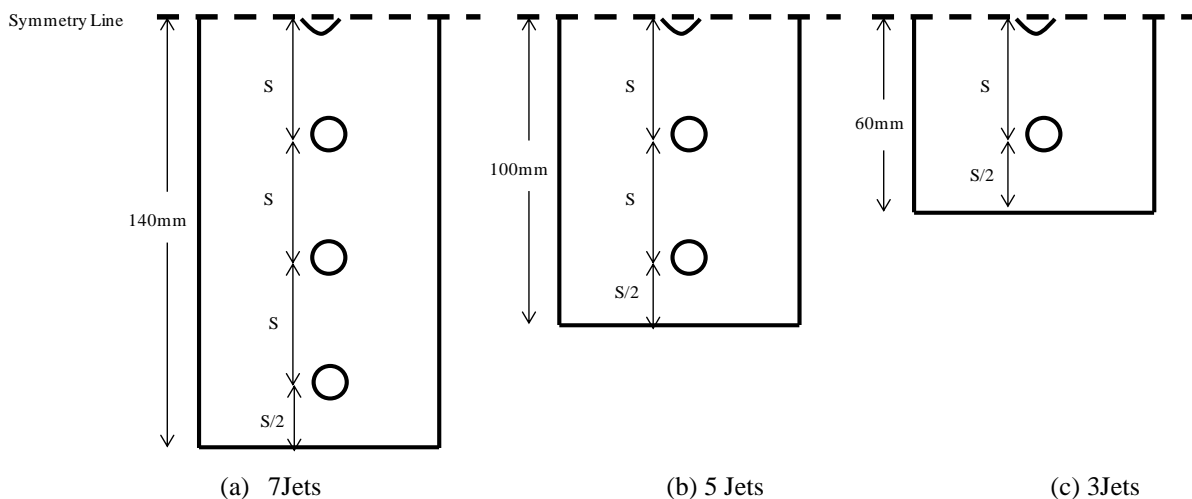
Fig. 6.14 Sketch of the different configurations with in-line arrangement and variation of jet numbers

The predicted Nusselt number distribution on the moving curved surface along the Z axis (the lines pass through the stagnation points of jets) for the multiple impinging jet system for various jet numbers, or indeed for various lengths of dryer, is shown in Figure 6.15. The more the number of jets increases, the stronger the interference of the of wall jets (see Fig. 6.15 at Z/d=6 and 10).
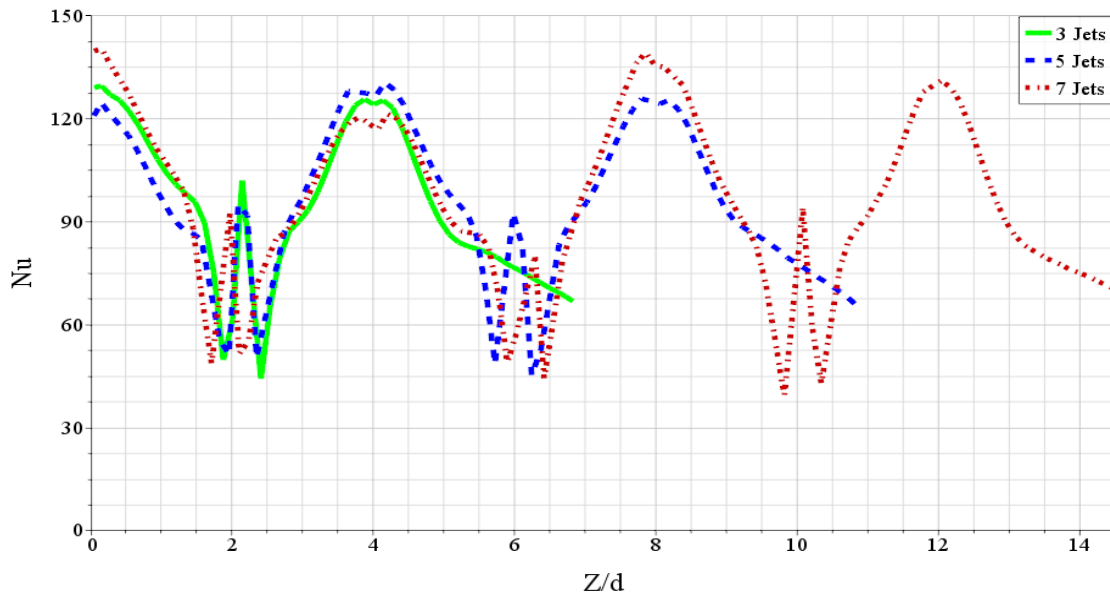
Fig. 6.15 Effects of jet number on the local Nusselt number along Z axis on the moving curved surface from CFD (in-line arrays, Re=23,000, H/d=5, S/d=4, Cr=0.8 and VR=0.28)

Figure 6.16 compares the effect of jet numbers on the total averaged Nusselt number on the moving curved surface from CFD. The results show that the averaged Nusselt number decreases as jet number increases from 120mm (3jets) to 200mm (5jets). There is no difference between other jet numbers, and maximum difference in the total averaged Nu number is around 2 %. This could be attributed to the wall jets interference (see Figure 6.15). For numerical simplification and in order to decrease the number of cells, a length of 120mm (3 jets) is used for future investigations.
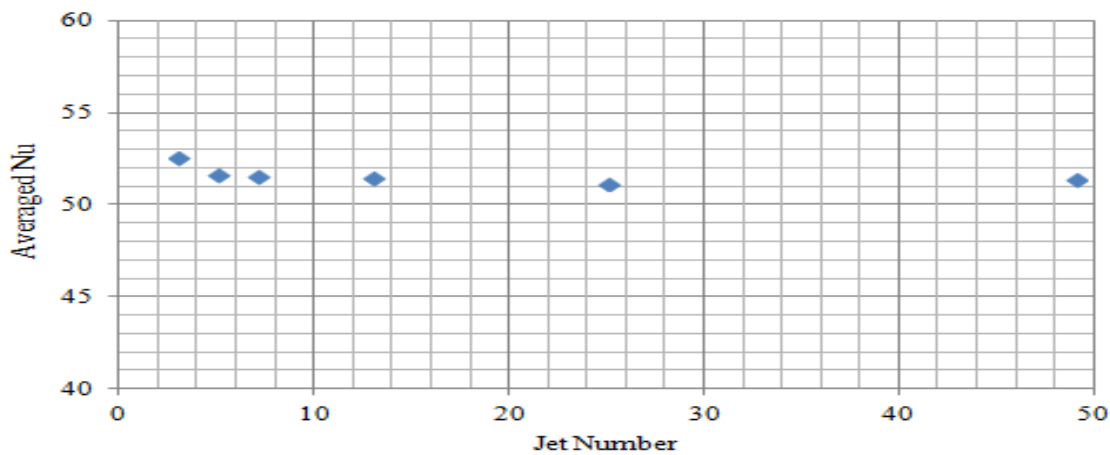
Fig. 6.16 Effects of jet number on the total average Nusselt number on the moving curved surface (in-line arrays, Re=23,000, H/d=5, S/d=4, Cr=0.8 and VR=0.28)

110

6.3.5.2 Number of Jet Rows

Figure 6.17 shows the contour plot for local Nu distribution for single row in-line and three row in-line configurations on the moving curved surface. For the single row case the contours are seen to be stretching more in an outward chordwise direction due to the jet-to-jet interaction in between two neighboring jets. However, for the three row case, the stretching is uniform in both chordwise and spanwise direction. It is observed that the peak Nu values for three row cases is higher than for single row cases. This slight difference is due to the much larger interaction of the three row cases, which increases the turbulence in the flow and thus improves the heat transfer at the stagnation region. These results are similar to the fixed curved surface (see Fig. 6.11).
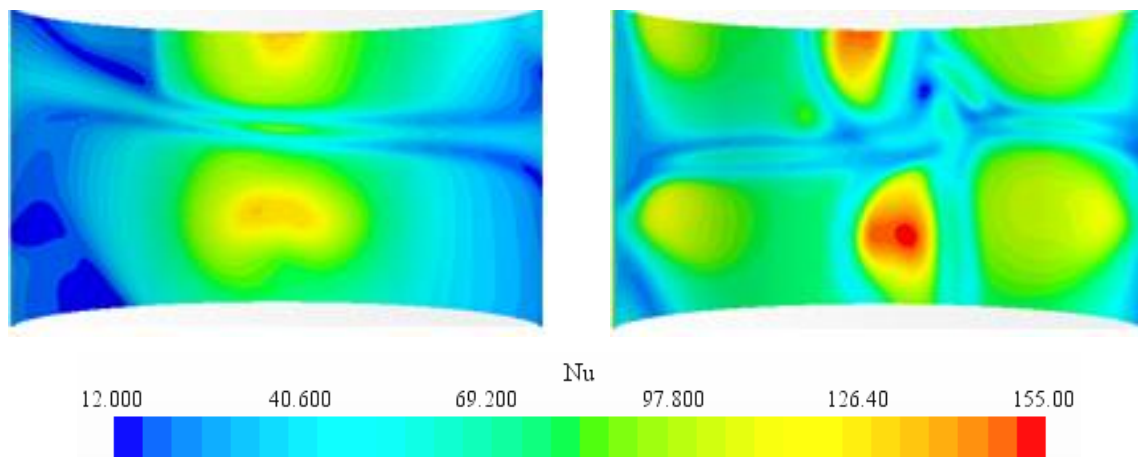
Fig. 6.17 Contour plots for single and multiple row configuration on the moving curved surface (in-line arrays, H/d=5, S/d=4, Cr=0.8 and VR=0.28)

The averaged Nu number along the Z-centerline (the line passes the stagnation points) from single and multiple rows (3 rows) is compared for in-line arrays on the moving curved surface at H/d = 5, S/d=4, Re=23,000, Cr=0.8 and surface velocity=10m/s. The level of heat transfer for single rows (=92.85) is higher than the multiple rows (=87.2) by approximately 6%. This can be attributed to the more powerfully associated cross-flow from multiple rows and surface motion, the heat transfer performance is considerably more dependent upon the number of rows on the moving surface (see Figure 6.17). Consequently, in terms of average heat transfer rates, increasing the number of rows degrades the performance. It was expected that the interaction might increase the turbulence in the flow and thus improve the heat transfer. However, the increase in the cross-flow apparently overweighs the other changes. There is observed the minor difference in the averaged Nu along Z-centerline between the single row and multiple rows.

6.3.5.3 Jet Arrangement

The arrays of jet arrangements as the in-line arrangement in (a) and the staggered arrangement in (b) are shown in Figure 6.18. The diameter d of each round orifice through a confinement plate of 120 mm length is 10 mm. Both jet arrangements have the same array of 1 row with 3 jet holes with constant jet-to-jet spacing S=4d and jet-to-surface distance H=5d. Note that due to symmetry, only half of the confinement plate is presented.

Symmetry line

(a)   (b)
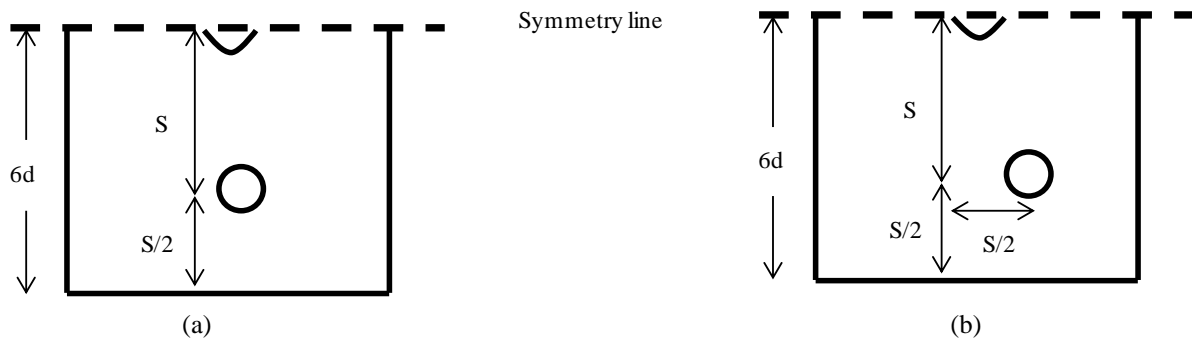
Fig. 6.18 Sketch of jet arrangement: (a) In-line arrangement and (b) staggered arrangement.

The contours of local Nusselt number on the moving flat and curved surface for the in-line and staggered arrangements are shown in Figure 6.19 and 6.20. It can be concluded from the literature for fixed flat surface [Xing&Weigand (2010), Wae-hayee et al. (2013)] that, for the in-line pattern, the jets are protected from the oncoming cross-flow by the upstream jets. For the staggered arrangement, the cross-flow influences the jets more directly, which causes stronger diffusion and leads to a reduced overall heat transfer performance. This trend can be observed for moving flat surface (see Figures 6.19 and 6.21), but this trend contrasts with the findings for moving curved surface. This could be attributed to the effect of the surface curvature. Confinement is one effect of the surface curvature and the staggered arrangement seems to decrease the effect of confinement (see Figures 6.19 and 6.21). However, there is a minor difference between the in-line and staggered arrangement on both the moving flat and the curved surface (see Figure 6.21). The in-line arrangement has a more uniform heat transfer distribution compared to the staggered arrangement for both moving flat and curved surface (see Figures 6.19 and 6.20). In the following, the in-line arrangement is considered for further investigation.

(a) In-line Arrangement   (b) Staggered Arrangement

Nu
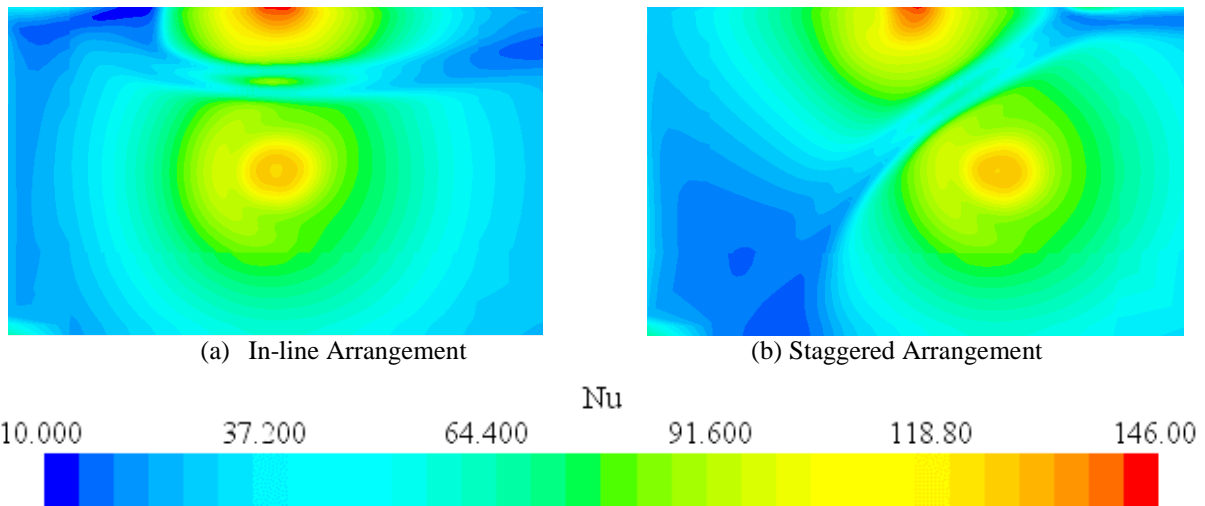
Fig. 6.19 Nu distributions on the moving flat surface for Re=23,000, H/d=5, S/d=4, Cr=0 and VR=0.28

(a) In-line Arrangement   (b) Staggered Arrangement

Nu
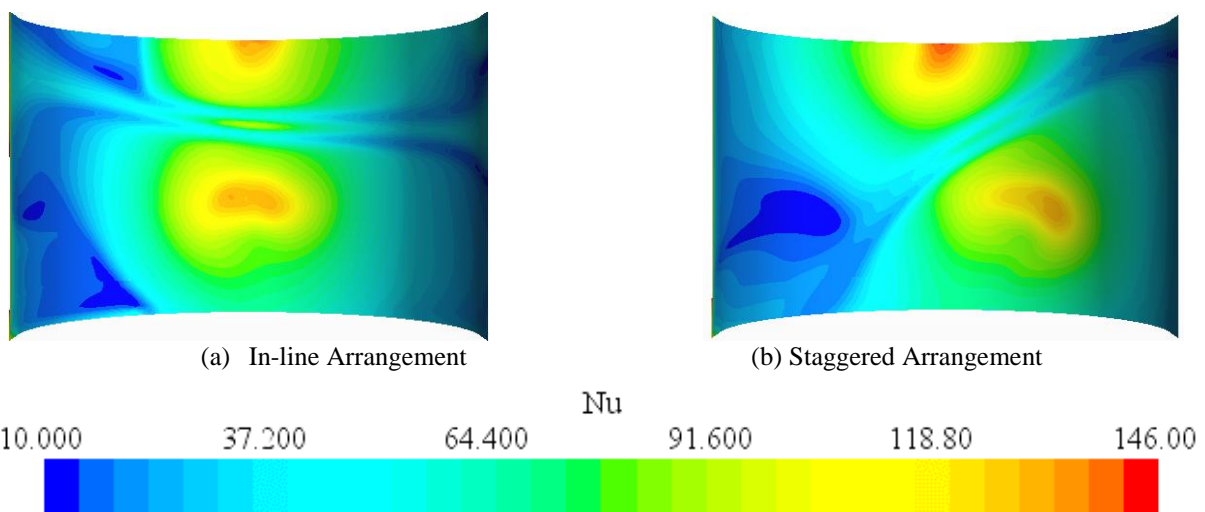
Fig. 6.20 Nu distributions on the moving curved surface for Re=23,000, H/d=5, S/d=4, Cr=0.8 and VR=0.28
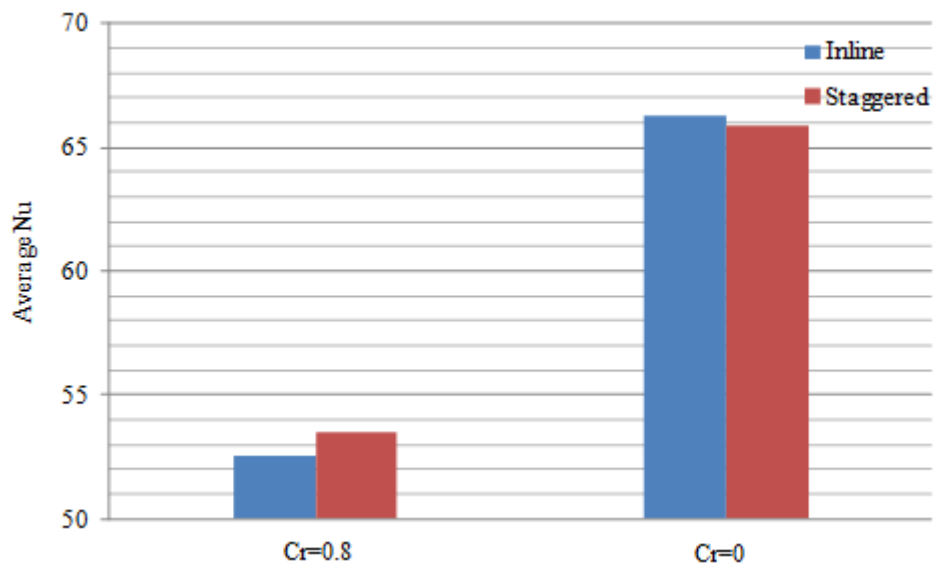
Fig. 6.21 Comparison of total average Nusselt numbers from CFD for different nozzle arrangements at H/d = 5, S/d=4, Re=23,000 and VR=0.28

6.3.5.4 Effect of Cross-flow

In the dryer application, there are two possibilities for the boundary condition in the front side of the dryer (see Figure 6.13). The selection of these boundary conditions, which are either the adiabatic wall boundary condition (equivalent to the wall of computational domain coinciding with the side walls of the dryer) or the pressure outlet (equivalent to a sufficiently large gap between the sheet and the side wall of the dryer), is dependent on the length of material being dried. It is very important to know how big the differences between both boundary conditions are. The contours of the local Nusselt number on the moving curved surface for both possible boundary conditions are shown in Figure 6.22.

| (a) Adiabatic wall | (b) Pressure outlet |

Nu

| 8.0000 | 34.400 | 60.800 | 87.200 | 113.60 | 140.00 |
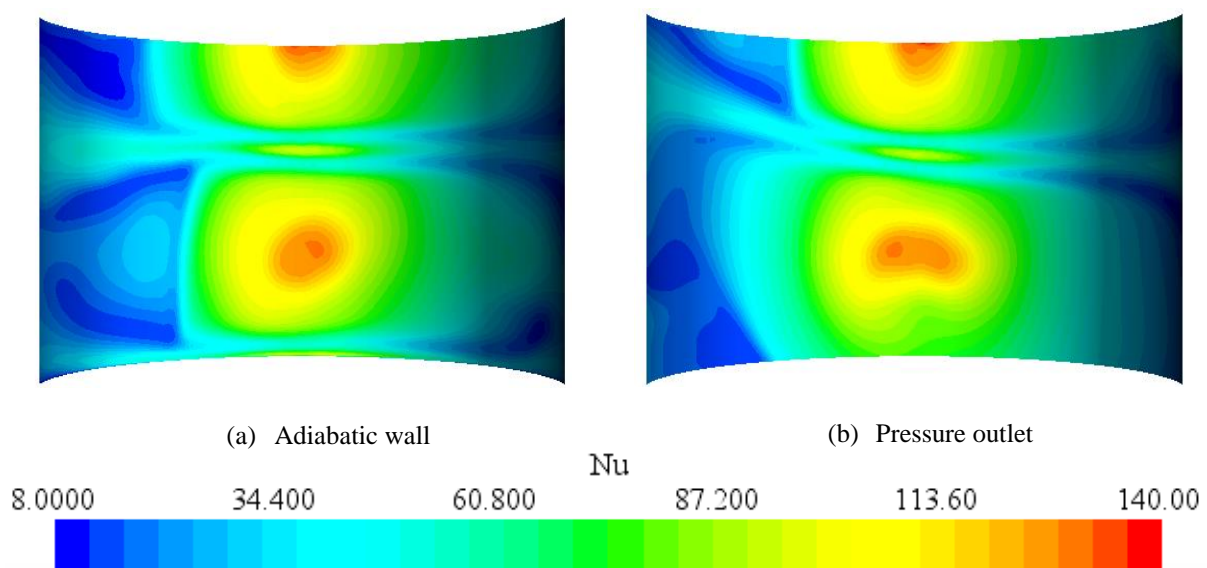
Fig. 6.22 Nusselt number distributions on the impingement surface for different boundary conditions at Re=23,000, H/d=5, S/d=4, Cr=0.8 and VR=0.28

If the wall or pressure outlet boundary condition on the front side of geometry is imposed, an intermediate and minimum cross-flow scheme is observed respectively (see Figure 6.22). The cross-flow is formed by the spent air of the jets, and its strength is based on the outflow design as displayed in Fig. 3.4. The total average Nu number for the boundary condition as adiabatic wall or pressure outlet is 50.62 and 52.57 respectively and the maximum difference is approximately 3.5%. The minimum cross-flow scheme performs as best design with regard to the magnitude and uniformity in heat transfer. Thus, the pressure outlet boundary condition in the front side of the dryer was considered for further investigation.

6.3.5.5 Surface Motion

6.3.5.5.1 Effect on Heat Transfer

Figure 6.23 compares the effect of velocity ratio of the moving surface to the jet velocity (VR) equal to 0, 0.0047 (surface velocity=0.17), 0.047(surface velocity=1.7) and 0.28 (surface velocity=10) on the total average Nusselt number on the moving flat and curved surface from CFD. For small velocity ratio (VR=0.0047 and 0.047), the motion has little effect on the total averaged Nu number on both flat and curved surface. It can be seen that the total averaged Nu on both flat and curved surface reduces with increase in the velocity ratio. Thus, the moving surface reduces the effectiveness of each individual jet and the observed Nusselt number decreases, the surface motion effects become more pronounced as the velocity ratio increases. Chen et al. (1994) and Chattopadhyay (2006) confirm this observation for moving flat surfaces. The slope of the averaged Nu number on the moving flat surface is sharper than the moving curved surface and the total averaged Nu number for the moving flat surface is higher than the moving curved surface. Both matters can be attributed to the effect of confinement. However, the higher velocity ratio helps to achieve more uniform heat transfer distribution on both moving flat and curved surfaces (see Figure 6.24 and 6.25).
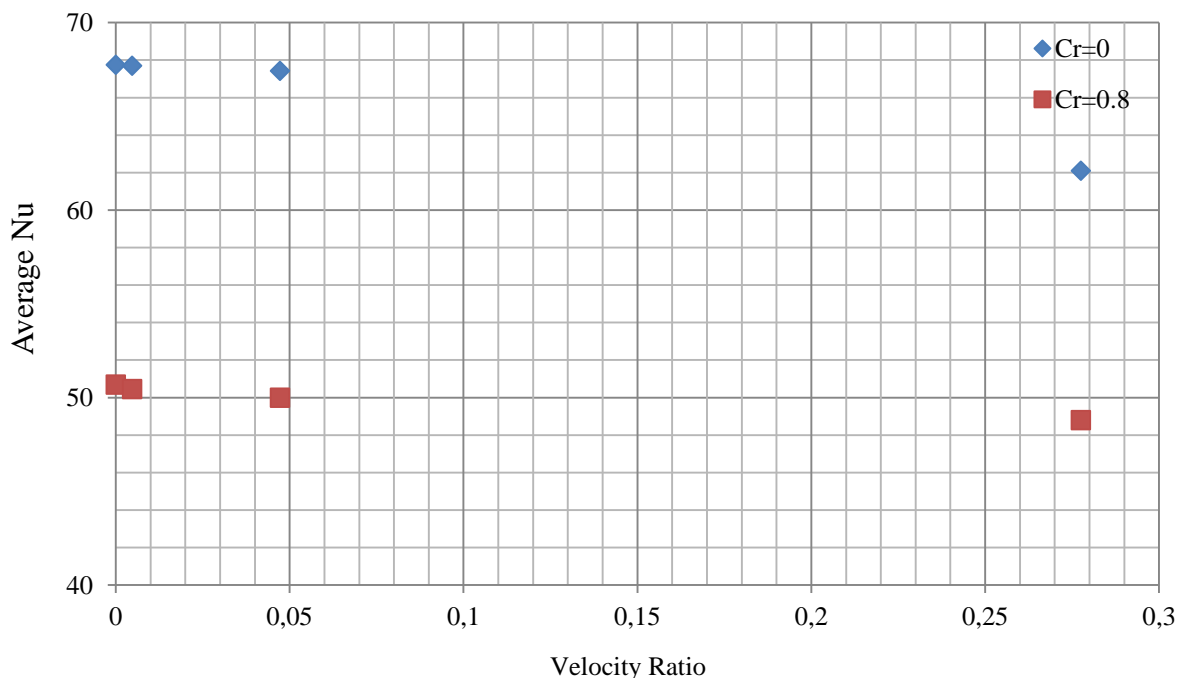
Fig. 6.23 Effects of velocity ratio on the total average Nusselt number on the moving flat and curved surfaces (in-line arrays, H/d=2, S/d=4, Re=23,000)

(a) VR=0   (b) VR=0.047   (c) VR=0.28

Nu

3.0   29.8   56.6   83.4   110.2   137.0
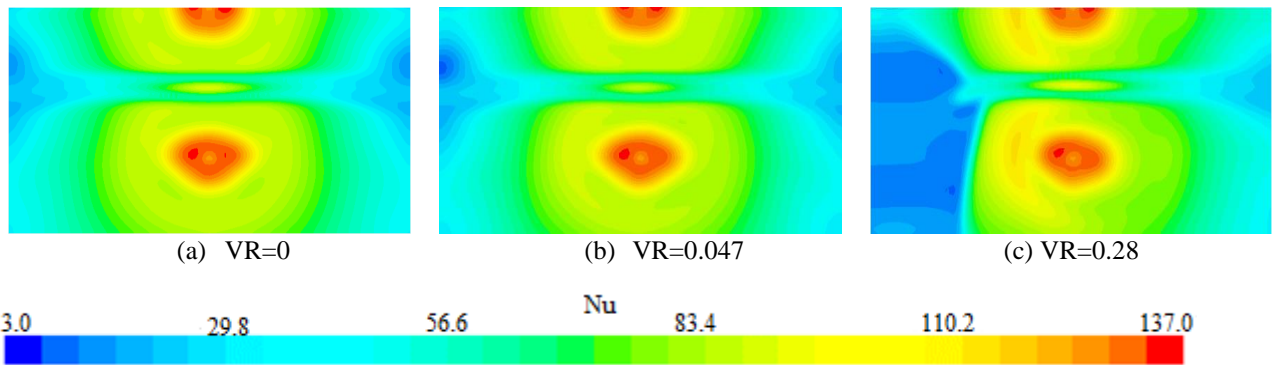
Fig. 6.24 Nusselt number distributions on the moving flat surface for different velocity ratio at Re=23,000, H/d=2, S/d=4and Cr=0

(a) VR=0.0   (b) VR=0.047   (c) VR=0.28

Nu

3.0   29.8   56.6   83.4   110.2   137.0
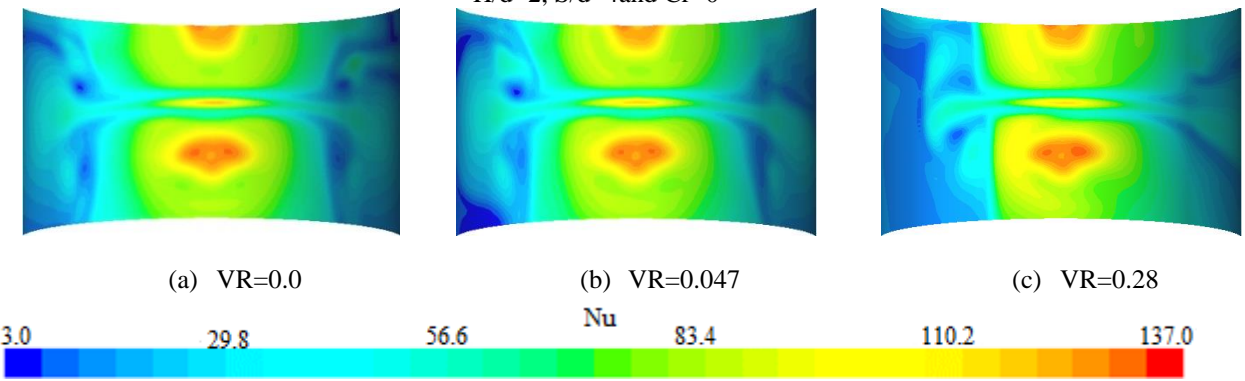
Fig. 6.25 Nusselt number distributions on the moving curved surface for different velocity ratio at Re=23,000, H/d=2, S/d=4 and Cr=0.8

6.3.5.5.2 Effect on Pressure Force

Figure 6.26 compares the effect of velocity ratio on the pressure force coefficient on the moving flat and the curved surface from CFD. When the velocity ratio increases, the pressure force coefficient on the moving flat surface reduces due to the decrease in pressure on the moving flat surface. The variation of the velocity ratio has no effect on the moving curved surface. There is a negligible difference in the pressure force coefficient between the moving flat and the curved surface. Therfore, the pressure force is relatively insensitive to the velocity ratio on both moving flat and curved surfaces.
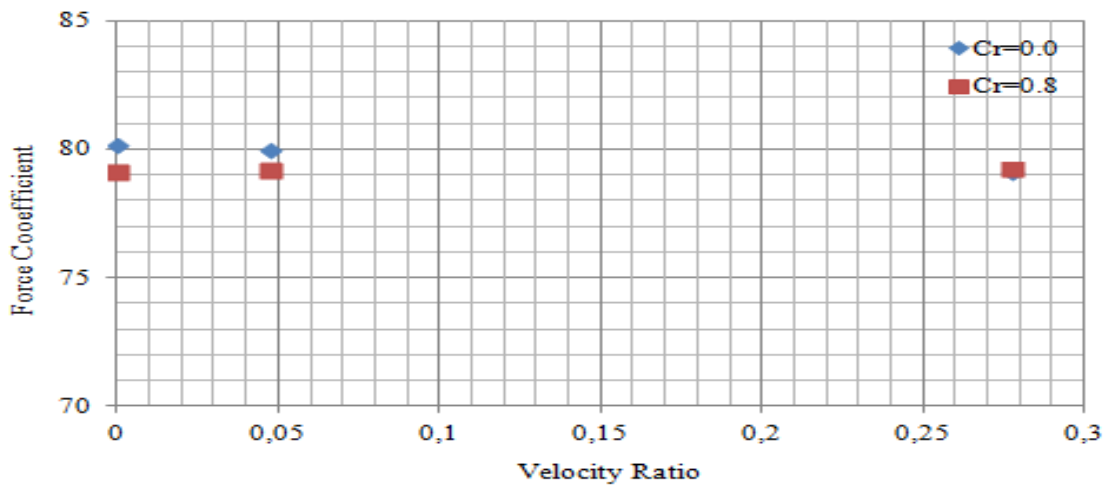
Fig. 6.26 Effects of velocity ratio on the pressure force coefficient on the moving flat and curved surface (in-line arrays, H/d=2, S/d=4 and Re=23,000)

6.3.5.6 Jet Reynolds Number (Re)

6.3.5.6.1 Effect on Heat Transfer

The predicted Nusselt number distribution on the moving flat and curved surface along Z axis (the lines pass through the stagnation points of jets) for the multiple impinging jet system for various Reynolds numbers over the range of Re=1,980-66,200 is shown in Figure 6.27.

(a) Cr=0

(b) Cr=0.8
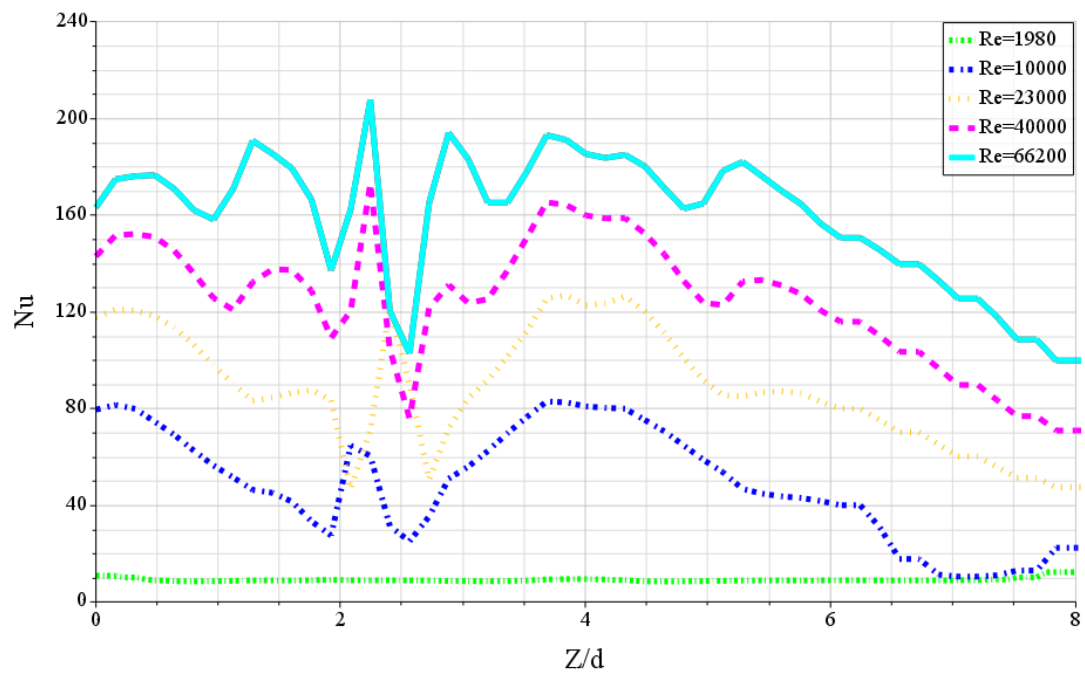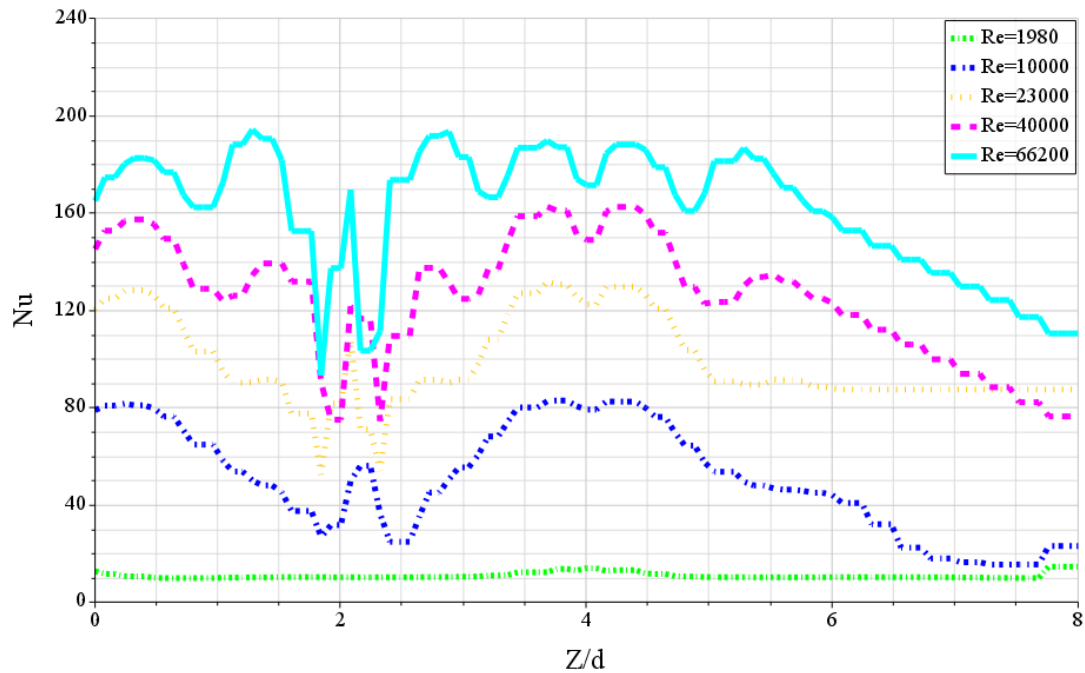
Fig. 6.27 Effects of Re number on the local Nusselt number along Z axis on the moving surface from CFD (in-line arrays, H/d=2, S/d=4 and VR=0.28)

The values of Nusselt numbers are highly dependent on the Reynolds number. When the Reynolds number increases, the stagnation point of jet impingement does not present the maximum heat transfer at high Reynolds number, and this is also reported in other studies. Secondary peaks are also observed at high Re number in Nu distribution of impinging jets. These secondary peaks are attributed to the transition from stagnation zone to wall jet and are observed relatively closer to the stagnation point. However, the secondary peaks near the stagnation point are not observed at low Reynolds number (Re<23000). Upwash fountain jets caused by the wall jet interaction have resulted in the local peaks. In fact along the Z axis the Nusselt number variation on the curved surface is nearly the same as on a flat surface. This similarity is normal, since in the Z direction the impingement surface is flat (Fig. 6.27 (a)). It seems that surface curvature reduces the intensity of these local minimum and maximum encountered with jets impinging on the flat surface. This observation has a correlation with the findings of Fenot et al. (2008) for fixed curved surface.

The predicted Nusselt number distribution on the moving flat and curved surface along motion direction for the multiple impinging jet system for various Reynolds numbers is shown in Figure 6.28. Twin peaks in the Nu distribution occur close to the stagnation point as Re increases. This phenomenon is believed to be the consequence of the strong flow acceleration associated with the higher jet velocities. Secondary peaks are also observed in Nu distribution of impinging jets on both moving flat and curved surface. However, the twin peaks near the stagnation point and the local maxima in Nu number distribution on both moving flat and curved surface are not observed at low Reynolds number (Re<23000). The surface motion has no significant effect on the Nusselt number distribution on both moving flat and curved surface at high Reynolds number. In general, the moving surface reduces the effectiveness of each individual jet and the observed Nusselt number decreases from the surface motion effects become more pronounced as the Reynolds number decreases and there is a more uniform heat transfer in both directions especially for jets at low Reynolds number (e.g. Re=1,980 and10,000) on both moving flat and curved surface. In fact along the curvilinear axis, the Nusselt number distribution is nearly the same as on a fixed curved surface at high Re number (see Fig. 6.9). Thus the importance of surface motion to optimize the heat transfer due to an array of impinging jets is reduced at high Reynolds number (Re>10,000).
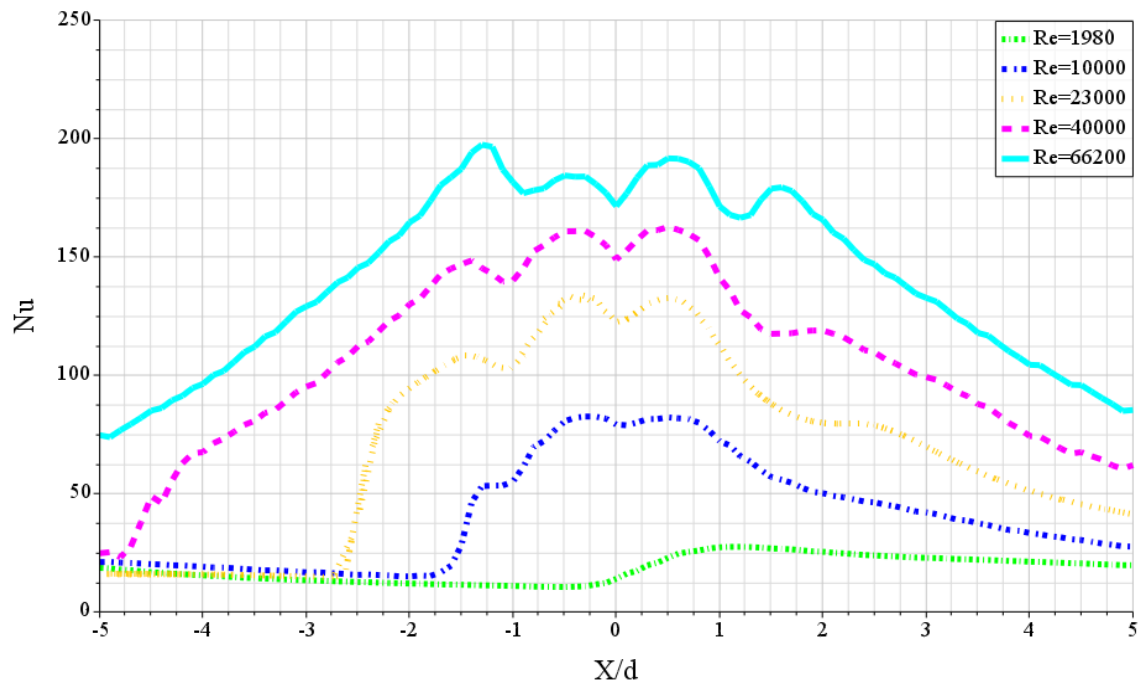
(a) Cr=0
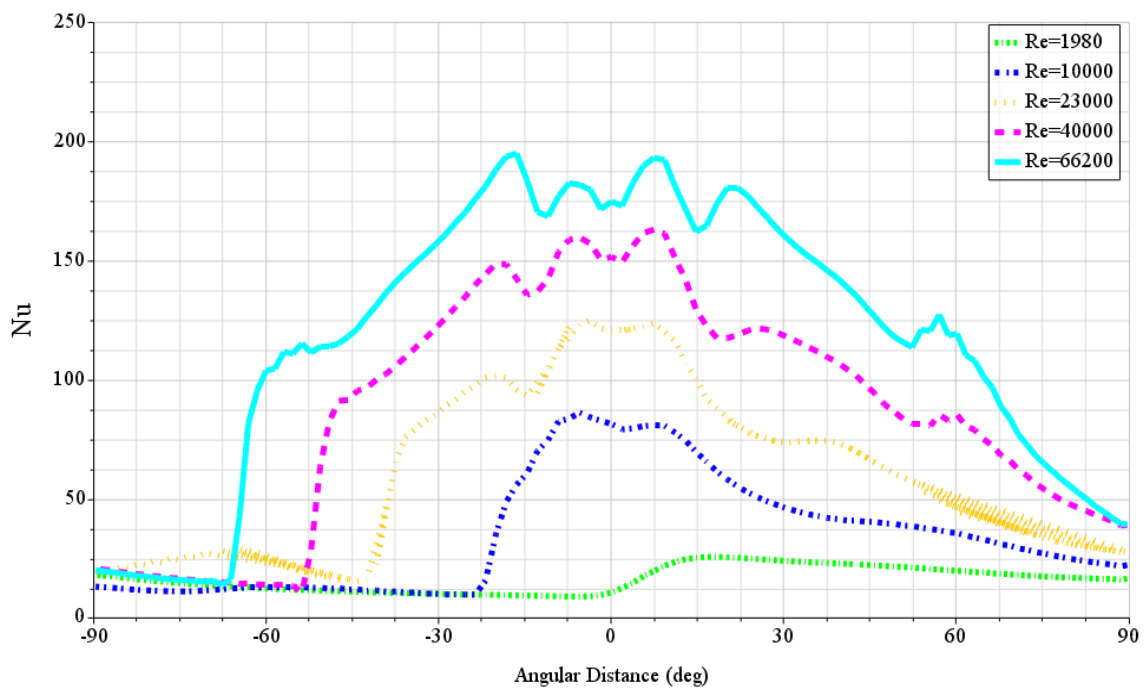
(b) Cr=0.8

Fig. 6.28 Effects of Re number on the local Nusselt number along curvilinear axis on the moving curved surface from CFD (in-line arrays, H/d=2, S/d=4 and VR=0.28)

Figure 6.29 compares the effect of the Reynolds number on the total average Nusselt number on the moving flat and curved surface from CFD. The results show that the Nu number increased as the Re number increased from 1,980 to 66,200. That is because a higher jet Re number corresponds to a higher jet velocity and subsequently a higher turbulence level

contributes greatly to the heat transfer enhancement. This result has correlation with the findings of Ito et al. (2007) for heat transfer on the fixed flat and curved surfaces. The trends and slope of the CFD predictions are the same for both moving flat and curved surface. There is a negligible difference between the moving flat and curved surface in the total average Nu number.
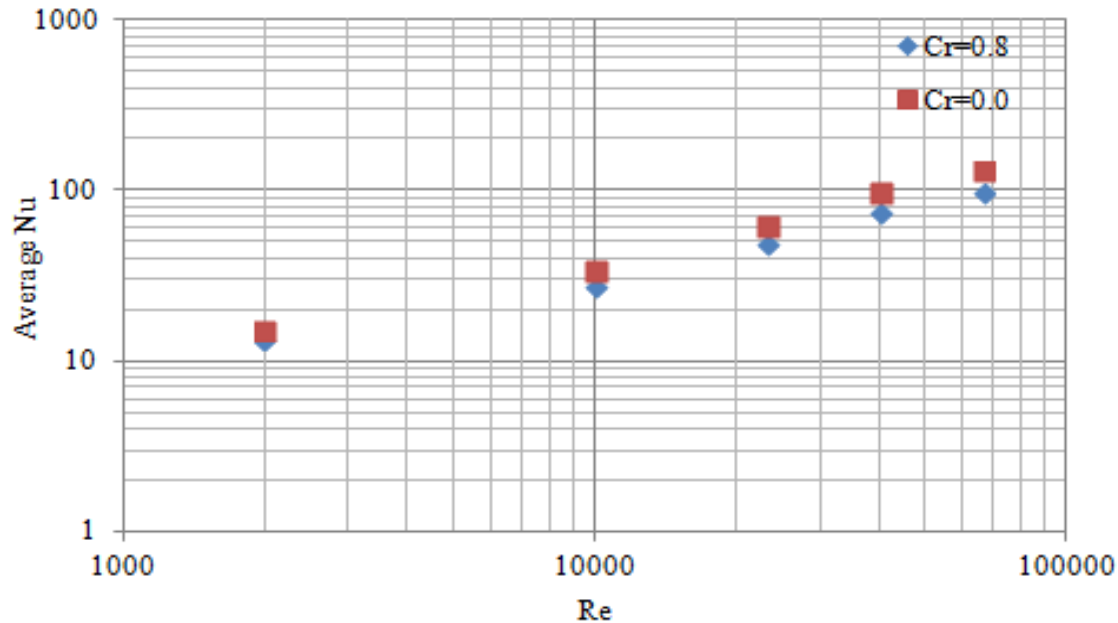
Fig. 6.29 Effects of Re number on the total average Nusselt number on the moving flat and curved surfaces (in-line arrays, H/d=2, S/d=4 and VR=0.28) in logarithmic scale

It is well established that averaged Nu increases with increasing Re following a power law in the form of $Nu \sim Re^{n}$. For the total area averaged Nu number, exponent n has dependency on the geometrical characteristics of the model. In this study, a value of 0.62 and 0.57 was assumed for the moving flat surface and the moving curved surface respectively. In order to test the Reynolds number dependence of the data better, $Nu_{ave}/Re^{0.6}$ is plotted over the Re number in Figure 6.30. As expected, $Nu_{ave}/Re^{0.6}$ is almost independent of the Reynolds number. For the present investigation, this allows the discussion of results to be reduced to only one Reynolds number as results for different Re can easily be obtained from these. Therefore, only the results for Re=23,000 will be presented in detail.
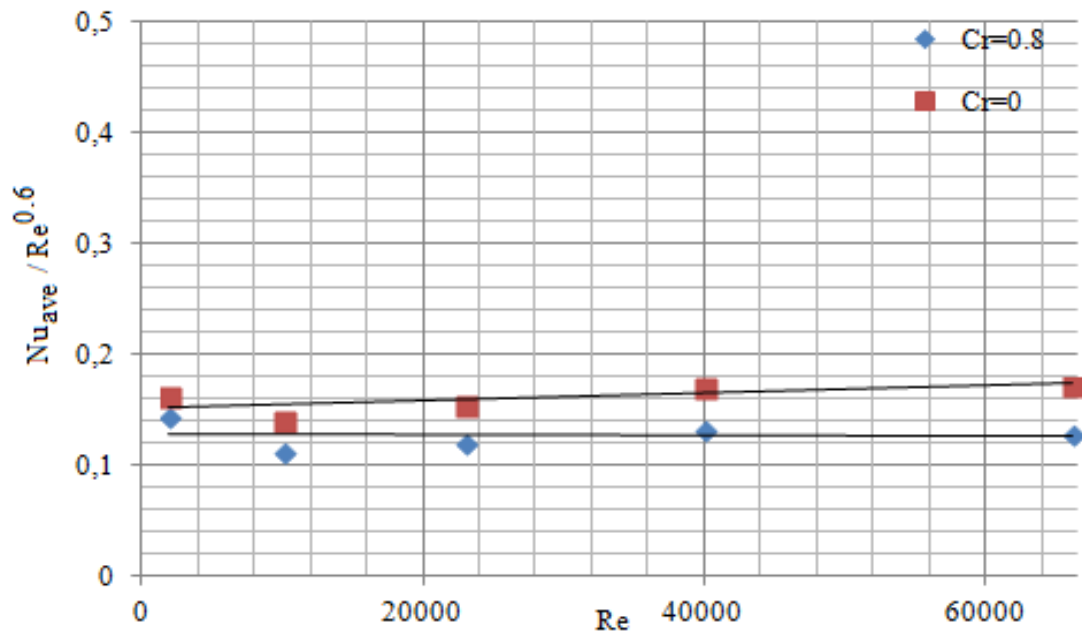
Fig. 6.30 Effects of Re number on the normalized total average Nusselt number on the moving flat and curved surfaces (in-line arrays, H/d=2, S/d=4 and VR=0.28)

6.3.5.6.2 Effect on Pressure Force

Figure 6.31 compares the effect of the Reynolds number on the pressure force coefficient on the moving flat and curved surface from CFD. The pressure force coefficients on both moving flat and curved surfaces are relatively insensitive to the Re number within the range examined. This result has a correlation with the findings of Wang et al. (2015) for single impinging jet on the fixed flat surface. The trend and slope of the CFD predictions are the same for both moving flat and curved surface. There is no significant difference in the pressure force coefficient between the moving flat and curved surface.
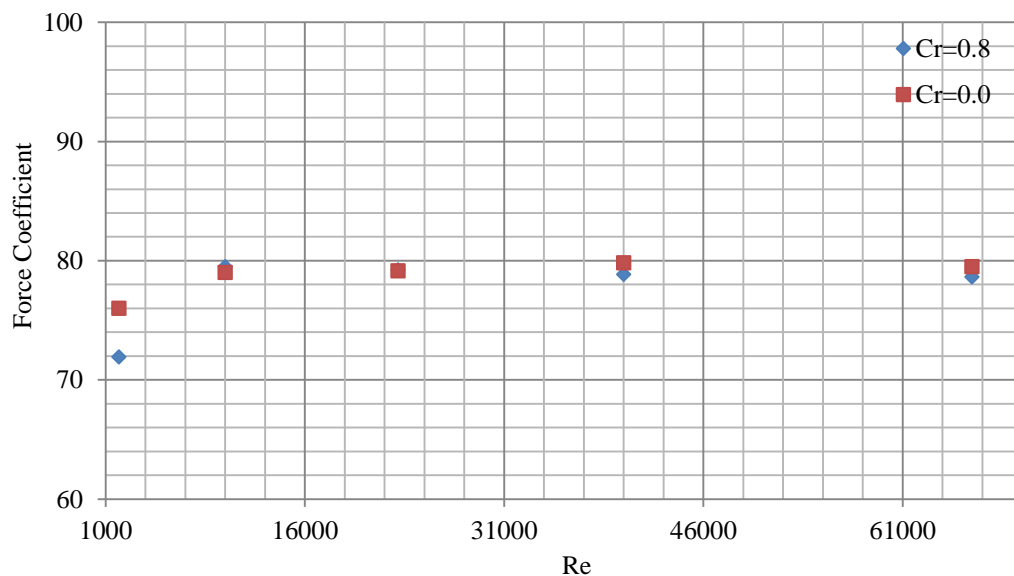
Fig. 6.31 Effects of Re number on the pressure force coefficient on the moving flat and curved surface (in-line arrays, H/d=2, S/d=4 and VR=0.28)

6.3.5.7 Nozzle to Surface Distance (H/d)

6.3.5.7.1 Effect on Heat Transfer

The predicted Nusselt number distribution on the moving flat and curved surface along the Z axis for the multiple impinging jet system for various nozzle-to-surface distances over the range of H/d=1–20 is shown in Figure 6.32. It shows a significant decrease in local Nusselt number distribution along the Z axis, with an increase in the jet-to-surface distance (H/d) due to the increase in the momentum exchange between the jet flow and ambient fluid. The heat transfer coefficient distributions contain the primary and secondary peaks in the stagnation and upwash stagnation zones respectively. However, the effect of H/d on the heat transfer is more striking, especially for the lower value of separation distance (H/d ≤ 5).
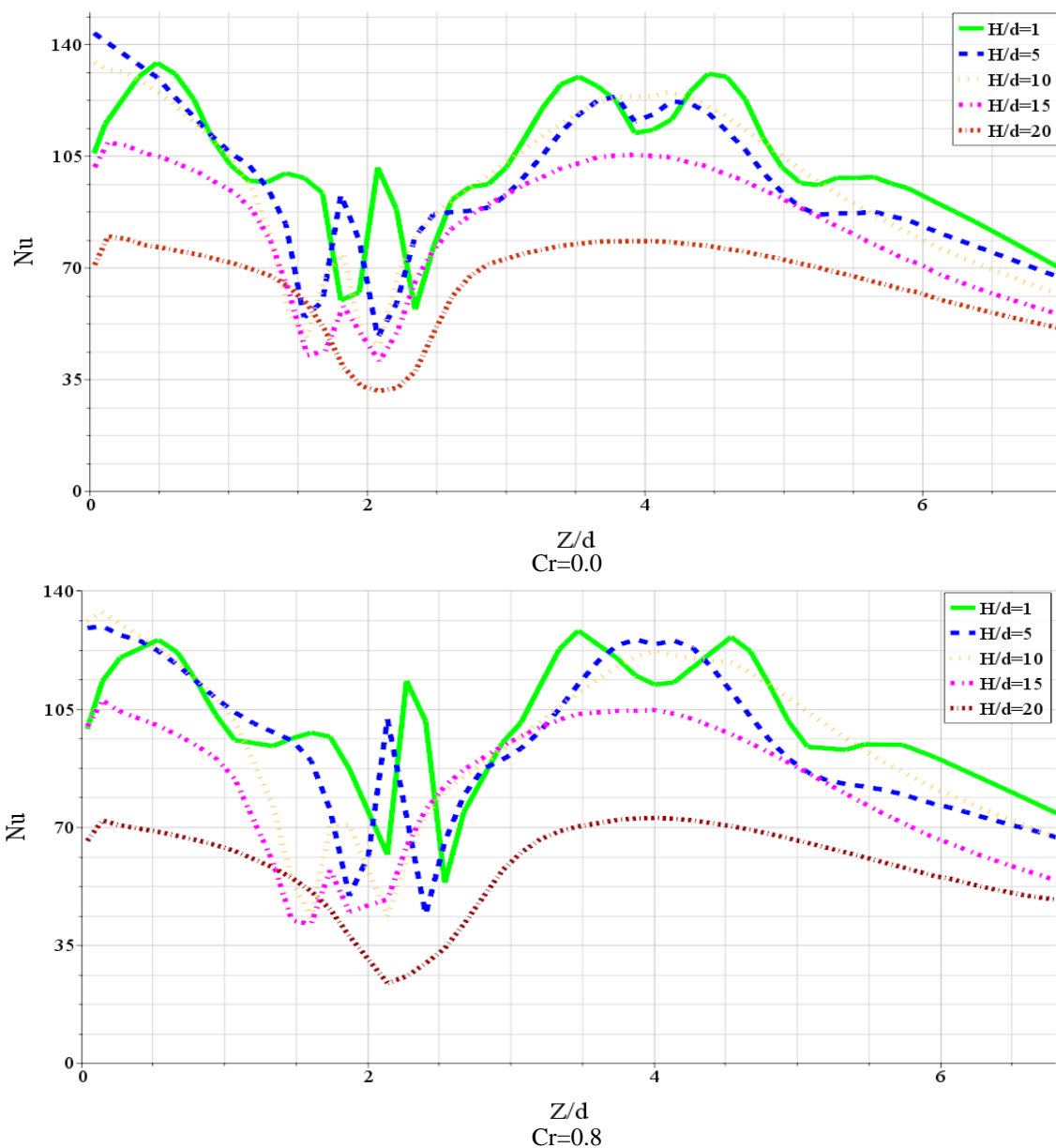
Fig. 6.32 Effects of separation distance on the local Nusselt number along Z axis on the moving flat and curved surface from CFD (in-line arrays, Re=23,000, S/d=4, VR=0.28)

Results show that further reducing the value of H/d to one creates a significant nonuniform distribution in the local Nu number over the target surface. At higher values of separation distance (H/d>5), the upwash fountain is weak, because, with a small separation distance, the jet interaction on the target surface increases significantly and the resulting heat transfer rates can differ substantially. In fact along the Z axis, the Nusselt number variation on the curved surface is nearly the same as on a flat surface. This similarity is normal, since in the Z direction the impingement surface is flat.

(a) Cr=0

(b) Cr=0.8

Fig. 6.33 Effects of separation distance on the local Nusselt number along motion direction on the moving flat and curved surface from CFD (in-line arrays, Re=23,000, S/d=4, VR=0.28)

The predicted Nusselt number distribution on the moving flat and curved surface along motion direction for various separation distances is shown in Figure 6.33. It shows a significant increase in local Nusselt number distribution along motion direction for both moving flat and curved surface with a decrease in jet-to-surface distance. The surface motion has more effect on the Nusselt number distribution on both moving flat and curved surfaces at high separation distance and there is a more uniform heat transfer on both surfaces for jets at high separation distance (H/d=15 and 20). This is because the flow in the case of low H/d (1 and 5) has a bigger impact compared to the higher H/d (see Fig. 5.21). Thus the importance of surface motion to optimize the heat transfer due to an array of impinging jets is reduced when the surface is in the low separation distances (H/d=1-10).

Figure 6.34 compares the effect of separation distance on the total average Nusselt number on the moving flat and curved surface from CFD. The results show that the average Nusselt number increases as H/d decreases due to the decrease in the adjacent jet interference before impingement. When H/d=1, the adjacent jet interference before impingement is minimized and the higher average Nu number is obtained compared to others cases. The average Nusselt number varies quite strongly with the separation distance. The trends of the CFD predictions are the same for both moving flat and curved surfaces. The average Nu number on the moving flat surface is higher than the moving curved surface and the maximum difference has occurred at low separation distance (H/d=1). This could be attributed to the effect of confinement.

Fig. 6.34 Effects of separation distance on the total average Nusselt number on both moving flat and curved surface (in-line arrays, Re=23,000, S/d=4 and VR=0.28)

6.3.5.7.2 Effect on Pressure Force

Figure 6.35 compares the effect of separation distance on the pressure force coefficient on the moving flat and curved surfaces from CFD. There is no significant effect of the curvature on the pressure force coefficient. The pressure force coefficients on the impingement surface were found to be highly dependent on separation distance and the pressure force coefficients always increase with decreasing H/d, because, for larger H/d, the pressure decreases due to the larger entrainment from the jet surroundings. The trend and slope of the CFD predictions are the same for both moving flat and curved surfaces. There is a negligible difference in the pressure force coefficient between the moving flat and curved surface.

Fig. 6.35 Effects of separation distance on the pressure force coefficient on the moving flat and curved surface (in-line arrays, Re=23,000, S/d=4 and VR=0.28)

6.3.5.8 Jet-to-Jet Spacing (S/d)

6.3.5.8.1 Effect on Heat Transfer

A sketch of the different configurations with in-line arrangement and different jet-to-jet spacing are shown in Figure 6.36. The diameter of each round orifice (d) through a confinement plate with the constant length 14d is 10 mm. All configurations have the same array of 1 row with different jet-to-jet distance over the range of S=2d-10d and jet-to-surface distance H/d=2. There is no change in the averaging area among the cases.

(a) S=2d   (b) S=4d   (c) S=6d   (d) S=10d
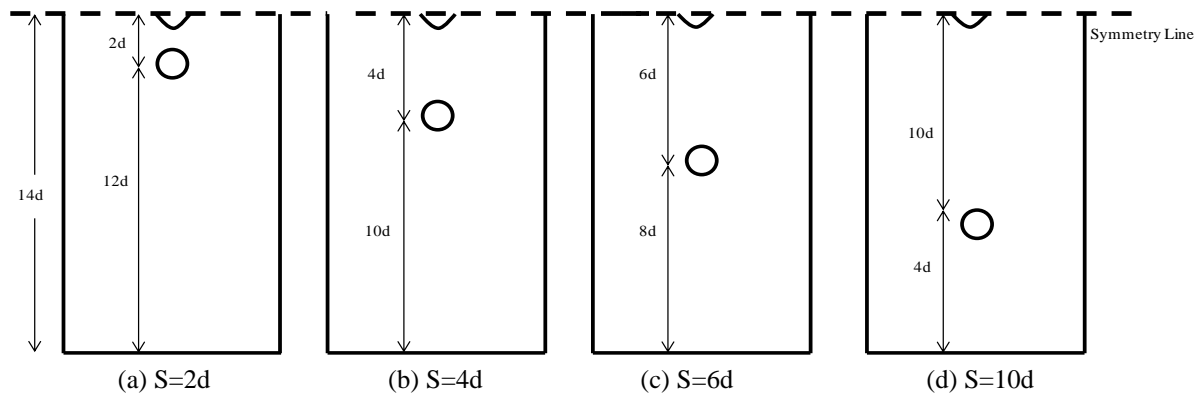
Fig. 6.36 Sketch of the different jet-to-jet spacing

Figure 6.37 shows the predicted Nusselt number distribution on the moving flat and curved surface along the Z axis (the lines pass through the jet stagnation points) for the multiple impinging jet system for various jet-to-jet spacing over the range of S/d=2–10.
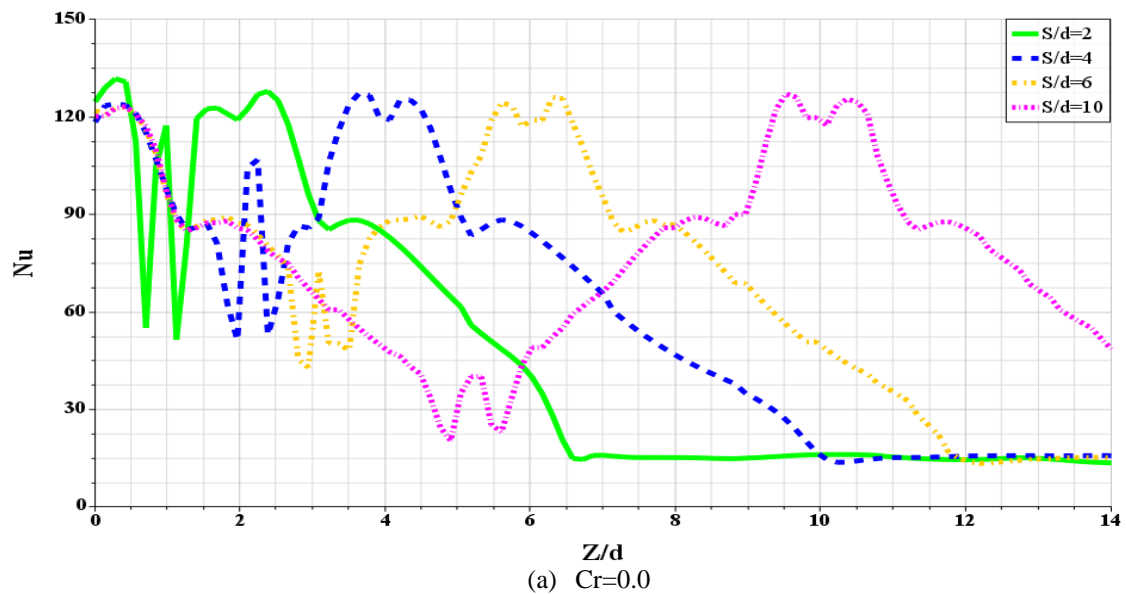
(a) Cr=0.0
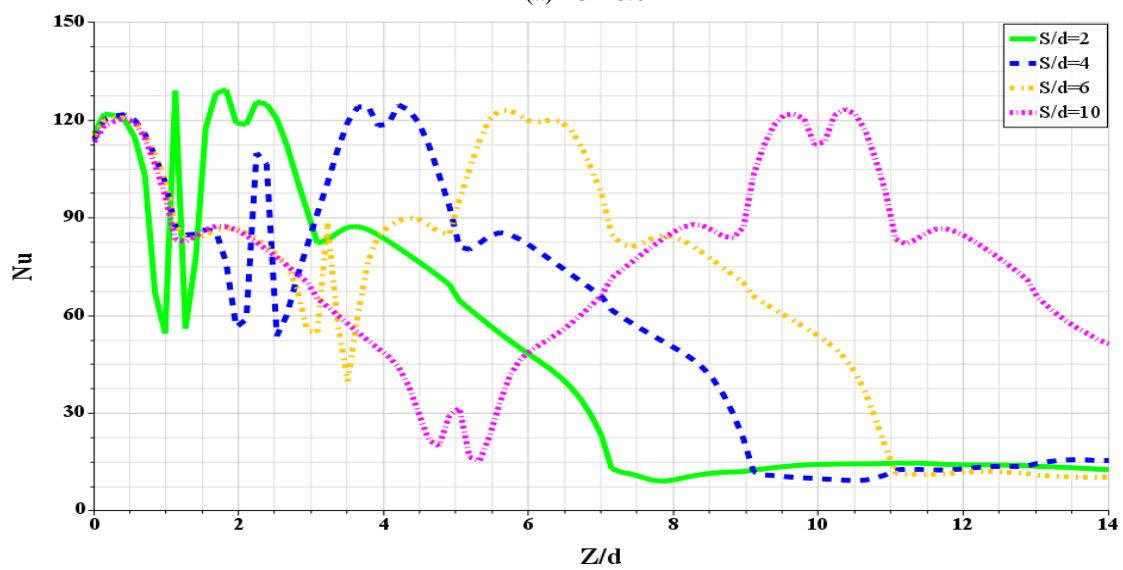
(b) Cr=0.8

Fig. 6.37 Effects of jet-to-jet spacing on the local Nusselt number along the Z axis on the moving flat and cured surface from CFD (in-line arrays, Re=23,000, H/d=2 and VR=0.28)

With decreased the jet-to-jet distances, the jet interaction increases significantly and the resulting heat transfer rates can differ substantially, because the wall flows of the two jets are impinging upon each other and forming a new stagnation region. This affects the stagnation and average distribution of the Nusselt number. However, the jets start to interact for S/d = 2 and 4 and this interaction is more obvious in the case of S/d =2. At a higher value of jet-to-jet spacing (S/d= 10), the jet interaction is very weak, where the jets are effectively not interacting with each other. In fact, the heat transfer distribution along the Z axis is nearly the same as on a flat surface.

(a) Cr=0

(b) Cr=0.8
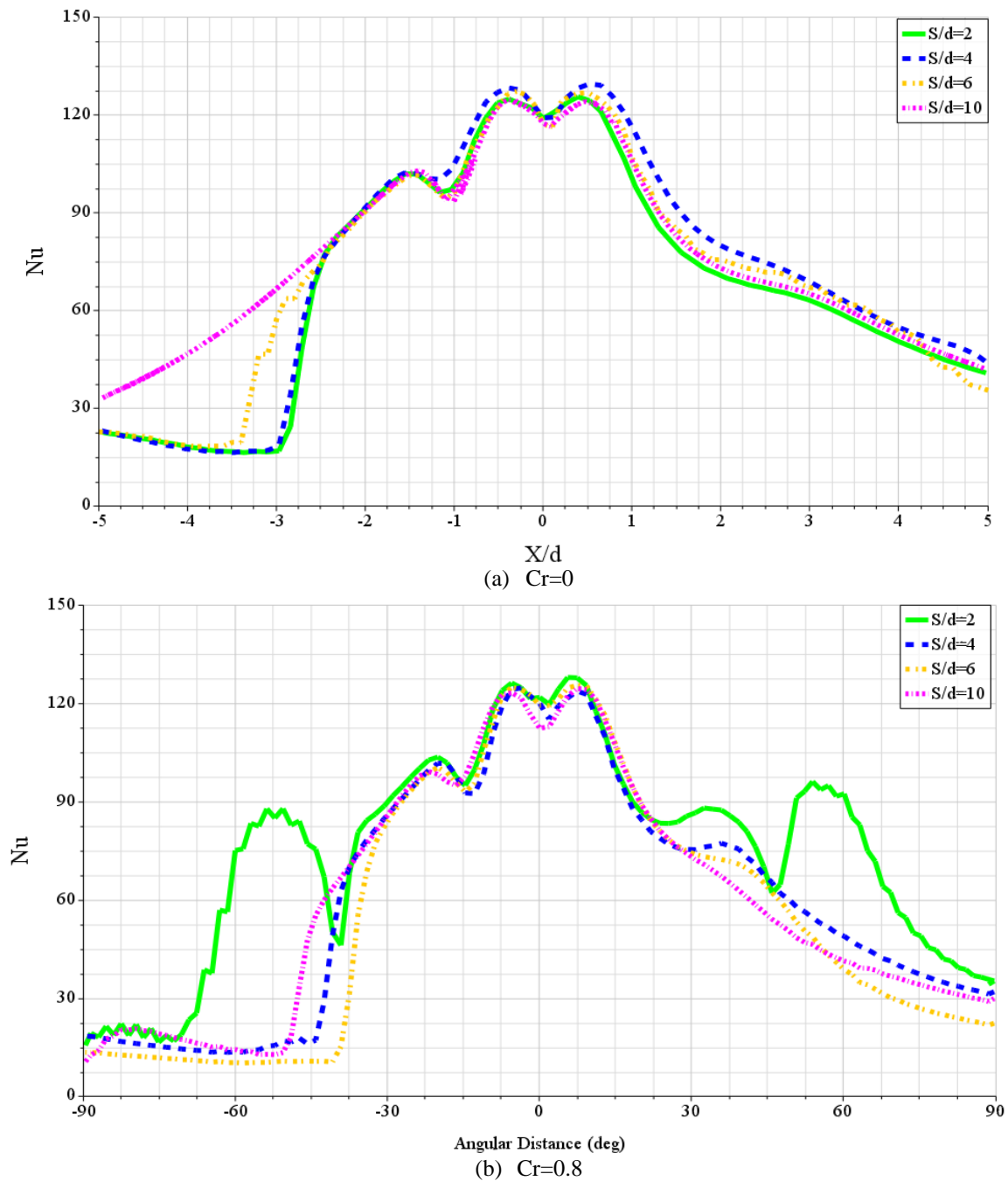
Fig. 6.38 Effects of jet-to-jet spacing on the local Nusselt number along the motion direction on the moving and flat curved surface from CFD (in-line arrays, Re=23,000, H/d=2, VR=0.28)

Figure 6.38 shows the predicted Nusselt number distribution on the moving flat and curved surface along motion direction for various jet- to-jet spacing. The surface motion has more effect on the Nusselt number distribution on both moving flat and curved surfaces at small jet-to-jet spacing, and the heat transfer on both surfaces is more uniform for jets at small S/d. This is because the flow in the case of small S/d has a lower momentum compared to the higher S/d due to the jet interaction, and the surface motion have an effect on the Nu number distribution on both the moving flat and curved surfaces at small S/d, with the exception of S/d=2 on the moving curved surface. This expectation can be attributed to the very complex flow at small S/d on the moving curved surface which results in the heat transfer at the upwash fountain being equal to the heat transfer at stagnation point (see Fig.6.37). However, the Nusselt number distribution along the surface motion is nearly the same as on a fixed flat and curved surface at high jet-to-jet spacing (see Fig.6.9).

Figure 6.39 compares the effect of jet-to-jet spacing on the total average Nusselt number on the moving flat and curved surface from CFD based on an equivalent mass flow rate per unit area. The area-averaged Nusselt number sharply decreases with a decrease in the jet-to-jet spacing in the range of 2–10d. The minimum Nusselt number is found in the lower jet-to-jet spacing (S/d = 2) compared to the other cases. However, as a smaller value of S/d allows for more jet interaction, this affects the average Nusselt number (see Figure 6.37). Trend and slope of the CFD predictions are same for both moving flat and curved surfaces. The magnitude of the average Nu number for moving flat surface is higher than the moving curved surface due to the confinement effect.
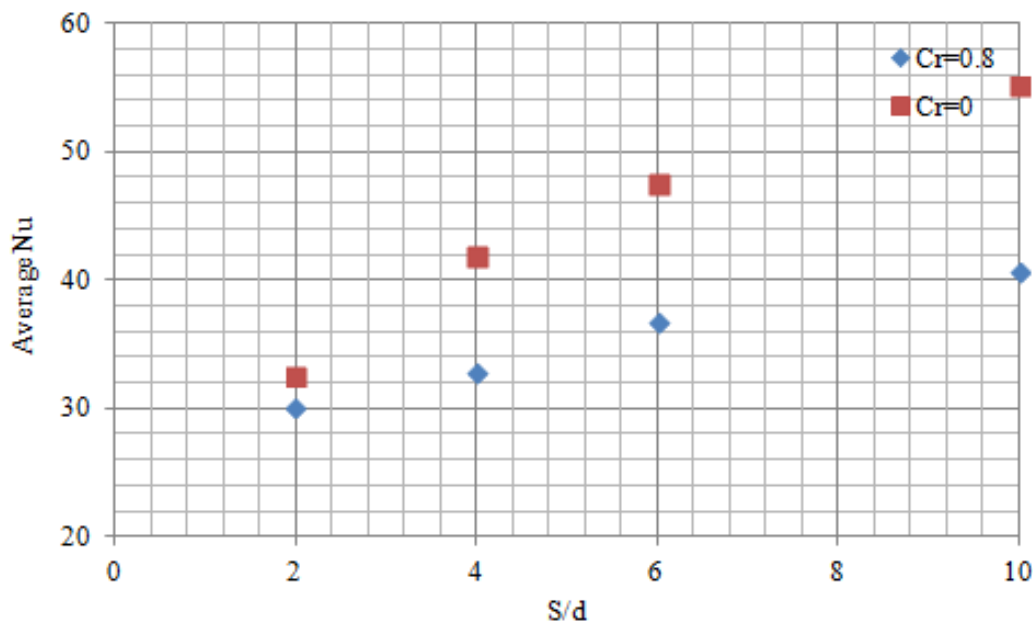
Fig. 6.39 Effects of jet-to-jet spacing on the total average Nusselt number on the moving flat and curved surfaces (in-line arrays, Re=23,000, H/d=2, VR=0.28)

6.3.5.8.2 Effect on Pressure Force

Figure 6.40 compares the effect of jet-to-jet spacing on the pressure force coefficient on the moving flat and curved surfaces from CFD. The pressure force coefficients on both moving flat and curved surfaces are relatively insensitive to the jet-to-jet spacing within the range examined. The pressure force coefficient on the moving flat surface is higher than the curved surface due to the higher pressure on the flat surface compared to the curved surface, except at S/d=2. This can be attributed to the very complex flow on the moving curved surface at very small jet-to-jet spacing. However, there is a negligible difference in the pressure force coefficient between the moving flat and curved surfaces.
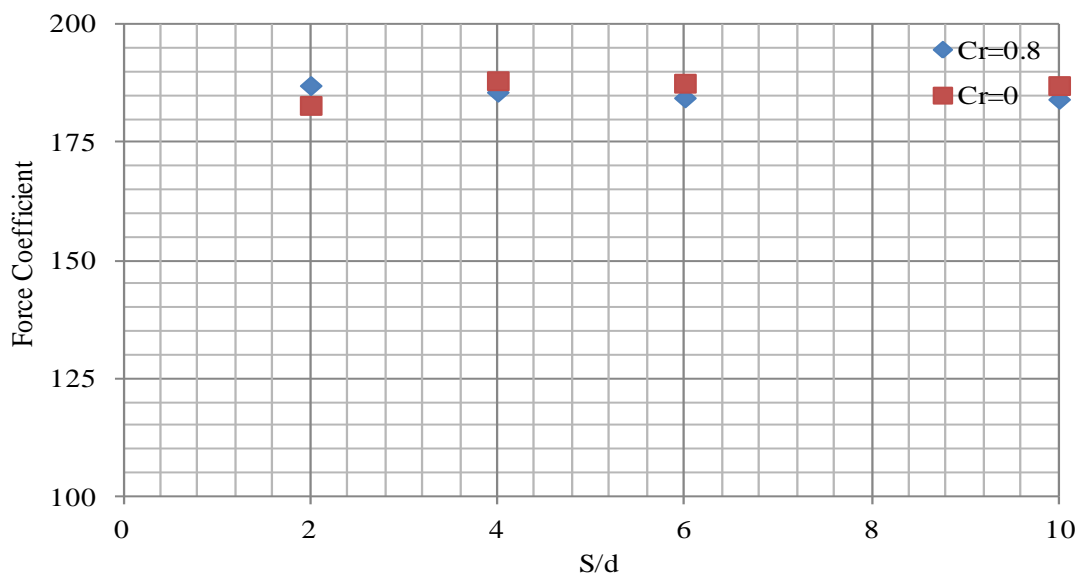
Fig. 6.40 Effects of jet-to-jet spacing on the pressure force coefficient on the moving flat and curved surfaces (in-line arrays, Re=23,000, H/d=2 and VR=0.28)

6.3.5.9 Jet Angle

6.3.5.9.1 Effect on Heat Transfer

Figure 6.41 shows the predicted Nusselt number distribution on the moving flat and curved surface along motion direction for various jet angles over the range of 45-90 degree. The primary and the secondary peaks are also observed in the Nu distribution of orthogonal impinging jets on both moving flat and curved surfaces and the secondary peak is only observed on the left side of the stagnation point compared to the fixed flat surface (see Fig. 5.27). However, primary and secondary peaks are not observed for angled jets. For both moving flat and curved surfaces, the value of the Nusselt number at the stagnation point shows no significant change for angled jets and is higher than the orthogonal jet with shifted locations of the peak values. The Nusselt number at the stagnation point for jets impinging on the moving

flat surface is higher than the moving curved surface due to the effect of surface curvature. Furthermore, the change of the circumferential angle of jets on the moving curved surface leads to variations of the curvature radius at the impinging point, the jet-to-surface distance and the jet impingement angle. The Nusselt number distribution is very similar on both moving flat and curved surfaces for corresponding angles.
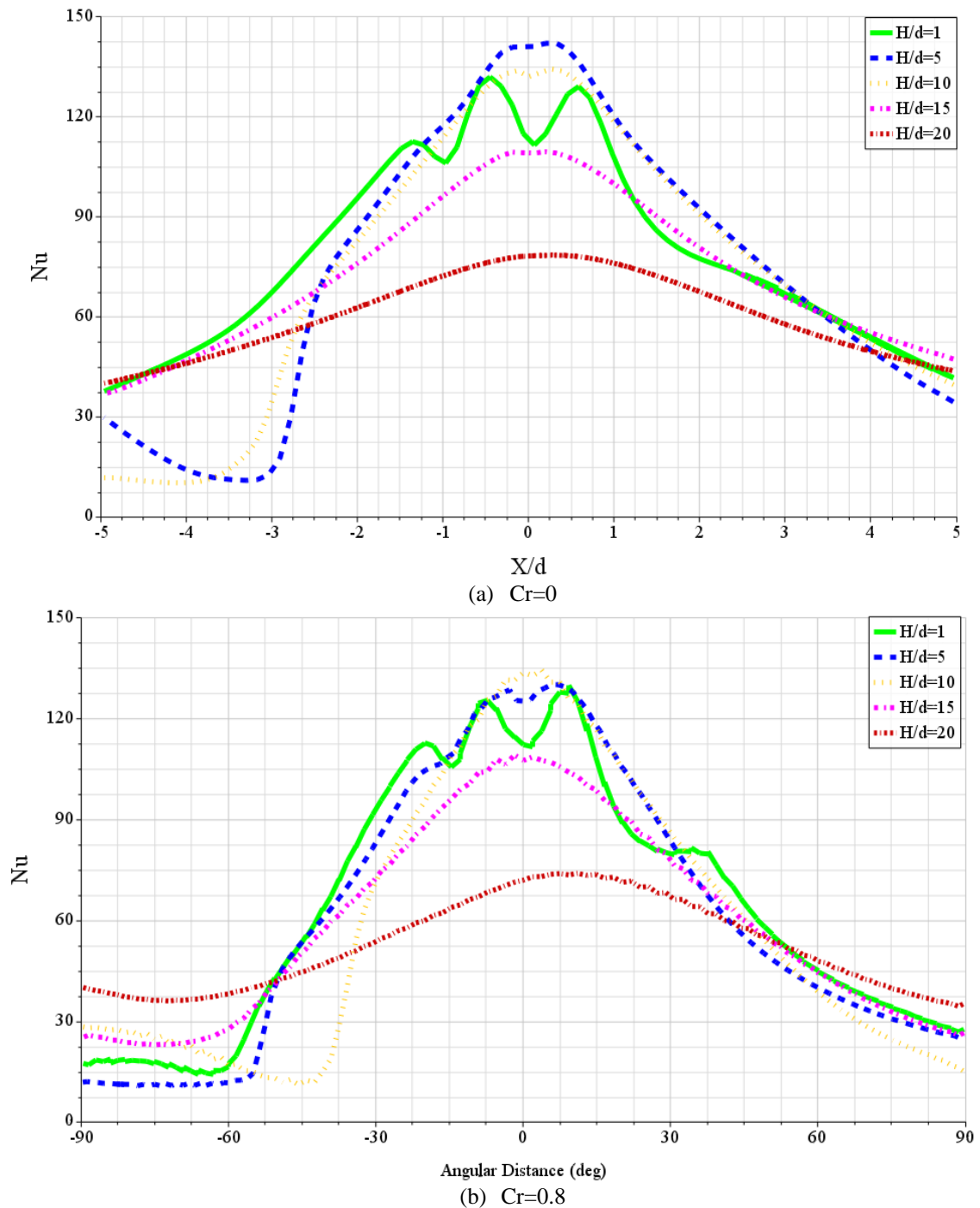

(a) Cr=0

(b) Cr=0.8
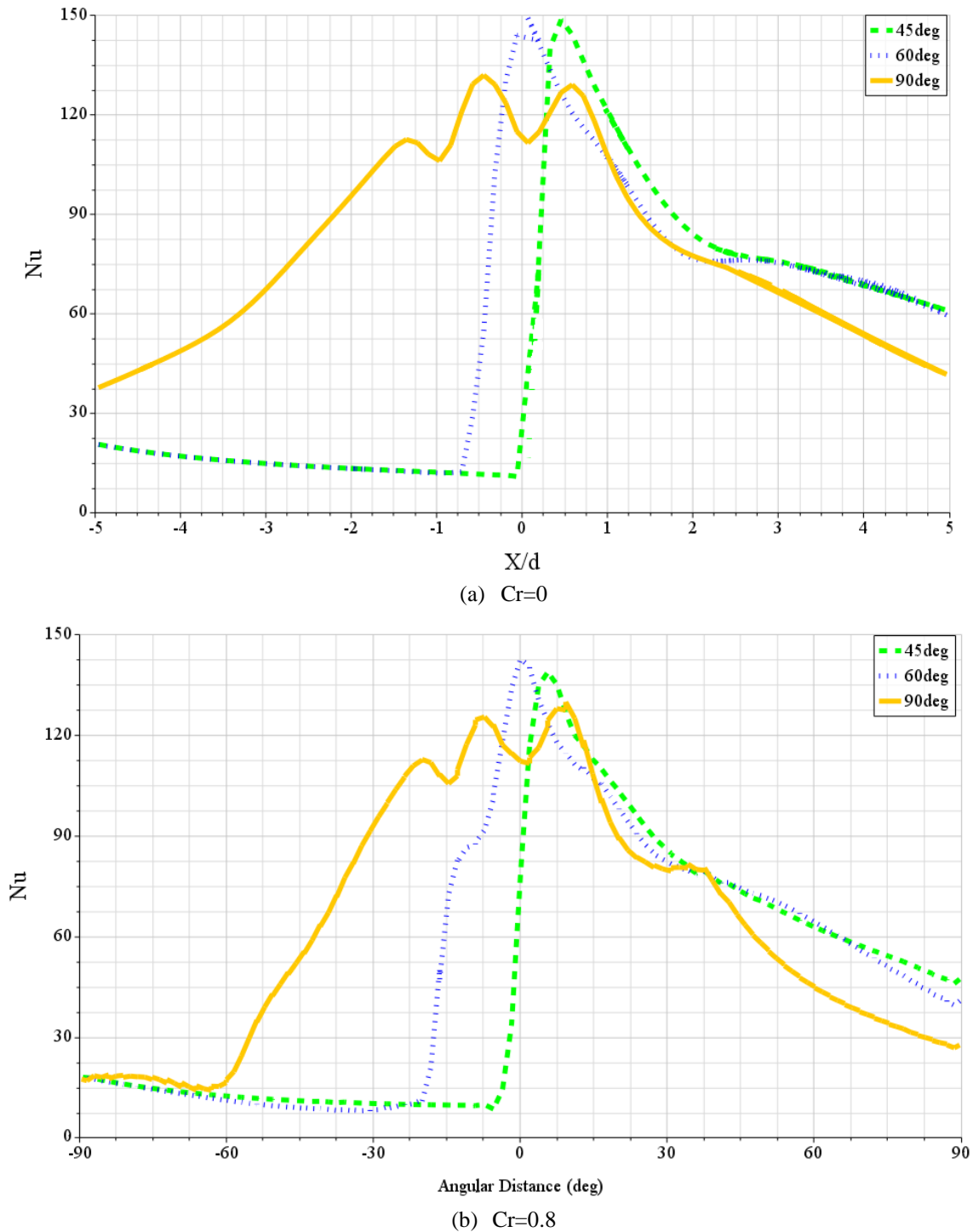
Fig. 6.41 Effects of jet angle on the local Nusselt number along the motion direction on the moving flat and curved surfaces from CFD (in-line arrays, Re=23,000, H/d=1, S/d=4 and VR=0.28)

For angled jets impinging on both the moving flat and curved surfaces, the Nusselt number on the left side is much lower than that on the right side. That is because the angled jet leads to a main flow toward the right side of the impinging surface, and the flow toward the left side will be confined. The surface motion has a minor effect on the Nusselt number distribution on both moving flat and curved surfaces for orthogonal jets compared to angled jets and the heat transfer is more uniform in both directions for angled jets, because for angled jets, the Nu curves exhibit an asymmetrical trend and the orthogonal jets have more momentum compared to the angled jets. Thus the importance of surface motion to optimize heat transfer due to an array of impinging jets is reduced for orthogonal jets.

Figure 6.42 shows the variation of the area-averaged Nusselt number on the moving flat and curved surface with the jet exit angle. The averaged value of the Nusselt number sharply increases with an increase in the jet exit angle. The heat transfer performance of the jet nozzles is largely improved by the orthogonal impinging jets compared to the angled jets. The average Nusselt number varies quite strongly with jet angle. The trend of the CFD predictions are same for both moving flat and curved surfaces. The slope of CFD prediction for moving flat surface is faster than the slope of CFD prediction for moving curved surface and, also, the impinging jets on the moving flat surface have a higher Nu number compared to the impinging jets on the moving curved surface. This could be attributed to the confinement effect.
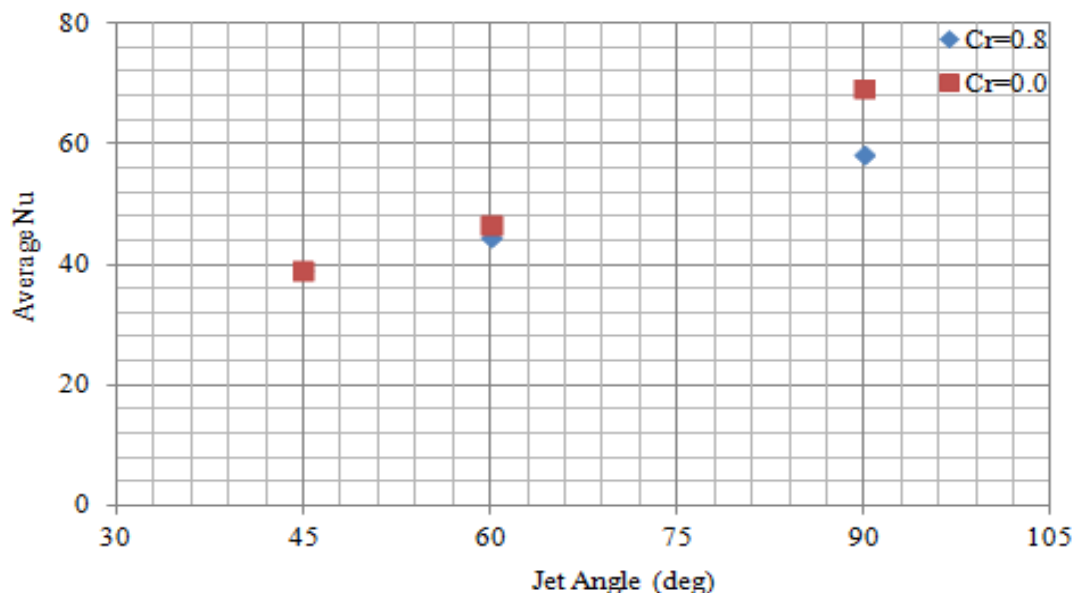
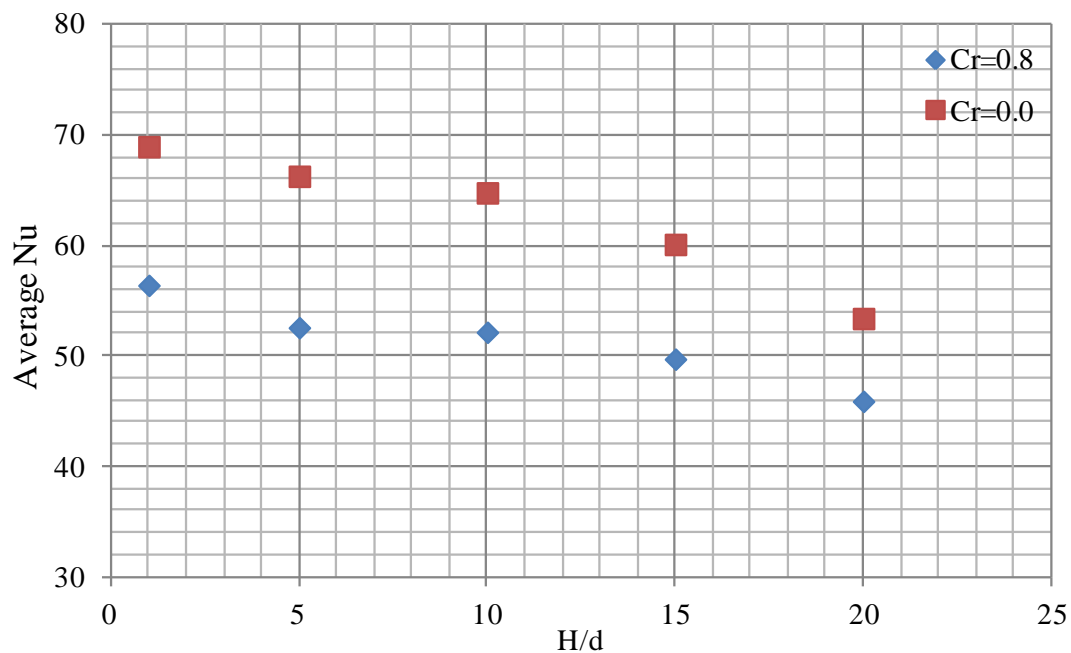**Fig. 6.42** Effects of jet angle on the total average Nusselt number on the moving flat and curved surfaces (in-line arrays, Re=23,000, H/d=1, S/d=4 and VR=0.28)

6.3.5.9.2 Effect on Pressure Force

Figure 6.43 compares the effect of jet angle on the pressure force coefficient on the moving flat and curved surfaces from CFD. The pressure force coefficient increases if the jet

angle on both moving flat and curved surfaces is increased, because increasing the jet angle increases the pressure on the impingement surface. The trend and slope of pressure force coefficient is the same on both moving flat and curved surfaces. For orthogonal jets, the pressure force coefficient is almost the same on both moving flat and curved surfaces. In contrast, the pressure force coefficient from angled jet impinging on the moving curved surface is higher than on the moving flat surface. This is due to the higher pressure on the curved surface compared to the flat surface, because for the moving flat surface, only the vertical component of velocity affects the pressure force coefficient, but for moving curved surface, both vertical and horizontal components of velocity have an effect on the pressure force coefficient, due to the effect of surface curvature.
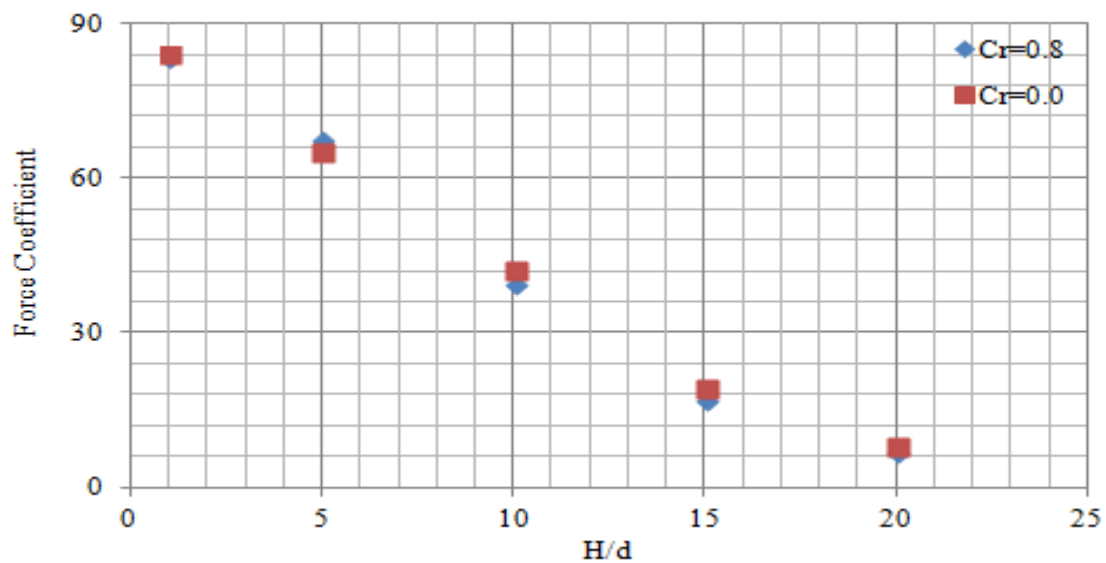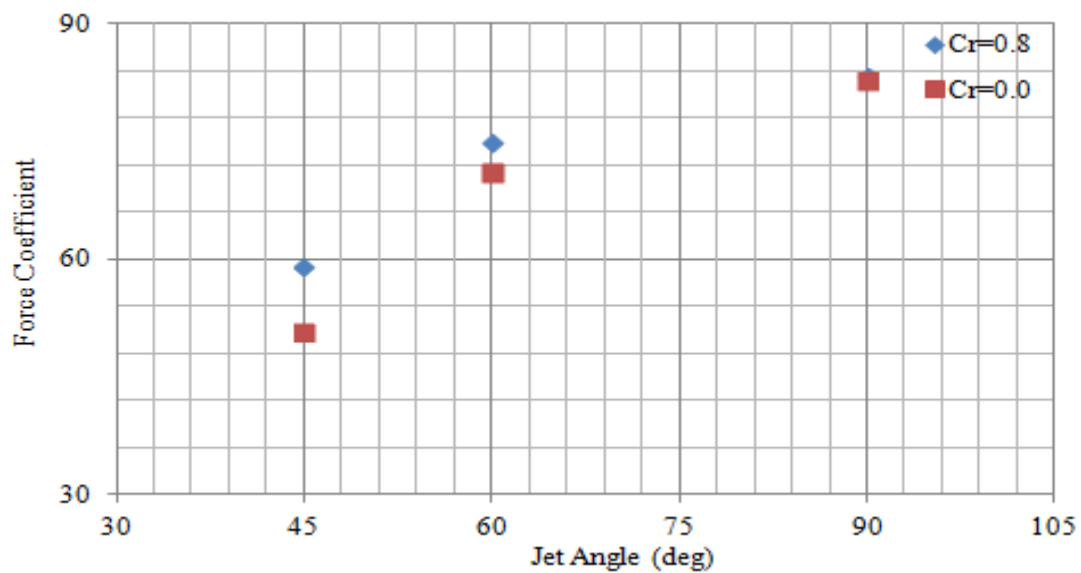

Fig. 6.43 Effects of jet angle on the pressure force coefficient on the moving flat and curved surfaces (in-line arrays, Re=23,000, H/d=1, S/d=4 and VR=0.28)

6.3.6 Correlation Equations

Two correlations for the average Nusselt number and pressure force coefficient from the numerical simulations are developed by a multiple regression fit for the single row of orifices impinging on a curved surface:

$$\text{Nu}_{ave} = 0.084\,\text{Re}^{0.6}(H/d)^{-0.046}(S/d)^{0.194}\theta_{rad}^{0.825}(1+VR)^{-0.0237}(1+Cr)^{-0.461} \tag{6-1}$$

$$C_f = 0.69\,\text{Re}^{0.0152}(133.6H/d^{-0.094} - 2.5H/d - 43.83)(S/d)^{-0.00416}\theta_{rad}^{0.6}(1+2.7VR)^{-0.03}(1+0.7Cr)^{-0.024} \tag{6-2}$$

The above correlations are proposed in terms of Re, H/d, S/d, θ, VR and Cr as the independent variables for Re number in the range of 1,980 to 66,200, H/d from 1 to 20, S/d from 2 to 10, θ from 45 to 90°, VR from 0 to 0.28 and Cr from 0 to 0.8. Prandtl number is set to Pr=0.71. The observed trends in the CFD simulations are shown by the exponents of the independent parameters in the correlations.

For Cr=0 the correlation equations for flat surface should be reproduced. But there are small differences in the exponents of the correlation equations in Chapter 5 (Eqs. 5.1 and 5.2). This is due to the difference in the flow regime for flat and curved surface and the limitation of the data base used for the correlation.

Figures 6.44 and 6.45 show the parity plot for comparison of the CFD simulation and predicted results by correlations. The agreement is found to be reasonable and all the data points deviate from the correlation by less than 6% and 5% for the average Nu number and force coefficient respectively.
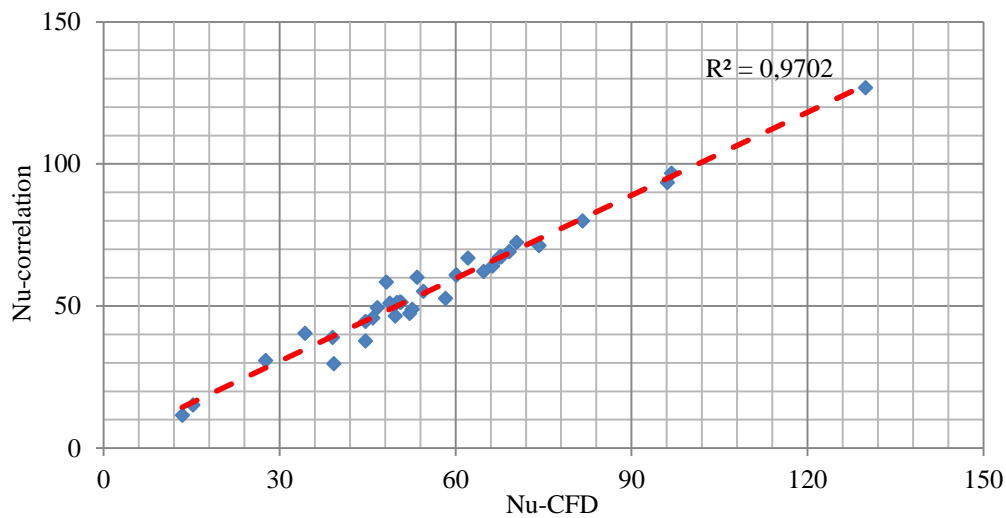
Fig. 6.44 Parity plot showing a comparison between the average Nu predicted by the CFD and correlation
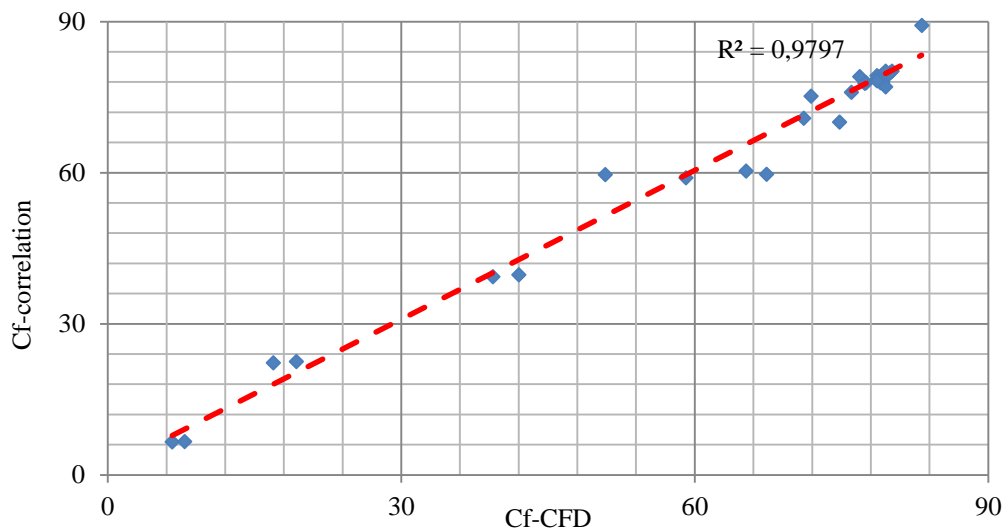
Fig. 6.45 Parity plot showing a comparison between the force coefficient predicted by the CFD and correlation

6.4 Summary

Numerical simulations of multiple circular jets impinging on a fixed curved surface are carried out and validated against the experimental data and computations of the heat transfer between multiple impinging circular jets and a moving curved surface are performed. The commercial CFD package STAR-CCM$^+$ is employed with SST k-ω turbulence model. This article presents full CFD calculations of the heat transfer between multiple impinging circular jets and a moving curved surface. The effect of surface curvature, number of jets, number of jet rows, cross-flow, nozzle arrangement, surface motion, Reynolds number, the distance between the jet nozzles to surface, jet-to-jet spacing and jet angle are discussed to gain the understanding of the physical mechanisms which affect the uniformity of the local heat transfer coefficient, the average heat transfer coefficient and pressure force coefficient on the moving curved surface. The findings can be summarized as follows:

Surface curvature of the impingement surface produces a kind of confinement and reduces the average heat transfer and pressure force coefficients. There is a minor difference between in-line and staggered arrangement and the in-line arrangement has more uniform heat transfer distribution compared to the staggered arrangement for both moving flat and curved surfaces. The surface motion has a stronger effect on the impinging jets if cross-flow is considered. The total averaged Nu on both moving flat and curved surfaces reduces as the number of jets, number of jet rows, jet-to-surface distance, relative velocity ratio and surface curvature increase in contrast to the jet Re number, jet-to-jet spacing and jet angle. The surface motion has more effect on the Nu number distribution on both moving flat and curved surfaces for angled jets and also at large jet-to-surface distance, low Re number and small-jet to-jet spacing and, consequently, the heat transfer distribution on both surfaces is more uniform under these conditions. Pressure force coefficient on both moving flat and curved surfaces is highly dependent on jet-surface distance, jet angle and relative surface curvature but relatively insensitive to the Re number, jet-to-jet spacing and relative velocity ratio. Therefore, identification of optimum jet-to-surface distance, jet angle and surface curvature is very important for products sensitive to the pressure force in order to reduce the force on the surface for stress-sensitive products. Two correlations describing the average Nu number and the pressure force coefficient for single row jet configurations have been developed as a function of Re, H/d, S/d, θ, VR and Cr. There is a reasonable agreement of the computed and the correlated values.

Chapter 7

7. Optimum Design

Many studies have been dedicated to the heat transfer optimization in the multiple impinging jet systems. Although the jet impingement heat transfer data are available in the literature, due to the large number of possible combinations of design parameters, such as the nozzle shape, jet distance from target surface, jet-to-jet spacing, jet exit velocity and temperature, surface curvature and motion, not all of these have been adequately investigated. At the present time, when the energy costs are quite high, an optimization with regard to achieve the minimum specific drying energy consumption is desirable. But also other optimization targets are possible such as the pressure force for the sensitive products and the drying time for increased productivity.

The chapter starts with a description of design variables and design space. The results section includes an optimization on five key controlling design variables such as jet-to-surface distance, the spacing between the jets, jet angle, jet exit velocity and surface velocity for averaged Nu number, specific energy consumption and pressure force coefficient on the moving curved surface as the objective functions to be maximized, minimized and minimized respectively. The chapter concludes with a summary of the main findings.

7.1 Design Variable and Space

In an optimization study, the objectives are evaluated with respect to the design variables using a CFD model. During the analysis, an optimization algorithm uses an embedded strategy to choose the values for the input parameters so as to best meet the analysis objectives.

The designer should optimize the design parameters of industrial drying equipment to achieve the minimum energy consumption. Maximizing the heat transfer may reduce the drying time but does not lead to minimum energy consumption. Jet impingement force on the surface is very important in drying applications for force sensitive products. Therefore, in the present optimization study, the heat transfer, pressure force and energy consumption in dimensionless form are selected as the objective functions to be maximized, minimized and minimized respectively. Optimization for the multiple jets impinging on a moving curved surface has been performed with respect to five key controlling design parameters such as, jet-to-surface distance, the spacing between the jets, jet exit velocity, surface velocity and jet angle. These parameters can play a critical role on the heat transfer rate, pressure force and energy

consumption and therefore optimization for design purposes is required. Other parameters, such as relative surface curvature (Cr=0.8), nozzle diameter (d=10mm), jet temperature (100 C), surface temperature (60 C) and ambient temperature (20 C) are held constant. The ranges of the design variables for the optimization have been fixed through a parametric study as shown in Table 7.1.

Table 7.1 Design Variables and Design Space

Design variable	Lower bound	Upper bound
H/d	2	10
S/d	2	10
θ	40°	90°
Re number	4337	21685
Relative surface velocity(VR)	0.0034	1
Inlet velocity	10 m/s	50 m/s
Surface velocity	0.17 m/s	10 m/s

Based on the definition of the Nu number (Eqs.3.2-3), force coefficient (Eqs. 3.15-16) and specific energy consumption (Eqs. 3.12-14), higher values of averaged Nu number and lower values of minimum specific energy consumption correlate somewhat. In contrast, the minimum force coefficient and minimum specific energy consumption are truly competitive, due to the presence of inlet velocity in the numerator of specific energy consumption definition and in the denominator of force coefficient definition. For optimization studies, the optimization type of the weighted sum of all objectives is used as one objective optimization for the average Nu to be maximized, pressure force coefficient and specific drying energy consumption are to be minimized separately. Multiple objective tradeoff study (Pareto Front) is used for the pressure force coefficient and specific drying energy consumption as objectives to be minimized simultaneously. STAR-CCM$^+$ uses the SHERPA algorithm when running an optimization study. If the number of design variables (m) is less than 10, STAR-CCM+ recommends choosing the minimum design number of runs (N) equal to 10×m to make good progress. Therefore, in the present optimization study, minimum N should be considered equal to 50. In order to increase the accuracy of the results, N is considered equal to 100.

7.2 Results of Optimization for Nu number

Figure 7.1 shows the design study with a logarithmic trend line during the one objective optimization for the area-averaged Nu number versus Re number. Increasing the Re number increases the average Nu number. Because increasing the Re number occurs with increasing the jet exit velocity from nozzle and finally leads to increase in the turbulent kinetic energy. Therefore, the maximum average Nu number is expected to occur at maximum inlet velocity.

Fig. 7.1 Design study during the one objective optimization for the area-averaged Nu number versus Re

Figure 7.2 shows the design study with a logarithmic trend line during the one objective optimization for the area-averaged Nu number versus nozzle-to-surface distance (H/d). The average Nu number is increasing as H/d decreases. Increasing the separation distance, the momentum exchange between the jet flow and the ambient increases, hence the flow in case of low H/d value has more momentum compared to the higher H/d values. Therefore, the maximum average Nu number is expected to occur at minimum H/d value.

Fig. 7.2 Design study during the one objective optimization for the area-averaged Nu number versus H/d

Figure 7.3 shows the design study with a logarithmic trend line during the one objective optimization for the area-averaged Nu number versus jet-to-jet spacing (S/d). It is clear that the

higher S/d values result in higher average Nu due to the lower jet interaction. Therefore, the maximum average Nu number is expected to occur at maximum S/d value.

Fig. 7.3 Design study during the one objective optimization for the area-averaged Nu number versus S/d

Figure 7.4 shows the design study with a logarithmic trend line during the one objective optimization for the area-averaged Nu number versus jet angle (θ). It is clear that the surface average Nu number increases with increasing the jet angle, because when the jet impinging orthogonal on the surface (90°); it can pick up the most heat upon striking the surface. Therefore, the maximum average Nu number is expected to occur for orthogonal jets.

Fig. 7.4 Design study during the one objective optimization for the area-averaged Nu number versus θ

Figure 7.5 shows the design study with a logarithmic trend line during the one objective optimization for the area-averaged Nu number versus relative surface velocity (VR). The

average Nu number decreases with increasing the relative surface velocity. The relative surface velocity increases the interaction between neighboring jet flows and leads to significant reductions in average Nu. Therefore, the maximum average Nu number is expected to occur at minimum relative surface velocity.
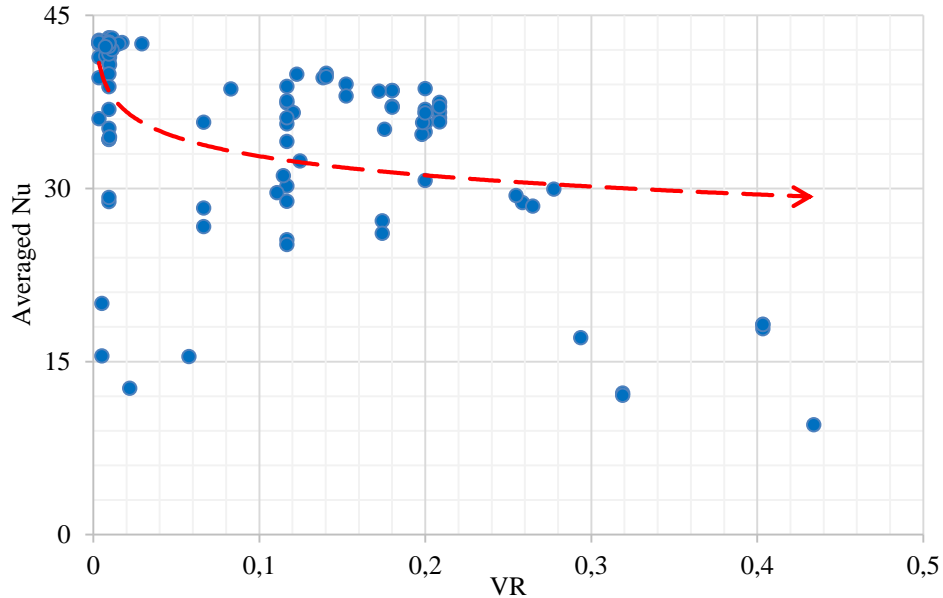
Fig. 7.5 Design study during the one objective optimization for the area-averaged Nu number versus VR

It can be concluded from Figure 7-1 to 7-5 that the maximum average Nu number correlates with high values of inlet velocity, jet angle and S/d and low values of H/d and relative surface velocity. These results coincide with the trends as represented by developed correlation equations (Eq. 6.1). Therefore, the best design study is found at H/d=2, S/d=10, angle=90°, inlet velocity=50m/s and surface velocity=0.47 for the investigated parameters in the range of H/d=2-10, S/d=2-10, angle=40-90°, inlet velocity=10-50 m/s and surface velocity=0.17-10 m/s under d=10 mm as shown in Table 7.2. Generally, the best designs are in the range of H/d= 2-5, S/d= 6.5-10, Angle= 60-90°, inlet velocity= 44-50 m/s and surface velocity= 0.17-7 m/s. These results also have a correlation with literature for optimum value of design parameters for maximum area-averaged Nu number[8].

7.3 Results of Optimization for Energy Consumption

Figure 7-6 shows the design study with a logarithmic trend line during the one objective optimization for the specific drying energy consumption versus Re number. Increasing the Re number increases the specific energy consumption. Because increasing the Re number occurs with increasing the jet inlet velocity. Therefore, the minimum specific energy consumption is

---

[8] Martin (1977), San&Lai (2001), Heo et al. (2012), Xing&Weigand (2013), Specht (2014), Bu et al. (2015)

expected to occur for minimum inlet velocity due to the role of inlet jet velocity in the numerator of specific energy consumption definition (Eqs. 3.12-14).
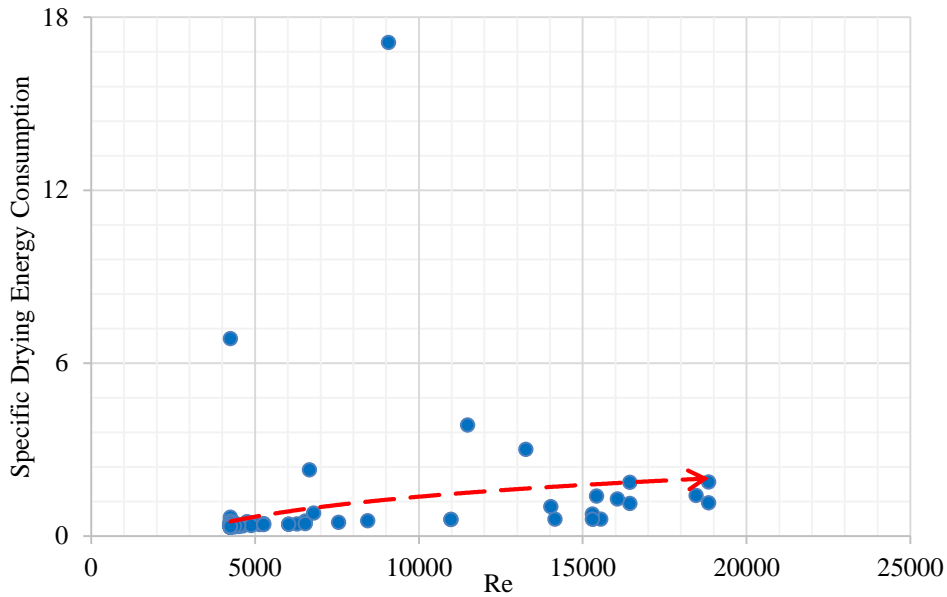
Fig. 7.6 Design study during the one objective optimization for the specific energy consumption versus Re

Figure 7-7 shows the design study with a logarithmic trend line during the one objective optimization for the specific drying energy consumption versus nozzle-to-surface distance (H/d). The specific energy consumption increases as H/d increases due to the decrease in average heat transfer coefficient (see Fig. 7.2). Therefore, the minimum specific energy consumption is expected to occur at minimum H/d value.
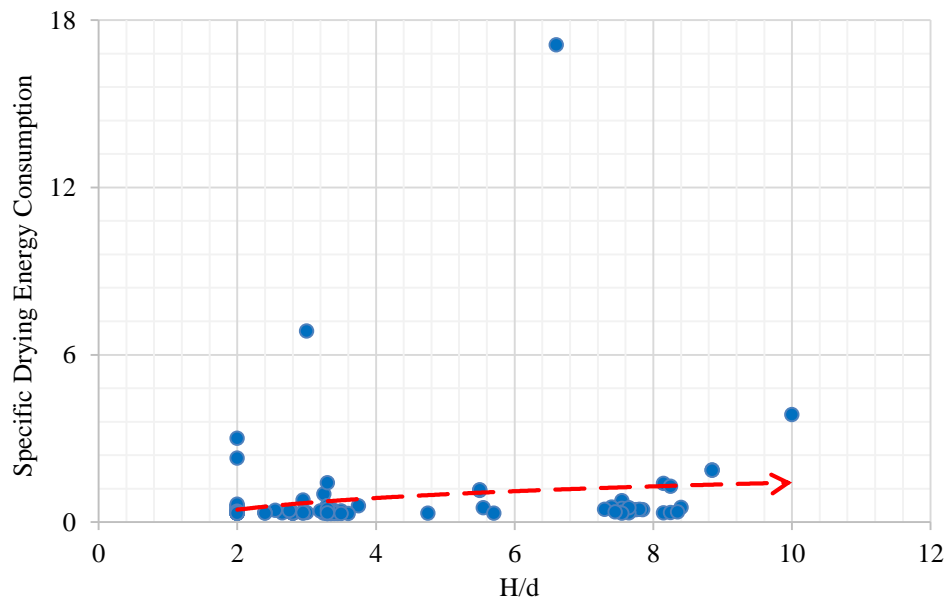
Fig. 7.7 Design study during the one objective optimization for the specific energy consumption versus H/d

Figure 7-8 shows the design study with a logarithmic trend line during the one objective optimization for the specific drying energy consumption versus jet-to-jet spacing (S/d). The

specific energy consumption is highly dependent on jet-to-jet spacing and it decreases with increasing S/d due to the role of jet-to-jet spacing in the denominator of specific energy consumption definition (Eqs. 3.12-14) and also increasing the jet-to-jet spacing increases the heat transfer coefficient (see Fig.7.3). Therefore, the minimum specific energy consumption is expected to occur at maximum S/d value.
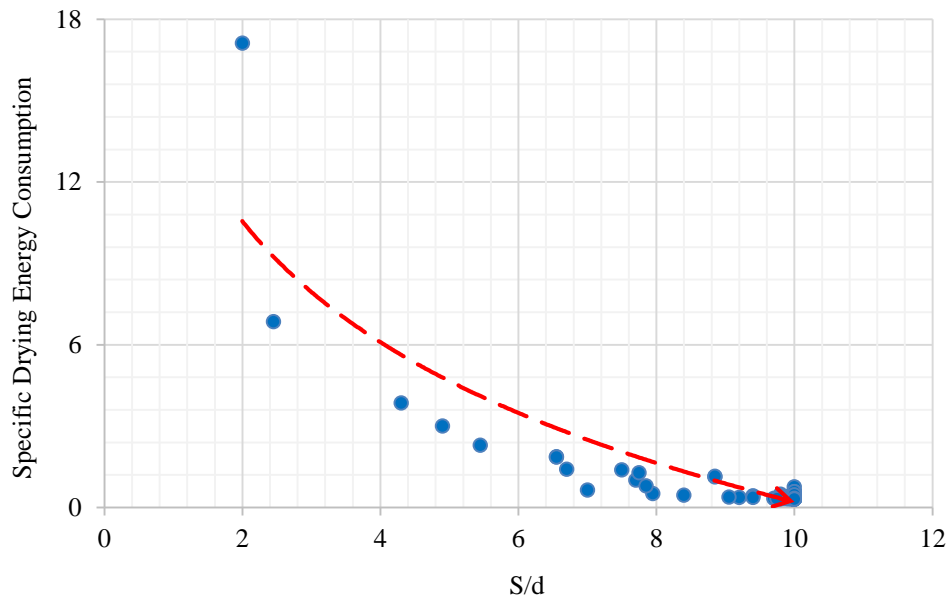
Fig. 7.8 Design study during the one objective optimization for the specific energy consumption versus S/d

Figure 7-9 shows the design study with a logarithmic trend line during the one objective optimization for the specific drying energy consumption versus jet angle (θ). Although increasing the jet angle increase the heat transfer coefficient, the specific energy consumption is relatively insensitive to jet angle.
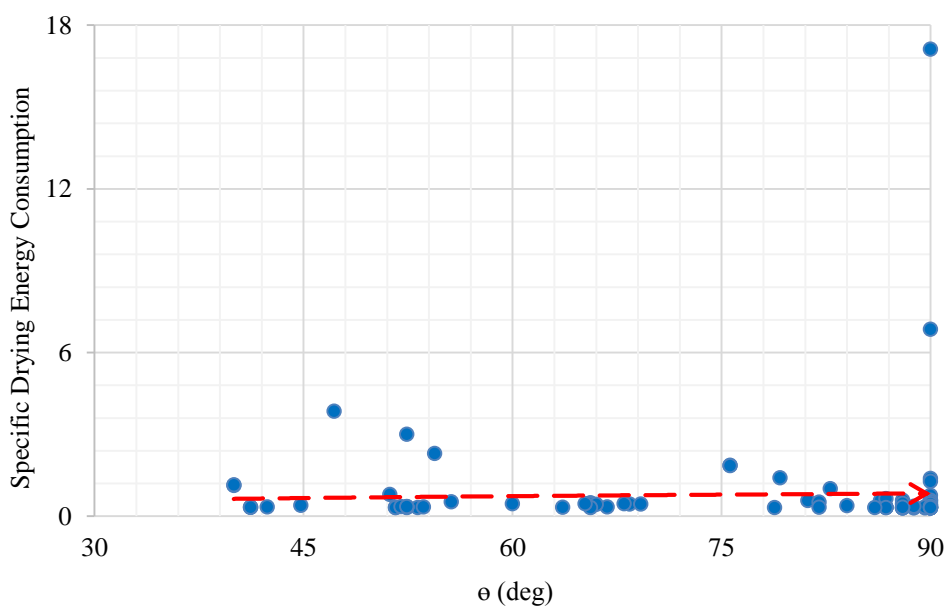
Fig. 7.9 Design study during the one objective optimization for the specific energy consumption versus θ

Figure 7-10 shows the design study with a logarithmic trend line during the one objective optimization for the specific drying energy consumption versus relative surface velocity (VR). The specific energy consumption decreases with increasing the relative surface velocity due to a lower time constant associated with the heat and mass transfer rate to or from the target surface. Therefore, the minimum specific energy consumption is expected to occur at maximum relative surface velocity.
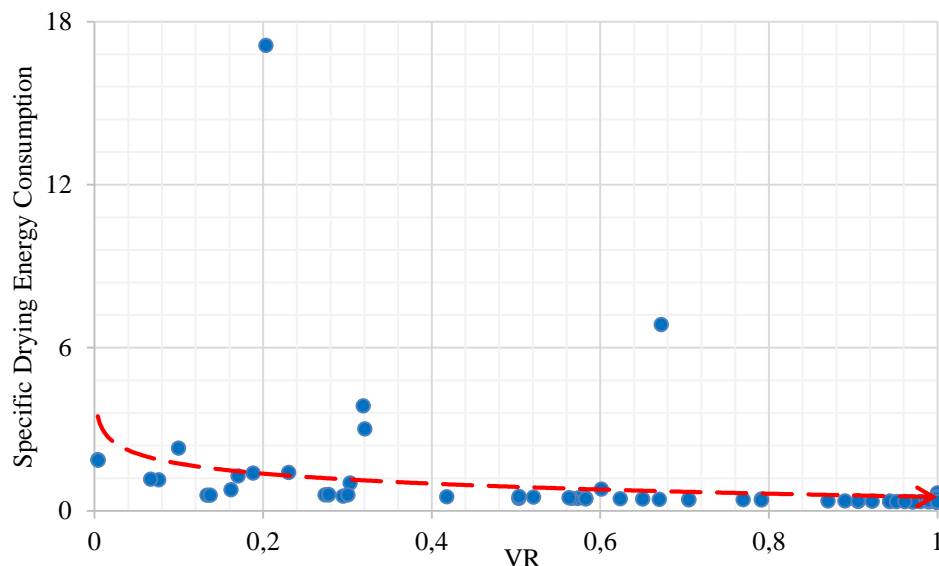
Fig. 7.10 Design study during the one objective optimization for the specific energy consumption versus VR

It can be concluded from Figure 7.6 to 7.10 that the maximum specific energy consumption occurs for minimum jet-to-jet spacing (S/d=2) due to the role of S/d in the denominator of specific energy consumption definition (Eqs. 3.12-14). The minimum specific energy consumption correlates with high values of S/d, jet angle and relative surface velocity and low values of H/d and inlet velocity. Therefore, the best design study is found at H/d=3.3, S/d=10, angle=88°, inlet velocity=10m/s and surface velocity=10 m/s for the investigated parameters in the range of H/d=2-10, S/d=2-10, angle=40-90°, inlet velocity=10-50 m/s and surface velocity=0.17-10 m/s under d = 10 mm as shown in Table 7-2. Generally, the best designs are in the range of H/d= 3.3-3.6, S/d= 10, Angle= 88-90°, inlet velocity= 10 m/s and surface velocity=10m/s. These results have a correlation with the findings of Specht (2014) who states that the energy required to heat the drying air decreases with slower outflow velocities and the distance between the nozzle and surface is not below four diameters. The minimum specific energy consumption is achieved with S/d=8-10.

7.4 Results of Optimization for Pressure Force Coefficient

Figure 7-11 shows the design study with a logarithmic trend line during the one objective optimization for the pressure force coefficient versus Re number. The pressure force coefficients on the impingement surface are relatively insensitive to the Re number within the range examined. This result has a correlation with the findings of Wang et al. (2015) for single impinging jet.
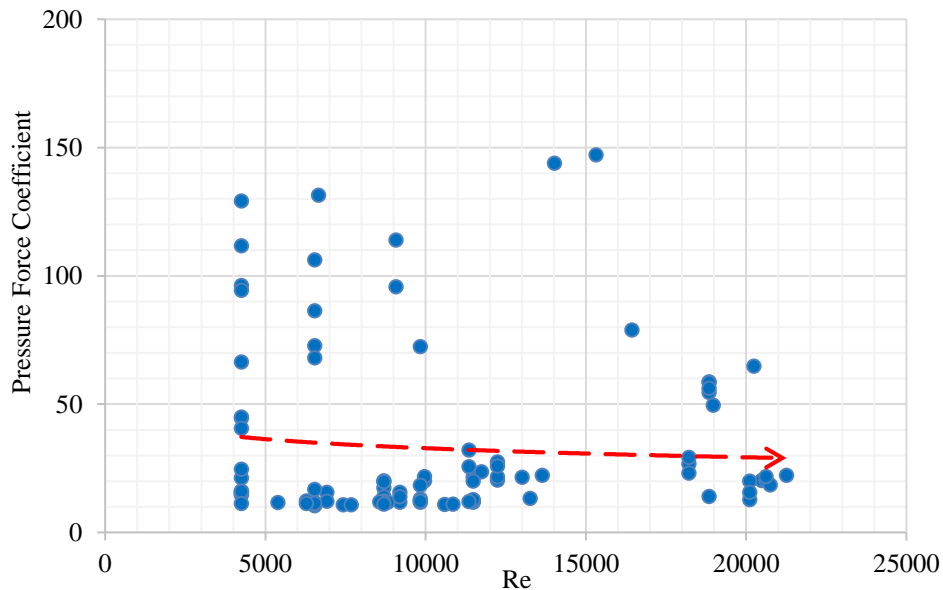
Fig. 7.11 Design study during the one objective optimization for the force coefficient versus Re

Figure 7-12 shows the design study with a logarithmic trend line during the one objective optimization for the pressure force coefficient versus nozzle-to-surface distance (H/d). The pressure force coefficients on the target surface are highly dependent on nozzle-to-surface distance and the pressure force coefficients increase with decreasing the H/d due to the decrease in the momentum exchange between the jet flow and the ambient leads to the increase in the pressure on the impingement surface. This result coincides with the findings of Wang et al. (2015) for single impinging jet. Therefore, for products sensitive to pressure forces a high value of H/d is advisable, as can be also concluded from the correlation equations (Eqs. 5.2 and 6.2) for the pressure force coefficient.
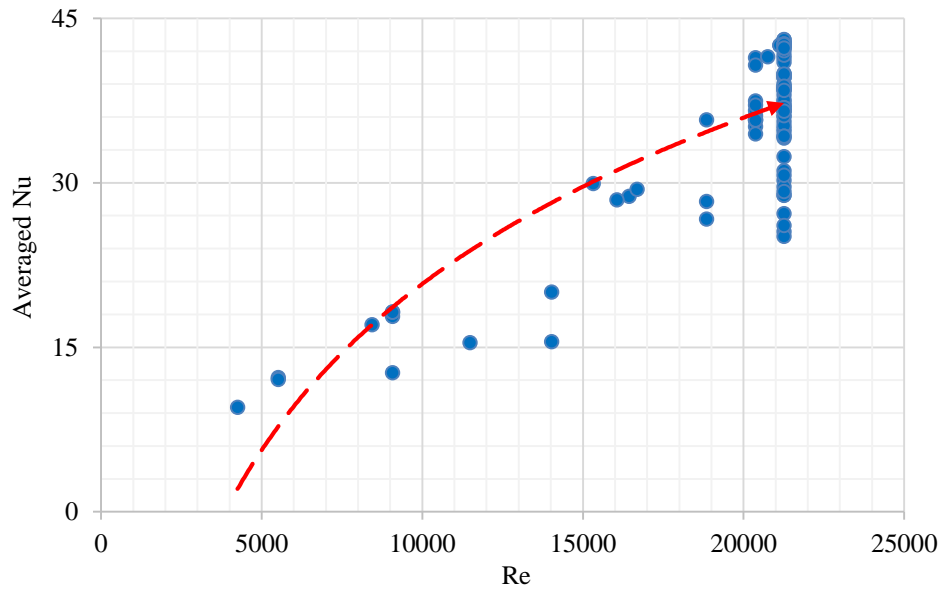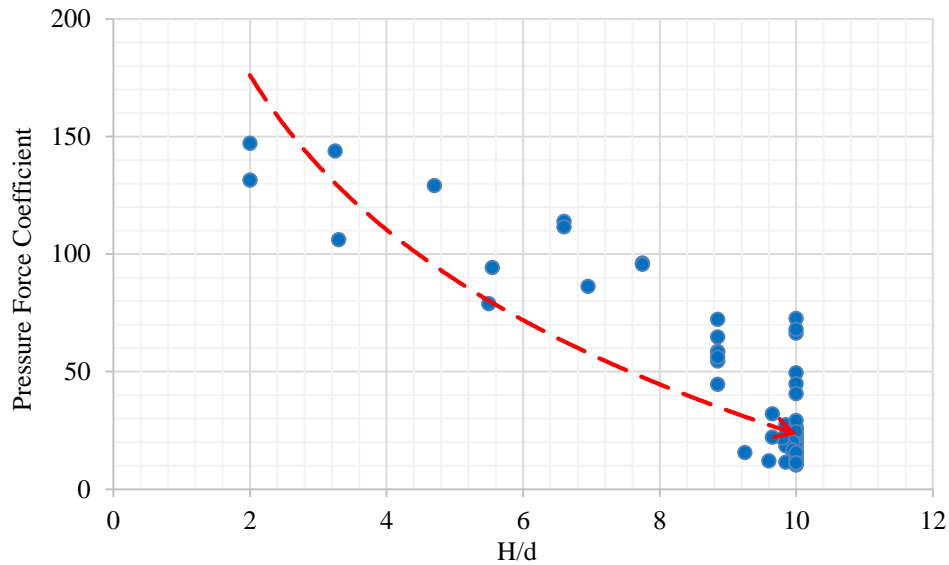
Fig. 7.12 Design study during the one objective optimization for the force coefficient versus H/d

Figure 7-13 shows the design study with a logarithmic trend line during the one objective optimization for the pressure force coefficient versus nozzle-to-nozzle spacing (S/d). The pressure force coefficients are relatively insensitive to the S/d within the range examined.
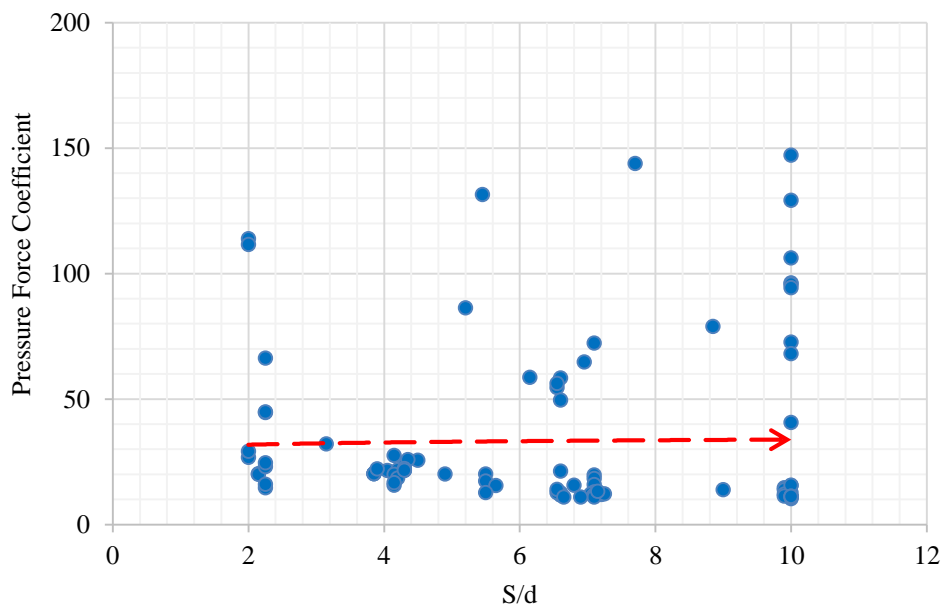
Fig. 7.13 Design study during the one objective optimization for the force coefficient versus S/d

Figure 7.14 shows the design study with a logarithmic trend line during the one objective optimization for the pressure force coefficient versus jet angle (θ). The pressure force coefficient highly dependent on the jet angle and increases with increasing the jet angle, because when the jet impinging orthogonal on the surface (90°); it can exert the most pressure upon striking the surface and leads to an increase of the pressure on the impingement surface. Therefore, the force on the impingement surface can be significantly controlled by altering the flow exit angle.
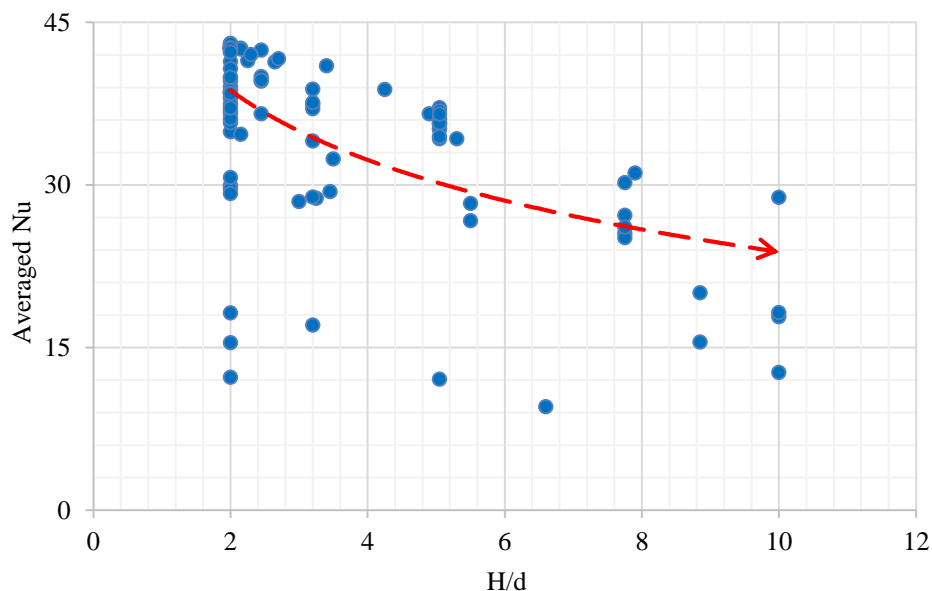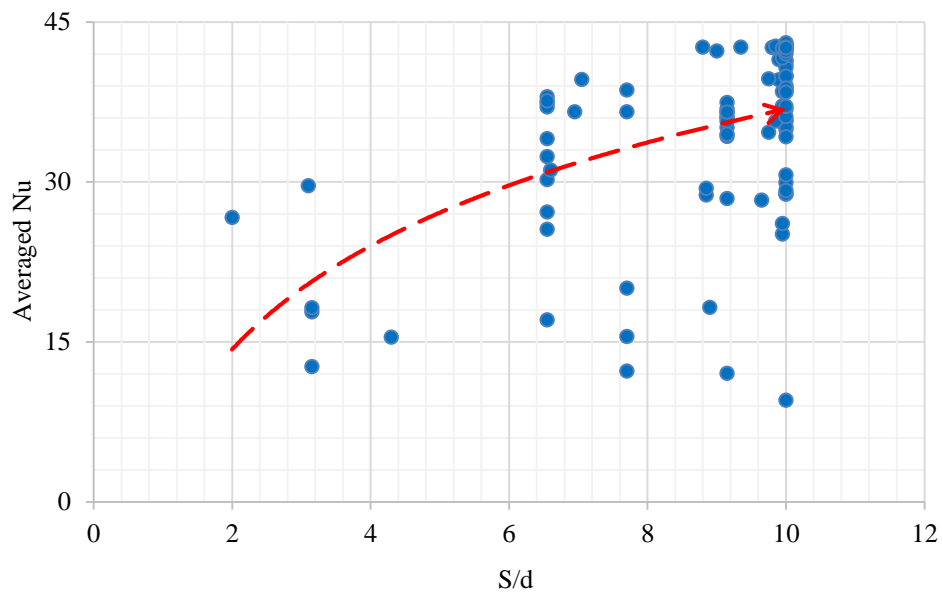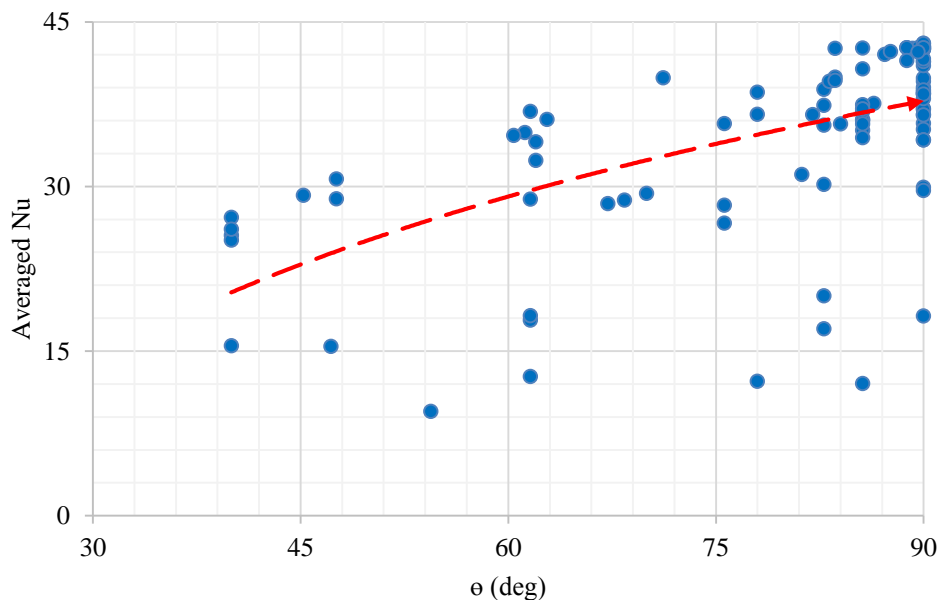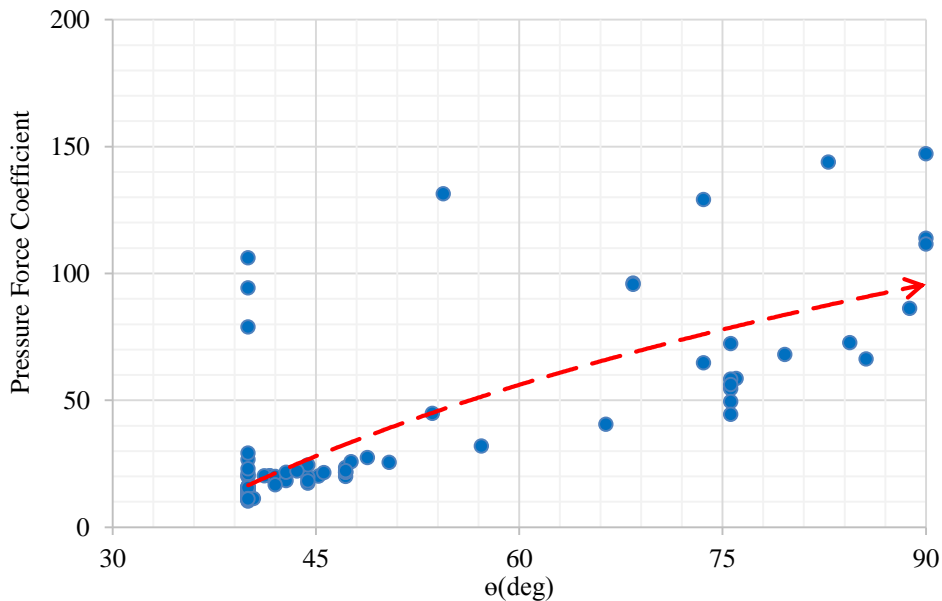
Fig. 7.14 Design study during the one objective optimization for the force coefficient versus θ

Figure 7-15 shows the design study with a logarithmic trend line during the one objective optimization for the pressure force coefficient versus velocity ratio (VR). The pressure force coefficients on the impingement surface are relatively insensitive to the velocity ratio within the range examined.
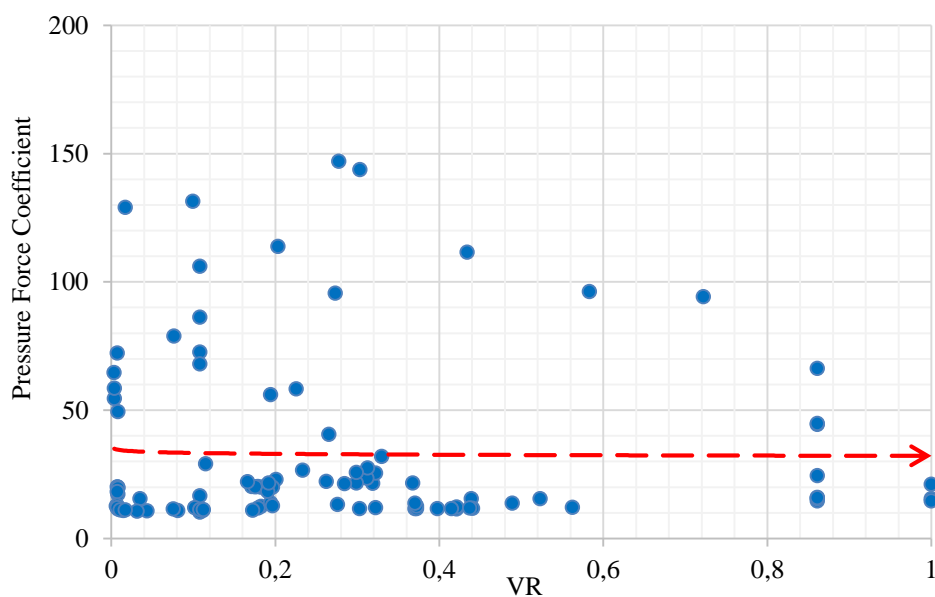
Fig. 7.15 Design study during the one objective optimization for the force coefficient versus VR

It can be concluded from Figure 7-11 to 7-15 that the pressure force coefficient is highly dependent on jet-to-surface distance (H/d) and jet angle (θ) but relatively insensitive to jet Re number, jet-to-jet spacing (S/d) and relative surface velocity (VR). These results also coincide with the trends as represented by developed correlation equations (Eq. 6.2). Therefore, the minimum pressure force coefficient almost occurred at maximum H/d and minimum jet angle.

However, the best design study is found at H/d=10, S/d=10, angle=40°, inlet velocity=15.37m/s and surface velocity=1.66m/s for the investigated parameters in the range of H/d=2-10, S/d=2-10, angle=40-90°, inlet velocity=10-50 m/s and surface velocity=0.17-10 m/s under d = 10 mm as shown in Table 7.2. Generally, the best designs are in the range of H/d= 9.85-10, S/d= 6.65-10, Angle= 40°, inlet velocity=10-25.5 m/s and surface velocity= 0.17-8.6 m/s. There is not observed any optimization with respect to the pressure force coefficient in the literature for comparison with present results.

7.5 Multi-Objective Optimization

Figures 7-16 shows the design study with two logarithmic trend lines during the multi-objective optimization for minimizing the pressure force coefficient (C_f) and specific drying energy consumption (SDEC) simultaneously for different Reynolds numbers. The pressure force coefficient and specific energy consumption show different trend compared to one objective optimization. This could be attributed to the presence of inlet velocity in the numerator of specific energy consumption definition (Eqs. 3.12-14) and in the denominator of force coefficient definition (Eqs.3.15-16).
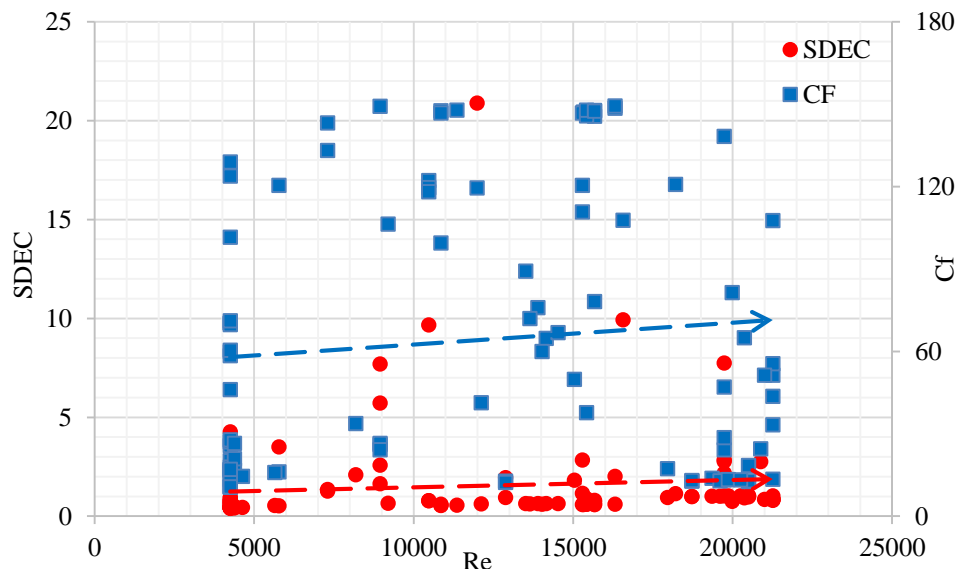
Fig. 7.16 Design study during the multi-objective optimization for different Re number

Figures 7-17 shows the design study with two logarithmic trend lines during the multi-objective optimization for different nozzle-to-surface distance (H/d). A similar trend is observed in the single objective optimization.
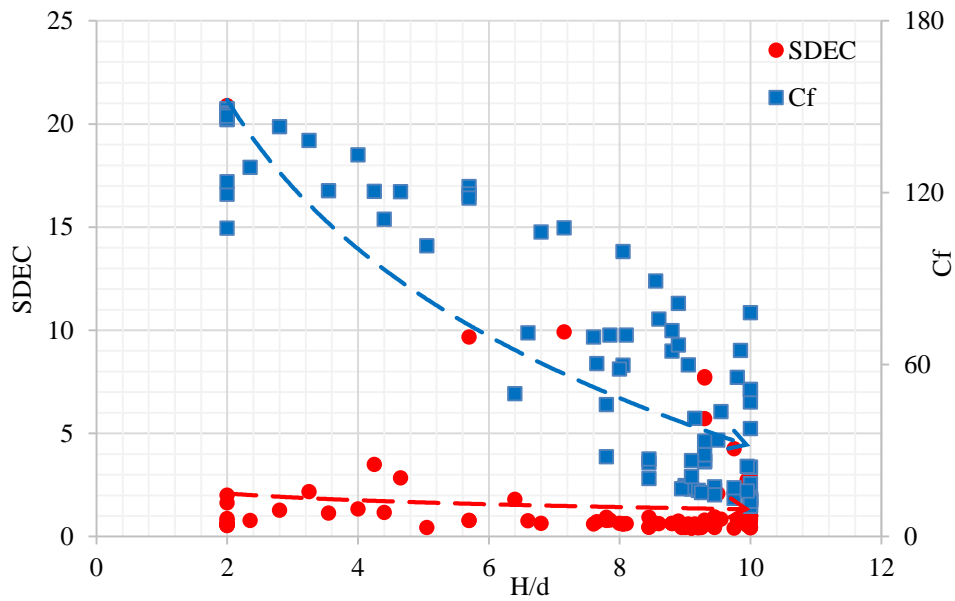
Fig. 7.17 Design study during the multi-objective optimization for different H/d

Figures 7-18 shows the design study with two logarithmic trend lines during the multi-objective optimization for different jet-to-jet spacing (S/d). The pressure force coefficient decreases with increasing the S/d in contrast to trend of results during one objective optimization.

The specific energy consumption is highly dependent on jet-to-jet spacing and it always decreases with increasing S/d. A similar trend is observed in the single objective optimization.
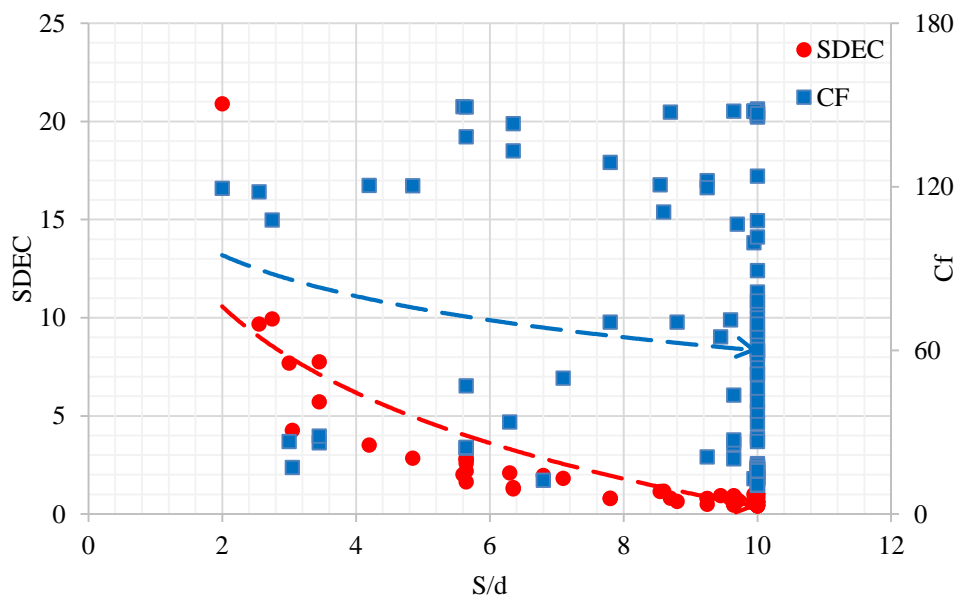
Fig. 7.18 Design study during the multi-objective optimization for different S/d

Figures 7.19 shows the design study with two logarithmic trend lines during the multi-objective optimization for different jet angles (θ). The pressure force coefficient is highly dependent on jet angle (θ) and increases with increasing the jet angle. On the other hand, the

specific energy consumption is relatively insensitive to the jet angle. This trend is similar to the single objective optimization.
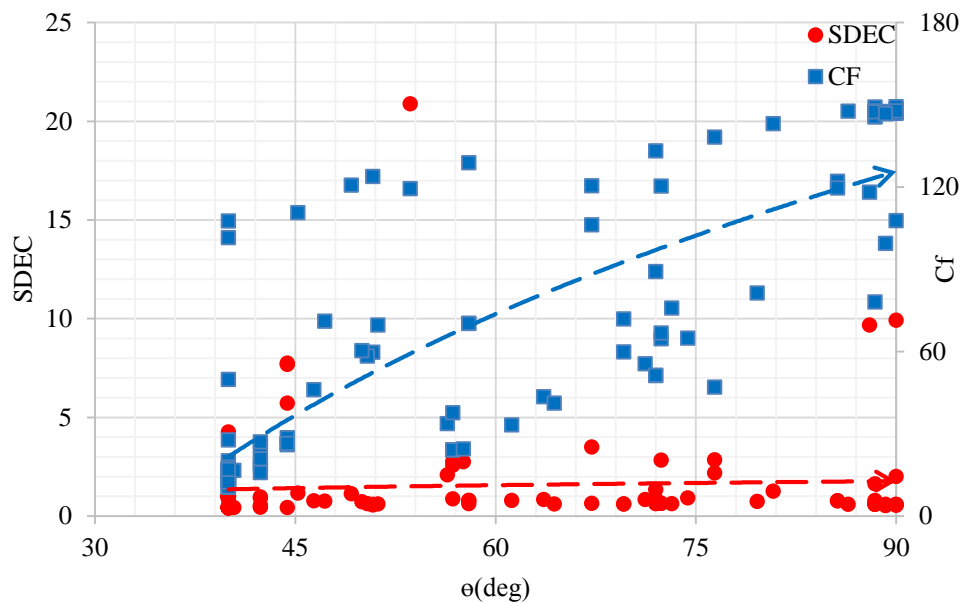
Fig. 7.19 Design study during the multi-objective optimization for different θ

Figures 7-20 shows the design study with two logarithmic trend lines during the multi-objective optimization for different velocity ratios (VR). The pressure force coefficient is relatively insensitive to the velocity ratio whereas the specific energy consumption decreases with increasing velocity ratio. This trend is similar to the single objective optimization.
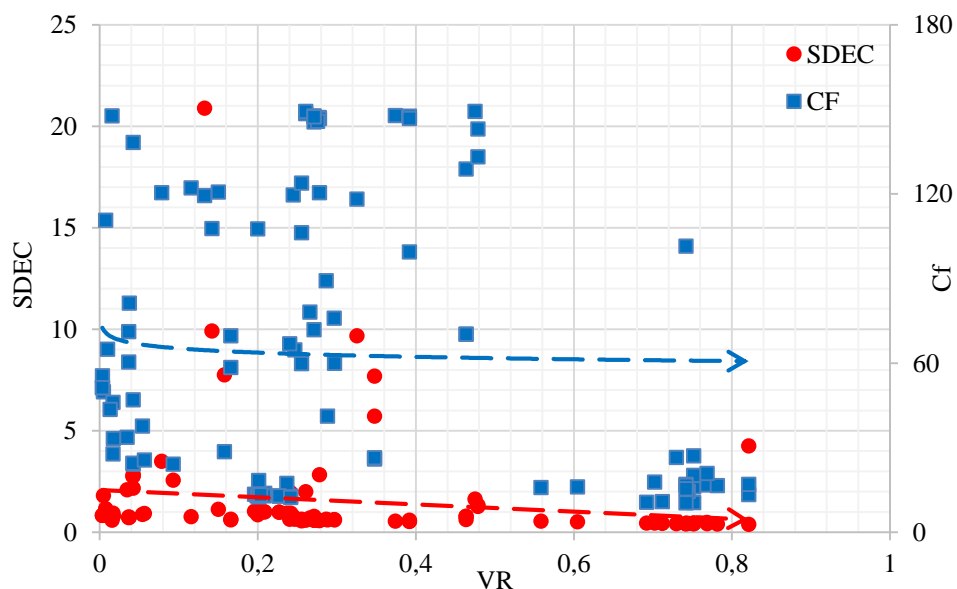
Fig. 7.20 Design study during the multi-objective optimization for different VR

Thus, as is shown in Figures 7.16 to 7.20, the best designs correlate with high values of H/d, S/d and surface velocity and low values of inlet velocity and jet angle. Hereby the best design is found at H/d=9.75, S/d=10, angle=40°, inlet velocity=10 m/s and surface velocity=8.2

m/s for the investigated parameters in the range of H/d=2-10, S/d=2-10, angle=40-90°, inlet velocity=10-50 m/s and surface velocity=0.17-10 m/s with d = 10 mm as shown in Table 7.2. Generally, the best designs are in the range of H/d= 8.45-10, S/d= 9.25-10, Angle= 40-44.5°, inlet velocity= 10-13.6 m/s and surface velocity= 7-8.2 m/s. There is not observed any similar optimization with respect to the pressure force coefficient and specific drying energy consumption simultaneously in the literature for comparison with present results.

In Table 7.2 a summary of the optimization results is shown. Optimum jet-to-jet spacing is the same for all objective functions during one and multi-objective optimization and occurs at maximum jet-to-jet spacing within the range examined. A big jet-to-surface distance leads to minimum pressure force coefficients (one and multi-objective optimization), smaller values in contrast lead to maximum average Nu numbers and minimum specific energy consumption. A similar dependence is for the optimum jet angle: minimum value for minimum force coefficient in contrast to maximum value for maximum average Nu and minimum specific energy consumption. The inlet velocity is included in the numerator of the specific energy consumption definition (Eqs. 3.12-14) and in the denominator of the force coefficient definition (Eqs. 3.15-16). Thus a high inlet velocity leads to a high average Nu number during one objective optimization in contrast to a relatively minimum value for the other objective functions. An optimum surface velocity has an almost maximum value for a minimum specific energy consumption (one and multi-objective optimization) in contrast to a minimum value for a maximum average Nu number and a minimum pressure force coefficient, because the higher surface velocity leads to a lower time constant associated with the heat and mass transfer rate to or from the target surface.

Table 7.2 Summary of results during the optimization

Objective	H/d	S/d	θ (°)	V_j (m/s)	V_w (m/s)
Max Nu_{ave}	2	10	90	50	0.467879
Min SDEC	3.3	10	88	10	10
Min C_f	10	10	40	15.3731	1.65939
Min C_f and SDEC	9.75	10	40	10	8.2

7.6 Summary

In the present chapter, the optimization for the multiple jets impinging on a moving curved surface has been performed with respect to five parameters such as, jet-to-surface distance, the spacing between the jets, jet exit velocity, surface velocity and jet angle. A

hundred design points are selected by the SHERPA Algorithm within the design space. The best design study for the pressure force coefficient and specific drying energy consumption as objectives to be minimized simultaneously are found to be H/d=9.75, S/d=10, angle=40°, inlet velocity=10 m/s and surface velocity=8.2 m/s for the examined range of parameters. Based on the definition of the Nu number, specific energy consumption and force coefficient, there is a significant difference between the optimum inlet velocity for the maximum averaged Nu number and the minimum specific energy consumption and pressure force because maximum averaged Nu number occurred at maximum inlet velocity in contrast to the minimum specific energy consumption and minimum pressure force coefficient due to the presence of inlet velocity in the numerator of the specific energy consumption definition and in the denominator of force coefficient definition. Furthermore, there is a significant difference for the optimum jet-to-surface distance and jet angle between the minimum pressure force and maximum Nu number and minimum specific energy consumption. This is because the minimum pressure force coefficient occurred at the minimum jet angle and maximum jet-to-surface distance, in contrast to the minimum specific energy consumption and maximum averaged Nu number.

Chapter 8

8. Conclusions and Recommendations for Future Work

This chapter summarizes the main findings from the numerical predictions of this project and re-emphasises the main conclusions drawn from the work. There is also a brief discussion of future work which could be undertaken to further understanding of this subject.

8.1 Conclusions

In the present work, aspects on the suitability of CFD for the prediction of jet impingement heat transfer and pressure force for various configurations and operating parameters were discussed. Quantification of numerical accuracy was achieved by application of an established method for the estimation of discretization errors (Grid Convergence Index) as a prerequisite for a meaningful conclusion on grid sensitivity and for an interpretation of the results. The numerical results were evaluated by detailed comparison with experimental data obtained from the literature review. Achievements of the main objectives can be summarized as follows.

As a general conclusion it can be said that the CFD simulations were well suited for the prediction of heat transfer and pressure force in the various jet impingement configurations investigated, and the used implementation of the SST turbulence model showed a particularly good performance with regard to both accuracy and computational effort. Irrespective of the complexity of the problem, average heat transfer coefficients can be summarized as being predictable within an accuracy range of approximately 10% on average.

The effect of multiple rows with regard to the impact on heat transfer and pressure force is negligible compared to the single row on both flat and curved surfaces (either fixed or moving surface).

Relative surface curvature has two opposite effects on the heat transfer distributions. Firstly, it makes an overall reduction in the heat transfer due to the confinement variety. Secondly, it enhances the heat transfer near the stagnation region due to the increase in relative curvature. The pressure force coefficient decreases with an increase of the relative curvature, because the higher relative curvature, which has lower surface curvature, leads to the lower surface area.

The transport processes adjacent to the moving flat and curved surfaces were strongly affected by the surface motion, leading to reduced, but more uniform, heat transfer. The

pressure force coefficient on the moving flat surface reduces as surface velocity increases. The moving curved surface has no significant effect on the pressure force coefficient.

The average Nu number and the pressure force coefficient increased as the Reynolds number increased on both the moving flat and curved surfaces and there is a more uniform heat transfer at a low Reynolds number on both moving flat and curved surfaces.

It has been shown that at low nozzle to the target surface spacings (H/d), the adjacent jet interference before impingement is minimized and the secondary maxima occur in the local heat transfer coefficient for a jet in an array. These secondary maxima enhance the average heat transfer coefficients. The results show that the average Nusselt number on both moving flat and curved surfaces increases as H/d decreases and the pressure force coefficient always increases when the H/d decreases.

The jet-to-jet spacing affects the heat transfer rate by changing the adjacent jet interference and fraction of the target surface covered by the wall jet region. Based on an equivalent mass flow rate per unit area, the area-averaged Nusselt number on both moving flat and curved surfaces sharply decreases with a decrease in the jet-to-jet spacing, and the heat transfer distribution on both moving flat and curved surfaces is more uniform for jets at small jet-to-jet spacing (S/d). The pressure force coefficient on both the moving flat and curved surfaces has no significant changes as S/d increases.

The angled jets reduce the heat transfer on both the moving flat and curved surfaces but tend to generate more uniform heat transfer distributions and the pressure force coefficient increases with an increase in the jet angle on both moving flat and curved surfaces.

Several correlations describing the average Nu number and the pressure force coefficient for single row jet configurations impinging on the flat and curved surfaces have been developed. The agreement between the CFD and correlation is found to be reasonable.

The selection of the jet configuration for industrial drying applications is undertaken not only by the relative magnitude of the average Nu number but also by the specific drying energy consumption and the pressure force for sensitive products, such as paper. The optimization for the multiple jets impinging on a moving curved surface was performed with respect to five design parameters, such as jet-to-surface distance, the spacing between the jets, jet exit velocity, surface velocity and jet angle. The proper use of these results should lead to either a more effective heat and mass transfer rate or a reduction in pressure force and energy consumption. The optimum configuration in terms of specific energy consumption and pressure force to be minimized simultaneously are found to be H/d=9.75, S/d=10, jet angle=40°, inlet velocity=10 m/s and surface velocity=8.2 m/s for the investigated parameters

in the range of H/d=2-10, S/d=2-10, angle=40-90°, inlet velocity=10-50 m/s and surface velocity=0.17-10 m/s under d = 10mm. Indeed, the optimum configuration almost occurred at maximum H/d, S/d and relative velocity (ratio of surface velocity to the jet velocity and close to one) and also at minimum jet angle and inlet velocity.

It is possible to address complex flow phenomena as encountered in industrial drying process using generic CFD models with good result. Thus complex and extensive computations based on LES may be avoided as well as the expensive measurements caused by jet arrays and moving surfaces. Using the correlation equations derived from the computations the dependencies for the main parameters over a wide range may be easily be determined. The analysis of the flow fields showed many different phenomena interacting, leading to different flow regimes. Here further investigations, preferably based on LES and DNS modelling and flow measurements are needed.

8.2 Recommendations for Future Work

The flow physics of multiple impinging jets in relation to heat transfer and pressure force is complex process. The author proposes the following topics to be studied and considered in future works for the continuation of the current study:

- This study shows that commercial CFD software such as STAR-CCM+ solves the jet impingement heat transfer reasonably well. However, the simulated results indicate some deviations from the experimental data near the stagnation point and secondary peak. Thus, there could be a strong benefit from improvements in the simulation using a transition model such as the low-Reynolds number damping modification in combination with a turbulence model. More work is needed to address this issue from two aspects: (i) develop modified turbulence models, and (ii) explore some other existing models such as large-eddy simulation model (LES) and direct numerical simulations approach (DNS).

- The characteristics of the heat transfer and pressure force from the multiple impinging jet systems were investigated numerically in this study. In future, the experimental investigations should take place on the multiple impinging round jets on both moving flat and curved surfaces and be compared with the results presented here, in order to verify the computational predictions.

References

Agrawal, C., (2017). Flow visualization of air jet impingement on convex heated surface - A Review. J. Science and Technology, Vol. 3, No. 8.

Aldabbagh, L.B.Y., Mohamad, A.A., (2009). A three-dimensional numerical simulation of impinging jet arrays on a moving surface. J. Heat and Mass Transfer, Vol. 52, No. 21-22, pp. 4894–4900.

Al-Hadhrami, L. M., (2006). Effect of orifice jet configuration on heat transfer in a rectangular channel. In International Heat Transfer Conference 13. Begel House Inc..

Al-Hadhrami, L. M., (2010). Study of Heat Transfer Distribution in a Channel with Inclined Target Surface Cooled by a Single Array of Staggered Impinging Jets. J. Heat Transfer Engineering, Vol. 31, No. 3, pp. 234 242.

Al-Mubarak Ali, A., Shaahid, S. M., Al-Hadhrami, Luai M., (2010). Effect of Orifice Jet Configuration on Heat Transfer in a Channel with Inclined Target Surface Cooled by Single Array of Impinging Jets with Outflow in Both Directions. Int. J. Applied Engineering Research, Vol. 5, No. 4, pp. 681.

Al Mubarak, A. A., et al., (2013). Heat transfer in a channel with inclined target surface cooled by single array of centered impinging jets. J. Thermal Science, Vol. 17, No. 4, pp. 1195-1206.

Ansu U., Godi, S. C., Pattamatta, A., Balaji, C., (2016). Experimental investigation of the inlet condition on jet impingement heat transfer using liquid crystal thermography. J. Experimental Thermal and Fluid Science, Vol. 80, pp. 363-375.

Ashforth-Frost, S., & Jambunathan, K., (1996). Effect of nozzle geometry and semi-confinement on the potential core of a turbulent axisymmetric free jet. International communications in heat and mass transfer, Vol. 23. No. 2, pp. 155–62.

Ashok Kumar, M., Prasad, B. V. S. S. S., (2009a, January). Computational investigations of flow and heat transfer on an effused concave surface with a single row of impinging jets for different exit configurations. In ASME Turbo Expo 2009: Power for Land, Sea, and Air, pp. 149-159.

Ashok Kumar M., Prasad, B. V. S. S. S., (2009b, August). Influence of height to diameter ratio on impingement heat transfer on effused concave surface. Int. Symp. on Heat Transfer in Gas Turbine Systems, Antalya, Turkey.

Attalla, M., Specht, E., (2009). Heat transfer characteristics from in-line arrays of free impinging jets. J. Heat Mass Transfer, Vol. 45, No. 5, pp. 537–543.

Attalla, M., (2015). Stagnation region heat transfer for circular jets impinging on a flat surface, experimental heat transfer. J. Thermal Energy Generation, Transport, Storage, and Conversion, Vol.28, No.2, pp.139-155.

Badra, J., Masri, A., Behnia, M., (2013). Enhanced transient heat transfer from arrays of jets impinging on a moving surface. J. Heat Transfer Engineering, Vol. 34, No. 4, pp. 361-371.

Bailey, J., & Bunker, R., (2002). Local heat transfer and flow distributions for impinging jet arrays of dense and sparse extent. In: Proc. ASME Turbo Expo, Amsterdam, Netherlands.

Barata, J. M. M., (1996). Fountain flows produced by multiple impinging jets in a cross-flow. J. AIAA, Vol. 34, No. 12, pp. 2523-2530.

Baughn, J. and Shimizu, S., (1989). Heat transfer measurements from a surface with uniform heat flux and an impinging jet. J. Heat Transfer, Vol. 111, No. 4, pp. 1096–1098.

Baughn, J., Hechanova, A., Yan, X., (1991). An experimental study of entrainment effects on the heat transfer from a flat surface to a heated circular impinging jet.J. Heat Transfer, Vol. 113, pp. 1023–1025.

References

Becko, Y., (1976). Impingement cooling: A review. Institute for Fluid Dynamics, Turbine Blade Cooling, 40 pages.

Behbahani, A. I., & Goldstein, R. J., (1983). Local Heat Transfer to Staggered Arrays of Impinging Circular Air Jets. J. Engineering for Power, Vol. 105, pp. 354–360.

Behnia, P., Parneix, S., & Durbin, P., (1998). Prediction of heat transfer in an axisymmetric turbulent jet impinging on the flat surface. Int. J. Heat Mass Transfer, Vol. 41, No.12, pp. 1845–1855.

Brevet, P., Dejeu, C., Dorignac, E., Jolly, M., & Vullierme, J., (2002). Heat transfer to a row of impinging jets in consideration of optimization. Int. J. Heat Mass Transfer, Vol. 45, No. 20, pp. 4191–4200.

Bu, X., Peng, L., Lin, G., et al., (2015). Experimental study of jet impingement heat transfer on a variable-curvature concave surface in a wing leading edge. J. Heat and Mass Transfer, Vol. 90. pp. 92-101.

Bu, X., Peng, L., Lin, G. et al., (2016). Jet impingement heat transfer on a concave surface in a wing leading edge: Experimental study and correlation development. J. Experimental Thermal and Fluid Science, Vol.78, pp. 199-207.

Can, M., Etemoglu, ,A. B. E., and Avci1, A., (2002). Experimental study of convective heat transfer under arrays of impinging air jets from slots and circular holes. J. Heat Mass Transfer, Vol. 38, No. 3, pp. 251–259.

Carlomagno, G. M., Ianiro A., (2014). Thermo-fluid-dynamics of submerged jets impinging at short nozzle-to-surface distance: A review. J. Experimental Thermal and Fluid Science, Vol. 58, pp. 15–35.

Chance, J. L., (1974). Experimental investigation of air impingement heat transfer under an array of round jets. J. Tech. Assoc. Pulp Paper Industry, Vol. 57, No. 6, pp. 108–112.

Chattopadhyay, H., Biswas, G., Mitra, N.K., (2002). Heat transfer from a moving surface due to impinging jets. J. Heat Transfer, Vol. 124, pp. 433–440

Chattopadhyay, H., (2006). Effect of surface motion on transport processes due to circular impinging jets – a numerical study. J. Drying Technology, Vol. 24, No. 11, pp. 1347-1351.

Chen, J., Wang, T., & Zumbrunnen D. A., (1994). Numerical analysis of convective heat transfer from a moving surface cooled by an array of submerged planar jets. J. Numerical Heat Transfer, Part A, Vol. 26, No. 2, pp. 141-160.

Chupp, R. E., Helms, H. E., & McFadden, W., (1969). Evaluation of internal heat-transfer coefficients for impingement-cooled turbine airfoils. J. Aircraft, Vol. 6, No. 3, pp. 203-208.

Chougule, N. K., Parishwad, G. V., Gore, P. R., Pagnis, S., & Sapali, S. N., (2011). CFD analysis of multi-jet air impingement on flat surface. Proceedings of the World Congress on Engineering, London, UK. Vol. 3.

Coussirat, M., Van Beeck, J., Mestres, M., et al., (2005). Computational fluid dynamics modeling of impinging gas-jet systems: I. Assessment of eddy viscosity models. J. Fluids Engineering, Vol. 127, No. 4, pp. 691-703.

Craft, T. J., Graham, L. J., W., & Launder, B. E., (1993). Impinging jet studies for turbulence model assessment-II. An examination of the performance of four turbulence models. Int. J. Heat Mass Transfer, Vol. 36, No. 10, pp. 2685-2697.

Dayal, Y., Paul, A., (2015). Heat transfer enhancement by using nanofluid jet impingement- a review. J. Ignited Minds, Vol. 2, No. 3.

Den Ouden, C., Hoogendoorn, C. J., (1974). Local convective-heat-transfer coefficients for jets impinging on a surface - Experiments using a liquid-crystal technique. In Heat transfer; Proceedings of the Fifth International Conference, Tokyo, Vol. 5, pp. 293-297.

References

Dewan, A., Dutta, R., Srinivasan B., (2012). Recent trends in computation of turbulent jet impingement heat transfer. J. Heat Transfer Engineering, Vol. 33, No.4-5, pp. 447–460.

Dianat, M., Fairweather, M., (1996). Predictions of axisymmetric and two-dimensional impinging turbulent jets. J. Heat and Fluid Flow, Vol. 17, No. 6, pp. 530–538.

Downs, S., & James, E. H., (1987). Jet impingement heat transfer - a literature survey. In ASME, AIChE, and ANS, 24th National Heat Transfer Conference and Exhibition.

Durbin, P., (1993). Application of a near-wall turbulence model to boundary layers and heat transfer. Int. J. Heat Fluid Flow Vol,14, No. 4, pp. 316–323.

Dyban, E. P., Mazur, A. I., & Golovanov, V. P., (1980). Heat transfer and hydrodynamics of an array of round impinging jets with one-sided exhaust of the spent air. Int. J. Heat Mass Transfer, Vol. 23, No. 5, pp. 667–676.

Ekkad, S., Huang, Y., & Han, J., (2000). Impingement heat transfer measurements under an array of inclined jets. J. Thermophysics and Heat Transfer, Vol. 14, No. 2, pp. 286-288.

Ekkad, S. V., Gao, L., & Hebert, R. T., (2002, January). Effect of jet-to-jet spacing in impingement arrays on heat transfer. ASME 2002 International Mechanical Engineering Congress and Exposition, pp. 237-244.

El-Gabry, L. A., Kaminski, D. A., (2004). Experimental investigation of local heat transfer distribution on smooth and roughened surfaces under an array of angled impinging jets. J. Turbomachinery, Vol. 127, No. 3, pp. 532-544.

El-Gabry, L. A., & Kaminski, D. A., (2005). Numerical investigation of jet impingement with cross-flow comparison of yang-shih and standard k–ε Turbulence models. J. Computation and Methodology, Vol. 47, No. 5, pp. 441-469.

Etemoglu, A. K., Can M., (2013). Performance studies of energy consumption for single and multiple nozzle systems under impinging air jets. J. Heat and Mass transfer, Vol. 49, No. 8, pp. 1057-1070.

Fenot, M., Dorignac, E., Vullierme, J.-J., (2008). An experimental study on hot round jets impinging a concave surface. J. Heat and Fluid Flow, Vol. 29, No. 4, pp. 945–956.

Filipovic J., Viskanta R., Incropera F. P., Veslockit, A. P., (1994). Cooling of a moving steel strip by an array of round jets. J. Steel Research, Vol. 65, No. 12, pp. 541-547.

Florschuetz, L., Metzger, D., Takeuchi, D., & Berry, R., (1980). Multiple jet impingement heat transfer characteristic: experimental investigation of in-line and staggered arrays with cross-flow, NASA-CR-3217.

Florschuetz, L., Metzger, D., & Truman, C., (1981). Jet array impingement with cross-flow: correlation of streamwise resolved flow and heat transfer distributions, NASA-CR-3373.

Florschuetz, L. W., Metzger, D. E., Su, C. C., Isoda, Y., and Tseng, H. H., (1982). Jet array impingement flow distributions and heat transfer characteristics. effects of initial cross-flow and nonuniform array geometry. Technical Report, NASA-CR-3630, NASA.

Florschuetz, L. W., & Su, C. C.; (1987). Effects of cross-flow temperature on heat transfer within an array of impinging jets. J. Heat Transfer, Vol. 109, No. 1, pp. 74–82.

Fregeau, M., Saeed, F., & Paraschivoiu, I., (2005). Numerical heat transfer correlation for array of hot-air jets impinging on 3-dimensional concave surface, J. Aircraft, Vol. 42, No. 3, pp. 665-670.

Fregeau, M., Gabr, M., Paraschivoiu, I., (2009). Simulation of heat transfer from hot-air jets impinging a three-dimensional concave surface. J. Aircraft, Vol. 46, No. 2, pp. 721-726.

References

Friedman, S. ,J., & Mueller, A. C.,(1951). Heat transfer to flat surfaces. Proceedings, General Discussion on Heat Transfer, pp. 138-142.

Funazaki, K., & Hachiya, K., (2003, January). Systematic numerical studies on heat transfer and aerodynamic characteristics of impingement cooling devices combined with pins. In ASME Turbo Expo 2003, collocated with the 2003 International Joint Power Generation Conference, pp. 185-192.

Galant, S., Martinez, G., (1982). Cross flow influence upon impingement convective heat transfer in circular arrays of jets-A general correlation. In International Heat Transfer conference, Vol. 3, pp. 343-347.

Garimella, S.V., Rice, R.A., (1995). Confined and submerged liquid jet impingement heat transfer. J. Heat Transfer, Vol. 117, No. 4, pp. 871–877.

Garimella, S., and Schroeder, V., (2001). Local heat transfer distributions in confined multiple air jet impingement. J. Electron. Packaging, Vol. 123, pp. 165– 172.

Gardon, R., & Cobonpue, J., (1962). Heat transfer between a flat surface and jets of air impinging on it. International Developments in Heat Transfer (ASME), pp. 454–460.

Gardon, R., & Akfirat, J. C., (1965). The role of turbulence in determining the heat transfer characteristics of impinging jets. Int. J. Heat Mass Transfer, Vol. 8, pp. 1261-1272.

Geers, Leon F. G., Tummers, Mark J., Hanjalić, Kemal, (2004). Experimental investigation of impinging jet arrays. J. Experiments in Fluids, Vol. 36, No. 6, pp. 946-958.

Geers, L. F. G., Tummers, M. J., Bueninck, T. J., Hanjalić K., (2008). Heat transfer correlation for hexagonal and in-line arrays of impinging jets. J. Heat and Mass Transfer, Vol. 51, No. 21–22, pp. 5389–5399.

Giovannini, A, Kim, N. S., (2006, August). Impinging jet: experimental analysis of Flow Field and Heat Transfer for Assessment of Turbulence Models, Proceedings of 13th International Heat Transfer Conference, Sydney, Australia.

Glaser, H., (1962). Untersuchungen an Schlitz- und Mehrdüsenanordnungen bei der Trocknung feuchter Oberflächen durch Warmluftstrahlen. J. Chemie Ingenieur Technik, Vol. 34, No. 2, pp. 200–207.

Goldstein, R. J., Timmers, J. F., (1982). Visualization of heat transfer from arrays of impinging jets. Int. J. Heat Mass Transfer, Vol. 25, pp. 1857-1868.

Goldstein, R. J., Seol, W. S., (1991). Heat transfer to a row of impinging circular air jets including the effect of entrainment. Int. J. Heat Mass Transfer, Vol. 34, No. 8, pp. 2133–2147.

Goodro, M., Park, J., Ligrani, P., Fox, M., and Moon, H. K., (2007). Effects of Mach number and Reynolds number on jet array impingement heat transfer. Int. J. Heat Mass Transfer, Vol. 50, No. 1, pp. 367–380.

Goodro, M., Park, J., Ligrani, P., Fox, M., & Moon, H. K., (2008). Effect of hole spacing on jet array impingement heat transfer. J. Heat and Mass Transfer, Vol. 51, pp. 6243–6253.

Goodro, M., Park, J., Ligrani, P., Fox, M., and Moon, H. K., (2009). Effect of temperature ratio on jet array impingement heat transfer. J. Heat Transfer, Vol. 131, No. 1, pp. 012201.

Goodro, M., Park, J., Ligrani, P., Fox, M., and Moon, H. K., (2010). Mach Number, Reynolds Number, Jet Spacing Variations: Full Array of Impinging Jets. J. Thermophysics and Heat Transfer, Vol. 24, No. 1, pp. 133-144.

Gromoll, B., (1978). Experimentelle Untersuchungen des Wärmeübergangs an von Düsensystemen senkrecht angeströmten ebenen Flächen, Ph.D. Thesis, University of Aachen.

Han, B., Goldstein, R. J., (2001). Jet-impingement heat transfer in gas turbine systems. Annals New York Academy of Sciences, Vol. 934, No. 1, pp. 147–161.

References

Harrington, J., Hossain, J., Wang, W., Kapat, J., Maurer, M., Thorpe, S., (2017). Effect of target wall curvature on heat transfer and pressure loss from jet array impingement. J. Turbomachinery, Vol. 139, No.5.

Hebert, R. T., Ekkad, S. V., Gao, L., Bunker, R. S., (2005). Impingement heat transfer, part II: effect of streamwise pressure gradient. J. Thermophysics and Heat Transfer, Vol. 19, No. 1, pp. 66-71.

Heikkilä, P., & Milosavljevic, N., (1998). Study of high temperature tissue drying, Proc. 11th International Drying Symposium – IDS 98, Halkidiki, pp. 1513–1520.

Heikkilä, P. and Milosavljevic, N., (2002). Investigation of impingement heat transfer coefficients at high temperatures. J. Drying Technology, Vol. 20, No. 1, pp. 211–222.

Heo, M. W., Lee, K. D., Kim, K. Y., (2012). Parametric study and optimization of staggered inclined impinging jets on a concave surface for heat transfer augmentation. J. Numerical Heat Transfer, Part A: Applications, Vol. 61, No. 6, pp. 442-462.

Hilgeroth, E., Wärmeübergang bei Düsenströmung senkrecht zur Austauschfläche Chem Ing. Tech., (1965), Vol. 37, No.12, pp. 1264–1272.

Hong, S. K., & Cho, H., H., (2005). The review of studies on heat transfer in impinging jet. Int. J. Air-Conditioning and Refrigeration, Vol. 13, No. 4, pp.196–205.

Hollworth, B. R., Berry, R. D. (1978). Heat transfer from arrays of impinging jets with large jet-to-jet spacing. J. Heat Transfer; Vol. 100, No. 2, pp. 352-357.

Hollworth, B. R., & Cole, G. H., (1987). Heat transfer to arrays of impinging jets in a cross-flow. J. Turbomachinery, Vol. 109, No.4, pp. 564–571.

Hofmann, H. M., Kaiser R., Kind, M., Martin, H., (2007). Calculations of steady and pulsating impinging jets-an assessment of 13 widely used turbulence models, Numerical Heat Transfer, Part B: Fundamentals. Int. J. Computation and Methodology, Vol. 51, No.6, pp. 565–583.

Hossain, J., Fernandez, E., Kapat, J., (2016). A detailed experimental and numerical investigation of flow physics in a single row narrow impingement channel using PIV, LES and RANS, 52nd AIAA/SAE/ASEE Joint Propulsion Conference, Salt Lake City, UT.

Hrycak, P., (1981a). Heat transfer from a row of impinging jet to concave cylindrical surfaces. Int. J. Heat Mass Transfer, Vol. 24, No.3, pp. 407–419.

Hrycak, P., (1981b). Heat transfer from impinging jets, a literature review, NEW JERSEY INST OF TECH NEWARK.

Huang, G. C., (1963). Investigations of heat transfer coefficients for air flow through round jets impinging normal to a heat transfer surface. J. Heat Transfer, Vol. 85, No.3, pp. 237-243.

Huber, A. M., & Viskanta, R., (1994). Effect of jet–jet spacing on convective heat transfer to confined, impinging arrays of axisymmetric jets. Int. J. Heat Mass Transfer, Vol.37, No.18, pp. 2859–2869.

Hwang, J. J., Cheng, C. S., (2001). Impingement cooling in triangular ducts using an array of side-entry wall jets. Int. J. Heat and Mass Transfer, Vol. 44, No.5, pp.1053-1063.

Ibrahim, M. B., Kochuparambil, B. J., Ekkad, S. V., & Simon, T. W., (2005, January). CFD for jet impingement heat transfer with single jets and arrays. In ASME Turbo Expo 2005: Power for Land, Sea, and Air, pp. 359-373.

Ichimiya, K., Okuyama, K., (1991). Characteristics of impingement heat transfer caused by circular jets with confined wall. Proc. 3rd Int. Cold Regions Heat Transfer Corzfi, pp. 5233532 (Edited by J. P. Zarling). University of Alaska-Fairbanks, AK.

References

Imbriale, M., Ianiro, A., Meola, C., Cardone, G., (2014). Convective heat transfer by a row of jets impinging on a concave surface. Int. J. Thermal Sciences, Vol. 75, pp.153–163.

Ito, R., Takeishi, K., Oda, Y., & Yoshida, N., (2007, January). Heat transfer for round air jets flowing along a concave surface. In ASME/JSME 2007 Thermal Engineering Heat Transfer Summer Conference collocated with the ASME 2007 InterPACK Conference, pp. 597-605.

Jambunathan, K. Lai, E., Moss, M. A., & Button, B. L., (1992). A review of heat transfer data for single circular jet impingement. Int. J. Heat Fluid Flow, Vol.13, No. 2, pp.106-115.

Journeaux, I. R. H., Crotogino, & Douglas, W. J. M., (1992). Impinging jet heat transfer in calendar control systems: Pan I and 11, in preparation.

Jung, E. Y., Park, C. U., Lee, D. H., Kim, K. M., Woo, T. K., & Cho, H. H., (2012, June). Heat transfer characteristics of an angled array impinging jet on a concave duct. In ASME Turbo Expo 2012: Turbine Technical Conference and Exposition, pp. 601-607.

Kadiyala, P. K., Chattopadhyay, H., (2017). Numerical simulation of transport phenomena due to array of round jets impinging on hot moving surface. J. Drying Technology, Vol. 35, No.14, pp.1742-1754.

Kaiser, E., (2001). Measurement and visualization of impingement cooling in narrow channels. J. Exp. Fluids, Vol. 30, No. 6, pp. 603–612.

Kamal, R. M., El Sayed Mostafa, M., Abdel Aziz, S. S., (2006, December). An experimental study of an oblique multiple circular air jet impingement on a flat surface, Eighth International Congress of Fluid Dynamics and Propulsion, Egypt.

Kanokjaruvijit, K., Martinez-Botas, R. F., (2010). Heat transfer correlations of perpendicularly impinging jets on a hemispherical-dimpled surface. J. Heat and Mass Transfer, Vol. 53, No. 15–16, pp. 3045–3056.

Katti, V., & Prabhu, S., (2008). Influence of spanwise pitch on local heat transfer distribution for in-line arrays of circular jets with spent air flow in two opposite directions. J. Exp. Thermal Fluid Sci., Vol. 33, No. 1, pp. 84-95.

Katti, V., Prabhu, S. V., (2009). Influence of streamwise pitch on the local heat transfer characteristics for in-line arrays of circular jets with cross-flow of spent air in one direction. J. Heat and Mass Transfer, Vol. 45, No. 9, pp 1167-1184.

Kaushik, M., Kumar, R., Humrutha, G., (2015). Review of computational fluid dynamics studies on jets. J. Fluid Dynamics, Vol. 5, No.3, pp.1-11.

Kastner, W., & Rippel, R., (1988). Jet impingement forces on structures - experiments and empirical calculation methods. J. Nuclear Engineering and Design, Vol. 105, pp. 269−284.

Kercher, D. M., .& Tabakoff, W., (1970). Heat transfer by a square array of round air jets impinging perpendicular to a flat surface including the effect of Spent Air. J. Eng. Power, Vol. 92, No.1, pp.73-82.

Koopman, R. N., & Sparrow, E. M., (1976). Local and average heat transfer coefficients due to an impinging row of jets. Int. J. Heat Mass Transfer, Vol. 19, No.6, pp. 673-683.

Krotzsch, P., (1986). Wärme- und Stoffübertragung bei Prallströmung aus Dosen- und Blendenfeldern. Chemie Ing. Tech., Vol. 40, pp. 339–344.

Kumar, B. V. N. R., and Prasad, B. V. S. S. S., (2008). Experimental investigation of flow and heat transfer for single and multiple rows of circular jets impinging on a concave surface. ASME Paper No. GT2008-51044.

Lee, J., Lee, S. J., (1999). Stagnation region heat transfer of a turbulent axisymmetric jet impingement. J. Experimental Heat Transfer, Vol. 12, No. 2, pp. 137–156.

References

Lee, J., Ren, Z., Haegele, J., et al., (2013). Effects of jet-to-target surface distance and Reynolds number on jet array impingement heat transfer. J. Turbomachinery, Vol. 136, No. 5, p. 051013.

Lee, J., Ren, Z., Ligrani, P., Lee, D. H., Fox, M. D., Moon, H. K., (2014). Cross-flow effects on impingement array heat transfer with varying jet-to-target surface distance and hole spacing, J. Heat and Mass Transfer, Vol. 75, pp. 534–544.

Lee J., Ren, Z., Ligrani, L., Fox, M. D., Moon, H. K., (2015). Cross-flows from jet array impingement cooling: Hole spacing, target surface distance, Reynolds number effects. J. Thermal Sciences, Vol. 88, pp. 7-18.

Levy, Y., Rao, A. G., Erenburg, V., Sherbaum, V., Gaissinski, I., & Krapp, V., (2012, June). Pressure losses for jet array impingement with cross-flow, In ASME Turbo Expo 2012: Turbine Technical Conference and Exposition, pp. 139-149.

Li, X. C., and Corder, P., (2008). Characteristics of cooling of the leading edge with a row of dual impinging jets. ASME Paper No. HT2008-56347.

Livingood, J. N. B., Gauntner, J. W., (1973). Local heat transfer characteristics of row of circular air jets impinging on a concave surface, TM-X-2657.

Livingood, J. N. B., and Hrycak, P., (1973). Impingement heat transfer from turbulent air jets to flat surfaces: a literature survey. NASA, Lewis Research Center.

Mahesh, K., (2013). The interaction of jets with cross-flow. Annual Review of Fluid Mechanics, Vol. 45, pp. 379-407.

Manceau, R., (2004). Impinging jet, Université de Poitiers, Retrieved May 22, 2017 from http://qnet-ercoftac.cfms.org.uk/w/index.php/UFR_3-09_Best_Practice_Advice

Martin, E.L., (2012). Experimental and numerical investigation of high temperature jet impingement for turbine cooling applications, MSc Thesis, Department of Mechanical Engineering, Baylor University.

Martin, H., (1977). Heat and mass transfer between impinging gas jets and solid surfaces. J. Advances in heat transfer, Vol.13, pp. 1-60.

Meola, C., Carlomagno, G. M., (2006, June). Intensive cooling of large surfaces with arrays of jets, Proc. Quantitative Infrared Thermography QIRT Conf., Padova, Italy, CD Rom 064.

Meola, C., (2009). A new correlation of Nusselt number for impinging jets. J. Heat Transfer Engineering, Vol. 30, No. 3, pp. 221-228.

Metzger, D. E., Yamashita, T. T., Jenkins, C. W.; (1969). Impingement cooling of concave surfaces with lines of circular air jets. J. Eng. Power, Vol. 91, No. 3, pp. 149-155.

Metzger, D. E., & Korstad, R. J., (1972). Effects of cross-flow on impingement heat transfer. J. Engineering for Power, Vol. 94, No.1, pp. 35-41.

Metzger, D. E., Florschuetz, L. W., Takeuchi, D. I., Behee, R. D., & Berry, R. A., (1979). Heat transfer characteristics for in-line and staggered arrays of circular jets with cross-flow of spent air. J. Heat Transfer, Vol. 101, No. 3, pp. 526-531.

Metzger, D. E., (1987, December). Heat transfer in gas turbine engines, Winter Annual Meeting of the American Society of Mechanical Engineers, Boston, Massachusetts, Vol. 87.

Miao, J. M., Wu, C. W., Chen, P. H., (2009). Numerical investigation of confined multiple-jet impingement cooling over a flat surface at different cross-flow orientations. J. Numerical Heat Transfer, Part A: Applications, Vol. 55, No. 11, pp.1019-1050.

References

Mujumdar, A. S., & Huang, B., (1995), Impingement drying. Handbook of Industrial Drying, Chapter 14, Marcel Dekker.

Mujumdar, A. S., (2004). Research and development in drying: recent trends and future prospects. J. Drying Technology, Vol. 22, No. 1-2, pp. 1-26.

Nastase, I., & Bode, F., (2018). Impinging jets – a short review on strategies for heat transfer enhancement. E3S Web of Conferences, Vol.32.

Obot, N. T., Trabold, T. A., (1987). Impingement heat Transfer within arrays of circular jets: Part 1 - effects of minimum, intermediate, and complete Cross-flow for small and large Spacings. J. Heat Transfer, Vol. 109, No.4, pp. 872-879.

Park, J., Goodro, M., Ligrani, P., Fox, M., Moon, H. K., (2007). Separate effects of Mach number and Reynolds number on jet array impingement heat transfer. J. Turbomachinery, Vol. 129, No. 2, pp. 269–280.

Patil, V. S., Vedula R. P., (2015, December). Heat transfer with single and two rows of axisymmetric jets impinging on a concave surface. 1st International ISHMT-ASTFE Heat and Mass Transfer Conference, Thiruvananthapuram, India.

Patil, V. S., Vedula, R. P., (2018). Local heat transfer for jet impingement on a concave surface including injection nozzle length to diameter and curvature ratio effects. J. Experimental Thermal and Fluid Science, Vol. 92, pp. 375-389.

Penumadu, P. S., Rao, A. G., (2017). Numerical investigations of heat transfer and pressure drop characteristics in multiple jet impingement system. J. Applied Thermal Engineering, Vol. 110, PP. 1511-1524.

Peper, F., Leiner, W., Fiebig, M., (1995). Drying performance and surface forces of a pair of impinging radial jets, Springer. J. Heat and Mass Transfer, Vol. 30, No. 5, pp 313-320.

Peper, F., Leiner, W., Fiebig, M., (1997). Impinging radial and in-line jets: A comparison with regard to heat transfer, wall pressure distribution, and pressure loss. J. Experimental Thermal and Fluid Science, Vol. 14, No. 2, pp.194–204.

Polat, S., Huang, B., Mujumdar, A. S., & Douglas, W. J. M., (1989). Numerical flow and heat transfer under impinging jets: a review. Annual Review of Heat Transfer, Vol.2, No. 2, pp. 157-196.

Polat S., (1993). Heat and mass transfer in impingement drying. J. Drying Technology, Vol. 11, No. 6, pp. 1147-1176.

Polat. S., Douglas, W.J.M., (1990). Heat transfer under multiple slot jets impinging on a permeable moving surface. J. AIChE, Vol. 36, No. 9, pp. 1370-1378.

Polat, S., Mujumdar, A. S., & Douglas, W. J. M., (1991). Impingement heat transfer under a confined slot jet. Part II: Effects of surface motion and throughflow. J. Chemical Engineering, Vol. 69, No. 1, pp. 274-280.

Prasad, K. D., Kumar, K. R., Sastry, M. R. C. H., (2012). Fluid flow and heat transfer analysis of turbulent multiple circular jets impinging on a flat surface. J. Engineering Research and Applications, Vol. 2, No. 5, pp.1976-1985.

Rama Kumar, B. V. N., Prasad, B. V. S. S. S., (2008). Computational flow and heat transfer of a row of circular jets impinging on a concave surface. J. Heat and Mass Transfer, Vol. 44, No. 6, pp. 667-678. Advances in heat transfer, Vol. 39, pp. 565-631.

Rao, G. A., Kitron-Belinkov, M., Levy, Y., (2009, January). Numerical analysis of a multiple jet impingement system. In ASME Turbo Expo 2009: Power for Land, Sea, and Air, pp. 629-639.

References

Rhee, D. H., Yoon, P. Y., Cho, H. C., (2003). Local heat/mass transfer and flow characteristics of array impinging jets with effusion holes ejecting spent air. Int. J. Heat Mass Transfer, Vol.46, No.6, pp. 1046–1061.

Roache. P. J., (1994). A method for uniform reporting of grid refinement studies. J. Fluids Engineering, Vol. 116, pp. 405–413.

Roache. P. J., (2003). Conservatism of the grid convergence index in finite volume computations on steady-state fluid flow and heat transfer. J. Fluids Engineering. Vol. 125, pp. 731–735.

Robertson, P., (2005). The Design and Validation of an Impinging Jet Test Facility, Master's Thesis, Baylor University, Texas.

Saeed, F., (2008). Numerical simulation of surface heat transfer from an array of hot-air jets. J. Aircraft, Vol. 45, No. 2, pp. 669-714.

San, J., Y., & Lai, M., (2001). Optimum jet-to-jet spacing of heat transfer for staggered arrays of impinging air jets. Int. J. Heat Mass Transfer, Vol. 44, No. 21, pp. 3997–4007.

San, J.-Y., Tsou, Y.-M., and Chen, Z.-C., (2007). Impingement heat transfer of staggered arrays of air jets confined in a channel. Int. J. Heat Mass Transfer, 2007, Vol. 50, No. 19–20, pp. 3718–3727.

San, J.-Y, Chen J. J., (2014). Effects of jet-to-jet spacing and jet height on heat transfer characteristics of an impinging jet array. J. Heat and Mass Transfer, Vol. 71, pp. 8–17.

Seyad-Yaggobi, J., Narayanan, V., Page, R. H., (1998). Comparison of heat transfer characteristics of radial jet reattachment nozzle to in-line impinging jet nozzle. J. Heat Transfer, Vol. 120, No. 2, pp. 335-341.

Shelke, R. E., and Bhuyar, L. B., (2009). Heat transfer between impinging circular air jet and finned flat surface and validation of results using artificial neural network. J. Computer Science & Technology, Vol. 2, No. 1, pp. 63-67.

Shi, Y., Ray, M. B., Mujumdar, A. S., (2002). Effects of Prandtl number on impinging jet heat transfer under a semi-confined turbulent slot jet. International Communications in Heat and Mass Transfer, Vol. 29, pp. 929–938.

Shukla, A. K., Dewan, A., (2017). Flow and thermal characteristics of jet impingement: comprehensive review. J. Heat and Technology, Vol.35, No.1, pp.153-166.

Specht, E., (2014). Impinging jet drying, Modern Drying Technology, Volume 5: Process Intensification, First Edition, Published by Wiley-VCH Verlag GmbH & Co. KGaA.

Spring, S., (2010). Numerical prediction of jet impingement heat transfer. PhD Thesis. Faculty of Aerospace Engineering and Geodesy. Universität Stuttgart.

STAR-CCM+ V13.02.013 User guide by CD-Adapco.

Taghinia, J., Rahman, M. M., Siikonen, T., (2014). Numerical investigation of twin-jet impingement with hybrid-type turbulence modeling. J. Applied Thermal Engineering, Vol. 73, pp. 648-657.

Taslim, M. E., & Rosso, N., (2012, June). Experimental/numerical study of multiple rows of confined jet impingement normal to a surface at close distances. In ASME Turbo Expo 2012: Turbine Technical Conference and Exposition, pp. 193-205.

Trabold, T. A. Obot, N. T., (1987). Impingement heat transfer within arrays of circular jets: Part II-Effects of cross-flow in the presence of roughness elements. J. Turbomachinery, Vol. 109, No. 4, pp. 594-601.

Uddin, N., Neumann, S. O., & Weigand, B., (2013). LES simulations of an impinging jet: On the origin of the second peak in the Nusselt number distribution. Int. J. Heat and Mass Transfer, Vol.57, No.1, pp. 356-368.

References

Van Treuren, K. W., Wang, Z., Ireland, P., Jones, T. V., & Kohler, S. T., (1996, June). Comparison and prediction of local and average heat transfer coefficients under an array of in-line and staggered impinging jets. In ASME 1996 International Gas Turbine and Aeroengine Congress and Exhibition, pp. V004T09A005-V004T09A005.

Viskanta, R., (1993). Heat transfer to impinging isothermal gas and flame jets. J. Experimental thermal and fluid science, Vol.6, No. 2, pp. 111-134.

Wae-hayee, M., Tekasakul, P., Nuntadusit, C., (2013). Influence of nozzle arrangement on flow and heat transfer characteristics of arrays of circular impinging jets. J. Science & Technology, Vol. 35, No. 2.

Wae-Hayee, M., Tekasakul, P., Eiamsa-ard, S., Nuntadusit, C., (2015). Flow and heat transfer characteristics of in-line impinging jets with cross-flow at short jet-to-surface distance. J. Experimental Heat Transfer, Vol. 28, No. 6, pp. 511-530.

Wang, X. K., Niu, G. P., Yuan, S. Q., Zheng, J. X., & Tan, S. K., (2015). Experimental investigation on the mean flow field and impact force of a semi-confined round impinging jet. J. Fluid Dynamics Research, Vol. 47, No. 2, p. 025501.

Webb, B. W., Ma, C., F., (1995). Single-phase liquid jet impingement heat transfer. J. Advance in Heat Transfer, Vol. 26, pp.105-217.

Weigand, B., Spring, S., (2011). Multiple jet impingements - a review. J. heat transfer, Vol. 42, No. 2, pp. 101-142.

Xing, Y., Spring, S., Weigand, B., (2010). Experimental and numerical investigation of heat transfer characteristics of in-line and staggered arrays of impinging jets. J. Heat Transfer, Vol. 132, No. 9, pp. 092201.

Xing, Y., Weigand, B., (2013). Optimum jet-to-surface spacing of in-line impingement heat transfer for different cross-flow schemes. J. Heat Transfer, Vol. 135, No.7, pp. 072201.

Xing, Y., Weigand, B., (2010, October). Experimental investigation on staggered impingement heat transfer on a rib roughened surface with different cross-flow schemes. In ASME Turbo Expo 2010: Power for Land, Sea, and Air, pp. 1-11.

Yamane, Y., Ichikawa, Y., Yamamoto, M., Honami, S., (2012). Effect of injection parameters on jet array impingement heat transfer. Int. J. Gas Turbine, Propulsion and Power Systems, Vol. 4, No. 1, pp.27-34.

Yamane, Y., Yamamoto, M., Motosuke, M., Honami, S., (2013, June). Effect of jet shape of square array of multi-impinging jets on heat transfer. In ASME Turbo Expo 2013: Turbine Technical Conference and Exposition, pp. V03AT12A014-V03AT12A014.

Yan, W. M., Liu, H. C., Soong, C. Y., (2003). Experimental study of impinging heat transfer of in-line and staggered jet arrays by transient liquid crystal technique. J. Flow Visualization and Image Processing, Vol.10, No.1-2, pp.119–141.

Yang, B., Chang, S., Wu, H., Zhao, Y., Leng, M., (2017). Experimental and numerical investigation of heat transfer in an array of impingement jets on a concave surface. J. Applied Thermal Engineering, Vol.127, pp. 473–483.

Yeranee, K., Wae-hayee ,M., Piya, I., Rao, Y., Nuntadusit ,C., (2017). The study of flow and heat transfer characteristics of impinging jet array mounting air-induced duct. IOP Conf. Series: Materials Science and Engineering, Vol. 243.

Yong, S., Jing-zhou, Z., Gong-nan, X., (2015). Convective heat transfer for multiple rows of impinging air jets with small jet-to-jet spacing in a semi-confined channel. J. Heat and Mass Transfer, Vol.86, pp. 832–842.

References

Yu, Z., Xu, T., Li, J., Xiu, H., Li, Y., (2013). Numerical simulation on the effect of turbulence models on impingement cooling of double chamber model. J. Mathematical Problems in Engineering, Vol. 2013.

Zhu, D., Wang, Y., Zhu, J., (2015). Heat transfer characteristics of multinozzle air impingement jet during die steel surface cooling progress. J. Advances in Mechanical Engineering, Hindawai Publishing Corporation, p. 698072.

Zu, Y. Q., Yan, Y. Y., Maltson, J. D., (2009, January). CFD prediction for multi-jet impingement heat transfer. In ASME Turbo Expo 2009: Power for Land, Sea, and Air, pp. 483-490.

Zuckerman, N., Lior, N., (2006). Jet impingement heat transfer: physics, correlations, and numerical modeling. J. Advances in heat transfer, Vol. 39, pp. 565-631.

Appendix A

A Related Literature on Multiple Impinging Jet Flow

Table A.1 Summary of studies of jet impingement heat and mass transfer

Source	Methods		Validity Range	Comments
	Experimental	Numerical		
Friedman et al.(1951)	***		d= 6.34-19.05mm H=57.2 -158.8	Correlation of Nu_{ave}
Gardon et al. (1962)	***		Re = 10^3- 13×10; H/d≥1; Af=0.0077-0.049	Correlation of Nu_{ave}
Huang (1963)	***		Re=1,000-10,000; A_f=0-10; H/d=1-25	Optimization of H/d and S/d
Metzger et al. (1969)	***		H/d=7-22.6; S/d=1.67-6.67; Re=1,000-5,500; L=25-51	Surface curvature and Correlation of St_{max}
Chupp et al. (1969)	***		Re=3,000-15,000; H/d= 1-10; d/D= 1.5-16; S/d= 4-16	Surface curvature and Correlation of Nu_{ave} and Nu_{st}
Kercher et al. (1970)	***		Re=330-37,000; S/d= 1.56-50; H/d=1-4.8	Correlation of Nu_{ave}
Metzger et al. (1972)	***		d=2.54; S/d= 2.5-5; H/d=2-6.7; G_c/G_j=1-3	Effects of cross-flow, Optimization of H/d and S/d, Correlation of Nu_{ave}
Livingood et al.(1973)	***		H/d=2-8, d/D=13.3-40, S/d=2-8, Re=2,500-30,000	Surface curvature and Correlation of local to average Nu
Koopman et al. (1976)	***		d=6.35mm; Re=2,500-10,000; H/d=2-10; S/d=4-6.67	mass transfer coefficients
Hollworth et al.(1978)	***		d=2-5.5; H/d=1-20; S_y/d=10-25; S_x/d=10-25; Re=3,000-35,000	Large jet-to-jet spacing and Correlation of Nu_{ave}
Martin et al. (1977)	***		Re=2,000-100,000; H/d=2-12; A_f=0.004-0.04	Optimization of H/d and S/d; Correlation of Nu_{ave}
Metzger et al. (1979)	***		Re= 5,000–20,000; d= 0.635–2.54; H/d= 2–3	Nozzle arrangement
Florschuetz et al. (1980)	***		S_x/d=5, 10,15; S_y/d= 4, 6,8; number of transverse hole rows=10; channel heights=1, 2,3d	Nozzle arrangement
Florschuetz et al. (1981)	***		Re=2,500-70,000; H/d=1-3; V_c/V_j=0-0.8; S_x/d=5-15 for in-line arrays, 5-10 for staggered arrays; S_y/d =4-8; S_x/S_y = 0.625-3.75	Correlation of Nu_{ave}
Hrycak et al. (1981a)	***		Re=25,000-66,000;H/d=3-20; S/d=2-8; d/D= 0.25-0.75	Surface curvature and Correlation of Nu_{ave}
Galant et al. (1982)		Mathematic modeling	d=5-12; H/d=4-18; S/d=4-8; Re=4,000-30,000	Correlation of Nu_{ave}

Behbahani et al. (1983)	***		S/d=4,8; d= 5–10; H/d=2-5; Re=10,000	Correlation of Nu_{ave}
Obot et al. (1987)	***		Re=1,000-21,000; H/d =2-16; A_f =0.0098- 0.0352	Effects of cross-flow and Correlation of Nu_{ave}
Trabold et al. (1987)	***		Re= 1,300-21,000; H/d=2-16	Cross-flow in presence of roughness elements
Florschuetz et al. (1987)	***		Re=6,000-20,000;S/d= 4-10; H/d=2-3; G_c/G_j=0.2-4.5	Effects of cross-flow temperature relative to jet temperature
Goldstein et al. (1991)	***		Re=10,000-40,000; H/d=0-6 ;S/d=4-8	Effect of Entrainment and Correlation of Nu_{ave}
Filipovic et al.(1994)		Mathematic Modeling		Surface Motion
Huber et al. (1994)	***		H/d=0.25-6; Re=3,400-20,500; S/d=4-8; A_f = 0.0123 - 0.0491	Small H/d and Correlation of Nu_{ave}
Barata et al. (1996)	***	k-ε	Re=6×10^4 and 1.05×10^5; H/d=5; V_j/V_c = 30	Characteristics of Fountain Flows
Van Treuren et al. (1996)	***		Re=10,000–40,000; H/d=1-4; $A_f \leq 0.0123$	Nozzle arrangement and Correlation of Nu_{ave}
Peper et al. (1997)	***		$+45° \leq \theta \leq +60°$	Jet angle and force
Ekkad et al. (2000)	***		S/d=4; H/d=3; Θ= $\pm45°$	Jet angle
San et al. (2001)	***		Re=10,000-30,000; H/d= 2-5; S/d=4-16	Optimum S/d and Correlations of Nu_{st}
Garimella et al. (2001)	***		Re=5,000-20,000; H/d= 0.5-4; S/d=3,4	Correlations of Nu_{ave}
Ekkad et al. (2002)	***		Re= 5,000-15,000; H/d=1-5; S/d =4 and 8	Effect of S/d
Can (2002)	***		d=5 and 10mm; V_j=20-60m/s;T_j=20-30º; H/d=4-20;A_f=0.5-12.5;	Optimum free area
Heikkila et al. (2002)	***		T_j=100 to 700 C	High Jet Temperatures
Brevet et al.(2002)	***			minimizing the amount of cooling air
Rhee et al. (2003)	***	RSM	H/d=2-10; Re= 10,000	Cross-flow and effusion holes
Yan et al. (2003)	***		H/d=3-9; Re = 1,500-4,500	Nozzle Arrangement
El-Gabry et al. (2004)	***		θ =30-90º; Re=15,000 35,000; H/d=1-2	angled jet and roughness
Geers et al. (2004)	***			measurements of the velocity field and turbulence fluctuations
Fregeau et al. (2005)		Spalart–Allmaras	H/ d = 5-15; Ma= 0.4-0.8; S/d=7.5-22.5	Surface curvature and correlation of Nu_{ave} and Nu_{max}

Hebert et al. (2005)	***		S/d=4 and 8; Re= 6,000and 1,000; H/d=1-5	nonparallel walls and streamwise pressure gradient
Ibrahim et al. (2005)		k-ε, k–ω, V2F	Re=3,000-23,000; H/d=2-14	V2F is recommended
El-Gabry and Kaminski (2005)		Standard k-ε and the Yang-Shih	Re= 10,000-35,000; H/d= 1-2; θ=30º-90º	Jet angle; Yang-Shih is recommended
Chattopadhyay et al. (2006)		realizable k-ε	Re=100-2,500; H/d=2; S/d= 10; V_w/V_j =0,0.1,0.5,1	Surface Motion
Kamal et al. (2006)	***		S/d = 2.5-5.5; H/d = 2-6; θ=60-90º	Jet angle and Optimization
Al-Hadhrami et al. (2006)	***		Re=9,300-18,800; H/d=5-9	Effect of orifice jet configuration
Meola et al. (2006)	***		H/d= 4–8.3; Re= 30,000–80,000; A_f =0.05	Correlation of Nu_{ave}
Goodro et al. (2007)	***		Re=60,000; A_f= 0.123; Ma= 0.21-0.74; S/d=8; H/d=3	Extention to correlation by Florschuetz et al. (1981)
Ito et al. (2007)	***	Realizable k-ε	D=2mm; Re =5,000-15,000; H/d=3.75, D/d=20	Surface curvature
Park et al. (2007)	***		Ma=0.2-0.6; Re=60,000; H/d=3; A_f=0.0123	Correlation of Nu_{ave}
San et al. (2007)	***		Re=5,000–15,000; H/d = 1.0–4.0; S/d=4-8;W/d = 6.25–18.75; L/d = 31.7 and 83.3	Correlation of Nu_{st}
Goodro et al. (2008)	***		Re= 8,200-30,500; Ma= 0.1-0.2; S/d=8-12	Effects of S/d
Geers et al. (2008)	***		Re=5×10³-2×10⁴; H/d=3-10; S/d=2-6	Nozzle arrangement and Correlation of Nu_{ave}
Rama Kumar et al. (2008)		SST K-ω	d=25.17-29.07 mm; D= 152.4 mm; Re=5,000-67,800; S/d=3.33-4.67; H/d = 1.3-4	Surface curvature
Fenot et al. (2008)	***		Re=10,000-23,000; H/d=2 to 5; d/D= 0.1, 0.15, 0.2; S/d=4or 8	High surface curvature and Correlation of Nu_{st}, Nu_{ave}
Saeed (2008)		Realizable k-ε	Re=149,402- 460,096; θ=0-20º	Jet angle and etched surface
Katti et al. (2008)	***		Re=3,000-10,000; H/d=1-3; S_y/d =2,4,6, S_x/d=5	Effect of spanwise pitch and Correlation of Nu_{ave}
Kumar & Prasad(2008)	***		Re= 2,847-19,300; d=10mm; D=300mm, H/d=1; S/d=6.8; number of rows= 1 and 5	Surface curvature and number of rows
Miao et al. (2009)		Realizable k-ε	Re=2,440-14,640;H/d=1-6; S/d=6	Nozzle arrangement and Correlation of Nu_{ave}
Aldabbagh et al.(2009)		Laminar Flow	Re=100-400;S/d=2-5; H/d= 0.25; V_w/V_j=0.25-1	square jets and surface motion

Katti et al. (2009)	***		Re= 3,000-10,000; H/d=1-3; S_x/d= 3-5; S_y/d=4	Effect of streamwise pitch
Fregeau et al. (2009)		Spalart Allmaras	d=2.5 mm; D/d=20; Ma= 0.4- 0.8; H/d=5-15; S/d= 7.5-22.5	Surface curvature
Rao et al. (2009)	***	SST k-ω	Re<1,000	a large square array of 29×29 submerged jets
Zu et al. (2009)		standard k-ε, renormalization group k-ε, realizable k-ε, standard k-ω, SST k-ω, RSM and LES	Re=10,000-30,000; S/d=6; H/d=2; θ=20º-90º	Jet angle and nozzle arrangement; SST k-ω is recommended
Ashok Kumar et al. (2009)		SST k-ω	H/d=1-5; S/d=5.4; Re= 10,000-37,500	Surface curvature with and without effusion holes; the effects of arrangement of jet orifices and effusion holes
Meola C., (2009)			Re=200-100,000; H/d=1.6-20; A_f = 0.0008	new correlation of Nu_{ave}
Goodro et al. (2009)	***		Re=18,000; Ma=0.2; S/d=8	Correlation of Nu_{ave}; effect of temperature ratio
Kanokjaruvijit et al. (2010)	***		Re=5,000-11,500;H/d=1-12; dimple depths= 0.15-0.29; dimple curvature= 0.25-1.15	Effect of dimples and Correlation of Nu_{ave}
Xing et al. (2010)	***		Re=15,000-35,000; H/d=3-5	Rib roughened surface
Xing et al. (2010)	***	SST k-ω	Re =35,000; H/d =3; A_f = 0.031	Nozzle arrangement
Al-Hadhrami (2010)	***		Re= 9,400-18,800; feed channel aspect ratios=5-9	Inclined target surface
Al-Mubarak et al.(2010)	***		Re= 9,400-18,800; feed channel aspect ratios=5-9	Inclined target surface and effect of orifice-jet surface configuration (centered, staggered, and tangential holes)
Goodro et al.(2010)	***		Re=17,300-60,000; Ma = 0.1-0.45; S/d =5-12	new correlation of Nu_{ave}
Chougule et al. (2011)	***	Standard k-ε, RNG k-ε, Standard k-ω and SST k-ω models	Re=7,000-50,000; H/d=6-10	SST is recommended
Heo et al. (2012)		SST k-ω	d/D=0.2; Re=23,000; S/d= 2-12; H/d=2-10; θ=40-90º	Inclined jets on concave surface and optimization of S/d and jet angle
Jung et al. (2012)	***		Re=3,000-10,000; H/d=1	Inclined jets on concave surface

Taslim et al. (2012)	***	realizable k–ε, standard k-ε, SST k–ω, V2F, LES	Re=10,000–50,000; S/d= 2-4; H/d=0.3-3	Small H/d; Realizable k–ε is recommended
Levy et al. (2012)	***	low Re k-ε;low Re k-ω	Re=200-3,000; H/d=5-7.5; S/d=5	Low Re with Cross-flow
Prasad et al. (2012)	***	SST k-ω	H/d=0.5-4; Re= 9,075-13,624; S/d=4	Pressure Distribution
Martin (2012)	***	SST k-ω	S/d=2-8; H/d=2- 8.5; Re= 5,000-25,000; D/d=3.6-5.5; T_j=60-1,000	Surface curvature and high temperature jet
Yamane et al. (2012)	***		H/d=2-8; S/d=2-8; Re= 4,680	Effect of injection parameters
Badra et al. (2013)		Standard k-ε, RNG $k-\varepsilon$, realizable k–ε, Standard k-ω, SST k–ω, V2F	Re=5,000-30,000; H/d=2-12; S/d=6; V_w= 0.01m/s	Surface motion and optimization of S/d and H/d; SST k–ω is recommended
Xing et al. (2013)	***		Re =15,000-35,000; H/d= 1.2-4.5	Optimum H/d
Yamane et al. (2013)	***		Re=4,680; H/d=2-6; S/d=6	Effect of jet shape
Lee et al. (2013)	***		Re= 8,200-52,000;Ma=0.1-0.2; H/d=1.5-8; S/d=8	effects of H/d and Re
Yu et al. (2013)		RNG k–ε, realizable $k-\varepsilon$, V2F, SST $k-\omega$, LES		Impingement cooling of double chamber model; SST k–ω and V2F is recommended
Wae-Hayee et al. (2013)	***	k–ε	H/d=2; S/d=3; Re=5,000-13,400	Nozzle arrangement
Imbriale et al. (2014)	***		H/d=5-15; S/d=5-15; θ =0-60º	Jet angle and surface curvature
San et al. (2014)	***		S/d=2-8; H/d=0.5-3; Re= 20,000	Small S/d and H/d
Lee et al. (2014)	***		Re=8,000; S/d=5-12; H/d= 1.5-8	Cross-flow effects
Taghinia et al. (2014)		LES and hybrid RANS-LES	Re =30,000-50,000;H/d=1-4; S/d=0.5-2	Hybrid RANS-LES is recommended
Lee et al. (2015)	***		Re= 8,000-50,000; H/d= 1.5-8; S/d=5-12,	combined and separate effects of hole array spacing, jet-to-target surface distance, and Reynolds number on cross-flows
Wae-Hayee et al. (2015)	***	SST k-ω	Re =13,400; H/d=2; S/d=3; V_j/V_c =3-7	Cross-flow at short H/d
Attalla (2015)	***		Re=1,000-45,000;H/d=2-6; S/d=2-8	Optimum S/d and correlation of Nu_{ave}, Nu_{st}
Bu et al. (2015)	***		Re=51,021- 85,340; H/d= 1.736-19.76; θ= -60° to 60°	Surface Curvature, Row number, Optimum H/d
Patil&Vedula (2015)	***		Re=10,000-35,000;H/d=2-4; S/d=4; d//D=0.1	Surface Curvature and Row number

Yong et al. (2015)	***		Re=5,000-25,000; S/d=2-5; H/d=2-4	Small S/d and nozzle arrangement
Zhu et al. (2015)		SST k-ω	H/d=12.5-75; S/d=7.5-17.5	High S/d and H/d, Optimum H/d and S/d
Bu et al. (2016)	***		Re =50,000-90,000; H/d= 1.74-20.0; θ= 66°-90°	Surface Curvature, Optimum H/d and Correlation of Nu_{st}, Nu_x/Nu_{st}
Ansu et al. (2016)	***		Re=5,000-15,000; H/d=2-6;S/d=4	Inlet Condition and Correlation of Nu_{ave}, Nu_{st}
Hossain et al. (2016)	***	SST k-ω, V2F, RSM, LES	Re=15,000; H/d=0.5-3;	Small H/d and LES is recommended
Harrington et al. (2017)	***	V2F	Re=55,000-125,000; S_x/d = 5.79; S_y/d=4.49; H/d=3; d/D= 0.0158	High Re; Surface curvature
Penumadu and Rao (2017)		k-ε, SST k -ω, LES	d=400µm;Re=100-3,000; S/d=5; H/d=5	LES is recommended
Yang et al. (2017)	***	RNG k-ε, Realizable k-ε, S-A, Standard k-ω and SST k- ω	H/d = 10-25; S/d =20-35; d =2-5 mm; θ= 0°- 30°	Surface curvature and optimization of H/d, S/d and θ; SST k-ω is recommended
Kadiyala& Chattopadhyay (2017)		SST k–ω	Re=100-5,000;H/d=2; V_w/V_j = 0-6	Surface Motion
Patil&Vedula (2018)	***		Re=10,000-50,000; H/d= 0.67-8; S/d=4; L/d=0.2- 6; d/D= 0.1-0.3	Effect of nozzle length to diameter& curvature ratio; Correlation of Nu

Appendix B

B Related Correlations on Multiple Impinging Jet Flow

Table B.1 Summery of available impingement heat and mass transfer correlations

Source	Configurations and parameter range	Correlations
Friedman et al.(1951)	Squarr array; d= 6.34-19.05mm; H=57.2 -158.8	$\mathrm{Nu}_{ave} = 0.0572\,\mathrm{Re}^{0.76}\,\mathrm{Pr}^{0.333}(d/S)^{0.24}$
Gardon et al. (1962)	Square array, minimum crossflow; $\mathrm{Re}_j = 10^3\text{-}13\times10^4$; $H/d \geq 1$; $A_f = 0.0077\text{-}0.049$	$\mathrm{Nu}_{ave} = 0.299\,\mathrm{Re}_j^{0.625}A_f^{0.1875}$
Glaser (1962)	Staggered arrays, minimum crossflow; Re_j=5000-50.000; H/d=1-8; A_f=0.016-0.1	$\mathrm{Nu}_{ave} = 1.063(A_f - 1.3)^{0.17}\varphi\,\mathrm{Re}^{0.9}\mathrm{Pr}^{0.42}$ Graphical evaluation of φ
Hilgeroth (1965)	Regular staggered arrays, intermediate crossflow; Re_j=40.000-300.000	$\mathrm{Nu}_{ave} = (9 - 0.354A_f^{-0.5})\mathrm{Re}_j^{0.75}[H/d]^{-0.2}$
Krotzsch (1968)	Regular staggered array, intermediate crossflow; Re_j=200-200.000; H/d=2-12; A_f=0-0.1	$\mathrm{Nu}_{ave} = \mathrm{Nu}_{sin\,gle\,jet}\left[\dfrac{(H/d)_{crit}}{H/d}\right]^{0.3}$ for H/d>(H/d)$_{crit}$ $\mathrm{Nu}_{single\,jet}$ for (H/d)<(H/d)$_{crit}$ $\qquad (H/d)_{crit} = 0.6\sqrt{A_f}$
Chupp et al. (1969)	One line of round jets; H/d= 1-10; D/d= 1.5-16; S/d= 4-16; Re=3,000-15,000	$\mathrm{Nu}_{st} = 0.44\,\mathrm{Re}^{0.6}(d/S)^{0.8}\exp\left[-0.85(H/d)(d/S)(d/D)^{0.4}\right]$ $\mathrm{Nu}_{ave} = 0.63\,\mathrm{Re}^{0.7}(d/S)^{0.5}(d/D)^{0.6}\times$ $\exp\left[-1.27(H/d)(d/s)^{0.5}(d/D)^{1.2}\right]$
Kercher et al. (1970)	Square array of round air jets; Re=300-30,000; H/d=1-4.8; A_f =0.005 0.08	$\mathrm{Nu}_{ave} = \varphi_1\varphi_2\mathrm{Re}_j^m\mathrm{Pr}^{0.333}H/d^{0.091}$ Grafical evaluation of φ_1, φ_2 and m
Metzger et al(1972)	single rows of air jets d=2.54, x/d= 2.5-5, H/d=2-6.7, M*=Q_t/Q_j =1-3	$\mathrm{Nu}_{ave} = 0.0652\,\mathrm{Re}^{0.662}\mathrm{Pr}^{0.333}/M^{*0.049}$
Livingood et al. (1973)	A row of air round jets; H/d=2-8; d/D=13.3-40, S/d=2-8; Re=2,500-30,000; X/L = 0.167-0.833	$\dfrac{\mathrm{Nu}_x}{\mathrm{Nu}_{ave}} = (B+1)(X/L)^B$ $B = -0.419\,\mathrm{Re}^{-0.097}(d/D)^{-0.311}(S/d)^{0.061}(H/d)^{-0.374}$

Chance (1974)	an array of round jets, maximum crossflow; H/d=2-8; A_f=0.012-0.7; $\dfrac{G_c}{G_j}\dfrac{H}{d}\leq 1.8$	$Nu_{ave}=\alpha_1\alpha_2\alpha_3 Re_j^m Pr^{0.333}A_f^{1.0146}$ $m=0.561/A_f^{0.0835}$ $\alpha_1=1.876\,(\text{cooling}),\ 2.06\,(\text{heating})$ $\alpha_2=1.0-0.236\dfrac{G_c}{G_J}\dfrac{H}{d}$ $\alpha_3=\left[1.0-H/d(0.23+0.182A_f^{0.71})\right]$
Hollworth et al.(1978)	Square arrays; H/d=1-20; S_y/d=10-25; S_x/d=10-25; Re=3,000-35,000	$Nu_{ave}=Re^{0.8}Pr^{0.33}f(X/d,H/d)$
Martin et al. (1977)	Regular array of round nozzles, Perforated surfaces; Re=2,000-100,000; H/d=2-12; S/d=1.4-14; A_f=0.004-0.04	$Nu_{ave}=Re^{0.67}Pr^{0.42}\left[1+(\dfrac{H}{d}\dfrac{\sqrt{A_f}}{0.6})^6\right]^{-0.05}\times$ $\sqrt{A_f}\ \dfrac{1-2.2\sqrt{A_f}}{1+0.2(H/d-6)\sqrt{A_f}}$
Gromoll (1978)	Square array; Re=4,000-24,000; H/d=2–37.5; S/d=25-150	$Nu_{ave}=0.863(S/d)^{0.65}(S/H)^n Re^{0.6}Pr^{0.3}$ $n=0.6$ at $S/H>1$ and $n=0.53$ at $S/H<1$
Dyban et al. (1980)	Regular in-line array, maximum crossflow; Re_j=1,100-17,000; H/d=1-10; A_f=0.006-0.57	$Nu_{ave}=Nu_\infty 10\left(\dfrac{X}{d_h}\right)^{-0.95}A_f^{-0.4}$ Nu_∞ : chanel Nusselt number d_h: channel hydraulic diameter
Florschuetz et al. (1981)	Array of round jets; maximum crossflow; Re=2,500-70,000; H/d=1-3; V_c/V_j=0-0.8; S_x/d=5-15 for in-line arrays, 5-10 for staggered arrays; S_y/d=4-8; S_x/S_y=0.625-3.75	$Nu_{ave}=A\,Re^m\left\{1-B\left[(H/d)(V_c/V_j)\right]^n\right\}Pr^{1/3}$ $A_{inline}=1.18(S_x/d)^{-0.944}(S_y/d)^{-0.642}[H\!/\!d]^{0.169})$ $m_{inline}=0.612(S_x/d)^{0.059}(S_y/d)^{0.032}[H\!/\!d]^{-0.022})$ $B_{inline}=0.437(S_x/d)^{-0.095}(S_y/d)^{-0.219}[H\!/\!d]^{0.275})$ $n_{inline}=0.092(S_x/d)^{-0.005}(S_y/d)^{0.599}[H\!/\!d]^{1.04})$ $A_{stagerred}=1.87(S_x/d)^{-0.771}(S_y/d)^{-0.999}[H\!/\!d]^{-0.257})$ $m_{stagerred}=0.571(S_x/d)^{0.028}(S_y/d)^{0.092}[H\!/\!d]^{0.039})$ $B_{stagerred}=1.03(S_x/d)^{-0.243}(S_y/d)^{-0.307}[H\!/\!d]^{0.059})$ $n_{stagerred}=0.442(S_x/d)^{0.098}(S_y/d)^{-0.003}[H\!/\!d]^{0.304})$
Hrycak et al. (1981a)	A row of round air jets; Re=25,000-66,000; H/d=3-20; S/d=2-8; d/D=0.25-0.75	$Nu_{ave}=0.72Pr^{0.33}Re^{0.63}(S/d)^{-0.16}(d/D)^{0.402}$
Behbahani et al. (1983)	Staggered array, maximum crossflow; H/d=2-5; Re=5,000-15,000; A_f=0.0123-0.049	$Nu_{ave}=aRe_j^{0.78}(4A_f/\pi)^{0.5b}$ Coefficiants tabulated in paper

Obot et al. (1987)	Irregular in-line array; Re=1,000-21,000; H/d=2-16; A_f =0.0098-0.0352	Minimum crossflow: $\mathrm{Nu_{ave}} = 0.863\mathrm{Re}_j^{0.8}\left(H/d\right)^a A_f^{0.815}$ Intermediate crossflow: $\mathrm{Nu_{ave}} = 0.484\mathrm{Re}_j^{0.8}\left(H/d\right)^a A_f^{0.676}$ Maximum crossflow: $\mathrm{Nu_{ave}} = 0.328\mathrm{Re}_j^{0.8}\left(H/d\right)^a A_f^{0.595}$ Graphical evaluation of a
Goldstein et al. (1991)	Row of round nozzles, Square-Edged orifice nozzles, Re=10,000-40,000; H/d=2-6; S/d=4-8; Z/d=0-6	$\mathrm{Nu_{ave}} = \dfrac{2.9\exp(-0.09(Z/d)^{1.4})\mathrm{Re}^{0.7}}{22.8+(S/d)\sqrt{H/d}}$
Huber et al. (1994)	Square arrays; H/d=0.25-6; Re=3,400-20,500; S/d=4-8; A_f =0.0123 - 0.0491	$\mathrm{Nu_{ave}} = 0.285\mathrm{Re}^{0.71}\mathrm{Pr}^{0.33}(H/d)^{-0.123}(S/d)^{-0.725}$
Van Treuren et al. (1996)	in-line and staggered arrays of circular jets with crossflow; Re=10,000–40,000; H/d=1; $A_f \leq 0.0123$	in-line arrays of circular jets, maximum crossflow $\mathrm{Nu_{ave}} = (0.436\mathrm{Re}_j^{0.52})\left(1-0.895(G_c/G_j)^{0.0816}\right)$ $+(0.0141\mathrm{Re}_j^{0.785})\left(0.895(G_c/G_j)^{0.0816}\right)$ staggered arrays of circular jets, maximum crossflow $\mathrm{Nu_{ave}} = (0.00916\mathrm{Re}_j^{0.934})\left(1-0.895(G_c/G_j)^{0.0816}\right)$ $+(0.0447\mathrm{Re}_j^{0.650})\left(0.886(G_c/G_j)^{0.0154}\right)$
San et al. (2001)	Staggered array; Re=10,000-30,000; H/d= 2-5; S/d=4-16	For H/d = 2 to 3.5 and S/d= 6 to 16 $\mathrm{Nu_{st}} = (S/d)\exp(\alpha_1+\alpha_2[S/d])\mathrm{Re}^{0.6}$ $\alpha_1 = -0.504-1.662(H/d)+0.233(H/d)^2$ $\alpha_2 = -0.281+0.116(H/d)-0.017(H/d)^2$ For H/d = 3.5 to 6 and S/d= 4 to 8 $\mathrm{Nu_{st}} = (S/d)\exp(\alpha_1+\alpha_2[S/d])\mathrm{Re}^{0.4}$ $\alpha_1 = -2.627+0.564(H/d)-0.049(H/d)^2$ $\alpha_2 = 0.132-0.093(H/d)+0.008(H/d)^2$ For H/d = 3.5 to 6 and S/d= 8to 16 $\mathrm{Nu_{st}} = (S/d)\exp(\alpha_1+\alpha_2[S/d])\mathrm{Re}^{0.5}$ $\alpha_1 = -4.752+1.007(H/d)-0.103(H/d)^2$ $\alpha_2 = 0.229-0.132(H/d)+0.013(H/d)^2$
Garimella et al. (2001)	Regular in-line arrays, minimum crossflow; Re_j=5000-20.000; H/d=0.5-4; S/d=3,4	$\mathrm{Nu_{ave}} = 0.127\mathrm{Re}_j^{0.693}\mathrm{Pr}^{0.4}\left(H/d\right)^{-0.105}$

Hwang et al. (2001)	an array of impinged jets, maximum crossflow; Re=3,000-12,600; S/d=3-6	$\theta = 30^\circ \Rightarrow Nu_{ave} = 0.0051 Re^{0.9791}$ $\theta = 45^\circ \Rightarrow Nu_{ave} = 0.0596 Re^{0.7501}$ $\theta = 60^\circ \Rightarrow Nu_{ave} = 0.0204 Re^{0.9013}$
Bailey et al.(2002)	Regular in-line arrays, maximum cross flow; Re=14,000-65,000; H/d=1.25-5.5; S/d=3-9; $A_f = 0.0097$-0.0873	$Nu_{ave} = 47.1 - 5.5 S/d + \dfrac{H}{d}\left(7.3 - 2.3\dfrac{H}{d}\right) +$ $Re_j\left(0.004 - 1.3e^{-4}S/d - 1.5e^{-8}Re_j\right)$ $+ G_c/G_j(61.2 - 13.7 S/d - 28 H/d)$
Fregeau et al. (2005)	single array of round air jets; H/d = 5-15; Ma= 0.4-0.8; S/d= 7.5,15,22.5	$Nu_{ave} = 10^{-10} Re_G^{1.1131}$ $Nu_{max} = 0.282 Ma^{0.49}(H/d)^{-1.69}(S/d)^{-0.856} \times$ $\exp[9.14(H/d)^{0.034}(S/d)^{0.074}] - 3$ $Re_G = \dot{m}\Big/ (HS)^2 (\pi d\mu/2)(H/d)(S/d)^{1.5}$
Meola et al. (2006)	Three staggered arrays of jets (round and rectangular nozzles); H/d= 4–8.3; Re= 30,000 −80,000; A_f=0.05	$Nu_{ave} = 0.5 Re^{0.625} Pr^{0.42}\left(\dfrac{H/d}{\sqrt{A_f}}\right)^{-0.3}$ for short impingement distances (inside the potential core region) $H/d \cong 4\sqrt{A_f}(S/d)^{5/4}$ while in the fully developed region $H/d \cong 2.15 A_f^{-0.46}(S/d)^{7/6}$
Park et al. (2007)	Staggered array; Ma= 0.2-0.6; Re=60,000; H/d=3; A_f=0.0123	$Nu_{ave}/Nu_{aveF} = (1.0 + 0.58 Ma^{1.35})$
San et al. (2007)	Staggered arrays; Re=5,000-15,000; H/d=1-4; W/d=6.25-18.75; L/d=31.7-83.3	$Nu_{st} = 0.41 Re^{0.7}(W/d)^{-0.49}$
Goodro et al. (2007)	Regular staggered arrays; Re =60,000; A_f =0.123; Ma=0.21-0.74; S/d=8; H/d=3; x/d=20-60	$Nu_{ave}/Nu_{aveF} = (1.0 + 0.325 Ma^{1.55})$
Geers et al. (2008)	Hexagonal and in-line arrays of jets; Re=5,000-20,000; H/d=3-10; S/d=2-6	$Nu_{ave} = Re^{\alpha_1}\dfrac{\exp\left\{\alpha_2(H/d)^{\alpha_3}\right\}}{(S/d)^{\alpha_4}(H/d)^{\alpha_5}}$ Coefficients tabulated in paper
Fenot et al. (2008)	A row of air jets; Re=10,000-23,000; H/d=2-5; d/D= 0.1-0.2; S/d=4or 8	$Nu_{st} = 0.18 Re^{0.69}(H/d)^{0.09}(d/D)^{0.24}$ $Nu_{ave} = 0.042 Re^{0.72}(H/d)^{-0.06}(d/D)^{-0.085}$
Katti et al. (2008)	in-line rectangular array; Re=3,000-10,000; H/d=1-3; S_y/d =2-6; S_x/d=5	$Nu_{ave} = a_o(Re^{a_1}Pr^{0.333})\left(\dfrac{G_j}{G_j}\right)^{a_2}\left(1 - b_1\dfrac{G_c}{G_j}\right)^{b_2}$ Coefficient tabulated in paper
Attalla and Specht (2009)	in-line arrays;	$Nu_{ave} = 0.104 Re^{0.7}$

	H/d=2-6; S/d=6; Re=1,400-41,400	$Nu_{st} = 0.71Re^{0.5}$
Meola (2009)	General correlation; H/d = 1.6-20; Re=200-100,000; A_f = 0.0008-0.02	$Nu_{ave} = 0.3Re^{0.68}Pr^{0.42}C_F^{0.56}\left(H/d\right)^{-0.3}A_f^{0.15}$ Flow coefficient C_F defined in paper
Miao et al. (2009)	Inline&staggered array; Hybrid crossflow; Re=2,440-14,640; H/d=1-6; S/d=6	$Nu_{ave} = CRe^b$ Constances tabulated in paper
Goodro et al. (2009)	Array of jets impinging on a flat surface Re=18,000; Ma=0.2; S/d=8	$\dfrac{Nu_{ave}}{Nu_{ave,cp}} = (\dfrac{T_w}{T_j})^{-0.35}$ $Nu_{ave,cp}$: Nu_{ave} at T_w/T_j=1.06
Katti et al. (2009)	In-line arrays; Re= 3,000-10,000; H/d=1-3; S_x/d = 3-5; S_y/d =4	$Nu_{ave} = a_o(Re^{a1}Pr^{0.333})(\dfrac{G_j}{G_j})(1-b_1\dfrac{G_c}{G_j})^{b2}$ Coefficient tabulated in paper
Goodro et al. (2010)	An array of jets impinging on a flat surface, Re=17,300-60,000; Ma =0.1-0.45; S/d =5-12	For S/d =5; $Nu_{ave} / Nu_{aveF} = 0.95+1.2Ma^{1.6}$ For S/d =8; $Nu_{ave} / Nu_{aveF} =1+1.2Ma^{1.9}$ For S/d =12; $Nu_{ave} / Nu_{aveF} =1.1+1.2Ma^{2.3}$
Attalla 2015	Five circular free jets, straight pipe, Re=1,000-45,000; H/d=2-6, S/d=2	$Nu_{ave} = 0.105Re_j^{0.68}Pr^{0.33}\left(H/d\right)^{-0.103}$ $Nu_{st} \propto Re^{0.61}$
Bu et al. 2016	Three rows jets on a concave surface; Re=50,000-90,000; H/d =1.74-20;θ=66°-90°; l_{arc}/d=13.2-34.8	$Nu_{st} = 1.827\times10^{-4} Re^{1.124} \theta_{rad}^{0.847}(H/d)^{-0.487}$ $Nu_x / Nu_{st} = 100-0.76828Re^{0.39970}(H/d)^{-0.19912}(l_{arc}/d)^{0.052781}$ $+[0.76828Re^{0.39970}(H/d)^{-0.19912}(l_{arc}/d)^{0.052781}]$ $\times\exp[-0.009385Re^{0.4970}(H/d)^{-0.1320}(l_{arc}/d)^{-2.1134}(x/d)^2$
Ansu et al. (2016)	A single row of jets; Re=5,000-15,000; H/d=1-6;S/d=0-6	Single row of orifice: H/d=2-6; S/d=0-6 $Nu_{ave} = \dfrac{2.9Re^{0.69}e^{-0.196(S/d)^{1.049}}}{22.8+4(H/d)^{0.122}}$ Single row of pipe: H/d=1-4;S/d=0-6 $Nu_{ave} = \dfrac{69.7Re^{0.36}e^{-0.243(S/d)^{1.29}}}{22.8+4(H/d)^{-0.082}}$ Single row of pipe: H/d=4-6;S/d=0-6 $Nu_{ave} = \dfrac{29.45Re^{0.47}e^{-0.267(S/d)^{1.16}}}{22.8+4(H/d)^{0.544}}$
Patil&Vedula (2018)	A row of circular jets on a concave surface; Re=10,000-50,000; H/d= 0.67-8; S/d=4; L/d=0.2-6; d/D= 0.1-0.3	Nu was averaged over a specific angular distance=25° $Nu_{ave} = 0.24Re^{0.637}(H/d)^{-0.159}(d/D)^{0.0095}(L/d)^{0.013}$ Nu was averaged over a specific angular distance=45°

		$Nu_{ave} = 0.233 Re^{0.647} (H/d)^{-0.169} (d/D)^{0.149} (L/d)^{0.008}$
		Nu was averaged over a specific angular distance=90º
		$Nu_{ave} = 0.232 Re^{0.666} (H/d)^{-0.159} (d/D)^{0.312} (L/d)^{0.004}$

Appendix C

C Description of the Grid Convergence Index (GCI)

The GCI method is based on the use of three successively refined grids addressed as fine grid (1), intermediate grid (2) and coarse grid (3). The fine grid convergence index can be determined as

$$GCI_{fine}^{21} = \frac{1.25 \left| \frac{\varphi_1 - \varphi_2}{\varphi_1} \right|}{r^p - 1} \tag{C.1}$$

The refinement factor r is defined as

$$r = (\frac{N_1}{N_2})^{1/3} \tag{C.2}$$

Where N is the total number of cells used for the computations, it is desirable that the refinement factor r be greater than 1.3. Therefore, the grid refinement was done systematically with r=1.3.

The apparent order of the method p is calculated using the equation

$$p = \frac{1}{\ln r} \left| \ln \frac{\varphi_3 - \varphi_2}{\varphi_2 - \varphi_1} \right| \tag{C.3}$$

Where φ_k denotes the solution on the *k*th grid.

Curriculum Vitae

Name: Ali Chitsazan

Date of birth: 11.09.1986

Place of birth: Ahvaz, Iran

Professional Career

2014-2020   **Research Assistant and Doctoral Researcher**

Institute for Energy Research, Ostwestfalen-Lippe University of Applied Sciences, Lemgo, Germany in cooperation with Institute for Multiphase Processes, Leibniz University Hannover, Hanover, Germany.

2011-2014   **Mechanical Engineer**

Scetiran Consulting Engineers Co., Ahvaz, Iran.

2012-2014   **University Lecturer**

Azad University, Susangerd, Iran

Studies

2020   **Ph.D. in Mechanical Engineering**

Leibniz University Hannover, Hanover, Germany

2012   **M.Sc. in Mechanical Engineering**

Shahid Chamran University, Ahvaz, Iran

2009   **B.Sc. in Mechanical Engineering**

Azad University, Ahvaz, Iran.